

Lecture Notes in Civil Engineering

Thanh Bui-Tien
Long Nguyen Ngoc
Guido De Roeck *Editors*

Proceedings of the 3rd International Conference on Sustainability in Civil Engineering

ICSCE 2020, 26–27 November, Hanoi,
Vietnam

 Springer

Lecture Notes in Civil Engineering

Volume 145

Series Editors

Marco di Prisco, Politecnico di Milano, Milano, Italy

Sheng-Hong Chen, School of Water Resources and Hydropower Engineering,
Wuhan University, Wuhan, China

Ioannis Vayas, Institute of Steel Structures, National Technical University of
Athens, Athens, Greece

Sanjay Kumar Shukla, School of Engineering, Edith Cowan University, Joondalup,
WA, Australia

Anuj Sharma, Iowa State University, Ames, IA, USA

Nagesh Kumar, Department of Civil Engineering, Indian Institute of Science
Bangalore, Bengaluru, Karnataka, India

Chien Ming Wang, School of Civil Engineering, The University of Queensland,
Brisbane, QLD, Australia

Lecture Notes in Civil Engineering (LNCE) publishes the latest developments in Civil Engineering - quickly, informally and in top quality. Though original research reported in proceedings and post-proceedings represents the core of LNCE, edited volumes of exceptionally high quality and interest may also be considered for publication. Volumes published in LNCE embrace all aspects and subfields of, as well as new challenges in, Civil Engineering. Topics in the series include:

- Construction and Structural Mechanics
- Building Materials
- Concrete, Steel and Timber Structures
- Geotechnical Engineering
- Earthquake Engineering
- Coastal Engineering
- Ocean and Offshore Engineering; Ships and Floating Structures
- Hydraulics, Hydrology and Water Resources Engineering
- Environmental Engineering and Sustainability
- Structural Health and Monitoring
- Surveying and Geographical Information Systems
- Indoor Environments
- Transportation and Traffic
- Risk Analysis
- Safety and Security

To submit a proposal or request further information, please contact the appropriate Springer Editor:

- Pierpaolo Riva at pierpaolo.riva@springer.com (Europe and Americas);
- Swati Meherishi at swati.meherishi@springer.com (Asia - except China, and Australia, New Zealand);
- Wayne Hu at wayne.hu@springer.com (China).

All books in the series now indexed by Scopus and EI Compindex database!

More information about this series at <http://www.springer.com/series/15087>

Thanh Bui-Tien · Long Nguyen Ngoc ·
Guido De Roeck
Editors

Proceedings of the 3rd International Conference on Sustainability in Civil Engineering

ICSCE 2020, 26–27 November, Hanoi,
Vietnam

 Springer

Editors

Thanh Bui-Tien
University of Transport
and Communications
Hanoi, Vietnam

Long Nguyen Ngoc
University of Transport
and Communications
Hanoi, Vietnam

Guido De Roeck
Department of Civil Engineering
KU Leuven
Heverlee, Belgium

ISSN 2366-2557

ISSN 2366-2565 (electronic)

Lecture Notes in Civil Engineering

ISBN 978-981-16-0052-4

ISBN 978-981-16-0053-1 (eBook)

<https://doi.org/10.1007/978-981-16-0053-1>

© The Editor(s) (if applicable) and The Author(s), under exclusive license to Springer Nature Singapore Pte Ltd. 2021

This work is subject to copyright. All rights are solely and exclusively licensed by the Publisher, whether the whole or part of the material is concerned, specifically the rights of translation, reprinting, reuse of illustrations, recitation, broadcasting, reproduction on microfilms or in any other physical way, and transmission or information storage and retrieval, electronic adaptation, computer software, or by similar or dissimilar methodology now known or hereafter developed.

The use of general descriptive names, registered names, trademarks, service marks, etc. in this publication does not imply, even in the absence of a specific statement, that such names are exempt from the relevant protective laws and regulations and therefore free for general use.

The publisher, the authors and the editors are safe to assume that the advice and information in this book are believed to be true and accurate at the date of publication. Neither the publisher nor the authors or the editors give a warranty, expressed or implied, with respect to the material contained herein or for any errors or omissions that may have been made. The publisher remains neutral with regard to jurisdictional claims in published maps and institutional affiliations.

This Springer imprint is published by the registered company Springer Nature Singapore Pte Ltd. The registered company address is: 152 Beach Road, #21-01/04 Gateway East, Singapore 189721, Singapore

Organizers and Sponsors

Organizer:



Sponsor:



ICSCE 2020 International Scientific Committee

Chairs and Co-chairs

Prof. Nguyen Ngoc Long, University of Transport and Communications, Vietnam
Prof. Guido De Roeck, KU Leuven, Belgium
Prof. Matt Evans, Oregon State University, USA
Prof. Yasuhiro Dosho, Meijo University, Japan
Prof. Jinhai Zheng, Hohai University, China
Prof. Yasuyuki Nakagawa, Kyushu University, Japan
Prof. Jose Campos e Matos, Universidade do Minho, Portugal
Prof. Sang-Woong Lee, Gachon University, Korea
Prof. Cheong Siew Ann, Nanyang Technological University, Singapore
Prof. Nasser Khalili, University of New South Wales, Australia

Scientific Members

Prof. Anand J. Puppala, Texas A&M University, USA
Prof. Günther Meschke, Ruhr University Bochum, Germany
Prof. Hajime Mase, Kyoto University, Japan
Prof. Farid Asma, Mouloud Mammeri University of Tizi-Ouzou, Algeria
Prof. Hocine Hammoum, Mouloud Mammeri University, Algeria
Prof. Shimizu Norikazu, Yamaguchi University, Japan
Prof. Tatsunori Matsumoto, Kanazawa University, Japan
Prof. Torsten Schlurmann, Leibniz University Hannover, Germany
Prof. Watabe Yoichi, Hokkaido University, Japan
Prof. Yakun Guo, University of Bradford, UK
Prof. Zhang Jisheng, Hohai University, China
Prof. Zoubir Mehdi Sbartäi, Université de Bordeaux, France
Prof. Takeshi Katsumi, Kyoto University, Japan

Prof. Tran Hoai Nam, Auburn University, USA
Prof. Magd Abdel Wahab, Ghent University, Belgium
Prof. Zhang Chi, Hohai University, China
Assoc. Prof. Pham Huy Giao, Asian Institute of Technology, Thailand
Dr. Nguyen Anh Minh, ODE—DORIS Group Company, UK
Dr. Nguyen Mai Lan, IFSTTAR, Nantes, France
Dr. Nguyen Minh Hai, University of Texas at Arlington, USA
Dr. Samir Khatir, Ghent University, Belgium
Dr. Tang Anh Minh, Ecole des Ponts ParisTech, France
Dr. Trinh Viet Nam, Egis Rail—Groupe Egis, France
Dr. Ho Manh Hung, Bentley, Singapore

ICSCE 2020 Organizing Committee

Local Organizing Committee

Assoc. Prof. Thanh Bui-Tien, University of Transport and Communications, Vietnam (Chair)

Assoc. Prof. Nguyen Viet Thanh, University of Transport and Communications, Vietnam (Co-chair)

Dr. Nguyen Xuan Tung, University of Transport and Communications, Vietnam (Co-chair)

Assoc. Prof. Nguyen Duy Tien, University of Transport and Communications, Vietnam

Assoc. Prof. Nguyen Thi Tuyet Trinh, University of Transport and Communications, Vietnam

Assoc. Prof. Do Anh Tu, University of Transport and Communications, Vietnam

Assoc. Prof. Nguyen Chau Lan, University of Transport and Communications, Vietnam

Dr. Bui Ngoc Dung, University of Transport and Communications, Vietnam

Dr. Dang Minh Tan, University of Transport and Communications, Vietnam

Secretariat

Dr. Nguyen Quang Tuan, University of Transport and Communications (Chair)

Assoc. Prof. Tran Thu Hang, University of Transport and Communications

Dr. Dang Hong Lam, Geotechnics Section, UTC

Dr. Ta Duy Hien, Section of Structural Mechanics, UTC

Dr. Tran Anh Tuan, Bridge and Tunnel Engineering Section, UTC

Dr. Le Van Hien, Geodesy Section, UTC

Dr. Mai Quang Huy, Hydraulics and Hydrography Section, UTC

Dr. Vu Ngoc Linh, Mechanics of Material, UTC

Dr. Pham Van Phe, Section of Structural Mechanics, UTC
Dr. Nguyen Trong Hiep, Section of Highway and Airfield Engineering, UTC
Dr. Le Vinh An, Highway Engineering Section, UTC
Msc. Tran Ngoc Hoa, Bridge and Tunnel Section, UTC
Msc. Nguyen Ngoc Lan, Bridge and Tunnel Section, UTC
Msc. Nguyen Thi Mai Anh, Accounting Department, UTC
Msc. Nguyen Thanh Minh, Administration section, UTC
Msc. Pham Phuong Thao, Administration section, UTC

Advisory Committee Members

Prof. Bui Xuan Cay, Highway Section, UTC
Prof. Pham Huy Khang, Highway and Airfield Engineering, UTC
Prof. Tran Duc Nhiem, Bridge and Tunnel Section, UTC
Prof. Pham Van Ky, Railway Section, UTC
Assoc. Prof. La Van Cham, Highway Section, UTC
Assoc. Prof. Le Hai Ha, Railway Section, UTC
Assoc. Prof. Nguyen Quang Phuc, Highway Section, UTC
Assoc. Prof. Hoang Ha, Urban Transport and Marine-Coastal Engineering Section, UTC
Assoc. Prof. Tran The Truyen, Bridge and Tunnel Section, UTC
Assoc. Prof. Luong Xuan Binh, Mechanics of Material, UTC
Assoc. Prof. Ho Anh Cuong, Transport-Public Works and Environment Section, UTC
Assoc. Prof. Ho Lan Huong, Geodesy Section, UTC
Assoc. Prof. Ngo Van Minh, Bridge and Tunnel Section, UTC
Assoc. Prof. Nguyen Trung Kien, Structural Mechanics Section, UTC
Assoc. Prof. Pham Hoang Kien, Informatics in Civil Engineering, UTC
Dr. Tong Anh Tuan, Hydraulics and Hydrography Section, UTC
Dr. Phung Duc Long, VSSMGE
Assoc. Prof. Nguyen Thanh Sang, Section of Building Materials, UTC
Assoc. Prof. Nguyen Xuan Huy, Section of Structural Engineering, UTC

Preface

This proceedings includes the full papers selected and accepted at the International Conference on Sustainability in Civil Engineering—ICSCE 2020, broadcasted online and offline from University of Transport and Communications, Hanoi, Vietnam, on November 26–27, 2020. ICSCE conference series is organized by Faculty of Civil Engineering under the approval of University of Transport and Communications (UTC). UTC was founded in 1945 as a leading university in Vietnam, with campuses in Hanoi and Ho Chi Minh City.

The ICSCE conference series is organized since 2016, and 2020 is its third edition, scheduled to take place with a 2-year interval. The ICSCE 2020 theme is “Building a Green Infrastructure for Living” Unfortunately, due to COVID-19 pandemic at the beginning of this year, we were forced to abandon the idea of a physical conference and organize a mix online and offline event. This transition created many administration complications. Nevertheless, UTC and the organizing committee have seen this as an opportunity to organize a different type of event and to propose a new approach for scientific collaboration and communication that respects both the legacy of the conference series and the health of the participants, who would otherwise have enjoyed nice trip to Hanoi.

ICSCE conferences have been established as the top scientific events in the area of sustainable civil engineering and are highly anticipated bi-annually by the international civil engineering community such as highway engineering, bridge engineering, and coastal engineering. For the ICSCE 2020 edition of ICSECE series, more than 200 abstracts and 135 full paper were submitted, of which 46 were selected for publishing in this proceedings and divided into 6 subthemes: Bridges and Structure Engineering, Structural Damage Detection and Health Monitoring; Geotechnical Engineering; Construction Materials; Pavement and Construction Management; River, Coastal, Environmental and Water Resource Engineering; and Transportation in General.

On behalf of Local Organizing Committee (LOC), sincere appreciation is expressed to NAFOSTED, DEOCA GROUP, VSL, NIPPON STEEL, FREYSSINET, PETROLIMEX, FECON, RONTAI, SAMJIN, TOTC, YURHSIN, KAWAKIN, TAIYU, SLS TECH for their support. Sincerely thanks are sent to the

international scientific committee for their great support and contribution. LOC thanks all keynote speakers, chairpersons, and reviewers for the efforts in preparing the manuscripts, reviewing, and managing the sessions, respectively. LOC also thanks all authors for their heartfelt contributions to the ICSCCE 2020. Without all of you, the ICSCCE 2020 will never be successful.

Assoc. Prof. Thanh Bui-Tien
LOC Chairman of ICSCCE 2020

Dean of Faculty of Civil Engineering
University of Transport and Communications (UTC)
Hanoi, Vietnam

Contents

Keynotes

An Effective Stress Framework for Bearing Capacity of Shallow Foundations in Unsaturated Soils	3
T. Matthew Evans and Josiah D. Baker	
Dynamical Motifs in Temporal Networks	15
He Sun and Siew Ann Cheong	
Field Measurements of Fine Sediment Transport Processes in Japanese Estuaries	23
Yasuyuki Nakagawa	
Bridge-Structural Engineering, Structural Damage Detection and Health Monitoring	
Damaged Detection in Structures Using Artificial Neural Networks and Genetic Algorithms	33
Lan Nguyen-Ngoc, Hoa Tran-Ngoc, Hieu Nguyen-Tran, Binh Nguyen-Duc, Dang Nguyen-Le-Minh, Thanh Bui-Tien, and Magd Abdel Wahab	
Effect of Metal Corrosion on the Structural Reliability of the 3D Steel Frames	39
Ngoc-Long Tran and Trong-Ha Nguyen	
Global Sensitivity Analysis of the Buckling Strength for Battered Built-up Columns Steel Considering Shear Deformations	45
Ngoc-Long Tran and Trong-Ha Nguyen	
Simulations of Local Scour Depth at Piers of the Ben Thuy Bridge, Nghe an Province	53
Chien Pham Van	

Load Carrying Capacity Old Steel Girder with Considering Corrosion Effect of Steel Material	61
Pham Van Hung, Nguyen Duc Hieu, Bui Thanh Tung, and Tran The Truyen	
Research on Monitoring Technology of Cable-Stayed Bridge	69
Jiabao Du, Zhao Hong, Yuan Chen, Yahui Li, Jinzhu Song, and Qiang Tang	
Geotechnical Engineering	
A Consolidation Solution of Soft Soil Deposits Improved with Prefabricated Vertical Drains and Deep Cement Mixing Columns	79
Ba-Phu Nguyen, Phuong Chau Ngo, Quang Dung Nguyen, Trong Thach Le, and Nhat-Phi Doan	
Effect of Grain Size on Shear Strength of Coral Gravel Sand	87
Cao Van Hoa, Vu Anh Tuan, Nguyen Thanh Sang, Nguyen Tuong Lai, and Pham Duc Tiep	
Landslide Susceptibility Mapping for the Thao River Catchment with High Spatial Resolution Rainfall Data	97
The Viet Tran, Manh Cuong Nguyen, Quang Toan Trinh, Hoai Nam Do, Trung Kien Nguyen, Kien-Trinh Thi Bui, Quoc Thanh Nguyen, and Duc Ha Nguyen	
Investigation of Anchor Load During the Construction of an Excavation in Hanoi	105
Tuan-Nghia Do	
Potential Using Municipal Solid Bottom Ash for Road Construction	113
Chau Lan Nguyen, Anh Tuan Nguyen, Hai Ha Nguyen, and Anh-Tuan Vu	
Performance of a New Low-Cost GPS Sensor with an Average Process for Slope Displacement Monitoring	119
Nguyen Trung Kien and Norikazu Shimizu	
Study on the Change of Deformation Modulus of Ho Chi Minh City' Soft Soil Under the Extension Stress Paths for Deep Excavation Calculation	127
Trung Ngo Duc	
The Shapes of Collapsed Sinkholes at Limiting Equilibrium	135
Rengifo Arakaki Kimiko, Vo Thanh, and R. Adrian Russell	

Construction Materials

A Study on Tunnel Lining Concrete with Crushed Aggregate from NATM Muck 145
 Thu-Hang Tran

Effect of Nano-Silica Content on Compressive Strength and Modulus of Elasticity of High-Performance Concrete 153
 Van Thuc Ngo, Tien Thanh Bui, Thi Cam Nhung Nguyen, Thi Thu Nga Nguyen, and Thanh Quang Khai Lam

Experimental Investigation of Fatigue Behavior for Polymer Modified Asphalt and Epoxy Asphalt Mixtures 161
 Quang Tuan Nguyen and Thi Cam Ha Tran

Effect of Steel Fiber Content on the Shrinkage of Steel Fiber Reinforced Concrete in the Tropical Environment in Vietnam 167
 Ngoc Tan Nguyen and Vinh An Le

Research on Using Polymer Concrete for Portland Cement Concrete Airfield Pavement Repair—An Experimental Application of Noi Bai International Airport of Vietnam 175
 Pham Huy Khang and Nguyen Trong Hiep

Strength, Water Porosity and the Shrinkage of Self-Compacting Concrete in Hot Climate 183
 Vinh An Le, Ngoc Tan Nguyen, Xuan Cay Bui, and Tuan Anh Bui

The Influence of Aggregate Size and Blocking Materials to the Water Infiltration Rates of Pervious Concrete 189
 Hung Viet Vu and Soo Yeon Seo

Research on the Reinforcement of Basalt Soil Using Natural Pozzolan, Cement, and Lime for Building Rural Roads in Dak Nong Province, Vietnam 195
 Truong Son Bui, Ba Thao Vu, Thi Nu Nguyen, and Thanh Duong Nguyen

Pavement and Construction Management

Evaluation and Recommendation for Management and Maintenance Specification of Rural Bridge in Vietnam 205
 Xuan Tung Nguyen and Tuan Dung Pham

Low Traffic Road Pavement Deterioration in Vietnam 213
 Thi Kim Dang Tran

Numerical Analysis of the Influence of Shield-Gap Pressure on the Volume Loss and Surface Settlement of the TBM Tunneling 221
 Thach Bich Nguyen, Thanh Le Le, and Phuong Duy Nguyen

**Developing the Success Index of Public-Private Partnership
Transportation Projects in Vietnam 229**
Thac Quang Nguyen, Dinh Thuc Le, and Duy Liem Nguyen

River, Coastal, Environmental and Water Resources Engineering

Applicability of Duct-Type Devices to Erosion Tests of Sediments 239
Dake Chen, Jinhai Zheng, Chi Zhang, Yigang Wang, and Yuan Li

**Experimental Measurements of Wave Transformation
on Coral Reefs 247**
Pham Thi Thuy, Le Hai Trung, and Nguyen Manh Linh

**Investigation the Influence of Cua Tien Urban Area on Flood
Drainage Capacity of Vinh River, Vinh City, Nghe an Province
by Numerical Model. 255**
Nguyen Viet Thanh, Hoang Nam Binh, and Bui Vinh Phuc

**Field Measurement of Wave Overtopping Frequency and Intensity
at Sea Dike Using Shore-Based Video Images 263**
Shanhang Chi, Chi Zhang, Zhubin Cao, and Jinhai Zheng

**Designing the Paradigm that Treats the Wastewater of Concrete
Batching Plants 271**
Vu Phuong Thao

**Research on Automated Monitoring to Access the Port Structure
Inspection in Operating Offloading Vessel Test 277**
Duong Thi Bach Nguyen, Van Hien Le, and Duc Cong Tran

**Sand-Spit Evolution and Inlet Dynamics Derived from Satellite
Images: A Case Study for Tien Chau Inlet, Vietnam 287**
Tran Thanh Tung, Nguyen Quang Chien, and Do Xuan Tinh

**Wave Energy Assessment Along Chinese Coasts Based
on a 40-Year Hindcast 295**
Jiali Xu, Jian Shi, and Chi Zhang

**A Framework to Develop Intensity-Duration-Frequency Curves
for Ungauged Sites in Vietnam: The Case of Hoa Binh Province 303**
Noi Thi Doan, Thanh Tien Nguyen, and Son Hoang Nguyen

**Assessment of Hydrodynamic Regime and Inundation Mode After
Construction of Hydraulic Project in Quang Ngai Province. 311**
Nguyen Phuong Dung, Nguyen Thai Binh, and Tran Thi Hoai Phuong

**River Water Level Prediction Based on Deep Learning: Case Study
on the Geum River, South Korea 319**
Xuan-Hien Le, Sungho Jung, Minho Yeon, and Giha Lee

Validation of Some Empirical Equations to Estimate Bridge Abutment Scour in Non-cohesive Soil Using Field Data 327
Huy Quang Mai, Phong Dang Nguyen, and Tuan Anh Tong

Transportation in General

A Neural Network Approach for Solving Traffic-Flow Forecasting Based on the Historical Voyage Datasets: A Case Study on Hai Phong Roads 337
Quang Hoc Tran, Van Truong VU, Quang LE, Thi Lan Huong HO, and Van Hien LE

ICD Concept: An Overview of the Development from an Original Purpose to a Global Viewpoint..... 343
Vu Quoc Hung, Vu Minh Tuan, and Nguyen Viet Phuong

Fatigue Life Evaluation of Bogie Frame of Railway Covered Goods Wagons Using a Combined FEA/MDS Approach 351
Tuan Duc Do, Dat Tuan Vu, Toan Duc Nguyen, and Tu Anh Do

Maximum Likelihood Estimation Method for Speed Prediction of Vehicles in Mixed Traffic Condition..... 359
Dang Minh Tan, Nguyen Hoang Tung, and Bui Xuan Cay

Transportation Development Strategy in Coordinating with Urban Dynamics: Case Study in Hanoi 367
Le Thu Huyen

Keynotes

An Effective Stress Framework for Bearing Capacity of Shallow Foundations in Unsaturated Soils



T. Matthew Evans and Josiah D. Baker

Abstract This manuscript presents a theoretical framework to model the bearing capacity of shallow foundations on partially saturated soils. The conventional Vesic bearing capacity equations for shallow foundations are modified to include the effects of matric suction and varying water contents and unit weights within the effective stress framework. Suction and water content are related through the familiar van Genuchten constitutive model, thus linking suction stress to density for a homogenous soil skeleton. A closed-form solution that modifies the overburden, unit weight, and cohesion terms in the conventional Vesic equation is proposed. Bearing capacity predictions from the modified equation for shallow foundations are compared to results from model- and full-scale load tests in partially saturated soils presented in the literature, showing good agreement with observed response.

Keywords Shallow foundations · Bearing capacity · Unsaturated soils

1 Review of the Theoretical Background

1.1 Bearing Capacity of Shallow Foundations

The ultimate bearing capacity and failure of a shallow foundation has been defined in a variety of ways. Defining ultimate bearing capacity with a critical state seems the most reasonable; however, this state is not often achieved as many soils will continue to increase capacity while loading (strain hardening), or when the soil strength/foundation size is large enough such that the critical state cannot be reached. In this case, a criterion for peak strength must be set. In this work, ultimate bearing capacity will be defined by either a peak strength, or the asymptote of a fitted hyperbolic curve as proposed by Kondner [1].

T. M. Evans (✉) · J. D. Baker
School of Civil and Construction Engineering, Oregon State University, Corvallis, OR, USA
e-mail: matt.evans@oregonstate.edu

Terzaghi [2] proposed the original ultimate bearing capacity for plane-strain failure of a strip (continuous) footing. This equation has been subsequently modified by researchers to account for other factors including embedment depth and variation in footing shape, or to modify the original bearing capacity factors [3–7]. Vesić [6] proposed Eq. (1) for the calculation of ultimate bearing capacity:

$$q_{ult} = c'N_cS_c d_c + \sigma'_{zD}N_qS_q d_q + 0.5\gamma'BN_\gamma s_\gamma d_\gamma \quad (1)$$

where c' is effective cohesion, σ'_{zD} is the effective stress at the depth of embedment, γ' is the effective soil unit weight, B is the footing width, N_c , N_q , and N_γ are bearing capacity factors, S_c , S_q , and s_γ are shape factors, and d_c , d_q , and d_γ are depth factors. The bearing capacity, shape, and depth, factors used in this work may be found in any standard textbook on the topic. The shape factors are those proposed by Hansen [4] whereas N_c and N_q are the original bearing capacity factors from Prandtl [8].

1.2 Suction, Stress, and Strength in Unsaturated Soils

Soil water characteristic curves (also known as soil water retention curves) describe the relationship between suction and water content in soils [9] and other porous media [10, 11]. Several models have been proposed to fit discrete laboratory data and to continuously describe the soil water characteristic curve [12–14]. Van Genuchten [13] proposed Eq. (2) as a model for the soil water characteristic curve (SWCC):

$$S_e = \frac{\theta - \theta_r}{\theta_s - \theta_r} = \left[\frac{1}{1 + (\alpha\psi)^n} \right]^{1-\frac{1}{n}} \quad (2)$$

where S_e is effective saturation, θ is the volumetric water content (i.e., V_w/V_t), θ_s is the saturated water content (numerically equal to the porosity), ψ is matric suction (i.e., $\psi = u_a - u_w$), and θ_r is the residual water content, and α , m and n are fitting parameters; however, both α and n do not have physical correlations. Soils above the groundwater table are partially saturated, where nonlinearity in stress arises due to the existence of both a gas and liquid phase in the pores. Bishop [15] proposed an effective stress parameter χ which is a function of suction and physical soil properties, into Terzaghi's effective stress equation:

$$\sigma' = \sigma - u_a + \chi(u_a - u_w) \quad (3)$$

$\chi = 1$ at saturation and $\chi = 0$ when dry. The last term in Eq. (3) is the suction stress, σ_s [9, 16]:

$$\sigma_s = \chi(u_a - u_w) \quad (4)$$

where χ is often approximated as equal to effective saturation, S_e . Using Bishop's definition of effective stress, the Mohr-Coulomb failure criterion can be modified such that it includes the effects of matric suction and partial saturation:

$$\tau_f = c' + (\sigma - u_a) \tan \phi' + \chi \psi \tan \phi' \quad (5)$$

where, τ_f is the shear stress at failure.

To account for the effects of partial saturation on soil response in situ, it is necessary to know the matric suction profile. Using the Gardner [17] conductivity function, Lu and Griffiths [18] derive an equation to calculate matric suction as a function of permeability, infiltration/evaporation rates, and height above the groundwater table:

$$\psi = -\frac{1}{\alpha} \ln \left[\left(1 + \frac{q}{k_s} \right) e^{-\alpha \gamma_w z} - \frac{q}{k_s} \right] \quad (6)$$

where q is the flux rate (evaporation is positive and infiltration negative), k_s is the saturated hydraulic conductivity, z is the distance above the ground water table, and α is the fitting parameter used in the van Genuchten equation (assumed to be the inverse of the air-entry suction). When there is no net flow, the equation reduces to the hydrostatic case, $\psi = \gamma_w z$.

1.3 Shallow Foundations Emplaced in Unsaturated Soils

More recently, researchers have studied the effects of partial saturation and suction stress in foundation performance through foundation load tests in partially saturated soils [19–24] and by continued modification of the conventional bearing capacity equation [25–27]. These studies have shown that partially saturated soils, especially silts and clays, often have bearing capacities greater than the predicted bearing capacity for a completely dry or completely saturated soil. To account for partial saturation, the cohesion term is typically modified within the bearing capacity equation to account for apparent cohesion caused by suction stresses [25, 27, 28].

2 Theoretical Development and Numerical Example

In traditional foundation design, resistance is derived from three primary components: cohesion, unit weight, and surcharge loads. These three components are directly influenced by the value of the friction angle through bearing capacity factors. The shape of the failure surface is understood to be a function of friction angle [8]. Here we assume that the shape of the failure surface does not change as a function of varying suction stresses and soil unit weights. We further assume that the mean apparent cohesion (\bar{c}'') defined in Eq. (7) can be directly implemented into the bearing capacity equation:

$$\bar{c}'' = \frac{1}{\ell} \int_{\ell} c'' ds = \frac{1}{\ell} \int_{\ell} \sigma_s \tan \phi' ds = \frac{1}{\ell} \int_{\ell} \psi \chi \tan \phi' ds \quad (7)$$

where ℓ is the length of the failure surface. This is appropriate since failure in the shallow foundation bearing capacity framework is defined by the Mohr-Coulomb (M-C) failure criterion and apparent cohesion due to suction stress shifts the failure envelope upward in M-C space. The general bearing capacity equation is thus modified as shown in Eq. (8):

$$q_{ult} = (c' + \bar{c}'')N_c s_c d_c + q_s N_q s_q d_q + 0.5 \bar{\gamma}' B N_{\gamma} s_{\gamma} d \quad (8)$$

where c' is the soil effective cohesion, q_s is the overburden stress at the base of the footing (including the suction stress), and $\bar{\gamma}'$ is the average effective soil unit weight within the log spiral failure surface. The modified overburden and effective unit weight terms in Eq. (8) are defined in Eqs. (9) and (10), respectively:

$$q_s = \begin{cases} \sigma_{zD} + \sigma_{s,D} = \sigma_{zD} + (\psi \chi)_D & \text{if } D < z_w \\ \sigma_{zD} - u & \text{if } D \geq z_w \end{cases} \quad (9)$$

$$\bar{\gamma}' = \frac{1}{A} \int_A \gamma'(\psi) dA \quad (10)$$

where σ_{zD} is the net normal vertical stress at the depth of embedment, $\sigma_{s,D}$ is the suction stress at the depth of embedment, z_w is the depth of the groundwater table, u is porewater pressure, A is the total area contained by the failure surface.

To demonstrate how this approach is implemented, an example strip footing embedded in partially saturated soil is considered. The following example includes soil with hydraulic properties selected such that the majority of suction stresses exist within 3 m of the groundwater table ($\{\theta_s, \theta_r, \alpha, n\} = \{0.385, 0.0385, 0.175 \text{ kPa}^{-1}, 2.5\}$); shear strength ($\phi' = 20^\circ$) was selected such that the failure surface extends to a depth of nearly 3 m (for a 2 m wide footing

embedded 0.5 m). The failure surface extends to just above the groundwater table, as shown in Fig. 1. In this example, the failure surface extends to a depth of 2.85 m. This foundation is considered loaded to the ultimate limit state, where continuous plastic flow occurs.

The saturation profile of the soil can be defined by the proximity of the layer to the depth of the groundwater table. For hydrostatic conditions in a homogenous soil, matric suction increases linearly above the groundwater table; this results in nonlinear variation of water content, Bishop’s χ , and suction stress (Eq. 4). Using this approach, the saturation of the soil can be determined at any point along the failure surface. This enables the calculation of average suction stress acting along the failure surface. Figure 2 shows the saturation and corresponding apparent cohesion $c'' = \sigma_s \tan \phi'$, across the failure surface according to its proximity from the groundwater table.

The averaged unit weight in the failure wedge is used directly in the modified framework. The moist unit weight profile is calculated with Eq. (11):

$$\gamma_m = (G_s(1 - \theta_s) + \theta_s S_e)\gamma_w \tag{11}$$

where γ_m is the moist unit weight, G_s is the specific gravity, γ_w is the unit weight of water, and all other terms are as previously defined. From Eq. (11), the average unit weight is $\bar{\gamma}' = 17.3 \text{ kN/m}^3$. The conventional approach assumes that the average unit weight varies between the buoyant unit weight when the groundwater table is above the depth of embedment and a dry/moist unit weight when the groundwater table is greater than the depth of embedment plus the footing width ($D + B$). For this particular soil, the unit weight using the conventional approach is estimated to be 16.4 kN/m^3 , a difference of 0.9 kN/m^3 .

The third term in Vesic’s bearing capacity equation is overburden—the effective stress at the base of the footing. In unsaturated soils, this effective stress will include the effects of suction stress. Overburden is the simplest consideration in the Vesic

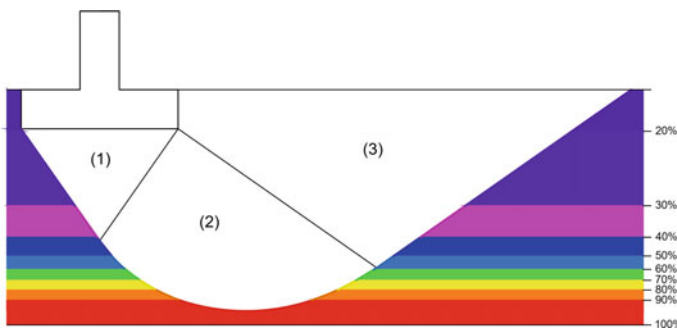


Fig. 1 Contours of degree of saturation in the soil profile for the numerical example. The groundwater table is at the base of the figure and total profile height is 3 m. Only one side of the failure surface is shown for clarity

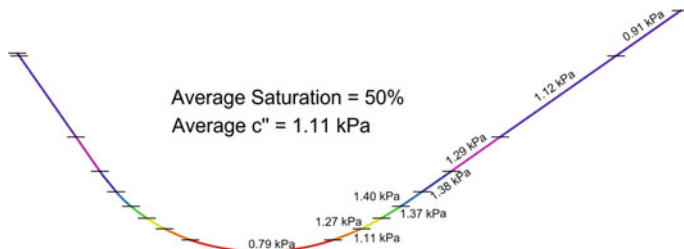


Fig. 2 Failure surface of the shallow foundation colored by the saturation profile. Lines of demarcation indicate apparent cohesion at that location

equation, requiring only knowledge of the soil unit weight above the footing and the suction stress at the embedment depth. In this example, the suction stress at the depth of embedment is 2.7 kPa. The net normal (total) stress can be calculated as the integral of the soil unit weight from the surface to the depth of embedment as shown in Eq. (12):

$$q_s = (\psi\chi)_{zD} + \int_0^D \gamma(z)dz = \sigma_s + \sigma_t \quad (12)$$

where all terms are previously defined. The calculated surcharge in this example is $q_s = 11.1$ kPa. The conventional approach would use the estimated soil unit weight of 16.4 kN/m^3 , as calculated previously, multiplied by the depth of embedment (0.5 m), resulting in an 8.2 kPa overburden.

Combining these considerations, the modified inputs can be used with the Vesic equation. The bearing capacity is calculated to be 187 kPa. If the unmodified approach was used, the bearing capacity would be calculated as 144 kPa. Thus, the modified approach predicts a 30% increase in bearing capacity relative to the conventional approach.

3 Comparison to Measured Results

In this section, we compare the measured responses of shallow foundation load tests from the literature and the calculated bearing capacity from the modified approach considering the effects of partial saturation. This section is important in assessing the ability of the proposed approach to reasonably predict bearing capacity for shallow foundations in partially saturated soils.

There are many works in the literature concerning the bearing capacity of shallow foundation, but there are very few that include soil water characteristic curve (SWCC) and permeability data. This information is crucial for implementation in this work, thus the SWCC must be either predicted or provided. The grain

Table 1 Literature van Genuchten [13] parameters used in the comparative study

	Source of SWCC data	Number of load tests	θ_s	θ_r	α (kPa ⁻¹)	n	m
Steensen-Bach et al. [19]	Provided	6	0.36	0.01	0.14	7.2	0.86
Briaud and Gibbens [31]	GSD	5	0.43	0.03	1.10	3.0	0.13
Viana da Fonseca and Sousa [32]	Classification	1	0.42	0.08	0.37	1.6	0.36
Rojas et al. [33]	Provided	7	0.40	0.00	0.05	1.5	0.33
Vanapalli and Mohamed [25]	Provided	4	0.39	0.00	0.11	5.6	5.60
Vanapalli and Mohamed [23]	Provided	7	0.39	0.00	0.11	5.6	5.60
Wuttke et al. [24]	Provided	4	0.40	0.02	0.91	3.4	0.70

size distribution and soil classification can be used to predict unsaturated soil properties using, e.g., pedotransfer functions. In this work, if the SWCC is not provided, it is estimated in one of two ways: (1) using the values presented by Carsel and Parrish [29] based on USDA soil classifications; or (2) by use of an unsaturated soil database/pedotransfer application, *SoilVision* (Fredlund 2011), if the grain size distribution curve is provided. Carsel and Parrish [30] collected unsaturated properties for over 15,000 soil samples and calculated mean values of van Genuchten [13] parameters according to the USDA textural classification. Average values were reported for each classification, organizing α , n , θ_s , θ_r , and k_s based on percent clays, silts, and sands. The *SoilVision* software (Fredlund [30]) can be used to categorize unsaturated soil based on soil type and grain size distribution either by pedotransfer functions or by comparison to an existing soil database. Through this process, unsaturated parameters can be predicted for implementation in this work.

Another requirement for the literature used in this comparative study is that either an ultimate bearing capacity was achieved in the load test or the ultimate bearing capacity can be calculated from the load displacement curve. If the ultimate state was not achieved, the Kondner [1] hyperbolic equation was fitted to the load displacement curve and q_{ult} taken as the hyperbolic asymptote. Table 1 lists the seven sources used for comparison. The modified bearing capacity was compared to the measured bearing capacity from the load tests presented in these works. Results from Vanapalli and Mohamed [25] and Vanapalli and Mohamed [23] are presented in Figs. 3, 4, and 5 to compare the bearing capacity equation proposed by Vanapalli and Mohamed and the modified approach proposed in this work. In these figures, matric suction is plotted against bearing capacity.

The predicted bearing capacity calculated using the modified approach proposed herein and the measured bearing capacities from Vanapalli and Mohamed [23, 25] show close agreement. For all three load tests, the bearing capacity predicted in this

Fig. 3 Bearing capacity versus variation in average matric suction for a 100×100 mm plate loaded on the surface

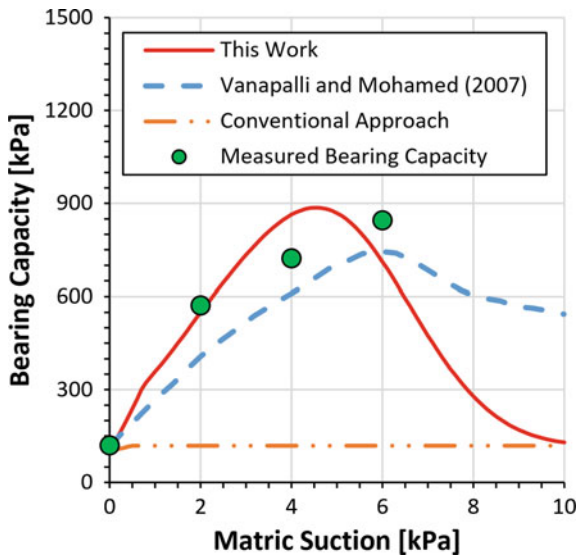
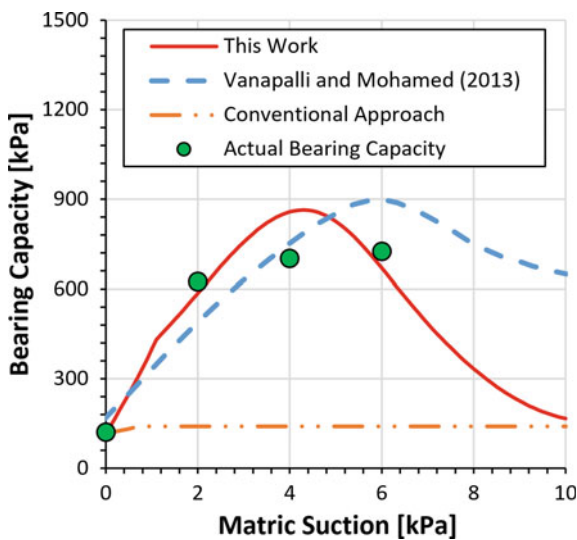


Fig. 4 Bearing capacity versus variation in average matric suction for a 150×150 mm plate loaded on the surface



work quickly reduces after suctions of 5–6 kPa to the conventional bearing capacity equation. This is quite different to the work of Vanapalli and Mohamed [23, 25], who predict a more gradual decline in bearing capacity with increasing suction. The solution proposed by Vanapalli and Mohamed does not decrease to the conventional bearing capacity equation.

The soil used for the tests presented in Figs. 4, 5, and 6 has an air-entry suction around 4–5 kPa and a high van Genuchten n fitting parameter (i.e., relatively

Fig. 5 Bearing capacity versus variation in average matric suction for a 150 × 150 mm plate embedded 150 mm

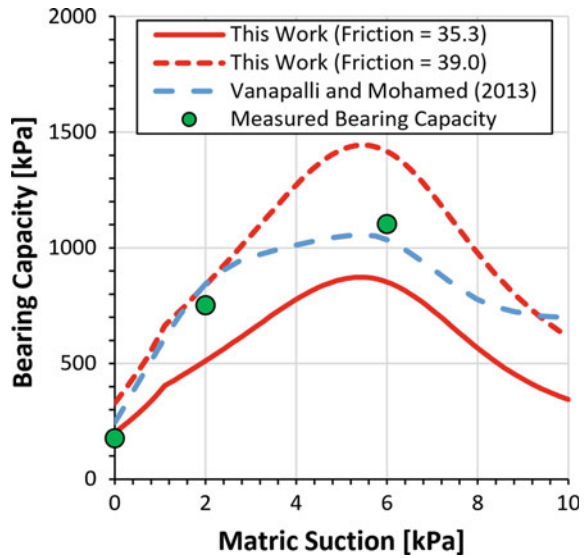
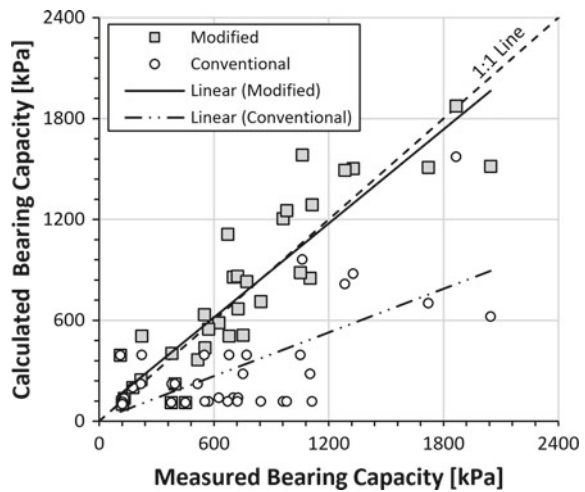


Fig. 6 Measured bearing capacity versus predicted bearing capacity for database of load tests



uniform pore size), so saturation decreases quickly as the matric suction is increased beyond the air-entry suction. The results from the proposed approach capture this rapid desaturation (and corresponding decrease in suction stress) in an organic way—it simply follows the trend dictated by the SWCC and the suction stress profile. The proposed method also shows better agreement with the conventional bearing capacity for dry (high matric suction) and saturated soils (zero matric suction) where suction stress should be very close to zero. The proposed approach does not require any assumption of fitting parameters, but is completely dependent on the soil water characteristic curve. In Fig. 5, Vanapalli and Mohamed [23]

suggest that a friction angle of $\phi' = 35.3^\circ$ be used for embedded foundations, while 39° ($1.1\phi'$) be used for surface foundations to account for dilation. This work shows that friction angles of 39° and 35.3° bracket the measured bearing capacity. This may imply that dilation cannot be ignored for embedded foundations, but rather, that dilation is merely partially suppressed, which is consistent with conventional shear strength theory.

Figure 6 presents a comparison between the measured bearing capacity and the predicted bearing capacity using the proposed and conventional approaches for the load tests listed in Table 1. Lines were fit to the data for comparison against the 1:1 line. The line fit to the modified approach shows closer agreement to the 1:1 line than the conventional approach. The conventional bearing capacity equation will generally underpredict bearing capacity. The slope of the best-fit line for the modified approach is 0.93 while the slope for the conventional approach is 0.43. Using linear regression against the 1:1 line gives a coefficient of determination of $R^2 = 0.806$ (versus 0.811 for the best-fit line). Figure 6 shows that the modified approach gives close agreement with measured data, implying that it is potentially a viable approach for calculating shallow foundation bearing capacity in unsaturated soils.

4 Summary and Conclusions

The purpose of this work was to develop a theoretical framework for calculating ultimate bearing capacity for shallow foundations in partially saturated soils. We have proposed a modification to the conventional Vesic shallow foundation bearing capacity equation to incorporate recent literature on unsaturated soil mechanics. Implementation of concepts from unsaturated soil mechanics included the consideration of apparent cohesion and soil unit weight as they vary with suction and water content, respectively, and the inclusion of suction stress on in calculating overburden stress.

The proposed modifications have been evaluated relative to load tests reported in the literature for shallow foundations in partially saturated soils. The modified bearing capacity equation shows closer agreement with measured bearing capacities than the conventional bearing capacity equation. This implies that the proposed theoretical model for bearing capacity is worthy of additional directed study for use in shallow foundation design. Based on the load tests considered, the conventional method underpredicts bearing capacities in unsaturated soils.

References

1. Kondner RL (1963) Hyperbolic stress-strain response: cohesive soils. J Soil Mech Found Division, ASCE 89(SM1):115–143
2. Terzaghi K (1943) Theoretical soil mechanics. Wiley, New York
3. Meyerhof GG (1963) Some recent research on the bearing capacity of foundations. Can Geotech J 1(1):16–26

4. Hansen JB (1970) A revised and extended formula for bearing capacity. *Geoteknisk Institut* 28:5–11
5. De Beer EE (1970) Experimental determination of the shape factors and the bearing capacity factors of sands. *Géotechnique* 4:387–411
6. Vesić A (1973) Analysis of ultimate loads of shallow foundations. *J Soil Mech Found Division* 1:45–71
7. Kumbhojkar AS (1993) Numerical evaluation of Terzaghi's N_p . *J Geotech Geoenvironmental Eng* 119(3):598–607
8. Prandtl L (1920) Über die Härte plastischer Körper. *Proc Kgl Ges Wiss Göttingen Math Phys* 74–85
9. Lu N, Likos WJ (2004) *Unsaturated soil mechanics*. Wiley, Hoboken, New Jersey
10. Stormont JC, Henry KS, Evans TM (1997) Water retention functions of four nonwoven polypropylene geotextiles. *Geosynth Int* 4(6):661–672
11. Stormont JC, Ray C, Evans TM (2001) Transmissivity of a nonwoven polypropylene geotextile under suction. *ASTM Geotech Test J* 24(2):164–171
12. Brooks RH, Corey AT (1964) Hydraulic properties of porous media. *Hydrology Paper No. 3*, Colorado State University
13. van Genuchten MT (1980) A closed-form equation for predicting the hydraulic conductivity of unsaturated soils. *Soil Sci Soc* 44:892–898
14. Fredlund DG, Xing A (1994) Equations for the soil-water characteristic curve. *Can Geotech J* 31:521–532
15. Bishop AW (1959) The principle of effective stress. *Teknisk Ukeblad* 106(39):859–863
16. Lu N, Likos WJ (2006) Suction stress characteristic curve for unsaturated soil. *J Geotech Geoenvironmental Eng* 132(2):131–142
17. Gardner WR (1958) Some steady state solutions of the unsaturated moisture flow equation with applications to evaporation from a water table. *Soil Sci* 85(4):228–232
18. Lu N, Griffiths DV (2004) Profiles of steady-state suction stress in unsaturated soils. *J Geotech Geoenvironmental Eng* 130(10):1063–1076
19. Steensen-Bach JO, Foged N, Steenfelt JS (1987) Capillary induced stresses—fact or fiction? *Groundwater Effects in Geotechnical Engineering: Proceedings of the Ninth European Conference on Soil Mechanics and Foundation Engineering* 9(1):83–89
20. Oloo SY, Fredlund DG, Gan JK-M (1997) Bearing capacity of unpaved roads. *Can Geotech J* 34:398–407
21. Costa YD, Cintra JC, Zornberg JG (2003) Influence of matric suction on the results of plate load tests performed on a lateritic soil deposit. *Geotech Test J* 26(2):1–9
22. Mohamed FMO, Vanapalli SK (2006) Laboratory investigations for the measurement of the bearing capacity of an unsaturated coarse-grained soil. *Sea to Sky Géotechnique* 219–226
23. Vanapalli SK, Mohamed FMO (2013) Bearing capacity and settlement of footings in unsaturated sands. *Int J Geomate* 5(1):595–604
24. Wuttke F, Kafle B, Lins Y, Schanz T (2013) Macroelement for statically loaded shallow strip foundation resting on unsaturated soil. *Int J Geomech* 13(5):557–564
25. Vanapalli SK, Mohamed FMO (2007) Bearing capacity of model footings in unsaturated soils. In: *Proceedings of the Experimental Unsaturated Soil Mechanics*, vol 112, pp 483–493
26. Oh WT, Vanapalli SK (2008) Modelling the stress versus settlement behavior of model footings in saturated and unsaturated sandy soils. In: *12th international conference of international association for computer methods and advances in geomechanics*. Goa, India, pp 2126–2137
27. Vahedifard F, Robinson JD (2015) Unified method for estimating the ultimate bearing capacity of shallow foundations in variably saturated soils under steady flow. *J Geotech Geoenvironmental Eng* 142(4)
28. Fredlund DG, Rajardjo H, Fredlund MD (2012) *Unsaturated soil mechanics in engineering practice*. Wiley, New Jersey
29. Carsel RF, Parrish RS (1988) Developing joint probability distributions of soil water retention characteristics. *Water Resour Res* 24(5):755–769

30. Fredlund M (2011) SoilVision: knowledge-based soils database. SoilVision Systems Ltd, Saskatoon, Canada
31. Briaud J, Gibbens R (1997) Large scale load tests and data base of spread footings on sand. Federal Highway Administration
32. Viana da Fonseca A, Sousa JA Hyperbolic model parameters for FEM analysis of a footing load test on a residual soil from granite—a database for numerical modelling. In: Proceedings of I'ENPC/LCPC, pp 429–444
33. Rojas JC, Salinas LM, Seja C (2007) Plate-load tests on unsaturated lean clay. In: Experimental unsaturated soil mechanics, Springer Proceedings in Physics, pp 445–452

Dynamical Motifs in Temporal Networks



He Sun and Siew Ann Cheong

Abstract In this paper, we explain the connection between information processing by complex systems and recurrent activity sequences in their dynamics. We argue that an understanding of information processing pathways in terms of these dynamical motifs is important for designing effective interventions. We then describe a recently completed study, where we video recorded 37 shared book reading (SBR) sessions, and thereafter annotated each of these sessions for 26 activities (reading the book, comments and questions, management talk by the teacher, and responses from the children). For all SBR sessions, the annotations consisted of sequences of one activity followed by another (transitions). We tested the empirical data against a null model where activities occur randomly, to identify 34 transitions that occur more frequently than by chance, and visualize these transitions that are statistically significant at the confidence level of $p < 10^{-3}$ in the form of a static network. We then chose six significant transitions, and tested their extensions against the same null model to identify statistically significant length-3 sequences. This extension procedure was repeated to obtain length-4, length-5, and longer sequences until no further statistically significant extensions can be found. Finally, we organized the longest significant sequences into five families of dynamical motifs, and discuss their implications on the effectiveness of SBR.

Keywords Complex systems · Information processing · Complex networks · Temporal networks · Dynamical motifs

H. Sun

National Institute of Education, Nanyang Technological University, Singapore, Singapore

S. A. Cheong (✉)

School of Physical and Mathematical Sciences, Nanyang Technological University, Singapore, Singapore

e-mail: cheongsa@ntu.edu.sg

1 Introduction

1.1 *Complex Systems*

We are surrounded by complex systems. Some believe that complex systems became complex as they adapt to processing complex information in their environments [1]. As such complex systems gain competitive advantage over simple systems to become more numerous, they add to the complex signals in environment. Other systems adapting to the successful complex systems in turn become complex themselves. In this way, complex systems beget more complex systems, examples of which include the brain, the economy, financial markets, societies, and ecosystems. Even engineered systems (for example vehicular traffic, supply chains, and the internet) can become complex through interactions with complex adaptive agents.

Complex systems adapt over long evolutionary time scales, but over short operational time scales they are extremely robust to perturbations. In other words, their behaviors appear to be resistant to engineering controls, and when they change it is often in catastrophic and seemingly unpredictable ways. Therefore, we must first understand how information is processed by a complex system, and the organization of information processing pathways, before we can develop effective interventions. To do so, a data-driven approach is often necessary.

1.2 *Complex Networks and Temporal Networks*

We now live in the era of Big Data, where it is cheap to amass huge amounts of data on complex systems (for example, social network platforms like Facebook and Twitter, or engineered systems like smart grids and shipping networks). Typically, this data consists of many microscopic variables sampled at high frequencies in time. To understand the underlying complex systems using such data, an increasing popular way (when first-principle theories and models are not available) is to organize the microscopic variables into a static complex network [2, 3], and measure such network characteristics [4] as degree distribution, degree-degree correlations, assortativities, centralities, and average path lengths. Since complex systems also frequently have modular structures, work has also been done on community detection in these static complex networks [5, 6].

Naturally, such a static representation of complex systems misses important details of their dynamics. The network science community started moving into network representations where time is shown explicitly about a decade ago. Called temporal networks [7, 8], such representations allow us to characterize interactions between microscopic variables in both time and space.

1.3 Motifs in Static and Temporal Networks

It has long been suspected that the information processing pathways of complex systems corresponds to specific organizations in their static network representations, inspiring previous studies to find such motifs [9, 10]. Again, motifs in static networks do not tell the whole story, and thus there are now concerted efforts to find motifs in temporal networks [11, 12]. In this paper, we will describe our own work in systematically identifying dynamical motifs in temporal networks.

2 Data and Methods

2.1 Pedagogical Data from Classroom Teaching

Presently, we have not completed any studies on engineered systems, so in this paper we will use pedagogical data collected from classroom teaching to illustrate our method. The raw data is in the form of video recordings of 37 shared book reading (SBR) sessions by 31 kindergarten teachers. In a SBR session, the teacher would select a Chinese picture book, and read from the book while showing the pictures to children in the class. Two trained coders then annotated classroom activities in these videos according to Table 1. There are four types of teacher activities: (1) reading from the book, (2) comments, (3) questions, and (4) management talk. Comments and questions are further classified depending on how challenging they are cognitively for the children. Children’s responses are classified into individual responses (5.1), and group responses (5.2), with the latter considered more desirable. The shortest annotation “1, 4, 1, 5.2, 4, 2.3.3, 1, 2.2.2, 1, 1, 1, 1, 1, 1, 1, 1, 1, 1, 4, 1, 2.3.2, 2.3.2, 1, 1, 2.3.3, 1, 1, 1, 1, 1, 1, 1, 3.3.3, 1, 1, 1, 3.3.3, 5.1, 2.3.5, 3.3.3, 5.1, 3.3.3, 1, 3.3.3, 2.3.3, 4, 1, 3.2.2, 5.1, 3.3.5, 5.1, 2.3.5, 3.2.2, 2.3.5, 3.2.2, 2.2.1, 1, 4” consisted of 59 activities, while the longest annotation consisted 572 activities. On average, there are 232.3 activities per annotation. These annotations are aggregated for subsequent analyses.

2.2 Static Network Representation

As we can see from the example above, a typical SBR consisted of one activity followed by another. Since engagement is important to the learning of a language, we asked what teacher activities are most effective in eliciting responses from the children. To answer this question, we counted the number of times f_{ij} we found activity i occurring before activity j in the data. We call these *transition frequencies*, and visualize them as a static network, where the nodes represent the different activities. In this network, we draw a directed link from i to j if $f_{ij} > 0$, weighted by

Table 1 The coding scheme for different classroom activities, including instructional strategies used by teachers, as well as different responses from the children. For identifying dynamical motifs, we mapped the 26 classroom activities to letters of the alphabet

Category	Code	Description
Teacher narrations	1 (A)	Text reading
Teacher comments (2) and questions (3) (high cognitive level)	2.1.1 (B)/3.1.1 (M)	Inference
	2.1.2 (C)/3.1.2 (N)	Reflection
	2.1.3 (D)/3.1.3 (O)	Classification
Teacher comments (2) and questions (3) (medium cognitive level)	2.2.1 (E)/3.2.1 (P)	Explanation
	2.2.2 (F)/3.2.2 (Q)	Recall
	2.2.3 (G)/3.2.3 (R)	Expansion
Teacher comments (2) and questions (3) (low cognitive level)	2.3.1 (H)	Enumeration
	3.3.1 (S)	Routine
	2.3.2 (I)/3.3.2 (T)	Demo
	2.3.3 (J)/3.3.3 (U)	Labeling/description
	2.3.4 (K)/3.3.4 (V)	Sequencing
	2.3.5 (L)/3.3.5 (W)	Clarification
Teacher others	4 (X)	Management talk
Child response	5.1 (Y)	Individual
	5.2 (Z)	Group

f_{ij} . However, if we show all transitions $i \rightarrow j$, there would be too many links in the network for us to visually digest the information. We can choose to show only the most frequent transitions, but infrequent transitions may also be important. Alternatively, we can show the minimal spanning tree [13] or planar maximally filtered graph [14] of the full network. These are useful for visualization, but are not statistically rigorous.

Therefore, we tested whether the empirical transition frequencies could have arisen by chance, against a null model where the activities occur randomly, according to their relative frequencies. From this null model, we drew $N \gg 1$ sample histories with the same length as the empirical history. For each transition $i \rightarrow j$, we then counted the number of times n_{ij} the empirical transition frequency f_{ij} is exceeded by the null-model transition frequency \hat{f}_{ij} . The transition $i \rightarrow j$ is statistically significant at the level of confidence p , if $n_{ij} < pN$.

2.3 Identifying Dynamical Motifs

While the instructional activities preceding children's responses may be important, we believe teachers string activities together strategically to elicit such responses. These strategic activity sequences are buried in the long annotations, but if they are truly effective, we expect teachers to use them repeatedly. They should therefore

appear more frequently than by chance in the histories. Since these dynamical motifs have varying lengths, we cannot check them against an exhaustive list of all possible sequences, which grows exponentially with length. Also, we do not know the starts and ends of motifs in the histories. Therefore, to efficiently search for them, we mapped each activity to a letter of the alphabet (see Table 1), so that a history becomes a long string, and motifs are recurring substrings within it. This worked well for the 26 different activities we chose to code in this study. If there are more than 26 activities to code for, we can map them to both upper- and lower-case characters, and if necessary to the digits 0–9. One might worry about there being too many activities or variables to code using small alphabets, but fortunately most complex systems contain few building blocks [15]. For example, the genomes of all life on Earth are composed of 4 bases, coding for the same 20 amino acids, which can then be assembled into 10^3 – 10^4 proteins.

We tested substrings found in the data against the same null model. However, generating all possible substrings from all N sample histories, and then checking which empirical substrings are statistically significant is computationally expensive. Therefore, we started with statistically significant transitions, which are length-2 sequences, and tested which of their extensions give statistically significant length-3 sequences. We repeated this procedure to get significant length-4 sequences from the significant length-3 sequences, and so on and so forth, until no statistically significant extensions can be found.

3 Results and Discussion

3.1 *Static Network Representation of SBR*

For 26 activities, $26^2 = 626$ transitions (including self-transitions) are possible. However, only 34 transitions were found to be statistically significant at the confidence level of $p < 10^{-3}$. None of them are self-transitions, and their frequencies range from 5 to 431. In Fig. 1, we show the network of these statistically significant transitions.

3.2 *Dynamical Motifs in SBR*

In this study, we tested for dynamical motifs selectively, by starting from six statistically significant transitions, $4 \rightarrow 4$, $3.1.1 \rightarrow 5.1$, $3.2.2 \rightarrow 5.1$, $3.2.2 \rightarrow 5.2$, $3.3.1 \rightarrow 5.2$, and $3.3.3 \rightarrow 5.2$. Most of the motifs found were between length-3 to length-7, but we also found two series of very long motifs, $4 \rightarrow 4 \rightarrow \dots \rightarrow 4$, consisting of up to 14 management talk activities (suggesting possibly a breakdown in classroom discipline), and more than 20 repetitions of the basic unit $3.3.1 \rightarrow 5.2$.

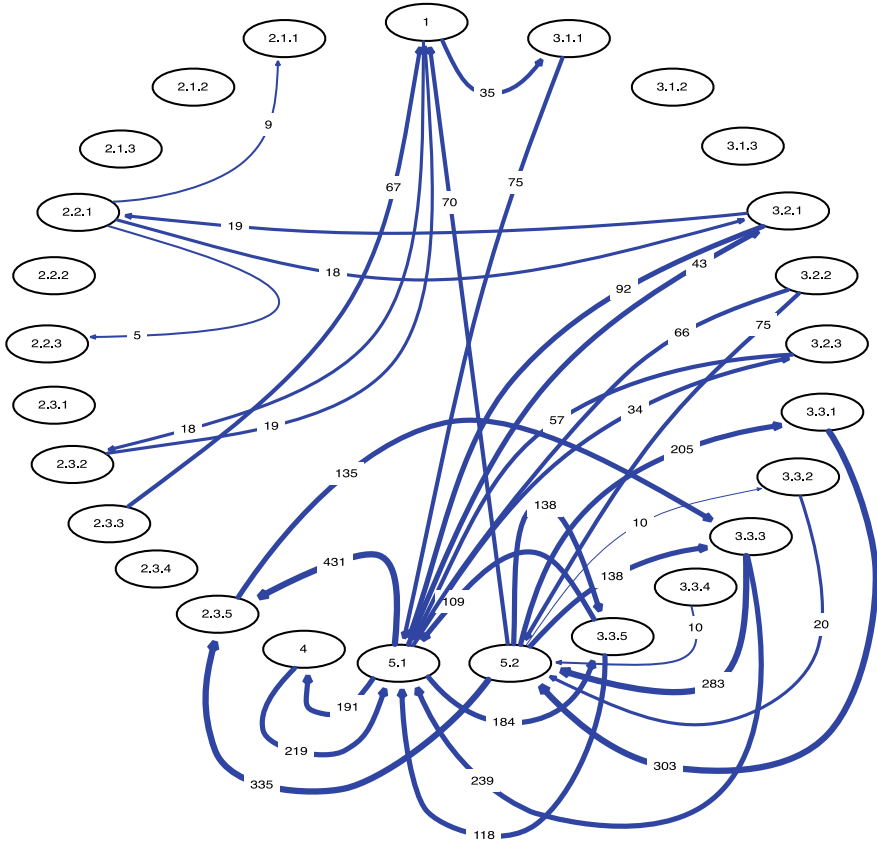


Fig. 1 Static network representation of the 34 transitions that are statistically significant at the $p < 10^{-3}$ level

We show the five more interesting families of dynamical motifs in Fig. 2. Apart from the family shown in Fig. 2c, in the other families it is easy to elicit individual responses from the children, but difficult to obtain group responses, especially if higher-cognitive-level comments or questions are used.

4 Conclusions

In summary, we explained why information processing by complex systems lead to recurrent activity sequences in their dynamics, and why it is important to identify such dynamical motifs for understanding the behaviors of complex systems. We then described a recently completed study, where we video recorded 37 shared book reading (SBR) sessions, and annotated each SBR session for 26 types of

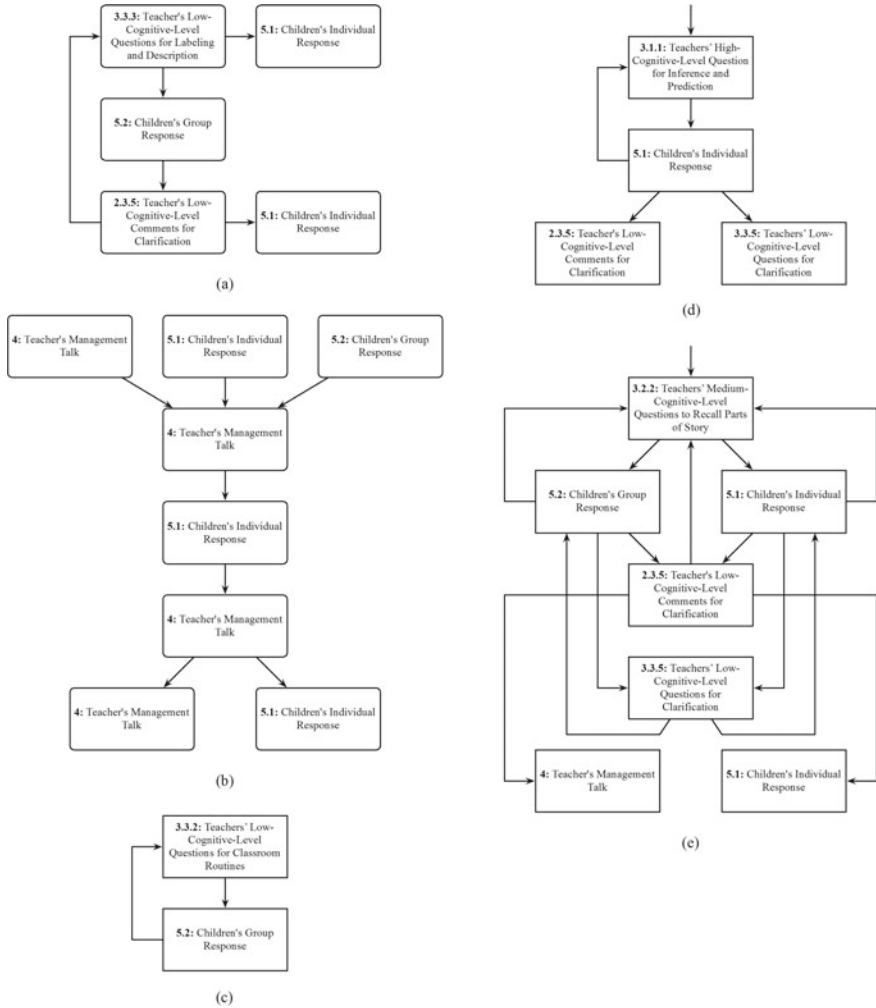


Fig. 2 The five families of dynamical motifs leading to or involving children’s responses (both individual and group)

activities, including the reading itself, comments and questions, management talks by the teacher, and the children’s responses. After testing against a null model where activities occur randomly, we constructed the network of 34 transitions that are statistically significant at the confidence level of $p < 10^{-3}$. We chose six such transitions to extend into longer and longer sequences, testing at each stage against the same null model, to end up with significant dynamical motifs that are mostly between 3 and 7 in length. This work has been submitted for publication, but we are continuing to interpret the motifs to understand what they mean in the SBR context.

References

1. Haken H (2006) *Information and self-organization: a macroscopic approach to complex systems*. Springer, Berlin
2. Albert R, Jeong H, Barabási AL (2000) Error and attack tolerance of complex networks. *Nature* 406(6794):378–382
3. Amaral LAN, Scala A, Barthelemy M, Stanley HE (2000) Classes of small-world networks. *Proc Natl Acad Sci USA* 97(21):11149–11152
4. Estrada E (2011) *The structure of complex networks: theory and applications*. Oxford University Press, Clarendon
5. Reichardt J, Bornholdt S (2006) Statistical mechanics of community detection. *Phys Rev E* 74(1):016110
6. Fortunato S, Barthelemy M (2007) Resolution limit in community detection. *Proc Natl Acad Sci USA* 104(1):36–41
7. Holme P, Saramäki J (2012) Temporal networks. *Phys Rep* 519(3):97–125
8. Lambiotte R, Masuda N (2016) *A guide to temporal networks*. World Scientific, Singapore
9. Milo R, Shen-Orr S, Itzkovitz S, Kashtan N, Chklovskii D, Alon U (2002) Network motifs: simple building blocks of complex networks. *Science* 298(5594):824–827
10. Shen-Orr SS, Milo R, Mangan S, Alon U (2002) Network motifs in the transcriptional regulation network of *Escherichia coli*. *Nat Genet* 31(1):64–68
11. Kovanen L, Karsai M, Kaski K, Kertész J, Saramäki J (2011) Temporal motifs in time-dependent networks. *J Stat Mech: Theory Exp* 2011(11):P11005
12. Kovanen L, Kaski K, Kertész J, Saramäki J (2013) Temporal motifs reveal homophily, gender-specific patterns, and group talk in call sequences. *Proc Natl Acad Sci USA* 110(45):18070–18075
13. Kruskal JB (1956) On the shortest spanning subtree of a graph and the traveling salesman problem. *Proc Am Math Soc* 7(1):48–50
14. Tumminello M, Aste T, Di Matteo T, Mantegna RN (2005) A tool for filtering information in complex systems. *Proc Natl Acad Sci USA* 102(30):10421–10426
15. Holland JH (2012) *Signals and boundaries: building blocks for complex adaptive systems*. MIT Press, Cambridge

Field Measurements of Fine Sediment Transport Processes in Japanese Estuaries



Yasuyuki Nakagawa

Abstract This paper presents some case studies of field measurements for better understanding of fine sediment transport processes in Japanese estuarine environments, including the inner Tokyo bay and the mouth of Shinanno river. The study at the Tokyo bay focused on the near bed transport processes of muddy bottom sediments and the monitoring has been captured a storm event with resuspension of muddy bottom sediments during a passage of Typhoon. The results of the sediment budget analysis with the monitored data shows the importance of the fluid mud flow near the bed. The other field study at the mouth of the Shinano river also demonstrates an importance of the fluid mud formation and their transport for the shoaling process of a dredged navigation channel in the water area. The area shows a specific flow system during a flood event with vertical three-layered stratification, where a discharged fresh turbid water flows over the sea water and the fluid mud layer formed in the lowest on the bottom.

Keywords Fine sediment transport • Field measurements • Fluid mud • Channel siltation

1 Introduction

An understanding of the distribution and transport processes of muddy sediment, which consists of silt and clay fractions, is crucial for predicting and evaluating the environmental evolution of water systems in estuarine and coastal areas. The predictions of the transport of the sediment and resulting change in the water depth in water ways and surrounding area are also crucial for safety navigations of the ships. The transport processes of muddy sediment, or cohesive one, are more complicated than sand or non-cohesive sediment, with several specific phenomena including flocculation and fluid mud formation.

Y. Nakagawa (✉)
Port and Airport Research Institute/PARI, Yokosuka, Japan
e-mail: nakagawa@p.mpat.go.jp

Many researchers have set up models of fluid mud dynamics, some of which have been applied to estuaries (e.g. [1]) and continental shelves (e.g. [2]). However, since the properties and dynamics of fluid mud are highly site-dependent, a universal model does not work for fluid mud dynamics. Another reason for this imperfection of the modeling is a limited knowledge of sediment dynamics, especially of intermittent events. It is, therefore, desirable to capture and analyze such events as storm-driven resuspension and sediment discharge during flood conditions by making long-term measurements in the field (e.g. [3]).

In this paper, several findings obtained from field measurements of the sediment transport process are demonstrated in some case studies of Japanese estuaries, where the muddy sediments are predominant. The study sites include the inner Tokyo Bay and the mouth of the Shinano River and the observation data and analysis are summarized from the previous papers by the author [4] and [5].

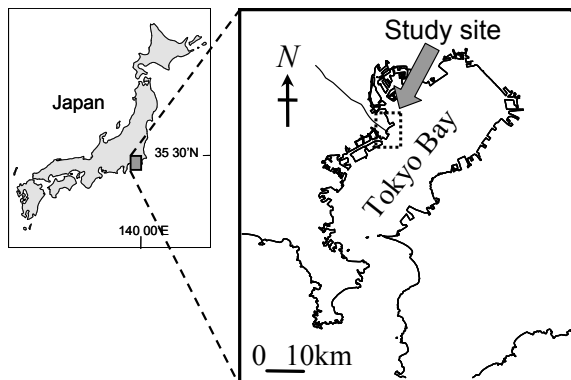
2 Muddy Bed Dynamics During a Storm Event

2.1 Site Description and Instrumentation

A field measurement with bottom mounted instruments were carried in the north-western part of inner Tokyo Bay, Japan (Fig. 1). The Bay has a surface area of 1,500 km² with an average depth of around 15 m, and a semi-diurnal, meso-tidal condition with a maximum spring tidal range of less than 2 m. Several rivers flow into the upper part of the Bay with a total drainage basin area of 6,000 km². The Tama River has the second largest basin (1,240 km²) and carries around 20 m³/s at typical background flow rates and 200–1,000 m³/s during flood events. The coastal area including the mouth of the Tama River region is highly industrialized and the Tokyo International Airport is located near the mouth of the river.

The monitoring campaign in the summer of 2007 covered a storm event with high waves followed by extensive flooding through the Tama River due to the

Fig. 1 Location of the Tokyo Bay and study area



passage of a typhoon. The near-bottom data set, including information about currents and turbidity, was obtained at the offshore site of Stn. B by using several acoustic and optical sensors as shown in Fig. 2. A Nortek Vector Acoustic Doppler Velocimeter (ADV) measured three-dimensional velocities at 10 cm above the bottom every half hour at 8 Hz in about 2-minute bursts (1024 data per burst). Optical backscatter sensors (OBS) (Compact-CLW, JFE Advantech Co.) were moored at several levels near the bottom to measure suspended sediment concentration (SSC) profiles. Measured optical backscatter intensity was calibrated using sediment samples taken from the site to the SSC in units of mg/l.

2.2 Sediment Budget Analysis with Measured Data

During the period of high shear stress caused by waves and currents, the near-bed SSC rapidly increased with a high concentration of 2,000 mg/l just above the bottom (B + 0.0 m), 1,000 mg/l at 10 cm, and 100 mg/l at 50 cm. During the high near-bed SSC event, the turbulent diffusion flux of sediments calculated as the Reynolds flux with the ADV data also showed higher values in the upward direction during the period [4].

Considering the estimation results of vertical sediment fluxes near the bed, sediment budget can be analyzed with the following sediment weight balance equation.

$$-\rho_d \frac{dZ(t)}{dt} = F_z + F_d + F_r \tag{1}$$

where ρ_d is dry density of sediment and $Z(t)$ is the observed bed level detected by the ADV's backscatter signal. The sediment density was assumed as $1,300 \text{ kg/m}^3$. F_z and F_d are upward and downward sediment fluxes and they are calculated with

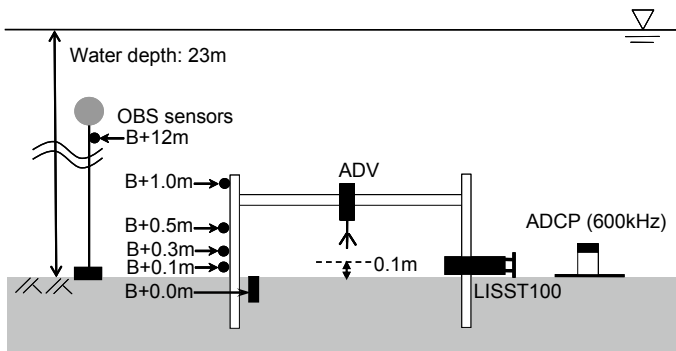


Fig. 2 Instrumentation layout

Eqs. (2) and (3), respectively. The settling velocity was assumed as 0.1 mm/s considering the sediment particle size. F_r is residual term and it deserves as the sediment flux that is contributed by horizontal flux in the layer under the ADV measurement height at 10 cm from the original bed level.

$$F_z = \overline{c'w'} \quad (2)$$

$$F_d = w_s C_b \quad (3)$$

The result of the analysis is shown in Fig. 3 for the duration of 24 h under the storm event condition. The solid line in the figure is the temporal change in the bed level, which is detected by the acoustic backscatter signal of the ADV [4]. Dashed black line is bed level change calculated as the contribution of net vertical flux of F_z and F_d , and red dashed line is residual term. Based on the assumptions mentioned above, the bed level change by the residual contribution becomes 6 cm of deposition through the storm event. The result means that this deposition should be compensated by the horizontal flux and the horizontal transport should be a key factor to account for the near bed sediment transport budget.

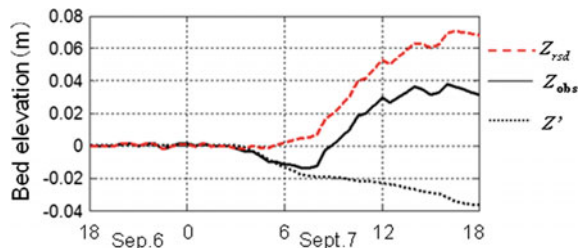
3 Mud Transport at River Mouth During Flood Event

3.1 Site Description

Another case study was carried out in the port of Niigata, at the mouth of the Shinano River, which is the longest river in Japan (Fig. 4). The channel of the port has been suffering from siltation by sediment discharged through the river and maintenance dredging is required frequently to keep depths of -5.5 to -12 m in the navigation channel and harbor basin. The daily discharge rates of the river in 2012 and 2013 are shown in Fig. 5. The data were monitored at the Teiseki-bridge observation station, 5 km upstream from the port, which is operated by the Ministry of Land, Infrastructure, Transport and Tourism (MLIT).

CTD and in situ bulk density measurements were carried out in January 2012, November 2012 and July–August 2013, at the points indicated in Fig. 5. The

Fig. 3 Estimated contribution of sediment flux components



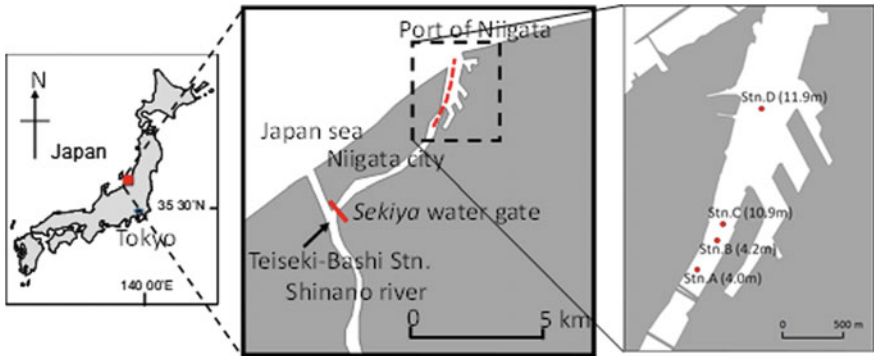


Fig. 4 Location of study site at the mouth of Shinano River

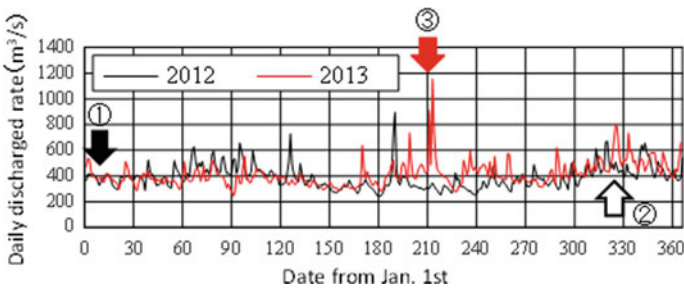


Fig. 5 Measured daily discharge rate at Teiseki-Bashi Station of Shinano River in 2012 and 2013. The three arrows mean the monitoring deployments

monitoring campaigns in 2012 were under normal flood conditions with a discharge rate of around 500 m³/s. In contrast, the monitoring in 2013 was under a flood event, with a higher discharge rate of over 1,000 m³/s in the main channel of the river. The water discharged into the port area is controlled by water gates. The actual discharge rate in the port was approximately 380–450 m³/s based on the water gates' operation rules.

3.2 Observed Data During a Flood Event

Observed vertical profiles of salinity and suspended sediment concentration (SSC) are shown in Figs. 6 and 7, respectively. Note that the SSC data during the flood event in 2013 also displays stratified profiles in the dredged downstream area at Stations C and D. Considering the salinity profiles, this stratification means that a more-turbid/less-saline water layer appears near the water surface over a less-turbid/more-saline layer. Another key point in the measured data is the rapid increase of

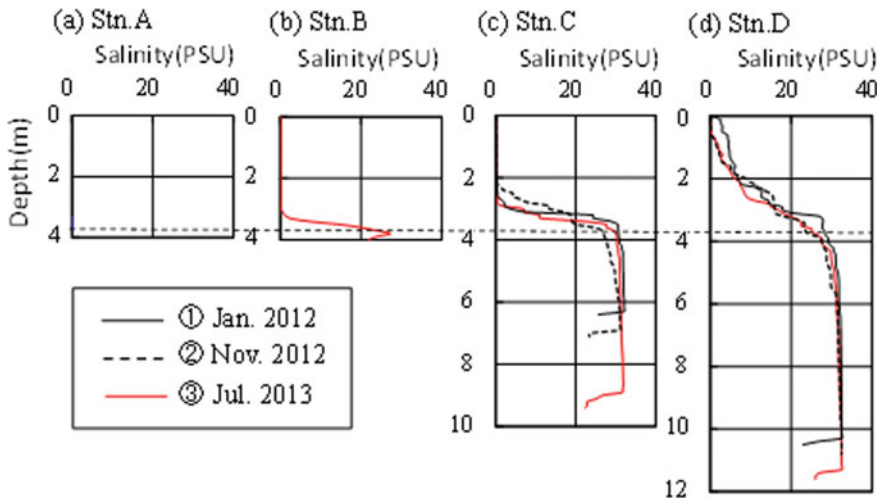


Fig. 6 Observed salinity profiles

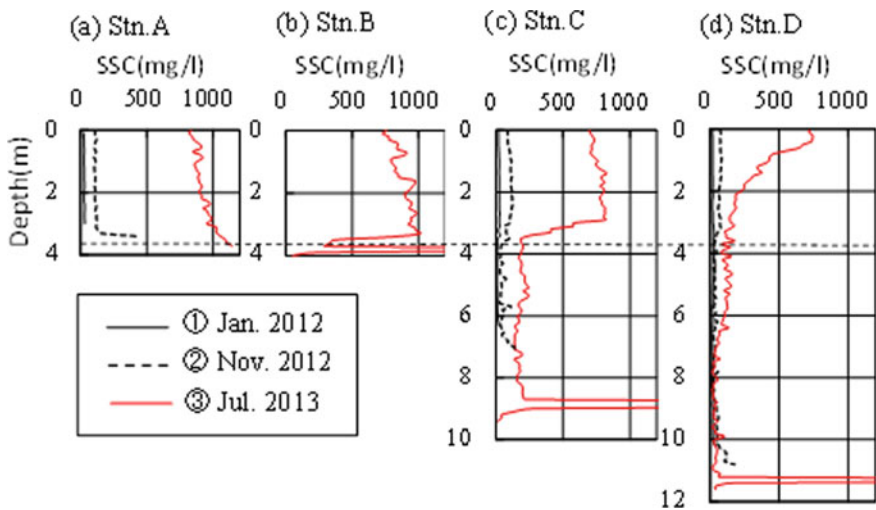


Fig. 7 Observed SSC profiles

SSC near the bed at Stations C and D. In this near-bottom layer, a highly concentrated mud layer with a bulk density of around $1,200 \text{ kg/m}^3$ was observed by the in situ bulk density measurement performed with the Mud Bag, a product of the Hydramation Company. The measured vertical profile at Station C is shown in Fig. 8. The near-bed highly concentrated layer appeared only during the flood event in 2013. It is conceivable that the near-bed highly concentrated layer could be

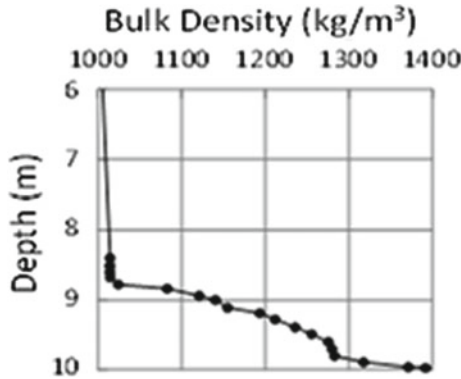


Fig. 8 Observed bulk density profile at Stn. C

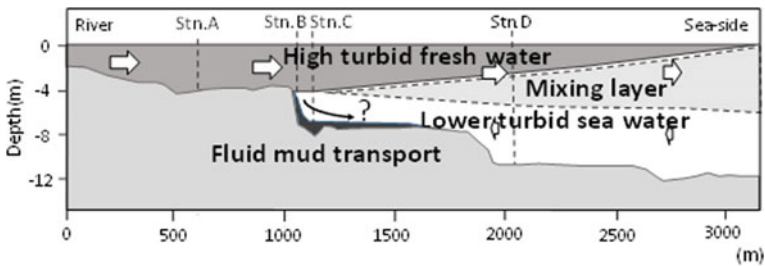


Fig. 9 Conceptual figure of discharge of turbid flow at the study site

formed by fluid mud transport from upstream, which is sometimes observed on shelves off river deltas [6].

Based on the field data set, the suspended sediment transport processes during flood conditions in the port can be schematized as in Fig. 9, showing the upper fresh water with higher turbidity layer above the lower turbid sea water in the dredged channel. Fluid mud may flow into the bottom of the uppermost dredged area as shown in Fig. 9. The generation process of the fluid mud is not clear and it is next challenge to elucidate the process.

4 Conclusions

As shown in the above sections, the field measured data of fine sediment dynamics obtained during the extreme storm and flood event show that the sediment budget at the bed is not simply determined only with the resuspension or upward flux and settling flux but horizontal advection of fluid mud layer on the bed might be

considered. Although several models of fluid mud transport have been presented, any model could not be applied for universal conditions due to the strong dependency of the processes on site specific situations. For the study sites of the present study, the models are under developing considering the field data and characteristics of the sites.

Acknowledgements Part of the studies are supported by the Ministry of Land, Infrastructure, Transport and Tourism (MLIT) for deployment of the field measurement works in the Tokyo Bay and at the Shinano River. Author also thank all members of Coastal and Estuarine Sediment Research group of PARI for their support of the works.

References

1. Odd NVM, Cooper AJ (1989) A two-dimensional model of the movement of fluid mud in a high energy turbid estuary. *J Coastal Res* 5:185–193
2. Harris CK, Traykovski PA, Geyer ER (2005) Flood dispersal and deposition by near-bed gravitational sediment flows and oceanographic transport: a numerical modeling study of the Eel River Shelf, northern California. *J Geophys Res* 110(110):C09025. <https://doi.org/10.1029/2004jc002727>
3. Traykovski P, Wiberg PL, Geyer WR (2007) Observations and modeling of wave-supported sediment gravity flows on the Po prodelta and comparison to prior observations from the Eel shelf. *Cont Shelf Res* 27:375–399
4. Nakagawa Y, Nadaoka K, Yagi H, Ariji R, Yoneyama H, Shirai K (2012) Field measurement and modeling of near-bed sediment transport processes with fluid mud layer in Tokyo Bay. *Ocean Dynamics* 62(10–12):1535–1544. <https://doi.org/10.1007/s10236-012-0570-4>
5. Nakagawa Y, Takashima N, Gotoh Y, Nagai I (2016) Fluid mud dynamics around dredged navigation channel at river mouth port. In: Proceedings of the PIANC-COPEDEC 9th Conference
6. Fan S, Swift DJP, Traykovski P, Bentley S, Borgeld JC, Reed CW, Niedoroda W (2004) River flooding, storm resuspension, and event stratigraphy on the northern California shelf: observations compared with simulations. *Mar Geol* 210:17–41

Bridge-Structural Engineering, Structural Damage Detection and Health Monitoring

Damaged Detection in Structures Using Artificial Neural Networks and Genetic Algorithms



Lan Nguyen-Ngoc, Hoa Tran-Ngoc, Hieu Nguyen-Tran,
Binh Nguyen-Duc, Dang Nguyen-Le-Minh, Thanh Bui-Tien,
and Magd Abdel Wahab

Abstract Recently, Structural Health Monitoring (SHM) has emerged to be one of the most effective tools for the diagnosis of damages in structures. Early identification and localization of damage not only help to reduce the maintenance cost but also extend the life cycle of the structures. In this paper, a novel approach using Artificial Neural Networks (ANNs) combined with Genetic Algorithms (GA) is proposed to increase the capacity of damage detection in SHM system. ANNs can make use of different algorithms such as recognition algorithms and regression algorithms to classify, detect, localize and evaluate the severity of the damage. Meanwhile, GA can be applied to identify training parameters as well as to solve the local minima problems from ANNs. To demonstrate the method, an analysis of a bridge is performed. Finite Element (FE) model of the bridge is created using measured vibration data and it is employed as training data for the combined ANN-GA method in the model updating process. The updated model will then be used as a baseline model for damage identification. The result shows that the proposed ANN-GA algorithm provides a high level of accuracy and efficiency in detecting damage in the considered structure.

Keywords Damage detection · Artificial neural networks · Genetic algorithms · Structural health monitoring (SHM)

L. Nguyen-Ngoc · H. Tran-Ngoc · H. Nguyen-Tran · B. Nguyen-Duc · D. Nguyen-Le-Minh ·
T. Bui-Tien (✉) · M. A. Wahab
University of Transport and Communications/UTC, Hanoi, Vietnam
e-mail: btphanh@utc.edu.vn

L. Nguyen-Ngoc · H. Tran-Ngoc · H. Nguyen-Tran · M. A. Wahab
Soete Laboratory, Faculty of Engineering and Architecture, Ghent University, Ghent,
Belgium

1 Introduction

Civil structures such as bridges, dams, skyscrapers are exposed to potential damages from service loads, environmental loads or natural disasters. Damages also tends to occur more frequently at structures which no longer guarantee their designed life cycle. The possibility of large-scale catastrophes those damages may bring to these structures has made regular monitoring and health assessment imminent during and after constructions, with the ultimate goal is to predict and detect damage of the structure.

With the development of technology, more and more new methods were developed to tackle this problem. Andrew Swartz et al. [1] used wireless device sensors with low-cost for SHM and the result showed that low cost wireless sensors allowed for the implementation of very dense sensor networks for monitoring civil engineering assets generating. Antunes et al. [2] applied optical FBG sensors to study the behavior of structures under damages scenarios with high accuracy results tested. Recently, Artificial Intelligence and Machine Learning-based methods have been used widely for damage detection problems [3, 4]. Some researchers also got further succeeded in solving optimization problem in SHM with the help of AI and ANN [5–7]. In [8–11], the researchers have applied ANN and GA-based method to detect damage of the experimented structures with much effective results.

In this paper, we proposed a novel ANN-GA method to tackle damage detection problem of a truss bridge. After the introduction, the novel ANN-GA method is introduced in the second section. In the third section, measured and calculated data of Chuong Duong bridge are analyzed and trained under different damage scenarios using ANN and the improved ANN-GA. Comparison of the two results are then conducted, followed by some remarked conclusions.

2 Proposed Artificial Neural Network-Genetic Algorithms (ANN-GA)

Artificial Neural Network (ANN) is a complex neural network that uses multi layers to extract more and deeper information from the input data. The structure of ANN consists of: One input layer to receive input data and transfer them to the next hidden layers; Two or more hidden layers to apply transformation to the data and one output layer to receive data from the hidden layers and provide output data.

The base elements of the ANN are the nodes, also called processing elements (PE), and the connections. Each node has its own input, from which it receives communications from other nodes and from the environment and its own output, from which it communicates with other nodes or with the environment. Finally, each node has a function through which it transforms its own global input into output. Each connection is characterized by the strength with which pairs of nodes are excited or inhibited.

In damage detection problem, a dataset of various damage scenarios of the structure is used as training data for the ANN. Damage is created by reducing the stiffness of structure components. However, during the process, ANN may trap into local minima and lead to the inaccuracy of the training. Hence, we proposed a novel method of combining ANN with GA to overcome the local minima problem ANN may face. In GA, mutations are introduced to add diversity to the sampled population and they are applied to some individuals of a generation. The higher the mutation rate is, the more ‘space’ will be searched and the higher chance that the global minimum could be found.

3 Analysis of Damage Scenarios of Chuong Duong Bridge

3.1 Modal Analysis of Chuong Duong Truss Bridge

To validate the effectiveness of the proposed ANN-GA, vibration data of Chuong Duong bridge (Vietnam) was collected and analyzed. In the context of this research, only the data of the first truss section with the length of 85.5 m was recorded using piezoelectric sensors. A Finite Element (FE) model of the first truss section of the bridge was constructed using Matlab as shown in Fig. 1.

Modal analysis of the model shows the first five natural frequencies of the truss bridge with respective mode shapes in Table 1.

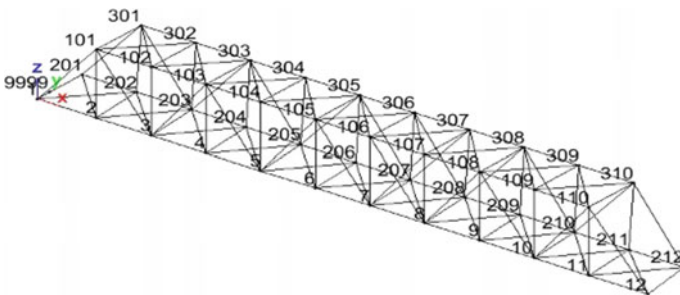


Fig. 1 FEM model of the truss section

Table 1 Summary of the natural frequencies and mode shapes obtained

No.	f (Hz)	Mode type
1	1.2290	Lateral bending
2	2.4167	Vertical bending
3	4.1954	Torsion
4	4.2623	Torsion
5	4.5925	Vertical bending

Model updating is then applied to optimize the discrepancy between the measured and calculated models. The updated model will be used as a baseline model for the next step, which is damage detection based on various damage scenarios of the structure.

3.2 Damage Detection Using Proposed ANN-GA Method

Different damage scenarios are created by decreasing the stiffness matrix of the beams in the lower chords of the truss. Damage can be then detected by comparing the modal parameters of the original structure to those of the damaged structure. The input data is the natural frequencies of the structure under different damage scenarios and the output data is the properties of the damage, hereby the scale of the damage and the location of the damage.

In each case, we introduced damage to one beam simultaneously with the stiffness of the beam is reduced from 1 to 50% for an interval of 1% while the rests of the beam remain undamaged. In total we have created a dataset of 550 samples with 11 elements to be considered as being damaged for training the network. We used 2 method for training of the network: the tradition method of using ANN and the proposed method of combining ANN and GA. The training result of data is shown in Fig. 2.

From the training result, we see that the R-values obtained by the proposed ANN-GA (0.9999) method is higher than that of the traditional ANN method (0.9997). The proposed ANN-GA method also gives better mean squares error values (MSE) than the ANN method 0.0051 in compare with 0.0120. The higher R-values of ANN-GA suggested that the network is trained well and can be used to detect damage in the proposed Chuong Duong bridge.

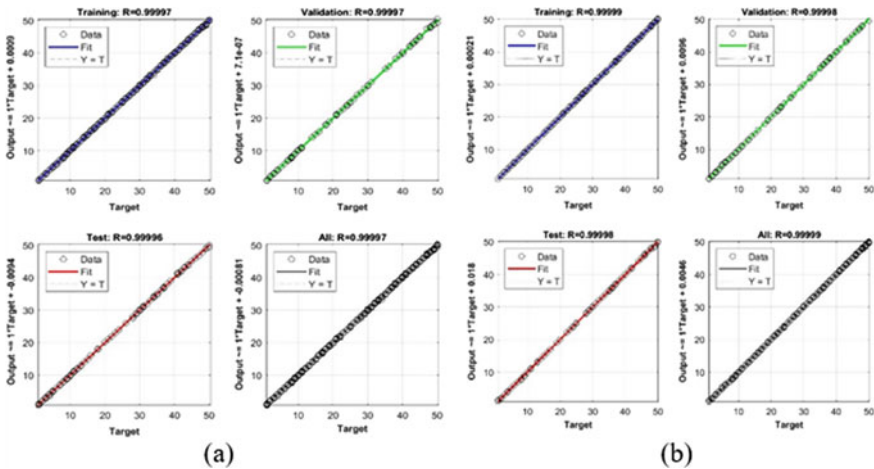


Fig. 2 Training data of **a** ANN and **b** proposed ANN-GA

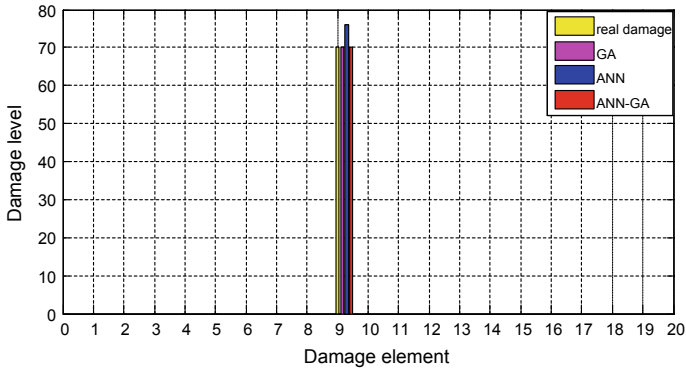


Fig. 3 Damage identification by different methods for 70% of stiffness reduction in beam element 9

Testing the networks for the case of 70% stiffness reduction in beam element 9 of the bridge structure, we can see as in Fig. 3 that while both ANN and the proposed ANN-GA are able to locate the position of damage accurately, ANN-GA outperformed ANN in term of identifying correctly the damage level of the beam.

4 Conclusion

In this paper, we proposed a novel method combining ANN and GA for damage detection of bridge structure. The integrated GA ameliorates the existing ANN by avoiding the network to trap into local minima, especially when more of best local solutions is created, thus increase the effectiveness of the ANN. The method was validated using measured data of Chuong Duong truss bridge with various damage scenarios. The results show that while ANN-GA is more effective than the current ANN in term of R and MSE values, the time needed to train the data is longer than the ANN. Although both methods are able to locate the position of damage, ANN-GA outperformed ANN in term of identifying correctly the damage level of the beam.


Acknowledgements The authors acknowledge the financial support of VLIR-UOS TEAM Project, VN2018TEA479A103, ‘Damage assessment tools for Structural Health Monitoring of Vietnamese infrastructures’ funded by the Flemish Government. Moreover, the first author needs to acknowledge the financial supports from Vietnam’s Ministry of Education under the research “B2018-GHA-04SP”.

References

1. Swartz R, Zimmerman A, Lynch J (2007) Structural health monitoring system with the latest information technologies
2. Antunes P, Varum H, André P (2011) Optical FBG sensors for static structural health monitoring. *Proc Eng* 14. <https://doi.org/10.1016/j.proeng.2011.07.197>
3. Lopes V Jr, Park G, Cudney H, Inman D (2000) Impedance-based structural health monitoring with artificial neural networks. *J Intell Mater Syst Struct* 11(206–214). <https://doi.org/10.1106/h0ev-7pwm-qyhw-e7vf>
4. Vallone G, Sbarufatti C, Manes A, Giglio M (2013) Artificial neural networks for structural health monitoring of helicopter harsh landings. *Appl Mech Mater* 390(192–197)
5. Califano A, Chandarana N, Grassia L et al (2020) Damage detection in composites by artificial neural networks trained by using in situ distributed strains. *Appl Compos Mater* 27:657–671
6. Huang Y, Ludwig SA, Deng F (2016) Sensor optimization using a genetic algorithm for structural health monitoring in harsh environments. *J Civil Struct Health Monit* 6:509–519
7. Soman R, Malinowski P (2019) A real-valued genetic algorithm for optimization of sensor placement for guided wave-based structural health monitoring. *J Sens* 2019. Article ID 9614630
8. Neves AC, González I, Leander J et al (2017) Structural health monitoring of bridges: a model-free ANN-based approach to damage detection. *J Civil Struct Health Monit* 7:689–702
9. Cruz A, Vélez W, Thomson P (2010) Optimal sensor placement for modal identification of structures using genetic algorithms—a case study: the olympic stadium in Cali, Colombia. *Ann Oper Res* 181:769–781
10. Maru Michael B, Lee Donghwan, Cha Gichun, Park Seunghee (2020) Beam deflection monitoring based on a genetic algorithm using lidar data. *Sensors* 20(7):2144
11. Tran H, Khatir S, De Roeck G, Bui-Tien T, Abdel Wahab M (2019) An efficient artificial neural network for damage detection in bridges and beam-like structures by improving training parameters using cuckoo search algorithm. *Eng Struct* 199. <https://doi.org/10.1016/j.engstruct.2019.109637>

Effect of Metal Corrosion on the Structural Reliability of the 3D Steel Frames



Ngoc-Long Tran and Trong-Ha Nguyen 

Abstract The worldwide design standards only consider safety or reliability at the beginning not concerning the deterioration of the material strength under the corrosive environment. This research presents an assessment method for reliability and durability of the 3D steel frame connections considering corrosion effects. A metal corrosion model which is proposed in previous studies was adopted to apply for this study. Monte Carlo simulation method is proposed and utilized to assess the reliability and durability of the 3D steel frames under corrosion. The random variables including the corrosion phenomenon, and applied load, have been considered. The safety deterioration of the steel structures due to the corrosion phenomenon until 100 years is investigated. Additionally, the effects of input parameters, which are safety factors and coefficient of variation, on the reliability of structures are examined in the present study. Finally, a verification of this study and previous results are performed, highlighting the capability of the proposed method.

Keywords Steel frame · Corrosion · Reliability analysis · Durability analysis · Monte Carlo simulation

1 Introduction

Impact assessment of corrosion on the structural mentioned in the design standards of some countries and EN ISO: 9223, these recommendations depend on each standard. The European structural design codes has been recommended for design structures [1, 2]. However, there is not a specific process with quantitative goals aimed at determining the reliability and durability of steel structures during exploitation.

M. E. Komp et al. [3] had proposed a corrosion model which has been widely applied by numerous authors. R. Landolfo had published a state of the art report on

N.-L. Tran · T.-H. Nguyen (✉)
Department of Civil Engineering, Vinh University, 182 Le Duan, Vinh 461010, Vietnam
e-mail: trongha@vinhuni.edu.vn

the modeling of metal structure corrosion damage [4]. In addition, M. Seccer et al. has used M. E. Komp model for investigating the corrosion damage of steel frame considering lateral torsional bucking [5].

The reliability assessment of the structure is also an interested subject to the researchers. Such as, A. Omishore and Z. Kala in [6], S. Afshan et al. in [7], T. H Nguyen et al. in [8, 9]. However, to the best of our knowledge, the reliability assessment of steel frame under metal corrosion environmental is far from fully investigated.

This paper intends to study the effect of the safety of the 3D steel frames considering metal corrosion. In this research, the metal corrosion modeling used to propose by M. E. Komp [3]. Reliability of the structure is evaluated using Monte Carlo simulation method. This program computer is written by using the MATLAB language. The results numbers are reliability and durability behaviors under corrosion are determined for exposure about from 10 to 100-years. Effects of input parameters are also investigated.

2 Monte-Carlo Simulation Method and Corrosion Modeling

Monte Carlo simulation or Monte Carlo experiments are on based the use of pseudo-random numbers and the law of large numbers to assess the reliability of any system. Monte Carlo simulation has been detailed in [10]. In this study, a reliability assessment using the Monte Carlo simulation is established on Matlab. The Matlab code is verified and used in many studies by the author in [8, 9, 11, 12].

The corrosion modeling of steel structures in various environments intensively had proposed by M. E. Komp in [3]. Corrosion models usually describe the corrosion depth as a function of time in the form of a power model and are written as follows.

$$d(t) = At^B \quad (1)$$

where, $d(t)$ is corrosion depth (μm , g/m^2), t is exposure time (years), A is corrosion rate in the first year of exposure, B is corrosion rate long-term decrease.

Obtains from [3] A and B are parameters depend on the environment in which the structure is located and they presented in Table 1. The modeling in Eq. (2) and average values for corrosion parameters in Table 1 have reliable. It is used for many studies in the literature [4, 13].

Table 1 Average values for corrosion parameters A and B for carbon and weathering steel

Environment	Carbon steel		Weathering steel	
	A	B	A	B
Rural	34.0	0.65	33.3	0.50
Urban	80.2	0.59	50.7	0.57
Marine	70.6	0.79	40.2	0.56

3 The Safety Condition of the 3D Steel Frames

In this study, the safety conditions of the 3D steel frames are must satisfy simultaneously: The safety condition of cross-section beams and the safety condition of cross-section columns based on Euro codes—Design of steel buildings EC3-1-1 [2] are written as follows.

$$G(X) = \begin{cases} \left(\frac{M_{Ed}}{M_{c,Rd}} - 1, 0 \right) \frac{1}{n} \leq 0 \\ \left(\left[\frac{M_{y,Ed}}{M_{pl,y,Rd}} \right]^\alpha + \left[\frac{M_{z,Ed}}{M_{pl,z,Rd}} \right]^\beta - 1, 0 \right) \frac{1}{n} \leq 0 \\ \left(\frac{V_{Ed}}{V_{c,Rd}} - 1, 0 \right) \frac{1}{n} \leq 0 \\ \left(\left(W_{pl,y} - \frac{\rho A_w^2}{4t_w} \right) \frac{f_y}{\gamma_{M0}} - M_{y,c,Rd} \right) \frac{1}{n} \leq 0 \\ \left(\frac{M_{Ed}}{M_{b,Rd}} - 1, 0 \right) \frac{1}{n} \leq 0 \\ \left(M_{Ed} - M_{N,Rd} \right) \frac{1}{n} \leq 0 \\ \left(\frac{N_{Ed}}{\chi_y \gamma_{M1}} + k_{yy} \frac{M_{y,Ed} + \Delta M_{y,Ed}}{\chi_{LT} \gamma_{M1}} + k_{yz} \frac{M_{z,Ed} + \Delta M_{z,Ed}}{\gamma_{M1}} - 1, 0 \right) \frac{1}{n} \leq 0 \end{cases} \quad (2)$$

where, n is safety factor, this is used to adjust to increase the reliability of the structure at a time design.

4 Reliability Assessment by the Combination of the FEM, Metal Corrosion Modeling and Monte Carlo Simulation

The program computer of reliability assessment of the 3D steel frames developed based on the finite element method (FEM), the Komp corrosion model, Monte Carlo simulation, and established in the MATLAB.

5 Numerical Examples

5.1 Convergence of the Monte Carlo Simulation at a Time Design

In this section in the paper, the proposed procedure is applied for the reliability assessment of the 3D steel frame shown in Fig. 1 at a time design ($t = 0$ -year). Nominal and distribution of input random variable shown in Table 2. The nominal and distribution of material properties had proposed in [14] and the cross-section and loading had proposed in [15].

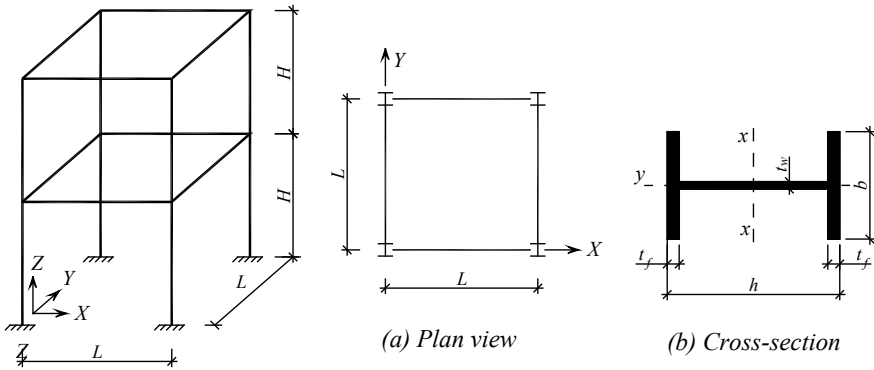


Fig. 1 Two-story space frame

Table 2 Statistical properties of random variables for reliability assessment

Properties	Variables	Nominal	Mean/ nominal	COV	Distribution	References
Geometric	H	400 (cm)	–	–	Deterministic	
	L	400 (cm)	–	–	Deterministic	
Material	f_y	248.0 (GPa)	1.10	0.06	Lognormal	[2]
	E	200.0 (GPa)	1.10	0.06	Lognormal	[2]
	G	81.0 (GPa)	1.10	0.06	Lognormal	[2]
Loading	DL	50.0 (kN/m ²)	1.05	0.10	Normal	[3]
	LL	30.5 (kN/m ²)	1.05	0.10	Normal	[3]
	WL	30.0 (kN/m ²)	0.92	0.37	Gumbel	[3]
Cross-section beam and column	b	250.0 (mm)	1.00	0.05	Normal	[3]
	h	380.0 (mm)	1.00	0.05	Normal	[3]
	t_f	15.0 (mm)	1.00	0.05	Normal	[3]
	t_w	8.0 (mm)	1.00	0.05	Normal	[3]

5.2 Effect of Metal Corrosion on the Safety Probability of the 3D Steel Frames

The study will be investigated effect of metal corrosion on the safety probabilities of the 3D steel frames about 10, 20, 50 and 100-years. The cross-section beams and columns of the 3D steel frames is considered due to the corrosion on based proposed by Komp [3], model in the Marine Environment. The nominal and distribution of material properties on based proposed in [15], the cross-section and loading on based proposed in [14]. The summaries of the safety probability in the Monte Carlo simulation of the 3D steel frames considering metal corrosion about 10, 20, 50, and 100-years are shown in Table 3.

Table 3 The safety probability of the 3D steel frames from 0-year to the 100-years

	0-year	10-year	20-year	50-year	100-year
Safety probability (%)	97.61	96.52	93.27	90.14	83.29

Table 3 as shown the safety probabilities of the 3D steel frames considering metal corrosion about 10, 20, 50, and 100-years by the Monte Carlo simulation to the value from 96.52 to 83.29 (%). The used convergence criteria of 2.5 (%) justify the confidence of the estimated reliability. It can be seen that the safe probability has a decrease compared to the time (t = 0-year) respectively 10-years is 1.09 (%), 20-years is 4.34 (%), 50-years is 7.47 (%), and 100-years is 14.32 (%). Relatively important numerical investigate results are the basis for adjusting the structure from at time design or forecasting the durability of the structure during used.

6 Conclusions

This paper proposed an algorithm to assess the structural reliability of the 3D steel frames considering the influence of metal corrosion. The numerical process is developed based on the corrosion model of Komp [3] and Monte Carlo simulation. A wide range of corrosive exposure time from 10 to 100-years is considered in the structural reliability assessment. The flowing conclusions are drawn based on numerical analysis. The proposed algorithm, which is numerically developed based on the Komp corrosion model and Monte Carlo simulation, FEM, the 3D steel frames is capable of and corrosion effect. Overall, as time increased the probability of safety is reduced, and an important recommendation for the selection of the input random variables when adjusting the reliability structure at time design.

Acknowledgements This research is funded by the Vinh University.


References

1. Afshan S, Francis P, Baddoo N, Gardner L (2015) Reliability analysis of structural stainless steel design provisions. *J Constr Steel Res* 114:293–304
2. Bartlett FM, Dexter RJ, Graeser MD, Jelinek JJ, Schmidt BJ, Galambos TV (2003) Updating standard shape material properties database for design and reliability. *Eng J AISC* 40(1):2–14
3. Ellingwood B, MacGregor JG, Galambos TV, Cornell CA (1982) Probability based load criteria: load factors and load combinations. *J Struct Div* 108(5):978–997
4. European Committee for standardization CEN, Brussels, EC3. Eurocode 3: Design steel structures-Part 1.4; General rules-Supplementary rules for stainless steel, 1996, Env 1993-1-4
5. Ha T (2019) Reliability assessment of frame steel considering semi-rigid connections. *J Mater Eng Struct (JMES)* 6(1):119–126
6. Kala Z (2007) Stability problems of steel structures in the presence of stochastic and fuzzy uncertainty. *Thin-Walled Struct* 45(10–11):861–865

7. Kencanawati NN, Merdana IN, Nuraida N, Hadi IR, Shigeishi M (2017) Improving of recycled aggregate quality by thermal-mechanical-chemical process. *Proc Eng* 171:640–644
8. Komp M (1987) Atmospheric corrosion ratings of weathering steels-calculation and significance. *Mater Perform* 26(7):42–44
9. Landolfo R, Cascini L, Portioli F (2010) Modeling of metal structure corrosion damage: a state of the art report. *Sustainability* 2(7):2163–2175
10. Ngoc-Long T, Ha T (2020) The effect of metal corrosion on the structural reliability of the pre-engineered steel frame. *J Mater Eng Struct (JMES)* 7(2):155–165
11. Secer M, Uzun ET (2017) Corrosion damage analysis of steel frames considering lateral torsional buckling. *Proc Eng* 171:1234–1241
12. Sobol IM (1994) A primer for the Monte Carlo method. CRC press
13. British Standard (2002) Eurocode—Basis of structural design: EN 1990
14. Tran N-L, Nguyen T-H, Phan V-P (2020) Reliability assessment of buckling strength for battened built-up columns steel considering shear deformations. In: Paper presented at the IOP conference series: materials science and engineering
15. Hung DX, Ha NT (2016) Assessment reliability of plan frame in the buckling condition using stochastic finite element method. *J Sci Technol Civil Eng* 10(2):23–30

Global Sensitivity Analysis of the Buckling Strength for Battered Built-up Columns Steel Considering Shear Deformations



Ngoc-Long Tran and Trong-Ha Nguyen 

Abstract The Battered built-up steel columns are widely used in civil engineering and industrial structures. The response of this structure depends on the material properties, geometric dimensions, shear stiffness, and also boundary conditions that are potentially random sources. The objective of this study is to perform the global sensitivity analysis, and then to assess the influence of input random parameters on the elastic critical column load of the battered built-up steel columns. The elastic critical column load of the battered built-up steel columns proposed in previous studies is adopted. The influence of the input random variables of the structure is evaluated using Sobol's global sensitivity analysis. Monte Carlo simulation is also employed to rank the influence of input random variables.

Keywords Buckling strength · Steel column · Sensitivity · Global sensitivity · Sobol's indices · Monte Carlo simulations

1 Introduction

The global sensitivity consists of individual sensitivity of each variable and its interaction with other variables. Sobol's sensitivity index was proposed and then widely applied in the structural engineering field [1–5]. The steel structures often present a high durability and include slender components. Therefore, sensitivity and reliability analyses for steel structures and other study have been interested by many researchers.

The sensitivity analysis of the structure has been of interest to many authors. In 2003, Hadianfard et al. [6] had performed a research on the effects of semi-rigid behavior of connections in the reliability of steel frames. Kala et al. [7] had announced a research variance-based sensitivity analysis of stability problems of steel structures using shell finite elements and nonlinear computation methods, in

N.-L. Tran · T.-H. Nguyen (✉)

Department of Civil Engineering, Vinh University, 182 Le Duan, Vinh 461010, Vietnam
e-mail: trongha@vinhuni.edu.vn

which the research deals with an analysis of the influence of initial imperfections on the ultimate limit state of slender steel members under axial compression. In 2010, A. Habib et al. [8] has performed a sensitivity analysis, in which necessary tasks for the design optimization of structures.

Concerning the buckling strength of the steel column, some studies were carried out. In 1961, Timoshenko et al. [9] had performed a numerical solution in a similar form to Euler's solution with an adjustment factor whose values are tabulated depending on the ratio between the maximum and the minimum moment of the inertia of the column. Lee et al. [10] had proposed calculates the buckling load of the tapered column via the one of a uniform column of the minimum section used a modification factor. That same idea, Hirt et al. [11] has used the equivalent section whose the moment of inertia is in practical form. Meanwhile, Marques et al. [12] has proposed an analytic solution for the buckling load of the tapered column. However, to the best of our knowledge, the global sensitivity analysis of the elastic critical column load of the battened built-up steel columns is far from fully investigated.

This paper studies the sensitivity assessments of the elastic critical column load of the battened built-up steel columns considering shear deformations. An algorithm using the global sensitivity method is proposed to utilize in analyses and assessments. In addition, the effects of input random variables on the elastic critical column load of the battened built-up steel columns are also examined.

2 Global Sensitivity Analysis

Ilya M. Sobol' [13] a Russian mathematician, elaborated one of the most coherent sensitivity analyses. In the paper presented, the Sobol's sensitivity analysis will be applied for study of the influence of input random quantities.

Sensitivity presents the influence of an input design parameters (variables) $X = (X_1, X_2, \dots, X_m)$ on the output model $Y = f(X)$ where, $X = (X_1, X_2, \dots, X_m)$ is the vector of design parameters in space \mathbb{R}^m and $Y = (Y_1, Y_2, \dots, Y_n)$ is the vector of output value in space \mathbb{R}^n . In this study, the sensitivity assessments using the Sobol's sensitivity analysis was established on Matlab. The Matlab code was verified and used in studies by the author in [3].

3 Sensitivity Analysis of the Elastic Critical Column Load

3.1 Evaluation of the Elastic Critical Column Load of the Battened Built-up Column

The effect of shear deformations on the elastic critical column load, the differential equation, the equilibrium of the column has been presented by the authors in [14].

In [14], considering the simple case of a pin-ended column as shown in Fig. 1, the elastic critical load $N_{cr, id}$ considering shear deformations may be rewritten as follows:

$$N_{cr, id} = \frac{1}{\left(\frac{1}{N_{cr}} + \frac{1}{S_v}\right)} = N_{cr} \frac{1}{1 + \frac{N_{cr}}{S_v}} \tag{1}$$

where, $N_{cr} = \pi^2 \frac{EI}{l^2}$ is the Euler buckling load obtained disregarding the deformations due to shearing force; S_v is the shear stiffness of the column. In this research considering battened built-up columns as shown in Fig. 2. According to [14] the shear stiffness be determined

$$\frac{1}{S_v} = \frac{a^2}{24EI_c} + \frac{ah}{12EI_b} \tag{2}$$

Fig. 1 Pin-ended column

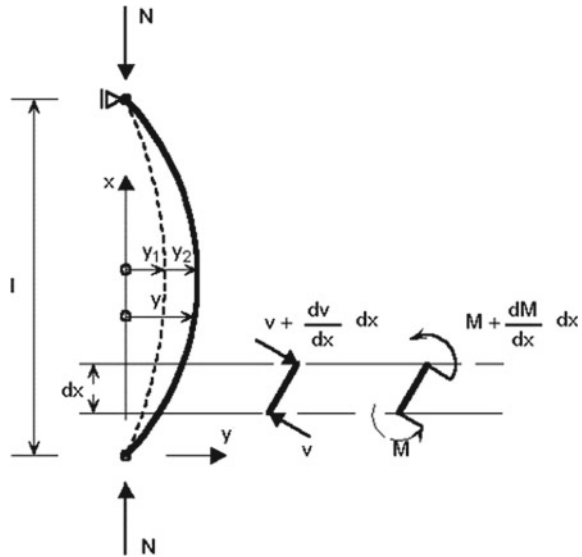
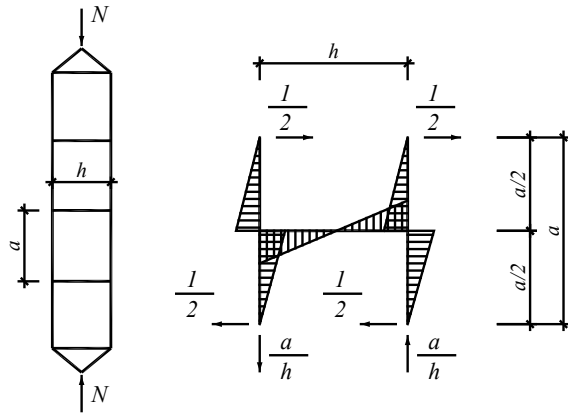


Fig. 2 Battered built-up columns



where, I_c is the in-plane second moment of area of one chord; I_b is the in-plane second moment of area of one batten; E is the modulus of elasticity (Young’s modulus).

The effect of shear deformations on the elastic critical column load of the battered built-up steel column has been verified by the author in [14].

3.2 Sensitivity Analysis

Let us now apply Sobol’s decomposition to the analysis of the elastic critical column load of the battered built-up steel columns considering shear deformations. Input random variables are listed in Table 1.

The inputs variables in Table 1 are fully uncorrelated, fully uncorrelated input variables represent one of the preconditions for the application of Sobol’s global sensitivity analysis. The global sensitivity base on Sobol’ indices are applied to

Table 1 Input random quantities

Properties	Variables	Distribution	Range	Units
Material	E	Uniform	/180–220/	(N/mm ²)
	μ	Uniform	/0.27–0.33/	–
Cross-section	a	Uniform	/180–220/	cm
	H	Uniform	/90–110/	cm
	I_c	Uniform	/7707.6–9420.4/	cm ⁴
	I_b	Uniform	/19199.7–23466.3/	cm ⁴
Geometry	L	Uniform	/540–660/	cm

Table 2 Mean estimation with 100.000 Monte-Carlo samples

	1st order effects	Total effects
$X_1 (E)$	0.2788	0.2669
$X_2 (I_c)$	0.2063	0.2071
$X_3 (I_b)$	0.0099	0.0035
$X_4 (a)$	0.1238	0.1235
$X_5 (h)$	0.0082	0.0035
$X_6 (L)$	0.3999	0.3938

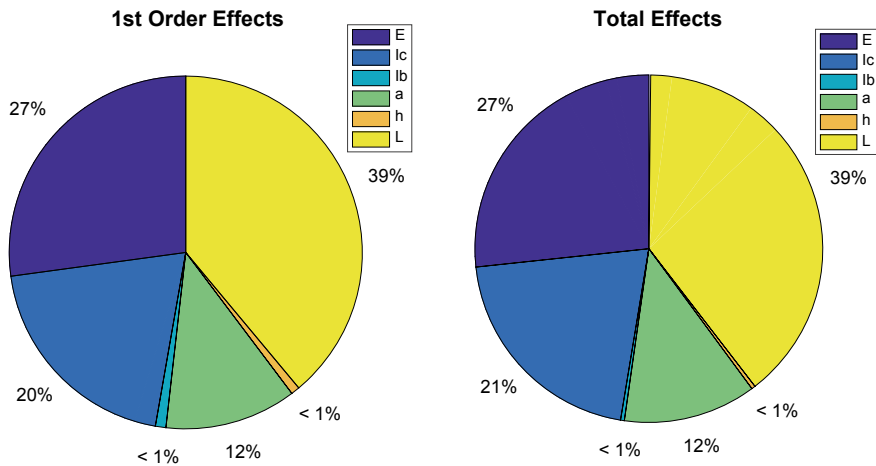


Fig. 3 First-order and total Sobol's sensitivity indices of the elastic critical column load of the battened built-up steel columns considering shear stiffness

evaluate the influence of input random variables on the elastic critical load of the battened built-up steel columns. After 100,000 simulations with 20.6 min, the results of the first-order and total-order affect Sobol's sensitivity indices as shown in Table 2 and Fig. 3.

Table 2 and Fig. 3 showed the first-order and total-order effect Sobol's sensitivity indices of input random variables on the elastic critical column load of the battened built-up steel columns considering shear deformations. We can be seen that E , I_c , L and a are the most influential input random variables with a proportion of 27.0 (%), 20.0 (%), 39.0 (%), and 12.0 (%). Meanwhile, the input random variables influential at least is I_b , h with a proportion of 1.0 (%). We can be seen the first-order and total-order effect Sobol' indices have not changed much. This proves that influence input random variables on the elastic critical column load of the battened built-up steel columns considering shear deformations has a very small interaction.

4 Conclusions

This paper proposed an algorithm to assess the structural sensitivity of the elastic critical column load of the battened built-up steel columns considering shear deformations. The numerical process is developed based on Sobol's sensitivity indices and Monte Carlo simulation. The elastic critical column load of the battened built-up steel columns considering shear deformations is considered in the structural sensitivity assessment. The flowing conclusions are drawn based on numerical analyses.

The algorithm, which is numerically developed based on Sobol's sensitivity indices and Monte Carlo simulation, is developed for sensitivity analyses of the elastic critical column load. A verification of the proposed algorithm is also conducted using the Ishigami's test function.

An important recommendation for the selection of the input random variables based on numerical analyses, the developed procedure in this study can be applied for the elastic critical column load of the battened built-up steel columns considering shear deformations.

An extended application for other types of other structures is highly feasible; however additional numerical tests and verifications are required.

Acknowledgements This research is funded by the Vinh University.

References

1. Abshari H, Azadi M. RE, Azar MS (2014) Reliability analysis of steel structures under buckling load in second-order theory. *Adv Res* 950–966
2. Cacuci DG (1981) Sensitivity theory for nonlinear systems: I—Nonlinear functional analysis approach. *J Math Phys* 22(12):2794–2802
3. Crisinel M, Hirt MA (2001) *Charpentes métalliques: conception et dimensionnement des halles et bâtiments: Presses polytechnique et universitaires romandes*
4. Ha NT, Hung DX (2018) Sensitivity analysis of the design portal frames of steel industrial buildings. In: Paper presented at the MATEC web of conferences
5. Habibi A, Moharrami H (2010) Nonlinear sensitivity analysis of reinforced concrete frames. *Finite Elem Anal Des* 46(7):571–584
6. Hadianfard M, Razani R (2003) Effects of semi-rigid behavior of connections in the reliability of steel frames. *Struct Saf* 25(2):123–138
7. Kala Z, Kala J (2009) Variance-based sensitivity analysis of stability problems of steel structures using shell finite elements and nonlinear computation methods. In: Paper presented at the WSEAS international conference. *Proceedings. Mathematics and Computers in Science and Engineering*
8. Lee G, Morrell M, Ketter R (1972) Design of tapered members, WRC bulletin, no. 173. New York (NY), Welding Research Council
9. Marques L, Taras A, da Silva LS, Greiner R, Rebelo C (2012) Development of a consistent buckling design procedure for tapered columns. *J Constr Steel Res* 72:61–74
10. Melchers RE (2005) The effect of corrosion on the structural reliability of steel offshore structures. *Corros Sci* 47(10):2391–2410

11. Morio J (2011) Global and local sensitivity analysis methods for a physical system. *Eur J Phys* 32(6):1577
12. Timoshenko SP, Gere JM (2009) *Theory of elastic stability*: Courier Corporation
13. Tran N-L, Nguyen T-H, Phan V-P (2020) Reliability assessment of buckling strength for battened built-up columns steel considering shear deformations. In: Paper presented at the IOP conference series: Materials Science and Engineering
14. Vrouwenvelder T (1997) Joint committee on structural safety. *Struct Safety* 19(3)

Simulations of Local Scour Depth at Piers of the Ben Thuy Bridge, Nghe an Province



Chien Pham Van

Abstract This study presents a numerical model based on the one-dimensional lateral distribution method and four classic formulae that can be used to simulate local scour depth at bridge piers. In order to accurate predictions of flow velocity, gravity, bed shear stress and turbulent diffusion forces are taken into account in hydrodynamic calculations. Four formulae are implemented and applied to evaluate local scour depth at bridge piers. Ben Thuy bridge located in Nghe An province is selected as an example. The results show that the local scour depth varied between 0.80 and 8.0 m at piers of this bridge. The maximum value of the local scour depth appeared at piers in the deep region (from 415 to 675 m) of the bridge river section, while small values occurred at piers in the shallow areas. Among four selected formulae, three formulae proposed by Laratslasev (1953), Zuravlev (1978), and Nguyen and Nguyen (1982) predicted similar trend and value of the local scour depth at piers in the shallow areas.

Keywords Local scour depth · Ben Thuy bridge · Lateral distribution method

1 Introduction

Bridge is the most important structure that is widely built for linking infrastructure in both sides of a river as well as for purposes of transportation and development in many cities located along rivers. Local scour at bridge piers has been studied in detail many years and the scour mechanism is well understood and described [1]. However, high flows often increase the river instability, local scour at bridge piers, and effect on the safety of existing bridges. Thus, accurate prediction of local scour depth at bridge piers is a key issue in bridge engineering and it still remains a subject of concern in hydraulic engineering.

C. Pham Van (✉)

Thuyloi University, 175 Tay Son, Dong Da, Hanoi, Vietnam

e-mail: pchientvct_tv@tlu.edu.vn

Local scour depth at bridge piers is often computed by using an empirical formula [2, 3], in which local hydrodynamic characteristics need to be determined in detail. Besides field measurements, different models can be used to simulate the local flow velocity (and water depth) in rivers and particularly in a river cross section. Regarding the river cross section, the water depth often is smaller than the width of the river by a factor of many orders of magnitude, and, thus the depth-averaged models are widely applied to simulate the flow in practical applications. This kind of depth-averaged model allows for significantly reducing the computational time in comparison with three-dimensional models and provides more detailed information of hydrodynamic characteristics of the flow than those obtained in cross-section averaged models [4]. Among the different depth-averaged models, one-dimensional lateral distribution method is widely used to simulate the flow characteristics [4].

This study presents a numerical model based on the one-dimensional lateral distribution method and four classic formulae that can be used to simulate local scour depth at bridge piers. In particular, the study aims to quantitatively estimate the local scour depth at piers for the Ben Thuy bridge, Nghe An province.

2 Numerical Model

2.1 Hydrodynamic Module

The hydrodynamic characteristics comprised of water depth and depth-averaged velocity at different locations across a river cross section are determined by solving Eq. (1) which is derived by integrating the Reynolds equations over the depth for steady and uniform flow and a horizontal water surface [4]

$$\rho g H S_x - B_g \tau_b + \frac{\partial}{\partial y} \left(\rho H v \frac{\partial U}{\partial y} \right) = 0 \quad (1)$$

where y indicates the lateral direction, g is the gravitational acceleration ($=9.81 \text{ m/s}^2$), ρ is the water density ($=1000 \text{ kg/m}^3$), H is the water depth (m), S_x is the bed slope in the streamwise direction, $B_g = \sqrt{1 + S_x^2 + S_y^2}$ is the geometrical factor, in which S_y is the local bed slope in the lateral direction that is computed based on the geometry of the river cross section, τ_b is the bed shear stress (N/m^2), v is the eddy viscosity (m^2/s), and U is the depth-averaged flow velocity (m/s).

The bed shear stress τ_b and the eddy viscosity v are computed using Eq. (2).

$$\tau_b = \rho \frac{gn^2}{H^{1/3}} U^2, \quad v = \lambda U_* H \quad (2)$$

where n is Manning’s coefficient representative of the bed friction, U_* is the shear velocity, and λ is the non-dimensional eddy viscosity coefficient.

Beside the depth-averaged flow velocity, sectional-averaged flow velocity is also computed when evaluating the local scour depth at bridge piers. The sectional-averaged flow velocity U_{sec} is calculated based on the water discharge and sectional area.

2.2 Scour Depth Module

The local scour depth at bridge piers is computed using four popular formulae (Table 1) that were proposed by Laratslasev (1953), Zuravlev (1978), Nguyen and Nguyen (1982), and Richardson and Davis (2001).

In Table 1, K_ξ is the coefficient depending on shape of piers and flow direction; K_v is the coefficient representative for the width of piers and the flow velocity; c is the coefficient ($c = 1$ for shallow areas and $c = 0.6$ for deep regions of the section); U_{ox} is the critical velocity for no erosion; K_H is the coefficient depending on the flow depth; K_d is the coefficient taking into account impact of shape of piers; b is the width of piers; α is the power coefficient ($\alpha = 3/4$ if $U/U_B > 1$, $\alpha = 2/3$ if $U/U_B \leq 1$ with U_B is the velocity determined based on sediment diameter; K_2 is the coefficient taking into account the flow direction; K_3 is the coefficient caused by state of river bed; K_4 is the coefficient reduced the local scour depth due to the coarse sediment particle with $d_{50} > 60$ mm; and Fr is the Froude number.

2.3 Numerical Implementation

In terms of numerical implementation, the river section of the bridge is firstly divided into a number of nodes. Then, Eq. (1) is solved numerically by using a

Table 1 Four formulae for estimating the local scour depth at bridge piers

Formulas	Abbreviated	References
$h_{xcb} = K_\xi K_v (K_H + c) \frac{U^2}{g} - 6 \frac{U_{ox}^2}{g}$	LARA	Nguyen and Nguyen (1982)
$h_{xcb} = K_d b^{2/3} H^{3/5} \left(\frac{U}{U_B}\right)^\alpha$	ZURA	Nguyen and Nguyen (1982)
$h_{xcb} = \begin{cases} 0.97 K_d b^{0.83} H^{0.17} \left(\frac{U}{U_{ox}}\right)^{1.04} & \text{if } U < U_{ox} \\ 0.52 K_d b^{0.88} H^{0.12} \left(\frac{U}{U_{ox}}\right)^{1.16} & \text{if } U \geq U_{ox} \end{cases}$	DHXD	Nguyen and Nguyen (1982)
$h_{xcb} = 2.0 K_d K_2 K_3 K_4 b^{0.65} H^{0.36} Fr^{0.43}$	RICH	Richardson and Davis (2001)

finite difference method, resulting in a discrete equation that is solved with the Newton-Raphson iteration method. The free slip condition also is applied at the river banks. Next, the local scour depth at bridges piers are computed using the four formulae in the scour depth module.

3 Application

3.1 Ben Thuy Bridge

Ben Thuy bridge is used as an applicable example of the proposed model in the present study. This bridge is the most important structure for linking infrastructure in both sides of Ca river as well as for transportation between Ha Tinh and Nghe An provinces (Fig. 1). The water discharge corresponding to the return period of 100 years at the bridge is $16,500 \text{ m}^3/\text{s}$. Regarding to the river bathymetry around the bridge, the deepest creek appears between T6 and T7 piers of the bridge (see Fig. 3), with the magnitude of 18.55 and 20.61 m at upstream and downstream of the bridge, respectively.

3.2 Results and Discussion

Figure 2 shows the lateral distribution of velocity and unit water discharge ($q = U \times H$) corresponding to the $Q = 16,500 \text{ m}^3/\text{s}$ at the Ben Thuy bridge. Different values of Manning coefficient, which are determined from the median sediment diameter (d_{50}) and from trial and error method, are tested. The proposed model reproduces logically the velocity and unit water discharge in the river section, i.e. large values of velocity and unit water discharge occur at the main channel (from $340 \text{ m} < y < 720 \text{ m}$) while the small values occur in the floodplain ($y < 340 \text{ m}$ and $y > 720 \text{ m}$). In the deep region of the section, the unit water discharge when using the sectional-averaged velocity is smaller than those when

Fig. 1 Map of the bridge of interest



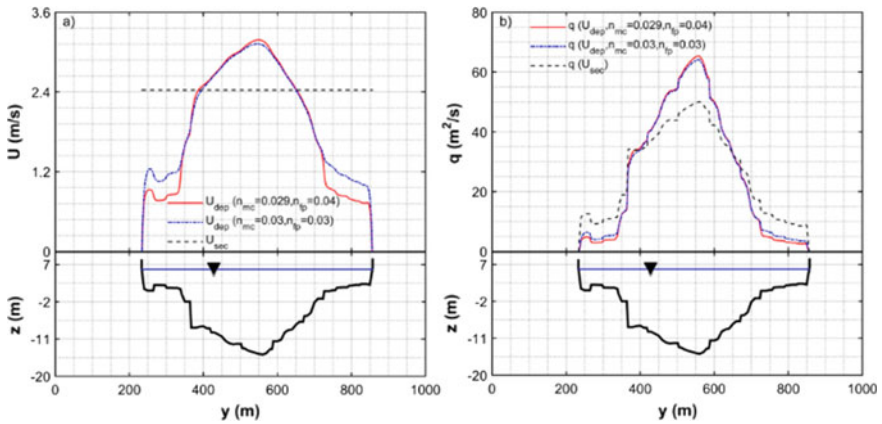


Fig. 2 Lateral distribution of: **a** velocity and **b** unit water discharge at $Q = 16,500 \text{ m}^3/\text{s}$ (and $H = 5.48 \text{ m}$). The subscripts mc and fp refer to the main channel and floodplain, respectively

using the depth-averaged velocity while opposite trend is observed in the shallow areas. This is due to the limitation of using the constant velocity in the sectional-averaged calculation.

Figure 3 illustrates the predicted values of the local scour depth at piers for the Ben Thuy bridge. All formulae present large values of the local scour depth at piers in the deep region of the river section while small values of the local scour depths happen at the piers in the floodplain. Among four formulas, the formula proposed

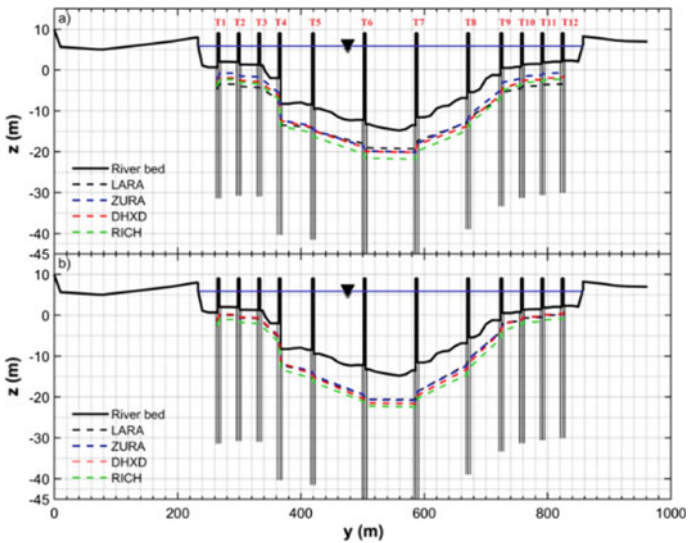


Fig. 3 Local scour depth values when using: **a** sectional- and **b** depth-averaged velocity

Table 2 Local scour depth when using sectional- and depth-averaged flow velocity

Piers	Using sectional-averaged flow velocity				Using depth-averaged flow velocity			
	DHXD	ZURA	LARA	RICH	DHXD	ZURA	LARA	RICH
T5	4.41	4.06	4.48	5.77	4.72	4.22	4.65	5.92
	4.40	4.11	4.47	5.79	4.73	4.28	4.66	5.95
	4.39	4.15	4.46	5.82	4.74	4.34	4.67	5.99
T6	5.59	5.36	4.69	7.18	7.17	6.19	6.23	7.87
	5.58	5.42	4.68	7.20	7.17	6.27	6.23	7.91
	5.56	5.47	4.67	7.23	7.18	6.34	6.23	7.94
T7	5.56	5.50	4.67	7.24	7.00	6.28	6.02	7.89
	5.58	5.40	4.68	7.19	6.99	6.15	6.01	7.82
	5.60	5.30	4.70	7.14	6.98	6.01	6.02	7.75
T8	5.74	4.69	4.91	6.84	5.20	4.43	4.08	6.59
	5.76	4.59	4.96	6.79	5.17	4.32	4.08	6.52
	5.78	4.50	5.02	6.74	5.14	4.20	4.09	6.45
T9	3.82	2.67	4.61	4.53	2.01	1.84	1.94	3.57
	3.86	2.55	4.74	4.46	1.95	1.72	1.91	3.46
	3.89	2.42	4.93	4.37	1.90	1.60	1.89	3.35

by Richardson and Davis (2001) predicts the largest values because this formula allows for predicting the maximum potential scour depth while the scour depth from three other formulas is not significant discrepancy.

If the sectional-averaged velocity ($U_{sec} = 2.43$ m/s) is applied, the maximum scour depths at piers are 5.02, 5.50, 5.78 and 7.24 m for the formula proposed by Laratlsasev (1953), Zuravlev (1978), Nguyen and Nguyen (1982) and Richardson and Davis (2001), respectively. These values equal to 6.23, 6.34, 7.18 and 7.94 m when using the depth-averaged flow velocity (Table 2). The difference of local scour depths at piers when using sectional- and depth-averaged flow velocity is ranging from 0.70 to 1.40 m. These results are consistent with the results reported by Moussa [1].

4 Conclusion

In this study, a numerical model based on the one-dimensional lateral distribution method and four classic formulae that can be used to simulate local scour depth at bridge piers was presented. The model was then applied to quantitatively simulate local scour depth at piers of the Ben Thuy bridge, Nghe An province for the water discharge corresponding to the return period of 100 years. The model predictions showed that a value of magnitude of 8.0 m was obtained when using the local flow velocity, while this value was of about 7.24 m if a uniform flow velocity was used. Among four selected formulae, the formula proposed by Richardson and Davis (2001) predicted the largest value of local scour depth for the bridge of interest.

References

1. Moussa AMA (2018) Evaluation of local scour around bridge piers for various geometrical shapes using mathematical models. *Ain Shams Eng J* 9(4):2571–2580
2. Nguyen XT, Nguyen HK (1982). Local erosion scour at bridge piers and proposed formula for estimation. National Proceeding of Science and Technology, No. 4 (In Vietnamese)
3. Richardson EV, Davis SR (2001) Evaluating scour at bridges. Federal Highway Administration
4. Van Pham C, Chua V (2020) Numerical simulation of hydrodynamic characteristics and bedload transport in cross sections of two gravel-bed rivers based on one-dimensional lateral distribution method. *Int J Sedim Res* 35(2):203–216

Load Carrying Capacity Old Steel Girder with Considering Corrosion Effect of Steel Material



Pham Van Hung, Nguyen Duc Hieu, Bui Thanh Tung,
and Tran The Truyen

Abstract There are many steel girder bridges that have been operated for a long time, particularly on the national railway system. These structures have not been maintained and repaired with a reasonable level which led to rust of steel girder. Corrosion has made a decrease of a cross-section along with the length or at local areas of steel girder; A significant degradation of the loading capacity of steel girder which could seriously affect the safety of these bridges. Rely on verification for structures, parameters of material, rust condition and detailed dimensions of the girder, service load is determined. Analyzing and summarizing these parameters have estimated the general condition of rust and loading capacity of operative constructions. Additionally, numerical simulations according to the finite element method to investigate the loading capacity of steel girder with relevant parameters of rust condition such as depth of rust layers, rust position and rust area have been implemented as well. Non-linear analyses have also been performed to determine the behavior of steel girders under loading. Results of investigation would assist to induct regulation of the operation, solution of repairmen.

Keywords Bridge · Steel girder · Rust · Corrosion · Non-linearity · FEM

1 Introduction

The steel beam structure has been popularly applied in the world and Vietnam is not out of this trend. Vietnam is a country with a long coastline, lots of steel bridges are, thus affected by corrosion in the characteristic marine climate. Corrosion significantly affects the working ability of steel beam structure, causing deterioration of the life cycle of the building. Typical girder corrosion forms are illustrated in Fig. 1. Over the years, the corrosion can be serious enough to disconnect the web from the flanges of the beam structure, which poses significant concerns for load resistance

P. Van Hung · N. D. Hieu (✉) · B. T. Tung · T. T. Truyen
University of Transport and Communications, Hanoi, Vietnam
e-mail: hieund_ph@utc.edu.vn

© The Author(s), under exclusive license to Springer Nature Singapore Pte Ltd. 2021
T. Bui-Tien et al. (eds.), *Proceedings of the 3rd International Conference on Sustainability in Civil Engineering*, Lecture Notes in Civil Engineering 145,
https://doi.org/10.1007/978-981-16-0053-1_8



Fig. 1 Typical corrosions on steel beam structure

especially at girder ends. The consequences of processing on the steel beam structure can be unexpected.

Based on state-of-the-art understanding and knowledge the content of the article raises the current understanding of load capacity analysis of corroded steel girders.

Performing full-scale physical experiments on bridges are expensive and sometimes impossible. As a result, modeling analysis has been adopted to conduct research on large scale structures, including bridges in the last decades. The power of the finite element method which is a type of modeling analysis lies in its versatility and ability to solve various physical problems. The analyzed domain can apply with a lot of shapes, loads, and boundary conditions with numerous types of elements and material properties. Another attractive feature of the finite element method is the close physical resemblance between the actual structure and its corresponding finite element model. ABAQUS offers powerful and complete solutions for both routine and sophisticated engineering problems covering a range of industrial applications including steel structures [1]. In this paper, ABAQUS is used as a numerical tool to study the mechanical behaviors of deteriorated girders.

2 Finite Element Modeling

3D finite element models are stimulated to analyze the buckling and shear capacity of the steel girder web. The boundary conditions are modeled properly to simulate the real behaviors of supports, such as displacement and rotation at the girder ends. The loads and the governing load cases are selected according to the load combinations specified in AASHTO LRFD Bridge Design Specifications [2, 3]. Area loss will be modeled by removing materials from the web, and web thinning will have simulated by uniformly reducing the web thickness. Change the size, shape and location of the loss zone with the numerical models resemble real steel corrosion

patterns. Web thinning due to rust mainly affects the strength and buckling of girder and web, respectively. The loading capacity of the deteriorated girders is analyzed.

The bridge model in this investigation is Km12 + 523 Bridge at Highway 14C, in Ngoc Hoi district, Kon Tum province. The bridge includes simply supported steel beams and a cast-in-place concrete deck. The span length of the bridge is 12 m. The overall width of the bridge is 6.6 m, and the bridge carries 2 lanes of traffic. The design live load for the bridge is the typical AASHTO HL-93 Live Load. The cast-in-place deck is 200 mm thick. The span structure has 9 girders with a girder space of 750 mm. The elevation of the bridge is shown in Fig. 2 and the typical section is shown in Fig. 3.

The I450 steel girder with the boundary conditions are pinned at one end of the top and bottom flanges to simulate the real girder end embedded into the abutment diaphragm. The other end is free in vertical movement but restricts horizontal movement along the girder. The 3D finite element model of the girder end is shown in Fig. 2.

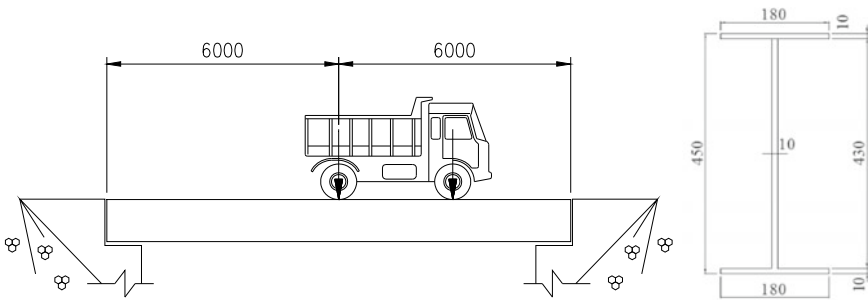


Fig. 2 Bridge elevation and dimensions of girder cross-section

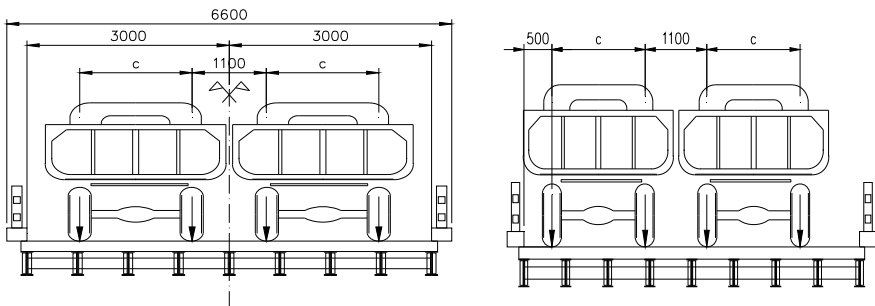


Fig. 3 Bridge typical section

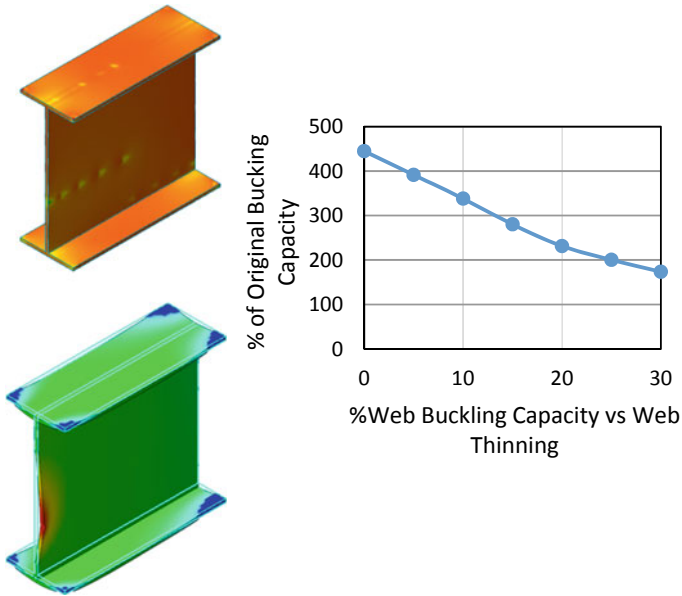


Fig. 4 Web buckling capacity versus web thinning

ABAQUS software is used to model two types of girder corrosion which are area loss and web thinning because of rust. The area loss is modeled by removing a part of the web area as shown in Fig. 4. The effects of different shapes and sizes of area loss on the loading capacity of the girder are investigated. The shapes of area loss are rectangular with the longer side parallel to the girder longitudinal direction, square, and rectangular with the longer side parallel to the web depth. Web thinning is modeled by reducing the thickness of the entire web [2, 3].

3 Results

In this article, a typical interior girder is used for calculating the shear force at the girder end. The dead load of steel girder and un-composite concrete slab (DC) without loading factor on the girder is 21.885 kN/m, and the un-factored wearing surface (DW) on the girder is 5.106 kN/m. The live load (LL) on the girder is AASHTO HL-93 live load, the dynamic impact factor of the design truck is 1.33, and the live load distribution factor for shear is 0.884, which is calculated according to AASHTO LRFD Bridge Design Specifications as shown in Eq. 1 [2].

$$mg_v = \begin{cases} 0.36 + \frac{s}{25} = 0.36 + \frac{9}{25} = 0.720 & \text{for one lane loaded} \\ 0.2 + \frac{s}{12} - \left(\frac{s}{35}\right)^2 = 0.2 + \frac{9}{12} - \left(\frac{9}{35}\right)^2 = 0.844 & \text{for more 2 lanes} \end{cases} \quad (1)$$

where: S—is the space between girders and mg_v —is the live load distribution factor for shear.

The maximum design shear force at the girder end is obtained by Strength I load combination specified in Eq. 2 according to AASHTO LRFD Bridge Design Specifications. [2]

$$\text{Strength I Load Combination : } 1.25DC + 1.50DW + 1.75LL \quad (2)$$

Removing portions of the web for modeling the area loss due corrosion. In this study, the shapes of the area loss include rectangles with the long side parallel to the girder line, rectangles with a longer side parallel to the web depth, and squares. The results of web buckling capacity versus different shapes and sizes of area loss are shown in Figs. 5, 6 and 7.

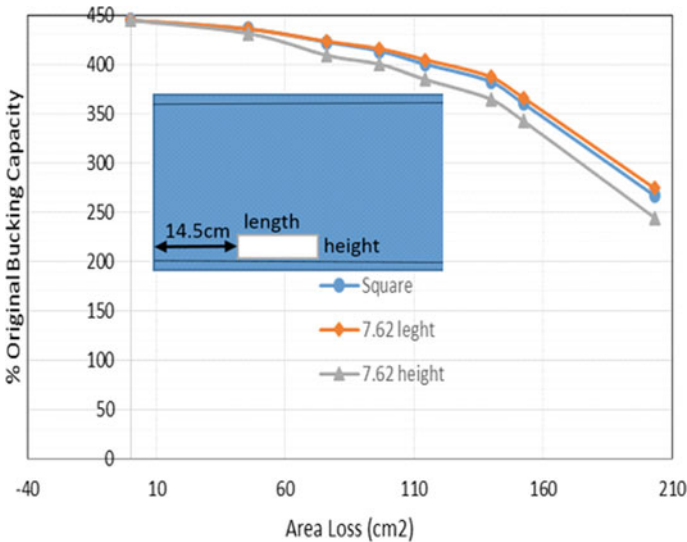


Fig. 5 Buckling capacity of web versus area loss—shapes and sizes

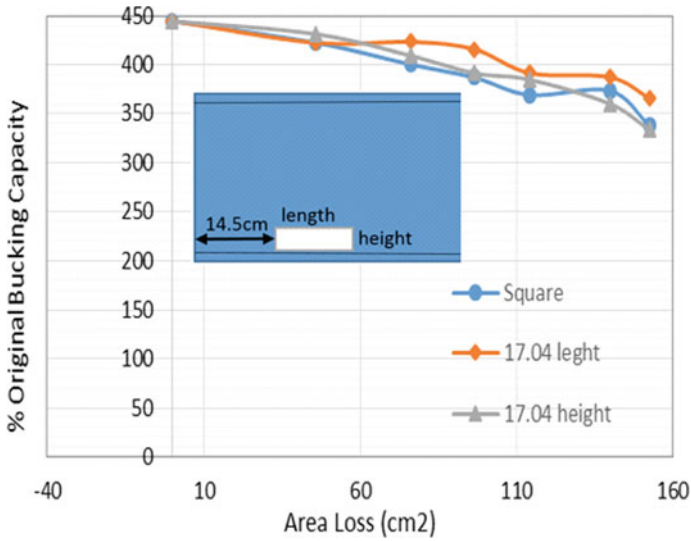


Fig. 6 Buckling capacity of web versus area loss—shapes and sizes

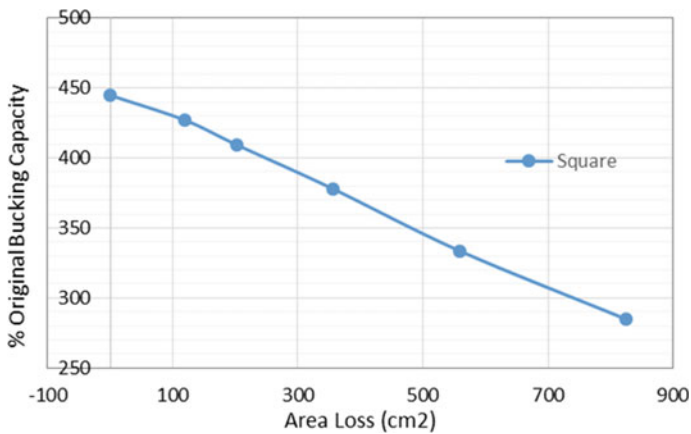


Fig. 7 Buckling capacity of web versus area loss—square

4 Conclusions

The article focuses on the investigation of common corrosion types in steel girder bridges and the effects of web thinning and web area loss on the loading capacity of steel beam due to rust.

According to the results of 3D finite element analyses, several can be concluded that are:

1. Web thinning due to corrosion has a significant effect on girder shear and buckling of girder web. The development of extensive rust can dramatically reduce the girder's structural capacity. 10% reduction in effective thickness of the web may result in 25% or more buckling loss.
Figures 5, 6 and 7 show consistently that the larger size of area loss, the lower the structural capacity. The strength may drop below the girder design load, once the size of area loss reaches a critical value, which represents structural deficiency.
2. The shape of the area loss plays an important role in the girder's residual strength. When extending area loss in the direct parallel to the girder line, the loading capacity decreases at a significantly higher rate than extending area loss in the direction parallel to the web depth.

References

1. ABAQUS/CAE, User's Guide (2016)
2. American Association of State Highway and Transportation Officials (2016) AASHTO LRFD Bridge Design Specifications 7th ed
3. NYSDOT (2017) Bridge Manual

Research on Monitoring Technology of Cable-Stayed Bridge



Jiabao Du, Zhao Hong, Yuan Chen, Yahui Li, Jinzhu Song,
and Qiang Tang

Abstract Monitoring of cable stayed bridge during service is the key to ensure the safety of the bridge. To improve the monitoring technologies, this paper summarized the relevant research and application, including Stay cable monitoring, tower column monitoring. The results show that the method of monitoring has changed from manual to machine. The principles of monitoring are more abundant, such as image analysis, acceleration analysis, magnetic flux analysis, temperature analysis and so on. This paper can provide reference for the further research on the monitoring technology of cable-stayed bridge.

Keywords Cable-stayed bridge · Stay cable · Monitoring technology

1 Introduction

Although the cable-stayed bridge has the advantages of large spanning capacity, reasonable stress, beautiful appearance, and small building height. However, under the influence of environmental factors such as vehicle load, temperature, wind, etc., the material, geometry and internal force state of the cable-stayed bridge will

J. Du · Q. Tang (✉)

School of Rail Transportation, Soochow University, Suzhou, China
e-mail: tangqiang@suda.edu.cn

Z. Hong · Y. Chen · Y. Li · J. Song

Nanjing Branch of CCCC Tunnel Engineering Company Limited, Nanjing, China

Q. Tang

Key Laboratory of Ministry of Education for Geomechanics and Embankment Engineering,
Hohai University, Nanjing, China

Jiangsu Research Center for Geotechnical Engineering Technology, Hohai University,
Nanjing, China

change. Once the main components of cable-stayed bridge are damaged, safety accidents may occur. It shows that the monitoring of cable-stayed bridge should be paid attention to.

In order to ensure the safety and normal operation of bridges, the monitoring of bridge health has been paid attention to and studied by scholars all over the world. This article summarizes and summarizes the previous research, aiming to provide reference for future research on cable-stayed bridge health monitoring.

2 Stay Cable Monitoring

2.1 Appearance Monitoring

The main inspection items for the visual inspection of oblique cables are polyethylene sheath inspection and steel wire inspection. The early detection method is to build a platform near the cable and conduct manual detection, which has high risk factors. Inspectors hold telescopes or portable telescopic poles for inspection, and the inspection accuracy and efficiency are low. New methods in recent years mainly include the use of imaging analysis, artificial intelligence and acceleration and so on. The application in image analysis includes the use of principal component analysis to enhance the image of protective layer defects and extract information, and then determine the degree of damage through the sample similarity [1]. MEMS remote sensing system can be used to collect acceleration to detect whether the protective layer is damaged, and the natural frequency and related vibration parameters of the cable can be obtained by this method [2]. In addition, the development and application of cable monitoring robot also greatly improves the applicability and accuracy of cable damage monitoring [3]. In terms of using acceleration to monitor, Kaloop use acceleration measurement to locate cable damage [4], which provides a more complete detection method for cable-stayed bridge detection. In the use of artificial intelligence for monitoring, Arangio developed the application of bridge detection calculation method, mainly discussed the applicability of Bayesian nervous system in cable-stayed bridge damage identification, and compared it with traditional methods [5]. In addition, the damage monitoring methods of cable-stayed bridges have been studied by many scholars. For example, Tabatabai mentioned the damage detection methods of the bridge cable system in his article [6]. There is also a magnetic flux leakage detection method for the detection of oblique steel wires. When the steel wire is dented or broken due to corrosion, it will cause magnetic flux leakage. The Hall element can be used to detect the magnetic flux leakage, thereby judging the damage. In many jobs, robots have gradually replaced humans, as shown in Fig. 1.



Fig. 1 Cable inspection robot

2.2 Stay Cable Force Monitoring

Whether the cable force of the cable-stayed bridge is at a normal level is an important indicator of the safe service of the cable-stayed bridge. Cable force detection methods during operation period mainly include frequency method, magnetic flux method and fiber grating method.

The frequency method is a method to detect the cable stress under artificial excitation or environmental excitation as shown in Fig. 2. The principle is to obtain the random vibration signal of the cable through the acceleration sensor, so that the natural frequency of the cable can be finally obtained. By comparing the cable force with the natural frequency, the measured cable force can be obtained. Since the actual cable force of the cable-stayed bridge is only about 40% of the ultimate strength of the cable-stayed bridge, there is usually no accident with stay cables. However, in order to better understand the working state of the cable, it is necessary to carry out more monitoring. The bending stiffness of the cable and the temperature during the measurement have a great influence on the results.



Fig. 2 A certain frequency method cable force measuring instrument

The magnetic flux method is a non-destructive method for measuring cable force and monitoring cable corrosion. A magnetic flux ring should be installed on the cable as a sensor. The cable force can be calculated by the change of magnetic flux. Except for temperature, it is almost unaffected by other interference factors, so it has higher accuracy than other detection methods. In recent years, more clever applications of the magnetic flux methods have been used. Xu studied the detection of magnetic flux to measure the damage of the stay cable, and used the robot to adjust the position of the detection tool in real time [7]. It can be used for remote real-time and long-term monitoring and analysis of the condition of existing bridge cables.

The fiber grating method is to irradiate the side of the fiber with ultraviolet light in the core range of the sensing fiber or write it by other methods, so that the refractive index in the range changes periodically along the fiber axis, and then the periodicity of the reflected wavelength of the grating changes cause changes in external physical quantities. It can be used for cable-stayed bridge construction phase measurement and long-term safety monitoring of the structure.

In addition, some scholars have studied the stay cables. For example, Ju and Park mainly studied the monitoring methods of stay cables in the case of typhoons, and also proposed some methods of strengthening stay cables when facing typhoons [8]. Asgari and Osman proposed an optimization method to calculate the optimal stress of stay cables [9]. In addition, Hua. proposed a method to detect the damage of stay cables by using the change of tension in cables [10]. Liang designed an evaluation model that can determine the cable's bearing capacity by studying the tensile capacity of the corroded stay cable [11]. Yang and Yi studied the relationship between temperature and cable tension and found that the change in cable tension caused by temperature cannot be ignored [12].

3 Tower Column Monitoring

In order to study the cracks and concrete strength of the tower column, it is necessary to inspect the tower column concrete. Conventional detection methods, such as manual detection, acoustic detection, photography and other detection techniques.

In the manual inspection method, inspectors conduct rigorous inspections of bridge components through measuring instruments, measure the width and length of the cracks in the bridge tower column, and then rate the safety level of the bridge. Manual detection has great shortcomings, consumes a lot of manpower and time, cannot detect the internal structure of the tower column, and has low detection efficiency. When inspecting tall towers, the personal safety of inspectors cannot be guaranteed.

The sound wave detection method is based on the principle of sound wave propagation in the structure. When a crack occurs, the sound wave will be refracted. The sound wave generator and receiver are installed on the surface of the structure to measure the length, width and depth of the crack. The detection equipment is



Fig. 3 Non-metallic ultrasonic instrument

shown in Fig. 3. Since the sound wave generating and receiving device needs to be attached to the surface, the surface needs to be relatively flat during measurement. Otherwise, the surface of the structure must be manually processed to meet the flatness requirements of the measuring equipment. In addition, the shortcomings of this method make it impossible to effectively eliminate the influence of the steel buried in the concrete on the emission of the ultrasonic source during the detection process.

Imaging analysis mainly uses photographic equipment to take images. Through magnification and image processing, crack information can be obtained intuitively. Imaging analysis is mainly used to study cracks on the surface of structures. Through ordinary camera, video recorder, radiation camera, infrared camera and other photographic equipment, the structure is photographed, and the image information is processed.

In recent years, tower column crack detection has been studied by many scholars. Tung developed an imaging system that can automatically check bridge crack cracks [13]. Jang and Lee Improved the automatic inspection of bridge crack imaging system and improved the accuracy [14, 15]. These methods can get the development of the surface cracks of the tower column, and carry out the quality inspection of the concrete, get the structure conditions of the concrete inside the tower column, such as the density, uniformity, etc. Combined with digital image processing technology, crack monitoring information processing technology and other methods, the high tower column crack monitoring system of cable-stayed bridge is realized, which actively promotes the intelligent development of the bridge.

4 Conclusions

The main conclusions are as follows:

- The monitoring of cable-stayed bridge mainly includes stay cable monitoring, tower column monitoring, tower displacement monitoring and so on. The monitoring of cable-stayed bridge can effectively improve the safety of the bridge.
- Machines are replacing manual work as the main means of monitoring, thus reducing the risk of injury to workers and improving the efficiency of monitoring.
- Monitoring methods are gradually enriched, such as image analysis, acceleration analysis, magnetic flux analysis, temperature analysis, etc. Different monitoring methods can be applied to different scenes. By adopting appropriate monitoring means, the accuracy of monitoring can be effectively improved.

Acknowledgements The research presented here is supported by the National Nature Science Foundation of China (52078317), Natural Science Foundation of Jiangsu Province (BK20170339), project from Jiangsu Provincial Department of Housing and Ur-ban-Rural Development (2020ZD05), and Bureau of Housing and Urban-Rural Development of Suzhou (2019-14, 2020-15).

References

1. Ho H, Kim K, Park Y, Lee J (2013) An efficient image-based damage detection for cable surface in cable-stayed bridges. *Ndt & E Int*, pp 18–23
2. Torbol M, Kim S, Shinozuka M (2012) Long-term monitoring of a cable stayed bridge using a SCADA system. In: *Proceedings of SPIE*
3. Yun H, Kim S, Wu L, Lee J (2013) Development of inspection robots for bridge cables. *Sci World J*, p 967508
4. Kaloop MR, Hu JW (2015) Stayed-Cable Bridge Damage Detection and Localization Based on Accelerometer Health Monitoring Measurements. *Shock and Vibration*, pp 1–11
5. Arangio S, Bontempi F (2015) Structural health monitoring of a cable-stayed bridge with Bayesian neural networks. *Struct Infrastruct Eng* 11(4):575–587
6. Tabatabai H (2005) *Inspection and Maintenance of Bridge Stay Cable Systems*. NCHRP Synthesis of Highway Practice
7. Xu F, Wang X, Wu H (2012) Inspection method of cable-stayed bridge using magnetic flux leakage detection: principle, sensor design, and signal processing. *J Mech Sci Technol* 26(3):661–669
8. Ju M, Park C, Kim G (2015) Structural Health Monitoring (SHM) for a cable stayed bridge under typhoon. *Ksce J of Civil Engg* 19(4):1058–1068
9. Asgari B, Osman SA, Adnan A (2014) A New Multiconstraint Method for Determining the Optimal Cable Stresses in Cable-Stayed Bridges. *Sci World J*, p 503016
10. Hua XG, Ni YQ, Chen ZQ, Ko JM (2009) Structural Damage Detection of Cable-Stayed Bridges Using Changes in Cable Forces and Model Updating. *J Struct Eng-Asce* 135(9):1093–1106

11. Chen WZ, Yang JX (2014) Inspection and Assessment of Stay Cables in Cable Stayed Bridges. *Applied Mechanics and Materials*, pp 954–960
12. Yang D, Yi T, Li H, Zhang Y (2018) Monitoring and analysis of thermal effect on tower displacement in cable-stayed bridge. *Measurement*, pp 249–257
13. Tung P, Hwang Y, Wu M (2002) The development of a mobile manipulator imaging system for bridge crack inspection. *Autom Constr* 11(6):717–729
14. Oh J, Jang G, Oh S, Lee JH, Yi B, Moon YS, Choi Y (2009) Bridge inspection robot system with machine vision. *Autom Constr* 18(7):929–941
15. Tang Q, Tang XW, Li ZZ, Chen YM, Kou NY, Sun ZF (2009) Adsorption and desorption behaviour of Pb(II) on a natural kaolin: equilibrium, kinetic and thermodynamic studies. *J Chem Technol Biotechnol*, pp 1371–1380

Geotechnical Engineering

A Consolidation Solution of Soft Soil Deposits Improved with Prefabricated Vertical Drains and Deep Cement Mixing Columns



Ba-Phu Nguyen, Phuong Chau Ngo, Quang Dung Nguyen, Trong Thach Le, and Nhat-Phi Doan

Abstract Recently, a new technique method has been developed in ground improvement field, namely the combined method. This method involving the utilization of both prefabricated vertical drains (PVDs) and deep cement mixing (DCM) columns was applied to improve shear strength and accelerate consolidation rate. The goal of this study is to propose a simple analytical solution for consolidation of soft soil improved by PVDs-DCM columns, in which effects of smear zone due to drains installation and nonlinear behavior of permeability and compressibility during consolidation process are considered. Subsequently, the proposed method was applied to a test embankment in China, which used the combined method for ground stabilization. The axisymmetric model of composite ground in finite element method (FEM) is also implemented to analyze the consolidation behavior of soft soil improved by the combined method under test embankment. The proposed solution provided a good result with the monitoring data and FEM results.

Keywords Consolidation · DCM columns · PVDs · FEM · Combined method

B.-P. Nguyen (✉) · Q. D. Nguyen
Industrial University of Ho Chi Minh City, Ho Chi Minh City, Vietnam
e-mail: nguyenbaphu@iuh.edu.vn

P. C. Ngo
Campus in Ho Chi Minh City, University of Transport and Communications,
Ho Chi Minh City, Vietnam

T. T. Le
Quality Assurance and Testing Center 3, Ho Chi Minh City, Vietnam

N.-P. Doan
Kyungpook National University, Daegu, South Korea

1 Introduction

It is well known that deep cement mixing (DCM) columns and prefabricated vertical drains (PVDs) were widely used to improve soft soils under embankment [1]. DCM columns were used to prevent excessive settlement of soft soil with high compressibility and very low shear strength, whereas PVDs were typically used to accelerate consolidation process of soft soil due to its low permeability.

When DCM columns is solely used to improve soft soil, the DCM columns installation process may reduce the strength of surrounding soil [1, 2]. Because the improvement depth of DCM columns is limited for thick soft soil ground, a high excess pore water pressure can be accumulated in unimproved soft soil layer. Thus, the large residual settlement can be occurred after construction period. Moreover, it can take a long time for the consolidation of the unimproved soft soil layer. This can affect the operation process of transportation constructions such as highway embankment, road of bridge approaches.

Evidently, PVDs significantly accelerate the soft soil consolidation. Consequently, the settlement of PVD-improved soft ground can complete during the preloading period and the post construction is reduced. However, the bearing capacity and slope stability of soft soil ground cannot be increased moderately.

To overcome the above problems, Xu et al. [2] suggested a combined method of DCM columns and PVDs for ground improvement. Figure 1 illustrates the soft soil improvement by the combined method.

Consolidation analysis is often essential in design of soft soil improvement by DCM columns or PVDs. There are many solutions for consolidation of DCM columns soil system and PVD-improved soil [3]. However, very few studies on consolidation behavior of soft soil improved by the combined method were carried out [4]. Ye et al. [4] developed a simple solution for consolidation analysis of the composite ground of DCM columns and PVDs with equivalent permeability, in which the length of PVD is equal to that of DCM column. Zhang et al. [5] extended

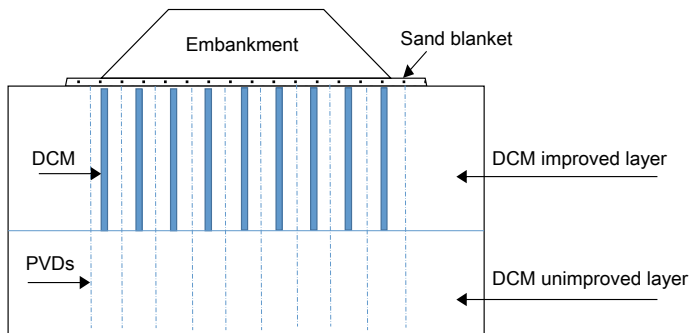


Fig. 1 The ground improvement with the combined method of DCM columns and PVDs

the solution of Ye et al. [4] in the case of short DCM columns and long PVDs. Generally, the effects of smear zone, well resistance of drains and nonlinear behavior of soil consolidation were omitted in these solutions.

The aim of this paper is to propose a simple analytical solution for consolidation of soft soil improved by PVDs-DCM columns, in which effects of smear zone due to drains installation and nonlinear behavior of permeability and compressibility during consolidation process are considered. The proposed method is then used to analyze consolidation behavior of test embankment in China, which was used in the combined method. The axisymmetric model of composite ground in finite element method (FEM) is also performed to analyze the consolidation behavior of soft soil improved by the combined method under test embankment.

2 The Proposed Solution

In order to analyze the simple consolidation behavior of the combined foundation of DCM columns and PVDs, vertical drains around DCM columns can be substituted by a continuous ring equivalent to a drain wall [4]. Therefore, the consolidation model of the composite ground can be expressed by axisymmetric model, as shown in Fig. 2, where E_s and E_c are the compression modulus of soil and DCM columns, respectively; k_{sh} and k_{ch} are the horizontal permeability of soil and DCM columns; r_c is the radius of influence zone and r_c is the radius of DCM columns.

To analyze the consolidation behavior of composite ground, the method of Ye et al. [4] was adopted in this paper. The main assumptions were used as following: (1) equal strain assumption in small strain theory and only one dimension (1-D)

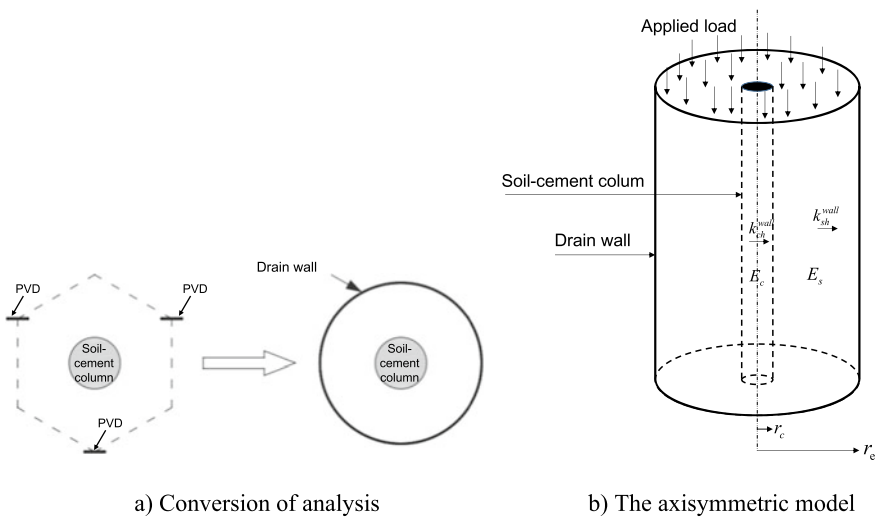


Fig. 2 The axisymmetric model of composite ground in consolidation analysis

deformation are considered; (2) the soil is fully saturated; (3) only radial flow is considered in consolidation process; (4) the cylindrical drain wall is ignored. When vertical drains were converted into an equivalent drain wall. Ye et al. [4] developed the equivalent permeability of soil and DCM columns in unit cell as follows:

$$\frac{k_{sh}^{wall}}{k_{sh}} = \frac{1}{4 \left(\ln \frac{n}{s} + \frac{k_{sh}}{k_{sh}'} \ln s - \frac{3}{4} \right)} \quad (1)$$

where k_{sh} is the permeability of disturbed soil due to PVDs installation; $s = r_s/r_w$, in which r_s and r_w is the radius of disturbed zone and drain, respectively; $n = r_e/r_w$. After Ye et al. [4], the average excess pore water pressure in the unit cell with only radial consolidation is expressed as:

$$\bar{u}(t) = r_e^2 \left[\frac{1}{8} \frac{\gamma_w}{k_{ch}^{wall} E_{sc}} m^2 + \frac{1}{8} \frac{\gamma_w}{k_{sh}^{wall} E_{sc}} (1 - m^2) \right] \left(\frac{\partial \sigma'_v}{\partial t} \right) \quad (2)$$

where E_{sc} is the compression modulus of composite foundation of soil and DCM columns; m is the area ratio, $m = A_c/A$. The average excess pore water pressure in the unit cell can be expressed as:

$$\bar{u}_r = \sigma'_{vo} + P(t) - \sigma'_v \quad (3)$$

From Eqs. (2) and (3), the consolidation equation can be expressed as follows:

$$\frac{\partial \sigma'_v}{\partial t} = \frac{8E_{sc}}{r_e^2 \gamma_w} \frac{k_{ch}^{wall} k_{sh}^{wall}}{[m^2 k_{sh}^{wall} + k_{ch}^{wall} (1 - m^2)]} \left(\sigma'_{vo} + P(t) - \sigma'_v \right) \quad (4)$$

In this paper, we assume that the permeability of DCM columns is constant with consolidation. However, it is need to consider effects of nonlinear consolidation of the soft soil with high compressibility. The variation of permeability and compression of soil is considered as following equations:

$$e = e_o - C_c \log \left(\frac{\sigma'_v}{\sigma'_{vo}} \right) \quad (5)$$

$$\log(k_h) = \log(k_{ho}) - \frac{e_o - e}{C_k} \quad (6)$$

where e_o and e are initial and current void ratio, respectively. k_{ho} and k_h are initial and current horizontal permeability of soil, respectively. C_c is compressive index of soil; and C_k is a constant used to depict the reduction of permeability as the void ratio reduction during consolidation process.

Combination of Eqs. (4), (5), (6) and Eq. (1), the consolidation equation can be written as follows:

$$\frac{\partial \sigma'_v}{\partial t} = \frac{8E_{sc}}{r_e^2 \gamma_w} \frac{k_{ch}^{wall} k_{sh0} 10^{-\frac{C_c}{C_k} \log \frac{\sigma'_v}{\sigma'_{v0}}}}{\left[m^2 k_{sh0} 10^{-\frac{C_c}{C_k} \log \frac{\sigma'_v}{\sigma'_{v0}}} + 4k_{ch}^{wall} (1 - m^2) \left(\ln \frac{n}{s} + \frac{k_{sh}}{k'_{sh}} \ln s - \frac{3}{4} \right) \right]} \left(\sigma'_{v0} + P(t) - \sigma'_v \right) \tag{7}$$

To solve Eq. (7), a finite difference method can be used with $\sigma'_v = \sigma'_{v0}$ as an initial condition for $t = 0$. The solving process of the above equation can follow the process of Nguyen et al. [3].

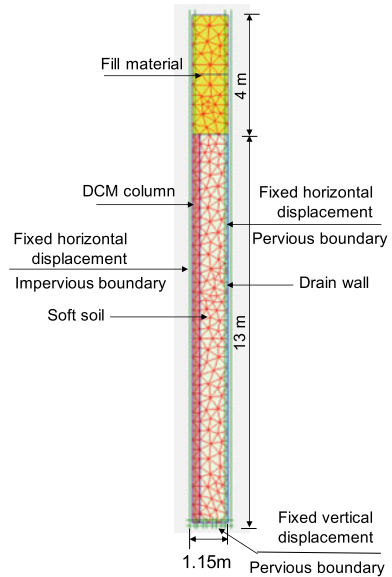
3 Verification

This section applies the proposed solution to analyze consolidation behavior of soft soil under Huai-Yan Highway embankment at stations K19 + 688–K19 + 798. The soft soil was improved by a combined method of DCM columns and PVDs. These structures were installed in a triangular pattern at a spacing of 2.2 m and depth of 13 m, in which radius of DCM columns is 0.25 m [4]. Because PVDs depth was shortly installed within a depth of 13 m, the well resistance can be ignored in this study. The disturbed soil due to PVDs installation is also considered with and $r_s/r_w = 2$. The subsoil consists of 1.5–2.0 m of grey to yellowish brown clay and overlies the soft clay. It extends to approximately 10.3–12.0 m below the surface and is underlain by the relatively hard grey to grey-blue clay. By a simplified analysis, the subsoil layers were solely assumed to be soft soil layer within a depth of 13 m. The unit weight of filling material is 20 kPa. The filling process of embankment comprises from two stages. The first 2.0 m of embankment was constructed in 50 days, followed by 75 days for dissipation of excess pore pressure. The second stage of 2.0 m embankment loading was applied in 50 days. The properties of the subsoil and soil-cement columns are presented in Table 1, in which the soils and DCM columns are modeled as Mohr-Coulomb model.

In consolidation analysis, the equivalent permeability of soft soil is equal to 1.67 of the equivalent permeability of DCM columns [4]. The C_c/C_k of composite foundation is assumed to approximately 3. This is a reasonable assumption because

Table 1 Properties of soft soil and DCM columns used in numerical solution

Material	E_s (MPa)	k_{sh} ($\times 10^{-9}$ m/s)	C_c/C_k	σ'_{v0} (kN/m ²)
Soft soil	1.68	3.26	3	32.5
DCM columns	80	0.1	3	32.5

Fig. 3 The numerical model

the reduction rate of permeability with void ratio reduction of composite foundation is smaller than that of natural soil. In most of the field cases, the plane strain model is adopted for simulation; however, the plane strain model for the soft ground improved by DCM columns and PVDs is still doubtful. Therefore, the axisymmetric model of composite ground in finite element method (FEM) is performed to analyze the consolidation behavior of soft soil. The mesh properties, geometries and the boundary conditions are depicted in Fig. 3.

Figure 4 shows the comparisons of settlement results between the predicted results obtained from the proposed solution, numerical analysis and the measured data. The results show that the proposed solution provided a good agreement with the measurement. The numerical results are also consistent with the results of field data and the proposed solution, although the numerical results slightly overestimates the monitoring data. These results could be explained that numerical model in this study considered both of the vertical and radial consolidation. Generally, the proposed solution is useful for the consolidation analysis of soft soil improved by DCM columns and PVDs.

4 Conclusions

This paper proposed a consolidation solution for soft ground improved by a combined method of DCM columns and PVDs. The effects of smear zone and variation of permeability and compressibility during consolidation process were also considered in this study. The proposed solution was applied to analyze

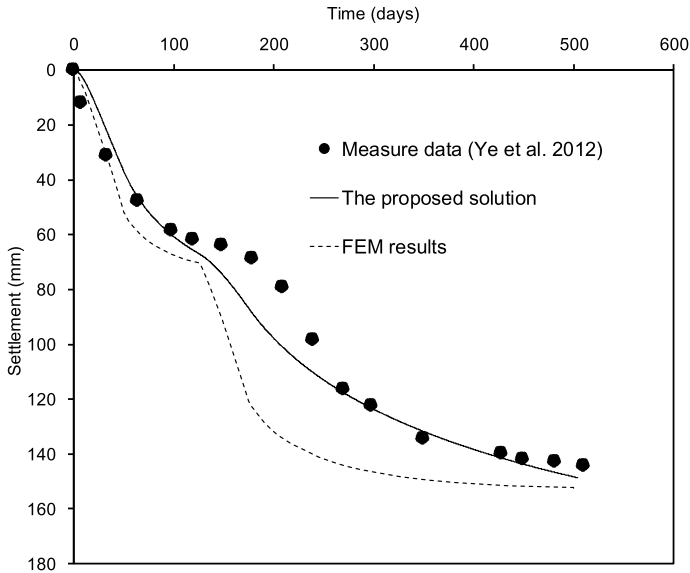


Fig. 4 Settlements results in numerical analysis

consolidation behavior of soft ground improved by the combined method in China. The results obtained from the proposed solutions are in good agreement with the measured data. The proposed solution is promising for the consolidation analysis of soft soil improved by DCM columns and PVDs.

Acknowledgements The support of this research by the Industrial University of Ho Chi Minh City is gratefully acknowledged.

References

1. Zhang DW, Liu SY, Hong ZS (2006) Consolidation calculating method of soft ground improved by DJM-PVD combined method. *Ground Modification and Seismic Mitigation—Proceeding of the GeoShanghai International Conference[C]*. Shanghai, China: ASCE Geotechnical Special Publication (GSP 152), 29–36
2. Xu C, Ye GB, Jiang ZS, Zhou QZ (2006) Research on mechanism of combined improvement of soft soils based on field monitoring. *Chin J Geotech Eng* 28(7):918–921 (in Chinese)
3. Nguyen B-P, Kim Y-T (2019) Radial consolidation of PVD-installed normally consolidated soil with discharge capacity reduction using large-strain theory. *Geotext Geomembr* 47(2):243–254
4. Ye GB, Zhang Z, Xing HF, Huang MS, Consolidation XC (2012) A composite foundation with soil-cement columns and prefabricated vertical drains. *Bull Eng Geol Env* 71(1):87–98
5. Zhang Z, Ye G, Xing H (2015) Consolidation analysis of soft soil improved with short deep mixed columns and long prefabricated vertical drains (PVDs). *Geosynth Int* 22(5):1–14

Effect of Grain Size on Shear Strength of Coral Gravel Sand



Cao Van Hoa, Vu Anh Tuan, Nguyen Thanh Sang,
Nguyen Tuong Lai, and Pham Duc Tiep

Abstract In the study, a series of triaxial tests were carried out on coral gravel sand to investigate the shear strength behaviour of the sand. The coral material were collected from Truong Sa island of Vietnam. To examine the effect of grain-size distribution on the shear strength behaviour, six kinds of coral gravel sand samples with different grain size distributions were used in the experiments. The experimental results indicate that the coral gravel sand contains not only internal friction angle, φ , as other granular materials but also apparent cohesion, c , and these parameters depends on the grain-size distribution. The results show that the strength parameters increase with the increase of the grain size of the coral.

Keywords Coral gravel sand · Triaxial test · Internal friction angle · Cohesion · Shear strength · Grain size distribution

1 Introduction

Coral ground is widely distributed in South East Asia sea area, especially in Truong Sa island of Vietnam. Coral ground is also called calcareous ground because the main chemical component is calcium carbonate. Recently, construction activities in coral ground have been carried out more and more popular. However, calcareous soil are considered as problematic soils due to high crushability, high void ratio. Physical properties of coral sands have been reported in [1, 2]. Brandes [3] investigated shear behaviour of calcareous and quartz sands through monotonic and cyclic simple shear tests. It is derived from the study that differences in behaviour between the calcareous and quartz sands are due to contrasts in grain geometry, hardness, gradation and the amount of intraparticle voids [3]. Shahnazari and Rezvani [4] studied on effective parameters for the partial breakage of calcareous sands. The results from the research showed that the input energy played an

C. Van Hoa · V. A. Tuan (✉) · N. T. Sang · N. T. Lai · P. D. Tiep
Le Quy Don Technical University, Hanoi, Vietnam
e-mail: vuanhtuan@mta.edu.vn

important role in the particle breakage behaviour of the soils. Vu [5] carried out experimental study and numerical simulation on mechanical behaviour of a coral sand in Truong Sa island of Vietnam. The studied results indicated that the coral sand had post-peak softening behaviour and it is better to use the Hypoplastic model to simulate the mechanical behaviour of the sand compared to the Mohr-Coulomb and Hardening soil models. Wang et al. [6] studied on shear characteristics of calcareous gravelly soil through large-scale direct shear tests. The results revealed that calcareous gravelly soil has greater apparent cohesion, larger friction angle, and lower softening value than quartz sand.

Overall, there are several studies on mechanical properties of coral or calcareous sands with particle size smaller than 2 mm, but few study on coral gravel sand with particle size larger than 2 mm. Hence, in this study, a series of triaxial tests were carried out on coral gravel sand to investigate the shear strength behaviour of the sand. The coral material were collected from Truong Sa island of Vietnam. To examine the effect of grain-size distribution on the shear strength behaviour, six kinds of coral gravel sand samples with different grain size distributions were used in the experiments. The results of the experiments are presented and discussed in this paper.

2 Physical Properties

In this research, only soil particles having a diameter smaller than 20 mm were used in the experiments. Six kinds of coral gravel sand samples are prepared as follows:

- Sample S1 is coral sand having only soil particles smaller than 2 mm.
- Sample S2 is a combination of S1 and soil particles from 2 to 10 mm, in which the mass percentage of S1 is 80%.
- Sample S3 is a combination of S2 and soil particles from 10 to 20 mm, in which the mass percentage of S2 is 80%.
- Sample S4 is a combination of S2 and soil particles from 10 to 20 mm, in which the mass percentage of S2 is 70%.
- Sample S5 is a combination of S2 and soil particles from 10 to 20 mm, in which the mass percentage of S2 is 60%.
- Sample S6 is a combination of S2 and soil particles from 10 to 20 mm, in which the mass percentage of S2 is 50%.

Sieve tests were conducted using the sieves set having the sizes of 20, 10, 5, 2, 1, 0.5, 0.25, 0.1 mm, and less than 0.1 mm. Figure 1 shows the grain size distributions of the sieve tests.

The physical properties of the coral gravel sands are summarised in Table 1.

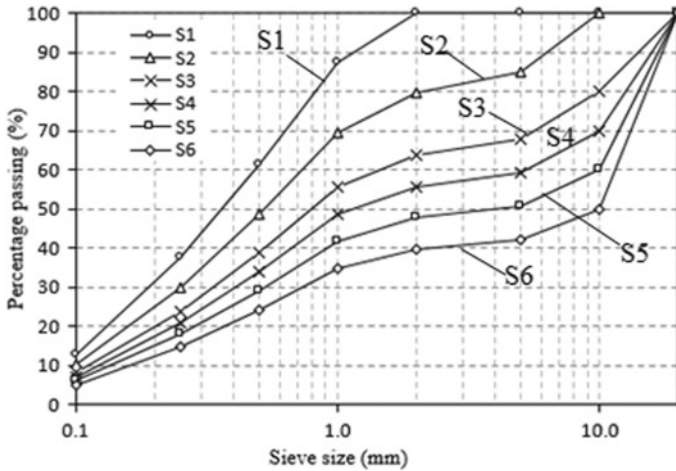


Fig. 1 Grain size distributions

Table 1 Physical properties of coral gravel sands

Properties	S1	S2	S3	S4	S5	S6
ρ_s (t/m^3)	2.671	2.67	2.616	2.589	2.562	2.535
e_{max}	0.927	0.888	0.763	0.749	0.736	0.741
e_{min}	0.600	0.573	0.469	0.462	0.451	0.444
D_{50} (mm)	0.38	0.53	0.83	1.19	4.16	10.02
C_u	6.31	7.94	13.20	40.74	67.33	68.92
C_c	1.11	0.84	0.68	0.26	0.19	0.28
Type	SW	SP	GP	GP	GP	GP

3 Triaxial Tests and Results

Triaxial monotonic consolidated-drained tests of the coral samples having a relative density of 70% were carried out with a confining pressure of 50, 100 and 150 kPa. The specimens having a diameter of 100 mm and a height of 200 mm were used in the experiments. Figure 2 shows the triaxial testing system and the specimen dimensions.

The results of the triaxial tests for samples S1, S2, S3, S4, S5 and S6 are shown in Figs. 3, 4, 5, 6, 7 and 8, respectively. Focussing on deviatoric stress versus axial strain curves, it is seen that nonlinear and post-peak softening behaviours are observed. The post-peak softening behaviour is more obvious in the cases of coarse aggregates (S3, S4, S5, S6) compared to fine aggregates (S1, S2). The location of the peaks vary according with the grain sizes and the confining pressures. Also, the differences in the locations of the peaks in the result comparison of the different confining pressures are reduced when the particle size increases. For example, the

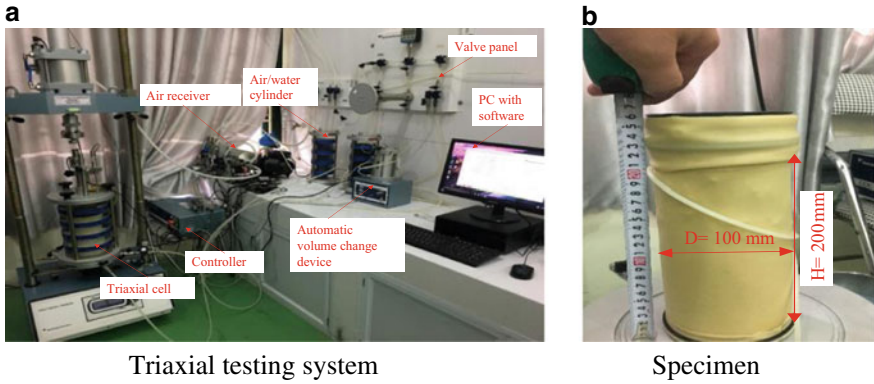


Fig. 2 Triaxial testing system and specimen dimensions (a) Triaxial testing system (b) Specimen

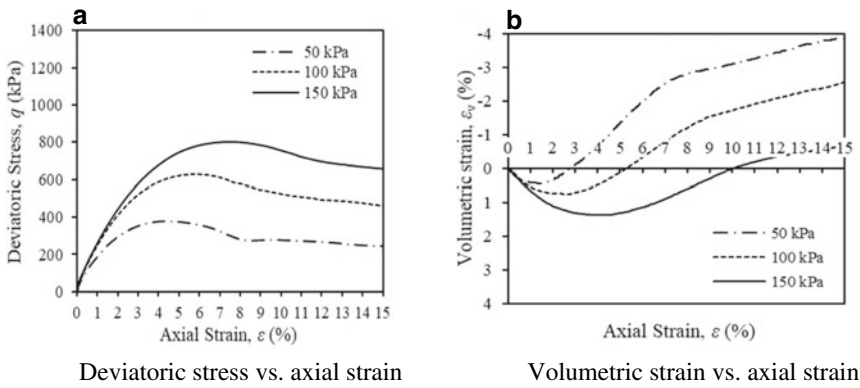


Fig. 3 Triaxial test results of sample S1 (a) Deviatoric stress versus axial strain (b) Volumetric strain versus axial strain

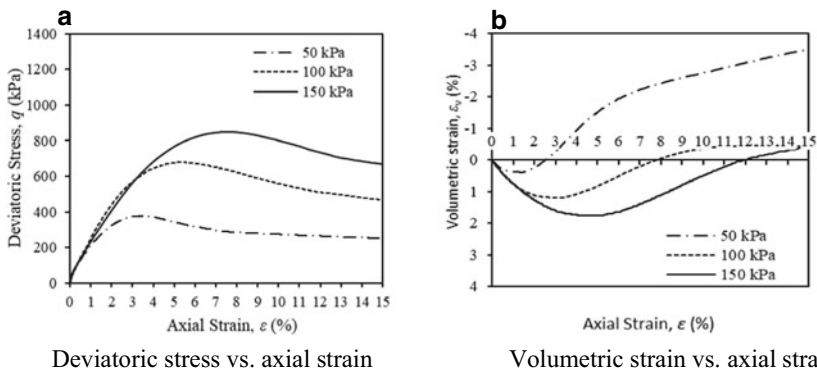


Fig. 4 Triaxial test results of sample S2 (a) Deviatoric stress versus axial strain (b) Volumetric strain versus axial strain

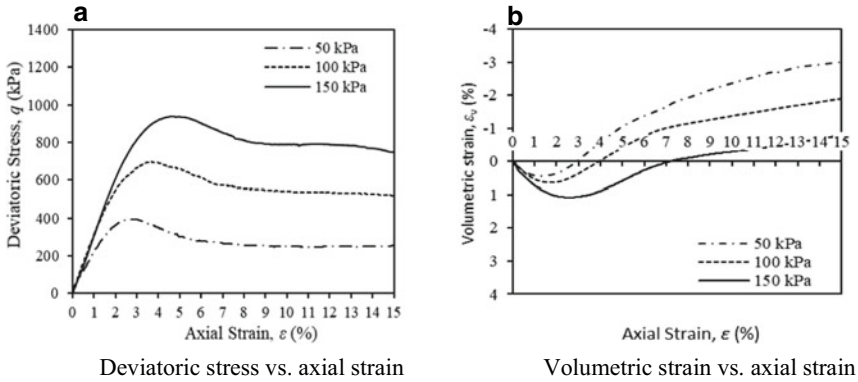


Fig. 5 Triaxial test results of sample S3 (a) Deviatoric stress versus axial strain (b) Volumetric strain versus axial strain

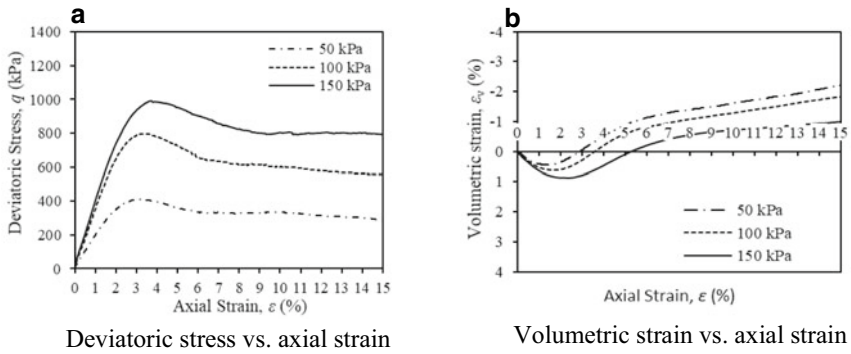


Fig. 6 Triaxial test results of sample S4 (a) Deviatoric stress versus axial strain (b) Volumetric strain versus axial strain

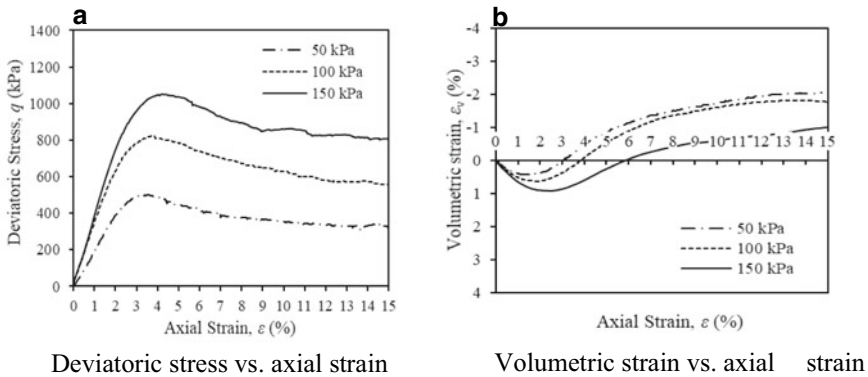


Fig. 7 Triaxial test results of sample S5 (a) Deviatoric stress versus axial strain (b) Volumetric strain versus axial strain

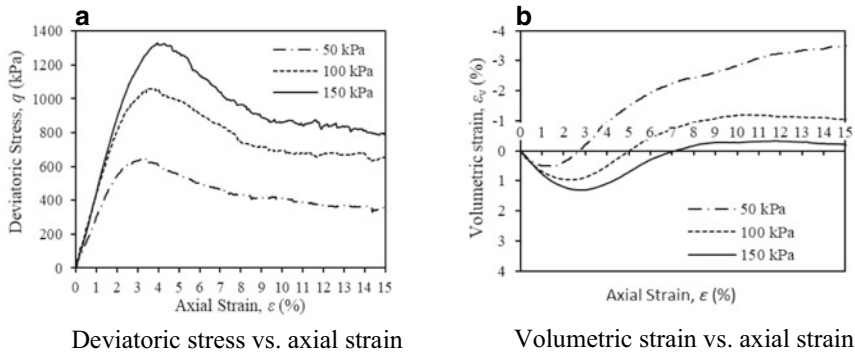


Fig. 8 Triaxial test results of sample S6 (a) Deviatoric stress versus axial strain (b) Volumetric strain versus axial strain

Table 2 Values of internal friction angle, cohesion and dilatancy angle

Sample	Peak strength		Residual strength		Dilatancy angle
	φ'_p (°)	c'_p (kPa)	φ'_r (°)	c'_r (kPa)	ψ (°)
S1	44.28	31.29	43.45	4.96	10.14
S2	45.15	31.54	42.79	9.94	9.17
S3	46.49	29.83	44.96	7.09	9.52
S4	48.14	28.43	45.07	12.69	10.33
S5	48.82	35.66	45.35	18.40	10.94
S6	50.72	57.59	43.85	38.56	11.64

peaks of sample S1 are at the axial strain of about 4%, 6% and 8% corresponding with the confining pressures of 50, 100 and 150 kPa, respectively. The corresponding results of sample S3 are about 3, 4 and 5%. Meanwhile, for samples S4, S5 and S6, the differences in the locations of the peaks are marginal, all the peaks are occurred at the axial strain of about 3.5–4%.

It is seen from the volumetric strain versus axial strain curves that the differences in volume change in the result comparison of the different confining pressures are more obvious in the cases of fine aggregates (S1, S2) compared to coarse aggregates (S3, S4, S5, S6). Also, the changes in volume are more considerable in the smaller confining pressure (50 kPa) compared to the larger confining pressures (100 and 150 kPa).

Table 2 shows values of the internal friction angle, φ , cohesion, c , at the peak state and residual state, and values of the dilatancy angle. The internal friction angle of the coral gravel sands is larger than that of the silica sand [7]. Otherwise, the material has a considerable value of apparent cohesion, c . The results indicate clearly that the shear strength is influenced by the grain size. Overall, the strength parameters (φ , c) increase with the increase of the particle size. Meanwhile, the dilatancy angle is rarely influenced by the grain size and remains at about 10°.

Table 3 Values of secant modulus E_{50} and Poisson's ratio

Sample	Secant modulus E_{50} (MPa)			Poisson's ratio
	$p_0 = 50$ kPa	$p_0 = 100$ kPa	$p_0 = 150$ kPa	
S1	18.90	23.14	22.97	0.37
S2	20.31	23.66	22.26	0.32
S3	22.40	30.86	31.31	0.34
S4	19.52	35.36	40.23	0.34
S5	19.52	34.76	38.61	0.35
S6	30.06	43.45	45.08	0.31

Table 3 presents values of the secant modulus E_{50} and Poisson's ratio of the samples corresponding to the confining pressures. The modulus generally increases with the increase of the confining pressures and it is dependent on the grain size, the samples with larger particle size have larger secant modulus and vice versa. Poisson's ratio is quite stable with the average value of 0.34.

Figure 9 shows the relationship between friction angle and mean grain size D_{50} . Figure 10 shows the relationship between the cohesion and mean grain size D_{50} . Figure 11 shows the relationship between the dilatancy angle and mean grain size

Fig. 9 Peak friction angle ϕ_p and residual friction angle ϕ_r versus mean grain size D_{50}

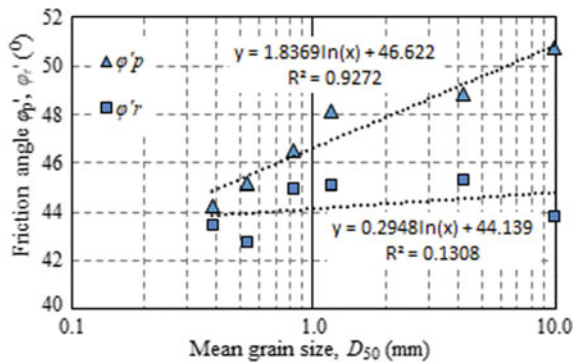


Fig. 10 Peak cohesion c_p and residual cohesion c_r versus mean grain size D_{50}

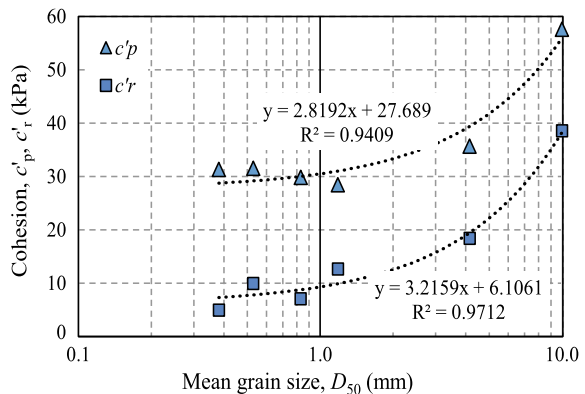


Fig. 11 Dilatancy angle versus mean grain size D_{50}

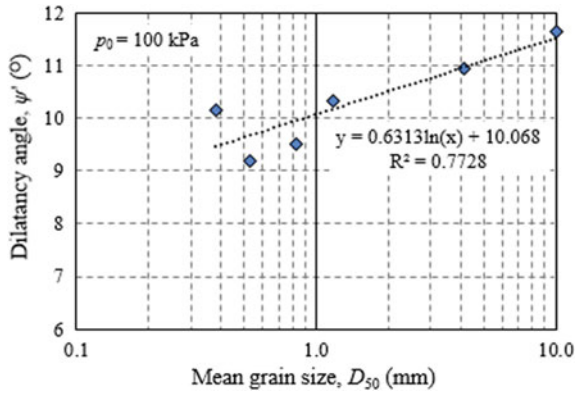
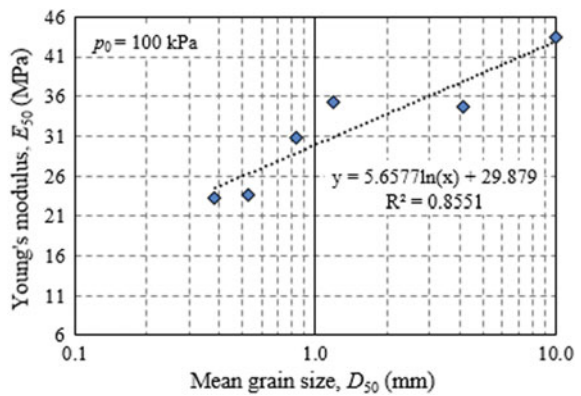


Fig. 12 Young's modulus versus mean grain size D_{50}



D_{50} . Figure 12 shows the relationship between the Young's modulus and mean grain size D_{50} . It is indicated that logarithm functions could be used to express the relationship between the peak friction angle, dilatancy angle, Young's modulus and mean grain size D_{50} . Meanwhile, the relationship between the apparent cohesion and mean grain size D_{50} could be expressed by a linear function.

4 Conclusions

The following conclusions are derived from the results of this study:

Shear strength parameters of the coral gravel sands include not only internal friction angle as other granular soils but also considerable apparent cohesion. The parameters are influenced by the grain size, increasing with the increase of the particle size. Meanwhile, the dilatancy angle is rarely influenced by the grain size.

Young's modulus is also dependent on the grain size, the samples with larger particle size have larger secant modulus and vice versa. Poisson's ratio is quite stable with the average value of 0.34.

Logarithm functions could be used to express the relationship between the peak friction angle, dilatancy angle, Young's modulus and mean grain size D_{50} . Meanwhile, the relationship between the apparent cohesion and mean grain size D_{50} could be expressed by a linear function.

References

1. Murff JD (1987) Pile capacity in calcareous sands; state of the art. *J Geotechnical Eng ASCE* 113(5):490–570
2. Poulos, HG (1988) The mechanics of calcareous sediments. *Aust Geomech*, 8–41
3. Brandes HG (2011) Simple shear behavior of calcareous and quartz sands. *Geotech Geol Eng* 29:113–126
4. Shahnazari H, Rezvani R (2013) Effective parameters for the particle breakage of calcareous sands: An experimental study. *Eng Geol* 159:98–105
5. Vu, AT (2017) Experimental study and numerical simulation on mechanical behaviours of coral sand in Truong Sa island. *Vietnam J Constr*, 163–167, July (in Vietnamese)
6. Wang XZ, Wang X, Jin ZC, Zhu CQ, Wang R, Meng QS (2017) Shear characteristics of calcareous gravelly soil. *Bull Eng Geol Env* 76:561–573
7. Vu AT, Matsumoto T, Kobayashi S, Shimono S (2017) Experimental study on pile foundations having batter piles subjected to combination of vertical and horizontal loading at 1-g field. *Geotech Eng J* 48(3):12–24

Landslide Susceptibility Mapping for the Thao River Catchment with High Spatial Resolution Rainfall Data



The Viet Tran, Manh Cuong Nguyen, Quang Toan Trinh, Hoai Nam Do, Trung Kien Nguyen, Kien-Trinh Thi Bui, Quoc Thanh Nguyen, and Duc Ha Nguyen

Abstract Geological disasters occur more and more frequently in mountainous regions causing considerable damage to lives and properties. As a tropical country, rainfall is often considered to be the most common triggering factor for the occurrence of landslides in Vietnam. This study used a high-resolution rainfall map of the extreme 1-day precipitation derived from a combined dynamical-statistical downscaling model outputs in the period 1981–2010, and eight other terrain factors to construct the landslide susceptibility map (LSM) for the Vietnam portion of Thao river catchment. The Analytical Hierarchy Process (AHP) was applied to determine the weights of every causative factor and their classes. Validation of the susceptible map was verified with existing landslide locations using the receiver operating characteristic (ROC) curve that comparing the actual and predicted landslide locations. The result shows that the predicted susceptibility map has good agreement with the past landslide occurrences. Therefore, the LSM predicted by the AHP method is useful for preventing potential landslides in the future for the study area.

Keywords Landslide · AHP · Thao river catchment · Landslide susceptibility map

T. V. Tran · T. K. Nguyen · K.-T. T. Bui (✉)
Thuyloi University, 175 Tay Son, Dong Da, Hanoi, Vietnam
e-mail: bktrinh@tlu.edu.vn

M. C. Nguyen
Vietnam Natural Resources and Environment Corporation, Hanoi, Vietnam

Q. T. Trinh
Department Civil and Environmental Engineering, University of California,
Berkeley, CA, USA

H. N. Do
Vietnam Academy for Water Resources, Hanoi, Vietnam

Q. T. Nguyen
Institute of Geological Sciences, Academy of Science and Technology, Hanoi, Vietnam

D. H. Nguyen
Vietnam Institute of Geosciences and Mineral Resources, Hanoi, Vietnam

1 Introduction

As a mountainous country in the tropical region, Vietnam has been significantly affected by geological disasters in general and landslide in specific [1]. Specially, Thao river—the largest main-stream of the Red River which is original from Yunnan province, China has been suffering from an increase in the frequency of landslide occurrences. Therefore, the construction of a LSM is an essential and effective way to prevent the negative influence of future landslides and minimize damages.

Landslide susceptibility assessment can be classified into three groups: empirical, statistical, and physical approaches [1]. The empirical method is a simplicity and applicability method base on estimation of rainfall threshold which is determined from the rainfall intensity or rainfall duration [2]. Landslide risk maps are generated statistically by linking the spatial distribution of past and present spatial landslides to predict the potential of landslides in each area in the future [3]. The limitation of this approach is the ability to predict the timing of landslide occurrence and a large amount of required data to run the analysis.

In literature, numerous different approaches have been proposed to determine landslide susceptibility, however, no specific method has been recognized as the standard approach [2]. This study applied the AHP a semi-quantitative method that considers nine different factors including rainfall, slope, elevation, geology, weathered crust, fault density, forest cover, horizontal and deep dissection to construct the landslide susceptibility map for the Thao river catchment. The predicted landslide susceptibility map was validated using past and present landslide occurrences.

2 Study Area and Methodolgy

2.1 Study Area

Thao river flows in the Northwest- Southeasterly direction through three provinces in Vietnam including Lao Cai, Yen Bai, and Phu Tho. The Vietnamese part of the Thao River watershed is about 14.5% of the total watershed area which mainly covers the area of Lao Cai and Yen Bai province. These are two provinces that have been severely suffering from landslides and slope instability problems [1, 4].

2.2 Methodology

For the Thao river catchment, LSM has been estimated based on the spatial resolution of 10 km² rain-fall map of the extreme 1-day precipitation derived from a

combined dynamical-statistical downscaling model outputs in the period from 1981 to 2010. The map was simulated using the Weather Research and Forecasting model with input provided from the European Centre for Medium-Range Weather Forecasts – Atmospheric Reanalysis coarse climate data of the twentieth century (ERA-20C) [5]. The simulated precipitation maps were bias-corrected [6] before being input into the AHP to determine the weights of every causative factors including slope, elevation, geology, weathered cover, horizontal and deep dissection.

The observed landslide locations (1468 points) [4, 7] were investigated in the relationship to the impact factors, then the weights of all layers in each map were determined. In this case, the AHP method [8] has been applied to derive weights from pairwise comparison matrices of impact factors. The score assignment was generated from researchers and engineers by doing visually inspected the site, running statistical analysis, conducting engineering experiments. In the final step, the LSM was created from the procedure of a weighted linear sum [9], and then can be classified using AHP susceptibility scores.

The LSM takes into account where the landslides occur and what causes them. For this study, a landslide inventory map including a recorded history of landslides (Fig. 1) and nine causative factor maps were constructed, as can be respectively seen in Fig. 2.

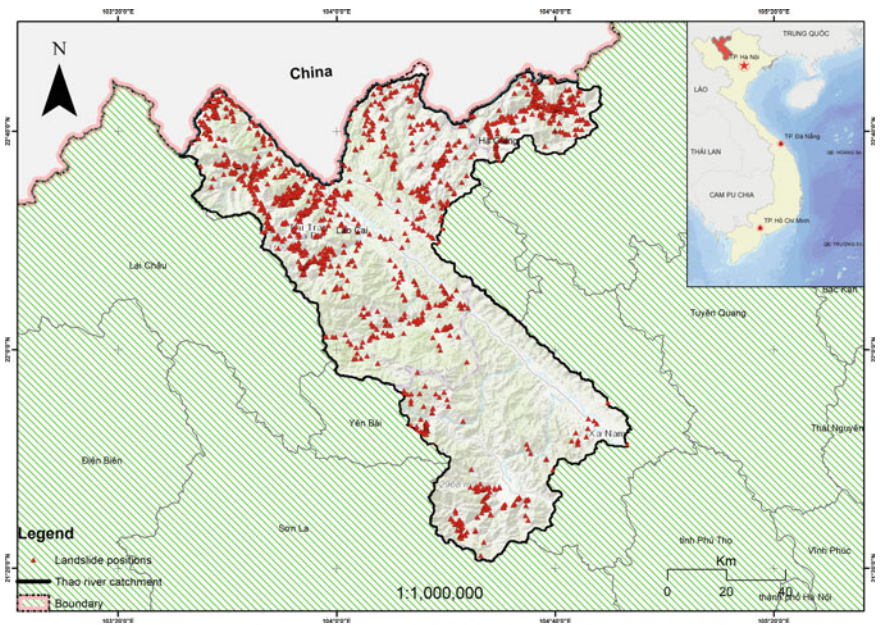


Fig. 1 Thao river catchment portion in Vietnam and observed landslide positions

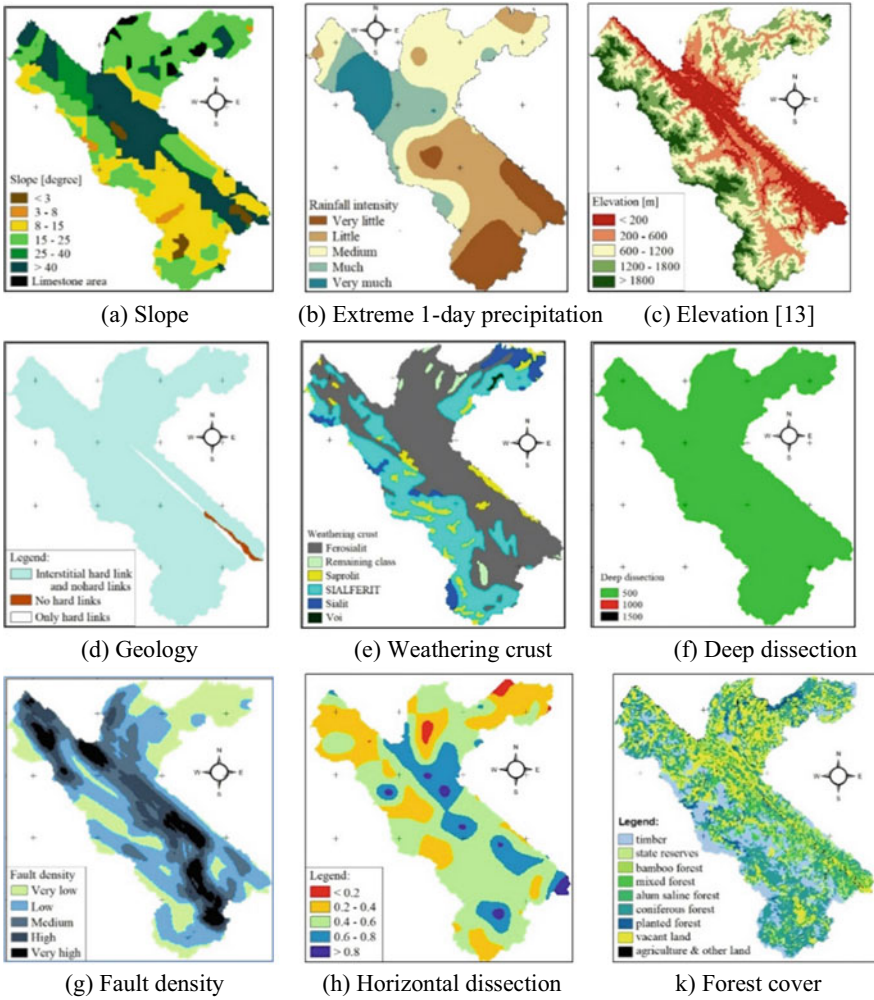


Fig. 2 Impact factor maps of landslide in Thao river catchment horizontal and deep dissection

3 Results

The respective weight value W_1 of a level in each impact factor map was determined by overlaying the landslide inventory map. Then pairwise comparison matrix of all impact factors was estimated (Table 1) and then the weight matrix was calculated to deliver the weight vector W_2 (Table 2).

The consistency ratio $CR = 0.31$ shows that the resulting map was accepted [8]. Based on the weights of map layers W_1 and individual impact factor map W_2 , the

Table 1 Pairwise comparison matrix

Factors	(a)	(b)	(c)	(d)	(e)	(f)	(g)	(h)	(k)
(a)	1	3	5	5	6	9	9	9	9
(b)	1/3	1	3	3	4	7	7	7	7
(c)	1/5	1/3	1	1	2	5	5	5	5
(d)	1/5	1/3	1	1	2	4	4	4	4
(e)	1/6	1/4	1/2	1/2	1	4	4	4	4
(f)	1/9	1/7	1/5	1/5	1/4	1	1	1	1
(g)	1/9	1/7	1/5	1/5	1/4	1	1	1	1
(h)	1/9	1/7	1/5	1/5	1/4	1	1	1	1
(k)	1/9	1/7	1/5	1/5	1/4	1	1	1	1

Table 2 Weight vector of impact factor maps

(a)	(b)	(c)	(d)	(e)	(f)	(g)	(h)	(k)
-0.325	-0.197	-0.107	-0.107	-0.075	-0.051	-0.022	-0.022	-0.022

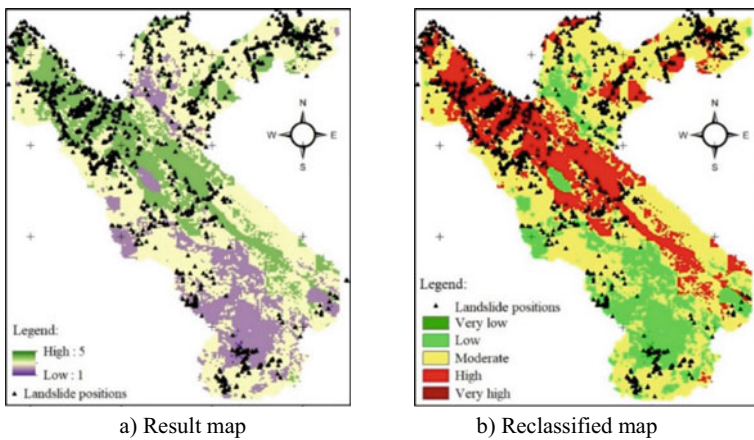


Fig. 3 LSM in the Vietnamese portion of Thao river catchment

LSM is extracted and shown in Fig. 3a. Using the natural break technique, the LSM was reclassified into five classes as seen in Fig. 3b and Table 3. The ROC technique of LSM was used for rating the occurrence landslide points. The area under the ROC is 0.82 indicating that LSM has good prediction capability. The predictive results have been proven usability, useful when using LSM.

The resulting map was also verified using the landslides inventory map itself. Accordingly, these 1468 landslide locations were overlaid on the proposed map

Table 3 Ranking of landslide susceptibility

Susceptibility level	Amount of landslide positions	Landslide position percent (%)	Area (km ²)	Percent area (%)
Very high	21	1.43	1.368	0.01
High	523	35.63	2489.052	25.13
Moderate	771	52.52	5542.575	55.96
Low	110	7.49	1861.660	18.80
Very low	43	2.93	9.575	0.10

(Fig. 3b). The result shows that 544 recorded landslides events (37% of the recorded landslides) occurred in the high and very high susceptibility zones, which they only cover 2490.2 km² (25.14%) of the study area. The data also points out that regions in the medium area recorded the majority of landslides: 771 recorded landslide events for 52.52%, about 5542 km². In addition, one can see that about 13 landslide points (2.93% of all recorded landslides) fall into the low susceptibility class of the LSM covering approximately 9.575 km² (0.10%) of the study area.

4 Conclusion

The authors presented a quantitative assessment method that uses landslide topography and microtopography and a method for predicting areas that will be affected by runoff of landslide masses which that are more precise than conventional methods. Some of these results are already being used by governments to carry out landslide prevention measures, but the development of risk analysis using GIS and digital elevation morphological data has just started in Vietnam and future development is awaited.

Acknowledgements The study is supported by the Ministry of Agriculture and rural development of Vietnam in a project that belongs to the 4757/QĐ-BNN-KHCN in 12/12/2019.

References

1. Tran TV, Lee G, An HU, Kim M (2017) Comparing the performance of TRIGRS and TiVaSS in spatial and temporal prediction of rainfall-induced shallow landslides. *Environ Earth Sci* 76 (315):1–16
2. An HU, Kim M, Lee G, Tran TV (2016) Survey of spatial and temporal landslide prediction methods and techniques. *K J of Agricultural Sci* 43(4):507–521
3. Guzzetti F, Carrara A, Cardinali M, Reichenbach P (1999) Landslide hazard evaluation: a review of current techniques and their application in a multi-scale study. *CentL Italy Geomorphol* 31(1–4):181–216

4. Bui DT, Tran AT, Hoang DN, Nguyen QT, Nguyen BD, Ngo VL, Pradhan B (2017) Spatial prediction of rainfall-induced landslides for the Lao Cai area (Vietnam) using a hybrid intelligent approach of least squares support vector machines inference model and artificial bee colony optimization. *Landslides* 14:447–458
5. Trinh T, Ho C, Do N, Ercan A, Kavvas ML (2020) Development of high-resolution 72 h precipitation and hillslope flood maps over a tropical transboundary region by physically based numerical atmospheric–hydrologic modeling. *J Water Clim Chang*
6. Nguyen XT, Ngo DT, Kamimera H, Trinh TL, Matsumoto JI (2016) The Vietnam gridded precipitation (VnGP) dataset: construction and validation. *SOLA* 12:291–296
7. Vietnam Institute of Geoscience and mineral resources. The warning system of the geological disasters In Vietnam, <http://canhbaotruotlo.vn/lienhe.html> Last accessed 30 September 2020
8. Saaty TL (1977) A scaling method for priorities in hierarchical structures. *Geomorphology* 31 (181):234–281
9. Hong H, Shahabi H, Shirzadi A, Chen W, Chapi K, Ahmad BB, Rodposhti MS, Hesar AY, Tian Y, Bui TD (2019) Landslide susceptibility assessment at the Wuning area, China: a comparison between multi-criteria decision making, bivariate statistical and machine learning methods. *Nat Hazards* 96:173–212

Investigation of Anchor Load During the Construction of an Excavation in Hanoi



Tuan-Nghia Do

Abstract This study investigates the development of anchor load during the construction of an excavation in Hanoi. The adopted excavation was a case study, which was modelled using PLAXIS 3D. The final excavation depth was 10.3 m. Behavior of soil was simulated with the elastic-perfectly plastic Mohr-Coulomb model. Results showed that when the d/L ratio decreased (d is the distance between the examined point to the nearest excavation corner and L is the excavation length), the maximum wall deformation was firstly unchanged as $d/L = 1/2-1/8$ and then reduced as $d/L = 1/8-0$ due to the corner effect. For each of the anchor layers, at the excavation stage right after preloading, the anchor load would increase because the wall deformation at the anchor head increased. However, at the other proceeding excavation stages, the anchor load would be reduced owing to the deep inward movement of the wall. For a given excavation stage, the variation of anchor load was compatible with that of the maximum wall deformation at the examined points. In particular, the anchor load was constant as $d/L = 1/2-1/8$ and reduced as $d/L = 1/8-0$.

Keywords Deep excavation · Stress-deformation analysis · Finite element method · Hanoi clay

1 Introduction

The existence of deep excavations during the construction of underground structures in the urban area has been an inevitable part since the underground space has been employed increasingly for many purposes such as: car parking, shopping mall, transportation, etc. In order to reduce the wall deformation caused by excavation, the anchor method is considered as the main solution to wide and deep excavations with few surrounding structures [1]. So far, there are many researches about the

T.-N. Do (✉)
Thuyloi University/TLU, Hanoi, Vietnam
e-mail: dotuannghia@tlu.edu.vn

variation of the wall deformation on the excavation plan, who have observed that due to the large rigidity of the wall at excavation corners, the maximum wall deflection will reduce nearby the corners, so-called corner effect. However, few of them investigate the variation of anchor load on the excavation plan during the course of construction.

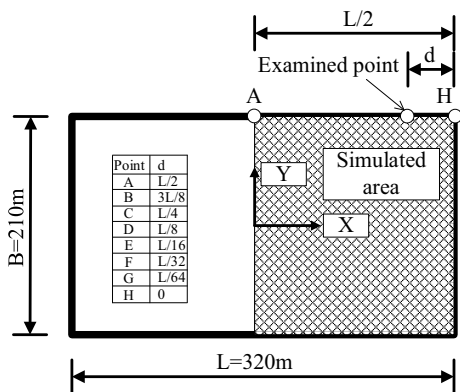
In this study, an excavation in Hanoi clay would be modelled using PLAXIS 3D to investigate the variation of anchor load on the excavation plan and during the excavation procedure. The retaining system, including wall and anchors, together with the construction sequence would be simulated comprehensively in analysis.

2 Excavation Case

The excavation adopted in this study was located in the western side of the West Lake in Hanoi. As shown in Fig. 1, the excavation was 210 m width and 320 m length. The cross section of the excavation was shown in Fig. 2. The maximum excavation depth was 10.6 m and performed in 4 stages at the elevations of -2.4, -5.1, -7.8, and -10.3 m, respectively. The retaining system was composed of a sheet-pile wall (type FSP-IV) with 16 m length and FSP-IV and 3 anchor layers at the elevations of -1.9, -4.6, and -7.3. The anchors were located at 1.6 m in spacing; the grout part was 8 m and the free parts were 11.5, 10, and 8 m at the 1st, 2nd, and 3rd layers, respectively; the preload force was 350 kN per each.

The subsoil conditions at the construction site were shown in Fig. 2. The top-most soil was 1.5-m-thickness fill (1st layer) with cobble and brick. Beneath this layer was the 1.2-m-thickness medium sandy clay (2nd layer) with PI = 12.8%, W = 32.9%, $\gamma_m = 19.1kN/m^3$, $c = 17kN/m^2$, $\phi = 10^0$. There was an 1.8-m-thickness organic soft clay (3rd layer) below this layer with PI = 21.6%, W = 75.5%, $\gamma_m = 15.6kN/m^3$, $c = 6.5kN/m^2$, $\phi = 3.1^0$, $N_{SPT} = 2$. The 4th layer was a 6-m-thickness medium sandy clay with PI = 8.8%, W = 24.5%,

Fig. 1 Excavation plan and examined points



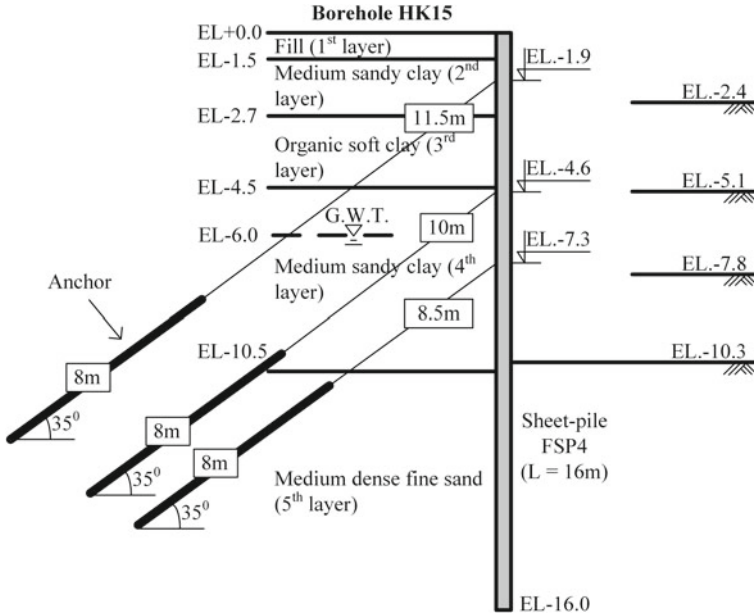


Fig. 2 Excavation profile

$\gamma_m = 20.0kN/m^3$, $c = 17.4kN/m^2$, $\phi = 7.2^0$, $N_{SPT} = 4 \sim 5$. The 5th layer was 25-m-thickness medium dense fine sand with $G_s = 2.66$, $N_{SPT} = 14 \sim 53$. The ground water table located at 6.9 m below the ground surface.

3 Finite Element Model

The Mohr-Coulomb model was adopted to simulate soil behavior. Although this model was simple and required few input parameters, it was still able to give reasonable result of wall deformation. Particularly, the undrained and drained materials were used to simulate clay (2nd, 3rd, and 4th layers) and sand (5th layer). The input parameters of soil were summarized in Table 1.

The retaining wall was simulated using plate elements with axial (EA) and flexural (EI) stiffnesses. The embedded pile and node-to-node anchor elements were used to model the grout and free parts of anchor, respectively. The main input parameters were summarized in Table 2.

Due to the symmetric characteristic, half of the excavation was simulated in analysis as shown in Fig. 3. In particular, the finite element model was 400 m width and 400 m length whereas the thickness was 50 m.

Table 1 Input parameters of soil

Symbol	Unit	2nd layer	3rd layer	4th layer	5th layer
γ_{unsat}	kN/m^3	18	14	19	20
γ_{sat}	kN/m^3	19.1	15.2	20.8	21
E_{ref}	kN/m^2	2.1E4	2700	3.6E4	5.4E4
ν		0.31	0.35	0.32	0.3
c	kN/m^2	17	6.5	17.4	0
ϕ	degree	10	3.1	7.2	34

Table 2 Input parameters of structural elements

Symbol	Unit	Fee part	Grout part	Wall
E	kN/m^2		3.3E6	2.1E8
A	m^2		0.02	2.4E-2
I	m^4			3.9E-4
EA	kN/m^2	1E5		

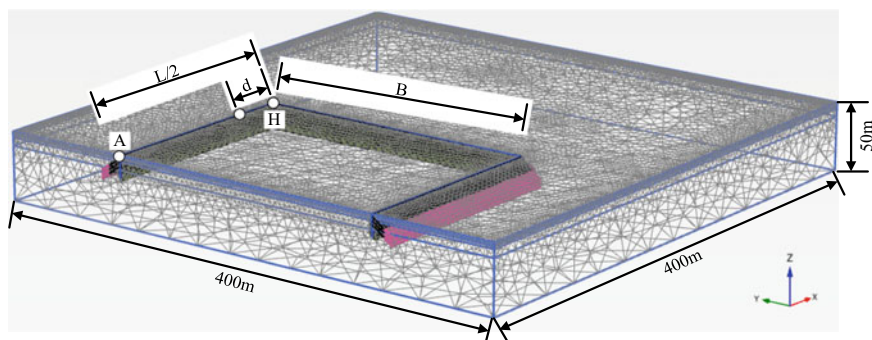


Fig. 3 Finite element model of the excavation

4 Results and Discussions

4.1 Wall Deformation

Figure 4 showed the variation of wall deformations with excavation stages. As shown in this figure, at the 1st excavate stage (EL -2.4 m), the wall deformation was cantilever in shape with the maximum wall deformation at the top of the wall. At the 2nd, 3rd, and 4th excavation stages (EL -5.1 , -7.8 , and -10.3 m), the wall deformation a deep inward shape with the maximum value near the dredge level. In general, the maximum wall deformation increased with the excavation depth.

Fig. 4 Wall deformation at different excavation stages

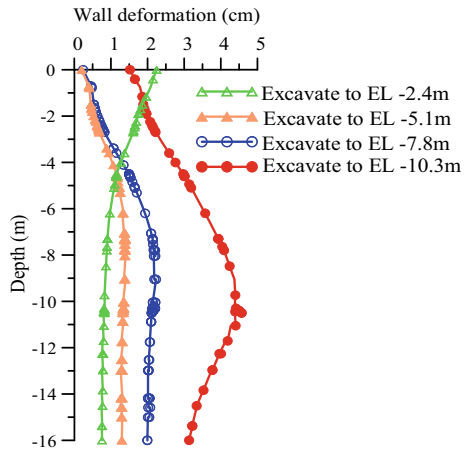


Figure 5 was the maximum wall deformation at the final excavation stage and different examined points. These points (A, B, C, D, E, F, G, H) located at distance $d = L/2, 3L/8, L/4, L/8, L/16, L/32, L/64, 0$ away from the nearby corner, respectively, as shown in Fig. 3. When the d/L ratio decreased, the maximum wall deformation was generally constant from the point A ($d/L = 1/2$) to D ($d/L = 1/8$). Then, the maximum wall deformation decreased from the point D to H ($d/L = 0$). The reason was the corner effect, which increased the wall rigidity near the corner (point H) and hence reduced the wall deformation.

4.2 Anchor Load

Figure 6 showed the variation of anchor load at the point A (center) at different excavation stages. Note that the 1st, 2nd, and 3rd anchor layers were preloaded at the end of the 1st, 2nd, and 3rd excavation stages. When excavation was proceeded, the anchor load initially increased and then decreased gradually. The reason was that right after preloading and performing next excavation, the wall deformation at anchor head developed, causing the increase of anchor load. However, the wall deformation at anchor head would reduce at further excavation stages due to its deep-inward movement so that the anchor load decreased.

Figure 7 was the variation of anchor load at the final excavation stage at different examined points. As shown in the figure, when d/L decreased, the anchor load was generally constant from the points A (center, $d/L = 1/2$) to D ($d/L = 1/8$). Then, the anchor load increased at the 1st layer but decreased at the 2nd and 3rd layers from the points D to H (corner, $d/L = 0$). This variation agreed well with that of the maximum wall deformation at Fig. 5 at the last excavation stage.

Fig. 5 Maximum wall deformation at final excavation stage at examined points

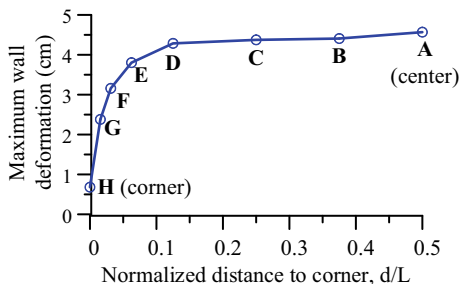


Fig. 6 Variation of anchor load at point A (center) at different excavation stages

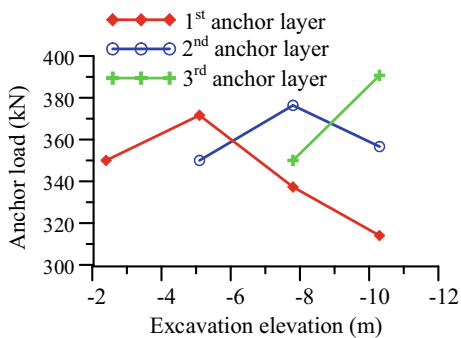
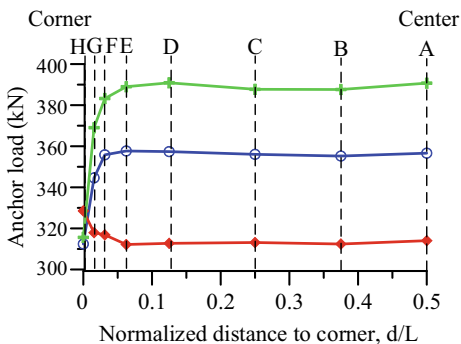


Fig. 7 Variation of anchor load at point A (center) at different excavation stages



5 Conclusions

Based on results of this study, some conclusions could be drawn as follows:

- At a given excavation stage, when d/L reduced, the maximum wall deformation was firstly constant as $d/L = 1/2-1/8$.
- Within a given anchor layer, the anchor load would increase right after preloading and excavation was performed. However, the anchor load would

decrease for further excavation stages because the wall deformation had a deep-inward movement, which affected the displacement of anchor heads.

- At the final excavation stage, the variation of the anchor load agreed well with that of the maximum wall deformation. Particularly, the anchor load remained unchanged as $d/L = 1/2-1/8$ and then decreased as $d/L = 1/8-0$.

Reference

1. Finno RJ, Roboski JF (2005) Three-dimensional responses of a tied-back excavation through clay. *J. Geotech Geoenviron Eng.* 131(3):273–282

Potential Using Municipal Solid Bottom Ash for Road Construction



**Chau Lan Nguyen, Anh Tuan Nguyen, Hai Ha Nguyen,
and Anh-Tuan Vu**

Abstract There is a limited treatment method for municipal solid waste in Vietnam and dumping in a landfill site is still the main solutions for big cities such as Hanoi and Ho Chi Minh city. Recently, incinerator plants are applied in Hanoi and municipal solid waste bottom ash (MSWIBA) is generated. However, in Vietnam, there is a lack of research on the mechanical properties of MSWIBA for recycling this material. Thus, this paper focuses on static and cyclic behaviors of MSWIBA. Static mechanical tests such as the direct shear test showed that the internal friction angle for MSWIBA was varied from 31° to 44° . For cyclic triaxial tests, the observed value of resilient modulus was high. In conclusion, MSWIBA can be used for road material such as fill embankment and subbase.

Keywords MSWIBA · Direct shear · Compaction · Cyclic triaxial test

1 Introduction

Currently, MSW generation in Hanoi is about 6400 tons/day. The MSW amount is treated mainly by landfilling in 8 municipal centers and waste treatment sites at the district level. The largest landfilling site in Hanoi is Nam Son land1 fill which can receive and process daily approximately 3800–4200 tons.

Recently, incineration is also applied for MSW treatment in Vietnam. Incineration is the process of control and complete combustion of solid wastes. The temperature in incinerators varies between 980 and 2000°C. One of the most attractive features of incineration is a reduction in the volume of combustible solid waste by 80–90%. Unfortunately, in Vietnam, the application of incineration for MSW treatment is still limited compared with other methods. Recently, several

C. L. Nguyen (✉) · A. T. Nguyen · H. H. Nguyen
Faculty of Civil Engineering, University of Transport and Communications, Hanoi, Vietnam
e-mail: nguyenchaulan@utc.edu.vn

A.-T. Vu
Le Quy Don Technical University, Hanoi, Vietnam

incinerators have been installed in Hanoi and a large amount of MSW incinerator bottom ash (MSWIBA) will be generated.

Previous research showed that MSWIBA can be utilized for road embankment, fill material, or base/sub-base [1–5]. In addition, the mechanical properties of MSWIBA were similar to dense sand. The direct test results showed that internal friction angle of MSWIBA was from 38°–55° [1].

However, there is limited research on cyclic behavior of MSWIBA for road construction material [3]. Thus, in this paper, static mechanical tests and cyclic triaxial test are conducted for on MSWIBA in order to utilized this material for fill material or base/sub-base in Vietnam.

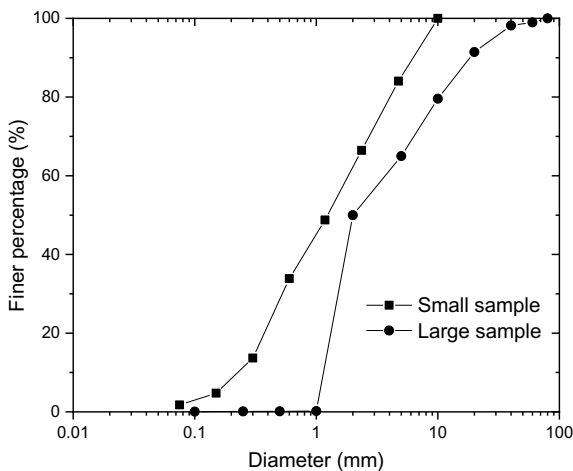
2 Material and Method

2.1 Material

The MSWIBA samples were obtained from the Thanh Quang incinerator in Hanoi capital. Approximately 200 kg of the wet waste samples were collected and then dried in a room with an average temperature of 20 °C. The water content of MSWIBA is 25% and the specific gravity of the waste sample was 2.635. The X-ray diffraction (XRD) and SEM analysis was conducted for MSWIBA sample according ASTM standard.

The maximum diameter of MSWIBA for the small and large direct shear test is 4.75 mm and 40 mm, respectively. Figure 1 shows the particle size distribution for small and large samples, determined according to ASTM D422 [6].

Fig. 1 Particle size distribution curve for small and large sample



2.2 Method

Compaction tests and direct shear tests were conducted according to ASTM standard (ASTM D698 for compaction test and ASTM D 3080 for direct shear test). Standard Proctor Compaction Test was conducted for the small sample and the Modified Proctor Compaction Test was conducted for a large sample of MSWIBA. Both types of samples were prepared by compacting to the compaction ratio which is reached 90% and 95% of maximum dry density.

For the direct shear test, a small sample of 60 mm in diameter was conducted with normal vertical stress of 50, 100, and 150 kPa. For the large direct shear test, specimens were prepared by a modified compaction test in the large direct shear box (300 mm × 300 mm × 140 mm).

In order to use MSWIBA as a subgrade soil or untreated base/sub-base materials, resilient modulus (M_r) test was conducted by using a cyclic triaxial machine. Basically, the system consists of a computer-controlled loading frame that can provide a cyclic loading on a soil sample mounted inside a triaxial cell. The testing standard AASHTOT307-99 (2007): “Standard method of test for determining the M_r of soils and aggregate materials” was employed in this study. MSWIBA sample (with 70 mm diameter and 140 mm height) was used in this study for the cyclic triaxial test. The samples were prepared at optimum moisture content and dry unit weight. The haversine shaped load form was used and cyclic load duration of 0.1 s followed by a recovery duration of 0.9 s was applied. The details of the loading sequences and the number of cycles are shown in Table 1.

Table 1 Details of testing sequence for the experimental soils

Sequence no.	Confining pressure, σ_3 kPa	Max. axial stress, σ_{max} kPa	Number of load cycles (cycle)
1	41.4	13.8	1000
2	41.4	27.6	100
3	41.4	41.4	100
4	41.4	55.2	100
5	41.4	68.9	100
6	27.6	13.8	100
7	27.6	27.6	100
8	27.6	41.4	100
9	27.6	55.2	100
10	27.6	68.9	100
11	13.8	13.8	100
12	13.8	27.6	100
13	13.8	41.4	100
14	13.8	55.2	100
15	13.8	68.9	100

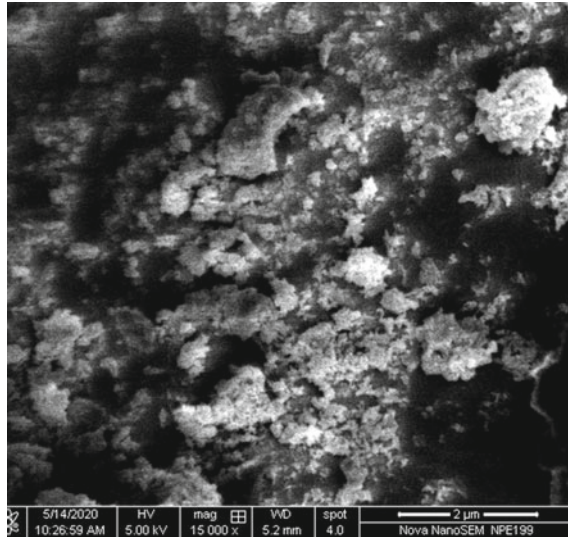


Fig. 3 SEM result for MSWIBA sample

Table 2 Direct shear test result for a small sample and large sample

Type of test	Shear strength parameters	
Small direct shear test results (60 mm in diameter)	c' (kPa)	1.2
	ϕ' (độ)	40°
Large direct shear test results (300 mm x 300mm)	c' (kPa)	73
	ϕ' (độ)	31°

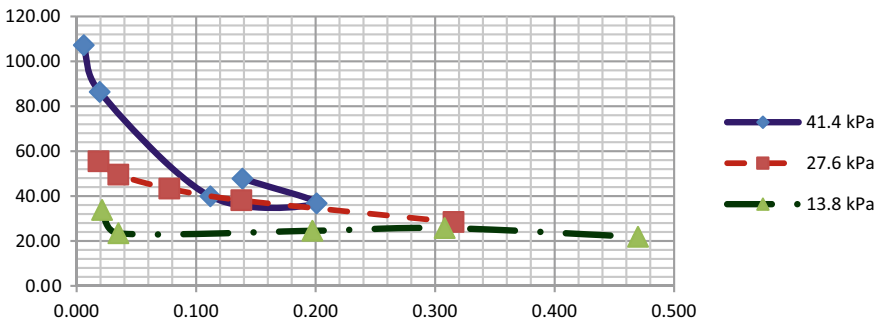


Fig. 4 Resilient modulus for MSWIBA sample

cell pressure of 13.8 kPa. However, M_r is observed the same at 0.2% strain (see Fig. 4). These values are compatible with the smallest for M_r of the MSWIBA (50–150 MPa) which presented by Chiminos (2005).

4 Conclusions

Based on the experimental results, the following conclusion can be drawn as follows:

1. In this research, large direct the shear test was conducted and the results show that higher friction and the cohesion of MSWIBA samples were obtained.
2. It is recommended that MSWIBA can be used for filling embankment due to its high friction angle.
3. Cyclic test showed that the resilient modulus of MSWIBA is suitable for construction material.

Acknowledgements This research is funded by the Ministry of Education and Training, Vietnam under grant number B-2019-GHA10.

References

1. Lynn CJ, Ghataora GS, Dhir RK (2018) Environmental impacts of MIBA in geotechnics and road applications. *Environ Geotech* 5(1)
2. Yang Z, Ji R, Liu L, Wang X, Zhang Z (2018) Recycling of municipal solid waste incineration by-product for cement composites preparation. *Constr Build Mater*
3. Ahmed AT, Khalid HA (2011) Effectiveness of novel and traditional treatments on the performance of incinerator bottom ash waste. *Waste Manag*
4. Toraldo E, Saponaro S, Careghini A, Mariani E (2013) Use of stabilized bottom ash for bound layers of road pavements. *J Environ Manage* 121:117–123
5. Chiminos JM, Fernández AI, Miralles L, Rosell JR, Ezquerro AN (2005) Change of Mechanical Properties during Short-Term Natural Weathering of MSWI Bottom Ash. *Environ Sci Technol*
6. ASTM (2007) ASTM D422–63(2007)e2, Standard Test Method for Particle-Size Analysis of Soils. 2007
7. Luo H, Chen S, Lin D, Cai X (2017) Use of incinerator bottom ash in open-graded asphalt concrete. *Constr Build Mater* 149:497–506

Performance of a New Low-Cost GPS Sensor with an Average Process for Slope Displacement Monitoring



Nguyen Trung Kien and Norikazu Shimizu

Abstract The Global Positioning System (GPS) has been widely used for monitoring displacements of civil engineering structures. The second author and his colleagues developed an automatic GPS system to continuously monitor 3-dimensional displacements with millimeter accuracies. The system has been used to hundreds of fields in Japan, e.g., landslides, dams, etc. However, the cost of the sensor and the monitoring system are still quite expensive compared to standard geotechnical instruments. In this paper, the performance of a new low-cost GPS sensor with an average process is investigated to verify the applicability and reliability for displacement monitoring. This is done by performing experiments in which data are processed by the kinematic method. The standard deviations are improved by taking the average of the kinematic results.

Keywords GPS · Low-cost · Average process · RTKLIB · Kinematic analysis

1 Introduction

The Global Positioning System (GPS) is a satellite-based positioning system. The second author and his colleagues developed an automatic GPS system to continuously monitor 3-dimensional displacements with millimeter accuracies [1–3]. The system has been widely used in Japan to monitor displacements. The International Society for Rock Mechanics and Rock Engineering (ISRM) suggested method for displacement monitoring using GPS has been published [4]. However, the price of the sensor and the monitoring system are still expensive compared to standard geotechnical instruments, e.g., extensometer, etc. This restricts the number of sensors employed in the field.

N. T. Kien (✉)

Thuyloi University, 175 Tay Son, Dong Da, Hanoi, Vietnam
e-mail: kiennt@tlu.edu.vn

N. Shimizu

Yamaguchi University, 2-16-1 Tokiwadai, Ube, Yamaguchi 755-8611, Japan

In this situation, the use of low-cost GPS sensors could be interesting. In the paper, the performance of a new low-cost GPS sensor with an average process is investigated to verify the applicability and reliability for displacement monitoring. Experiments using the new low-cost GPS sensor were conducted. Then, data were processed by the kinematic method. An average process is taken to improve the standard deviations of the kinematic results.

2 Low-Cost GPS Sensor

Figure 1 shows the GPS sensors for displacement monitoring. The MG31 sensor (Furuno Electric Co. Ltd.), with a flat antenna (Fig. 1a) [2] was employed to monitor displacement, and has the accuracy of 1–2 mm in the horizontal direction and 3–4 mm in the vertical one [5]. The sensor and the monitoring system are quite costly compared to standard geotechnical instruments, e.g., extensometer, etc.

A new low-cost GPS sensor (prototype), SB35, is being developed by a collaboration of Shimizu laboratory, Yamaguchi University and a manufacturer (Fig. 1b). The cost of the SB35 sensor is about \$3000 lower than the MG31 one. Table 1 shows the specifications of the new sensor. The sensor uses a U-blox GPS module with the L1 frequency of 1575.42 MHz and an update rate of 1 Hz. It allows for the performance of the real-time kinematic method by a radio link of 920 MHz.

3 Performance of Low-Cost GPS Sensor

3.1 Fundamental Experiments

In order to investigate the standard deviations of the new low-cost GPS sensor for displacement monitoring, experiments were conducted. Data obtained by the new low-cost GPS sensor were processed by the kinematic method. Fundamental

Fig. 1 GPS sensors:
(a) MG31 and (b) SB-35

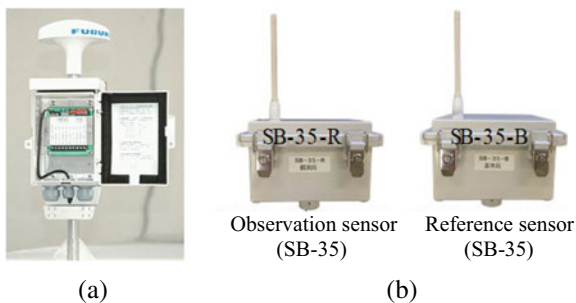


Table 1 Specifications of new sensors

Antenna: Tallysman TW-1421	Radio link: 920 MHz
GPS module: U-blox NEO-M8T	Data acquisition: SD card (max.: 32 GB)
Frequency: L1, 1575.42 MHz	Dimensions (l × w × h): 150 × 150 × 123 (mm)
Update rate: 1 Hz	Working temperature: -20 °C ~ 70 °C
Power supply: DC 5 V ~ 30 V	Weight (approx.): 500 g

experiments were conducted at the Tokiwa Campus of Yamguchi University without any obstacles above the antennas. The baseline length between the reference point and the monitoring point is 10 m, and the difference in height is approximately 0 m. Figure 2 shows the measurement results. The standard deviations of the kinematic analysis with the 1-second measurement interval are about 3 mm in the horizontal direction and 7 mm in the vertical one (Fig. 2a), while those of the analysis with the 1-hour interval are about 1–2 mm in the horizontal direction and 2–3 mm in the vertical one (Fig. 2f).

The results of the kinematic analysis are too poor to precisely monitor displacements. This shortcoming is a well-known fact [6]. In order to improve the accuracy, the arithmetic average of the kinematic results is calculated. The average process can be done by taking average of the 1-second kinematic results in periods. The average periods are 1 minute, and 5, 10, 20, 30, and 60 minutes. The average results are shown in Figs. 2b–e.

Figure 3 shows the relationship between the average periods and the standard deviations in the fundamental experiment. The standard deviations of the 60-minute average results are almost the same as those of the 1-hour static results. When the

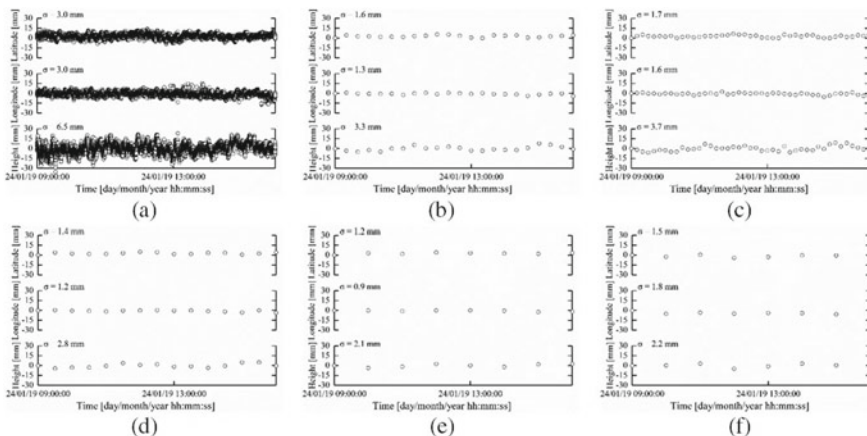
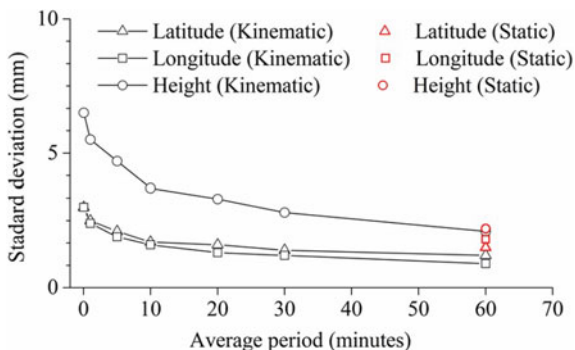


Fig. 2 Measurement results (baseline length: 10 m, height difference: 0 m): (a) Real-time kinematic results with measurement interval of 1 second, (b) 10-minute average of kinematic results, (c) 20-minute average of kinematic results, (d) 30-minute average of kinematic results, (e) 60-minute average of kinematic results, and (f) Static analysis with 1-hour observation

Fig. 3 Relationship between average periods and standard deviations



10–30-minute average is taken, the standard deviations become half of those of the 1-second kinematic results. It can be seen that the average process of the kinematic results improved the standard deviations. If lower accuracies (standard deviations) are acceptable for displacement monitoring, the interval can be shortened by taking the average of the kinematic results over 10–30 minutes.

3.2 Experiment for Detecting Displacement

In order to verify the reliability of the new low-cost GPS sensor, the experiment for detecting displacement was performed by applying given displacement to the sensor. A slider was used to simulate horizontal displacement (Fig. 4). Figure 5 shows the measurement results for the case of given displacement of 10 mm in the longitude direction. Figure 5a presents the 1-second kinematic results that are also taken average for periods of 10, 20, 30, and 60 minutes (Figs. 5b–d).

Table 2 shows the results for the detection of displacements. Although there are discrepancies of 0.1–1.5 mm between the detected and given displacements, the new low-cost GPS sensor allows for the detection of the 10-mm given displacement.

3.3 Field Experiment

Under the condition at the Tokiwa Campus of Yamaguchi University, the new low-cost GPS sensor shows a potential to monitor displacement. Therefore, field experiments were conducted with the new low-cost GPS sensor.

Figure 6 shows the experiment site and locations of the new GPS sensor. The reference sensor, SB-35-B, was installed in the lower area of the slope, while the observation sensor, SB-35-R, was installed in the upper area of the slope. The baseline length and the height difference between SB-35-B and SB-35-R are 170 m

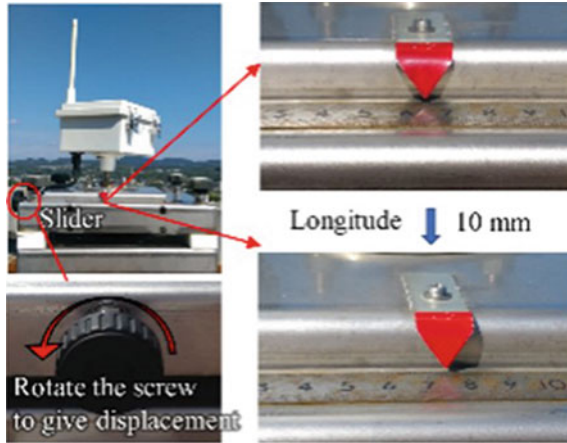


Fig. 4 Slider to simulate displacement

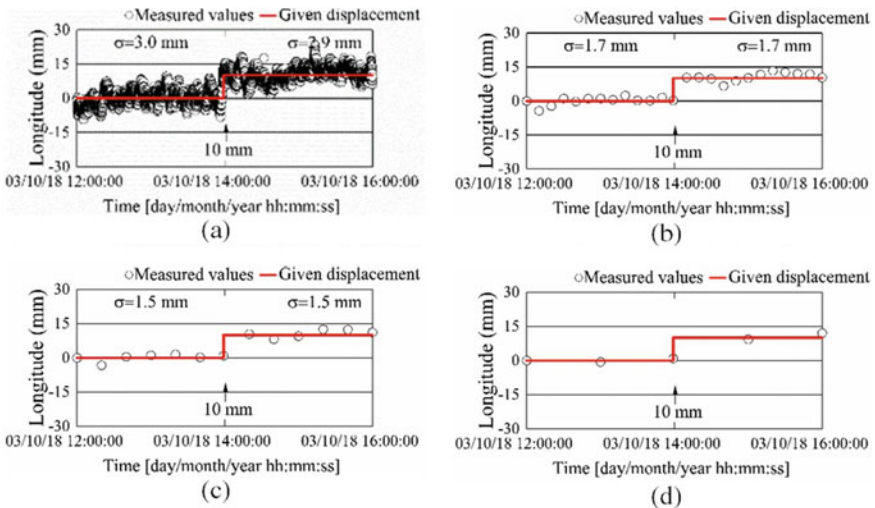


Fig. 5 Measurement results (10-mm given displacement in longitude): (a) Real-time kinematic results with measurement interval of 1 second, (b) 10-minute average of kinematic results, (c) 20-minute average of kinematic results, (d) 60-minute average of kinematic results

Table 2 Detection of displacement

Detected displacement (mm)	10 min.	20 min.	30 min.	60 min.
	10.1	9.4	9.5	8.5
Given displacement in Longitude (mm)	10.0			
Discrepancy (mm)	0.1	0.6	0.5	1.5

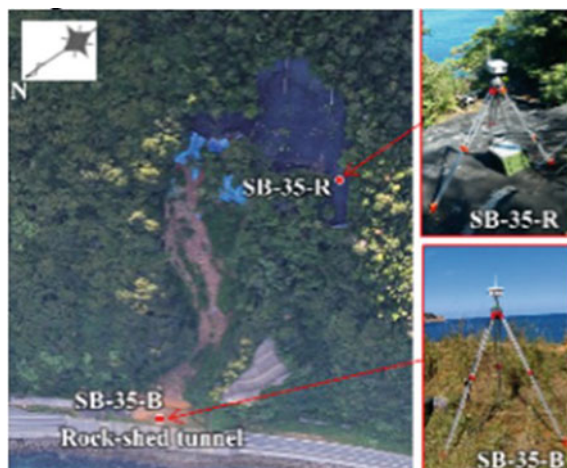


Fig. 6 Experiment site and locations of new low-cost GPS sensors

and 91 m, respectively. Since vegetation covered on the slope surface and might disturb data transmission from the reference sensor to the observation one, the radio transmission was not used in this experiment. The post processing kinematic was conducted.

Figure 7 shows the measurement results by SB-35. The standard deviations are about 5–6 mm in the horizontal direction and 17 mm in the vertical one. The average process of the kinematic results is also calculated. The average results are shown in Figs. 7b-d. When the average periods are 10–30 min, the standard deviations are reduced to about 2–3 mm in the horizontal direction and 4–5 mm in the vertical one which are almost the same as those by MG31 [5].

4 Conclusions

The performance of the new low-cost GPS sensor, SB35, was investigated using the kinematic method. Some experiments were conducted to verify the applicability and the reliability of the new sensor for displacement monitoring. The following conclusions can be drawn:

1. The standard deviations, 1–2 mm in the horizontal direction and 2–3 mm in the vertical one, are obtained by the new low-cost GPS sensor when using the static analysis with the 1-hour interval or taking the average over a period of 60 minutes of the kinematic results.
2. The average process improved the standard deviations. The measurement interval can be shortened by taking the average of the kinematic results over a period of 10-30 minutes.

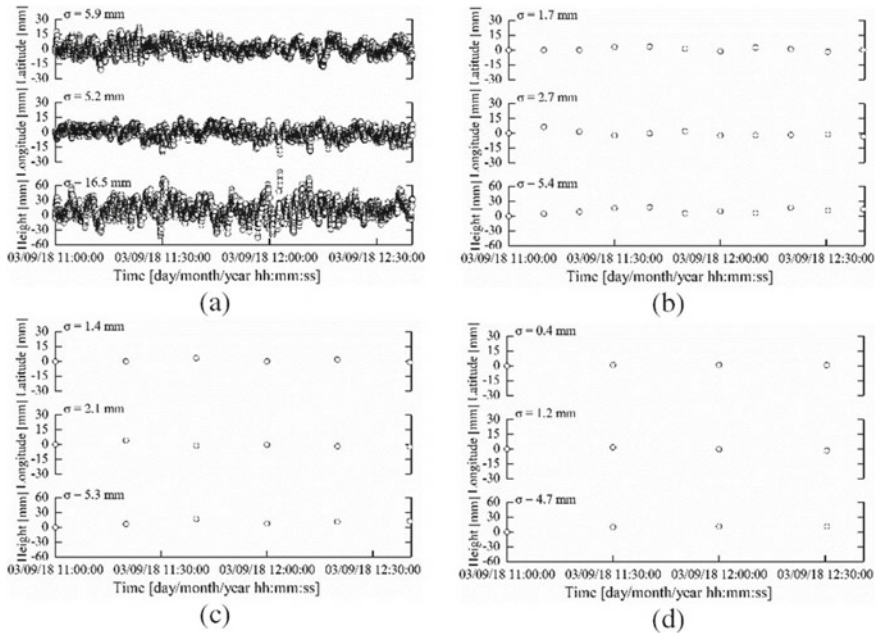


Fig. 7 Measurement results: (a) Post kinematic results with measurement interval of 1 second, (b) 10-minute average of kinematic results, (c) 20-minute average of kinematic results, and (d) 30-minute average of kinematic results

3. The new GPS sensor was able to detect the 10 mm given displacement and the field experiment at the slope site also showed the applicability of this sensor.

References

1. Iwasaki T, Takechi K, Takeishi A, Masunari T, Takechi Y, Shimizu N (2003) Web-based displacement monitoring system using GPS for the maintenance of roadside slopes. In: Proceedings of the 6th International Symposium on Field Measurements in Geomechanics, FMGM03, pp 137–143, Oslo
2. Masunari T, Tanaka K, Okubo H, Oikawa H, Takechi K, Iwasaki T, Shimizu N (2003) GPS-based continuous displacement monitoring system. In: Proceedings of the 6th International Symposium on Field Measurements in Geomechanics, FMGM03, pp 537–543, Oslo
3. Shimizu N, Matsuda H (2002) Practical applications of the Global Positioning System for the assessment of slope stability based on the Displacement Monitoring Approach. In: Proceedings of 3rd Korea-Japan Joint Symposium on Rock Engineering, ISRM Regional Symposium, pp 57–70, Seoul
4. Shimizu N, Nakashima S, Masunari T (2014) ISRM suggested method for monitoring rock displacements using the Global Positioning System (GPS). *Rock Mech Rock Eng* 47:313–328

5. Shimizu N, Masunari T, Iwasaki T (2011) GPS displacement monitoring system for the precise measuring of rock movements. In: Qian, Zhou, editors. *Harmonising Rock Engineering and the Environment: Proceedings of 12th ISRM International Congress on Rock Mechanics*, ISBN 978-0-415-80444-8, pp 1117–1120, Taylor & Francis Group, Beijing
6. Shimizu N, Koyama S, Ono H, Miyashita K, Kondo H, Mizuta Y (1997) Field experiments and data processing for continuous measurements by the GPS displacement monitoring system. *Journal of the Mining and Materials Processing Institute Japan*, pp 113, 549–554

Study on the Change of Deformation Modulus of Ho Chi Minh City' Soft Soil Under the Extension Stress Paths for Deep Excavation Calculation



Trung Ngo Duc

Abstract To predict the displacement and deformation of the deep excavation, it is necessary to determine the ground characteristics of the soil surrounding the deep excavation to include in the soil models. However, geological data for the design of the deep excavation is mainly obtained from conventional geological experiments, which have not yet described the behavior of the soil surrounding the excavation. Therefore, the problem is to use an experimental model with a reasonable stress path to determine the input parameters that match the behavior of the ground around the excavation pit, which is manifested by the changes in soil stiffness during the excavation work. This is what the current experimental protocol considers unchanged. This paper uses a triaxial test device to analyze the stiffness behavior of soft soil in Ho Chi Minh City (HCMC) according to the stress paths of extension in calculating deep excavation.

Keywords Stress paths · Deep excavation · Extension · Deformation modulus

1 Introduction

Many studies [1, 2] have divided the area affected by the excavation process into four parts, as shown in Fig. 1.

Zone I: when removing soil out of the excavation, horizontal stress decreases while vertical stress remains unchanged. Stress paths as the AC segment in Fig. 1.

Zone II: during excavation, vertical stress decreases, and lateral stress increases due to wall displacement. The stress path for this region is represented by the AMF segment in Fig. 1.

Zone III: During the excavation process, vertical stress decreases continuously; horizontal stress changes a little, and the stress path is shown in the AS segment in Fig. 1.

T. Ngo Duc (✉)

Nguyen Tat Thanh University, Ho Chi Minh City, Vietnam

e-mail: ndtrung@ntt.edu.vn

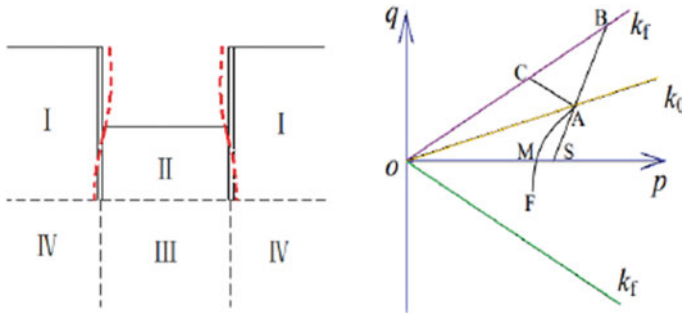


Fig. 1 Area of influence of deep excavation and stress paths

Zone IV: Vertical stress is constant; there is a slight change in horizontal stress, and the stress path is still near the AC segment in Fig. 1.

Soil productivity change is very complicated. It can be seen that to analyze the behavior of zone I (behind the retaining wall) and zone II (at the bottom of the excavation pit), we should focus on analyzing the shear strength and stiffness parameters of the soil in these two areas.

In this study, the author performed a series of undrained triaxial tests (CU) on 36 soft soil samples with a depth of 4–24 m, respectively the test was performed with different stress paths to analyze shear behavior and stiffness of soft soil in HCMC.

2 Apparatus

The test was carried out with the load frame system of Humboldt according to ASTM D4767. This system includes pressure, deformation, pressure, and volume sensors connected to the ADAM View 32-channel data logger system.

Testing samples and parameters according to different stress paths. The test according to the stress paths as follows:

- Conventional triaxial compression model (CTC— $\text{increase } \sigma_1 \text{ and fixed } \sigma_3$): Saturated soil samples are isotropic consolidation and undrained samples according to the usual compression schedule: 12 samples;
- Triaxial drag model (RTE— $\text{reduced } \sigma_1 \text{ and fixed } \sigma_3$): Saturated soil samples are isotropic consolidation and non-draining samples according to vertical stress reduction schedule: 12 samples;
- Model of cell pressure reduction (RTC— $\text{reduction } \sigma_3 \text{ and fixed } \sigma_1$): Saturated soil samples are isotropic consolidation and non-draining samples according to horizontal stress reduction schedule: 12 samples;

3 Analysis and Evaluation of Testing Results

3.1 Stress and Strain Relationship ($q - \epsilon_1$)

The triaxial test according to the CTC, RTE, and RTC stress paths is performed with the CU diagram. The testing results are shown from Figs. 2, 3, 4, 5, 6, 7, 8, 9.

In the conventional triaxial compression test (CTC stress path), the pore water pressure is always positive and also increases immediately along with the deformation in the axial stress increase process. In contrast, for the RTE stress path in a triaxial tensile test, the pore water pressure decreases at low-stress levels and gradually increases at higher stress levels. The initial pressure of the pore water is negative and the positive sign is changed according to the increase of the deviation stress due to the reduction of σ_1 .

The pore-water pressure shows the elastic state, which corresponds to the actual volume elasticity of the external ground when unloading during the excavation process. This expansion behavior may be partly explained by the change in the pore water pressure of the soil sample at the end of the saturation and consolidation period during shear stress. In most cases, these soil samples were damaged by declining deformation. The destruction of the sample is seen in the middle of the sample like the bottleneck shape. It can be seen that, during the increase in stress, the pore water pressure also increases similarly corresponding to each stress paths. The sample damage when the deformation reaches about $6 \div 8\%$.

With the RTC stress path, when reducing horizontal stress during the sample shear process, the strain also increases, but it is slower than the deformation compared to the CTC stress path. Test results show that in the RTE stress path, the

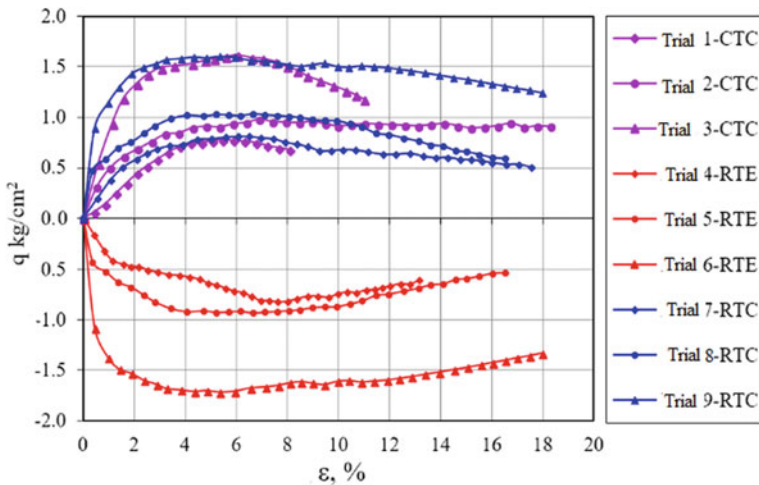


Fig. 2 ($q - \epsilon$) of stress paths at depths 4–6 m

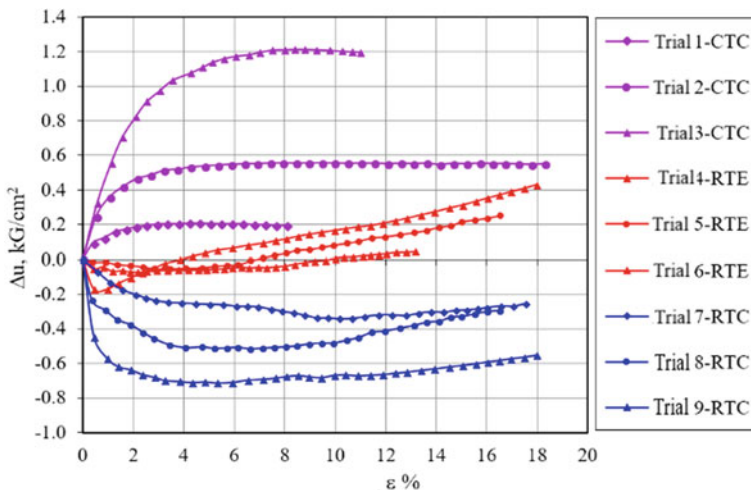


Fig. 3 ($\Delta u - \varepsilon$) of stress paths at depths 4–6 m

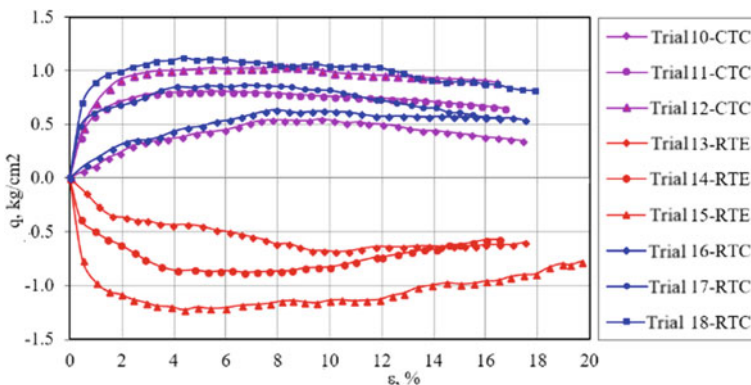


Fig. 4 ($q - \varepsilon$) of stress paths at depths 12–14 m

axial strain increases more slowly than the CTC stress path. So, the initial tangent modulus is higher in the RTE stress path and they have a lower value for the CTC stress path. Thus, it can be concluded that the initial modulus increases during unloading. Therefore, the calculated module from the RTC stress path has a higher value than that calculated from the CTC stress path due to the larger slope of the stress and strain relationship. The pore water pressure in the RTC stress path is opposite to the CTC stress path but has a significantly smaller magnitude and has a different nonlinearity, this pressure gradually increases to the destructive threshold of the sample and decreases when the sample starts destructive.

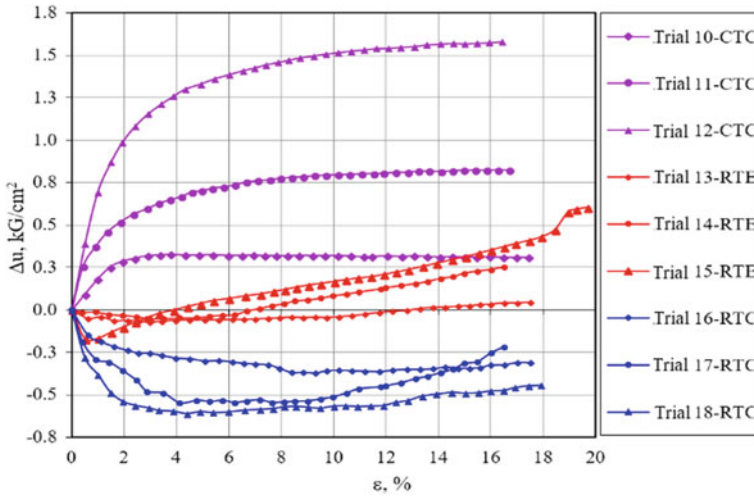


Fig. 5 ($\Delta u - \epsilon$) of stress paths at depths 12–14 m

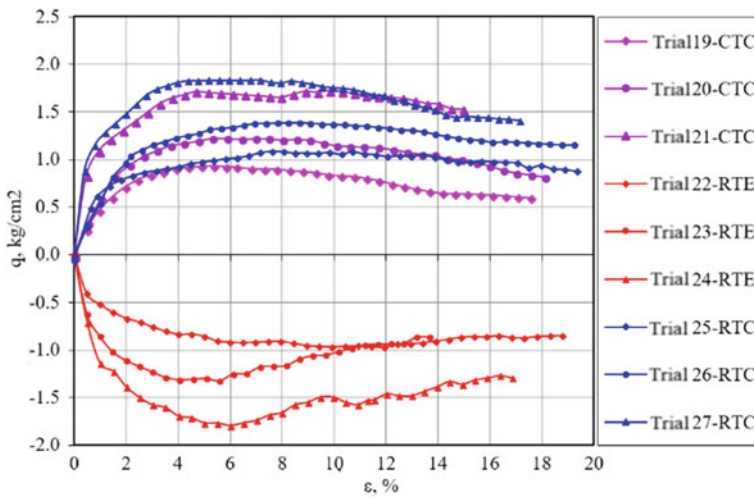


Fig. 6 ($q - \epsilon$) of stress paths at depths 18–20 m

3.2 Analysis of Deformation Modulus of Stress Paths

The relation (q, ϵ_1) (Figs. 2, 3, 4, 5, 6, 7, 8, 9), the author calculates the deformation modulus (E_{50}) of soft clay samples at different depths and corresponding cell pressures. The results are shown in Table 1.

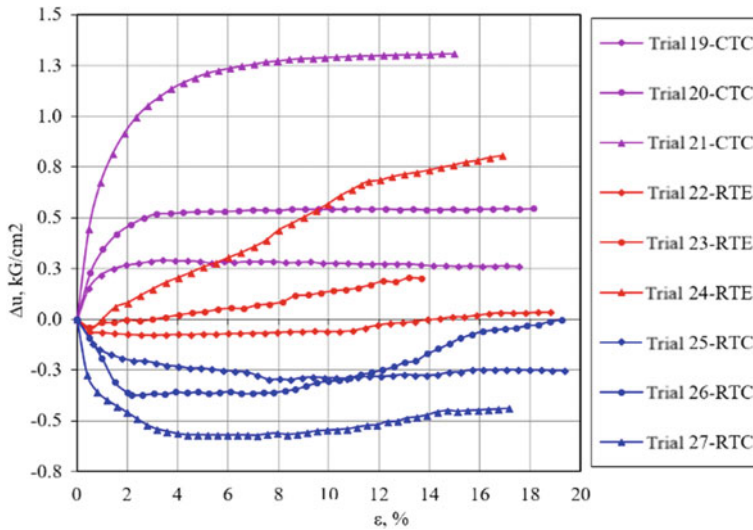


Fig. 7 ($\Delta u - \epsilon$) of stress paths at depths 24–26 m

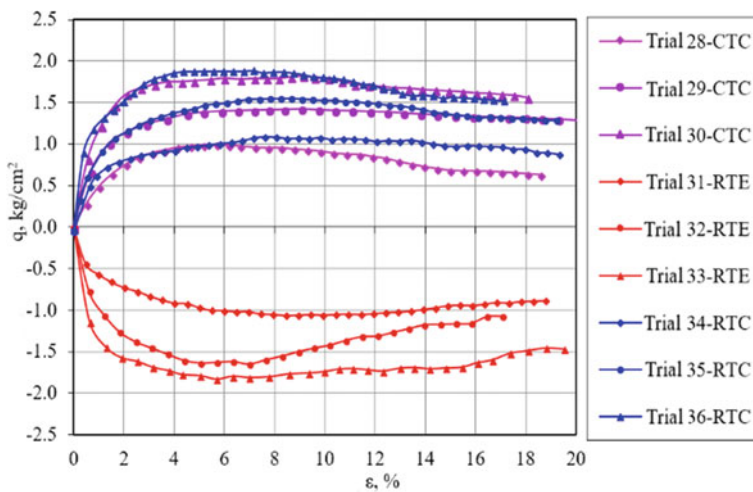


Fig. 8 ($q - \epsilon$) of stress paths at depths 24–26 m

The difference in the value of the elastic modulus according to the stress paths can be explained by the dependence of the elastic modulus according to each stress path on the plastic strain level. The magnitude of plastic deformation depends on the flexible potential function and flexible flow function. Thus, the elastic modulus of the ground at some point has only one value in the state without deformation. When the ground is deformed, the value of the elastic modulus decreases with a

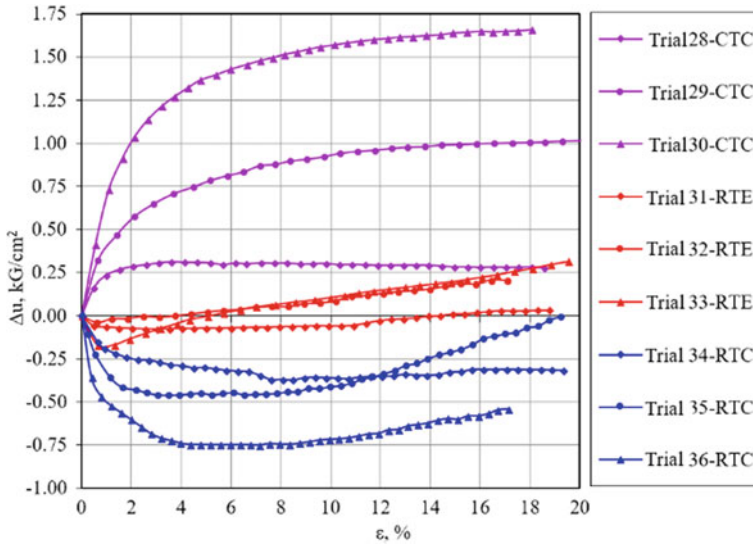


Fig. 9 ($\Delta u - \epsilon$) of stress paths at depths 24–26 m

Table 1 E_{50} deformation modules from CTC, RTE, and RTC stress paths

Depth (m)	σ_c (kPa)	RTE	RTC	CTC	$\frac{E_{50,RTE}}{E_{50,CTC}}$	$\frac{E_{50,RTC}}{E_{50,CTC}}$
		E_{50} (kPa)	E_{50} (kPa)	E_{50} (kPa)		
<i>Very soft clay</i>						
4 ÷ 6	50	3611	3494	2085	1.73	1.68
	100	8202	7495	4774	1.72	1.57
	200	14,528	13,997	8553	1.70	1.64
12 ÷ 14	50	2750	2968	1853	1.48	1.60
	100	11,575	9427	5981	1.94	1.58
	200	15,194	17,774	9389	1.62	1.89
<i>Soft clay</i>						
18 ÷ 20	50	5811	5391	3673	1.58	1.47
	100	8640	6442	4510	1.95	1.48
	200	14,652	14,121	9273	1.58	1.52
24 ÷ 26	50	4579	4201	2861	1.60	1.47
	100	7765	7026	4922	1.58	1.43
	200	16,688	15,107	9161	1.82	1.65
The average value					1.69	1.58

degree of dependence on the stress path. The value of the elastic modulus of the ground soil is determined by the initial slopes of the strain-strain relationship curve in such a conventional triaxial compression test that results in a large error in the

calculation. Therefore, it is recommended to use the value of the elastic modulus from the unloading triaxial compression test.

With a triaxial test according to RTE and RTC stress paths, the values of the deformation modulus are much larger than those calculated from the test results according to the normal triaxial compressive stress path:

$$E_{50,RTE}/E_{50,CTC} \approx E_{50,RTC}/E_{50,CTC} = 1.58 \div 1.69 \quad (1)$$

4 Conclusions

- The behavior of soil depends greatly on stress paths. Determining the shear strength and the stiffness parameters for the deep excavation calculation should be determined from the triaxial test with the unloading stress paths because these experiments describe the actual working state of the ground during the construction process.
- The triaxial test according to the RTE and RTC stress paths shows the same modulus values but their modulus is larger than the conventional triaxial test CTC stress paths. With the soft soil layer of HCMC magnitude ranges from [1.58 ÷ 1.69] times:

$$E_{50,RTE}/E_{50,CTC} \approx E_{50,RTC}/E_{50,CTC} = 1.58 \div 1.69$$

References

1. Becker P (2008) Time and stress path dependent performance of excavations in soft soils. In: 19th European young geotechnical engineers' conference, Gyor, Hungary
2. Wong KS (2009) A short course on deep excavations, New Zealand

The Shapes of Collapsed Sinkholes at Limiting Equilibrium



Rengifo Arakaki Kimiko, Vo Thanh, and R. Adrian Russell

Abstract Experiments show that the sinkholes' sizes and shapes are related to their stability. After a sinkhole has been created, its geometry continually evolves towards a more stable form. This process is governed by characteristics of the surrounding geomaterials, and various physical interactions, such as weathering, stress variations caused by cycles of wetting-drying. Buried, dropout and suffosion sinkholes are formed in the soil layer overlying bedrock. Dropout sinkholes (i.e. those with overhanging arches) are more likely to form in cohesive soil; suffosion sinkholes (i.e. those without overhanging arches) are more likely to form in non-cohesive soil. In the literature, most mechanistic analyses focus on dropout sinkhole. Few researchers conduct stability analysis of suffosion sinkhole. The geometry of a sinkhole is an input into most stability analyses, but it is often idealised or back-calculated from post-failure data. There is a need to know the geometry of a sinkhole approaching the point of failure (i.e. the limiting equilibrium). This paper reports on the geometry of collapsed suffosion sinkholes at limiting equilibrium obtained by the slip line theory. Analyses consider nonhomogeneous soils satisfying static equilibrium with soil strength governed by the Mohr-Coulomb failure criterion. The limiting sinkhole geometry is shown to be governed by dimensionless parameters. Exemplary charts are presented for determining this critical geometry given different combinations of soil parameters. Applications are illustrated via an example.

Keywords Sinkholes · Unsaturated soils · Slip line theory · Slope stability

R. A. Kimiko
Golder Associates, Perth, Australia

V. Thanh (✉) · R. A. Russell
School of Civil and Environmental Engineering, Centre for Infrastructure Engineering
and Safety, The University of New South Wales, Sydney, Australia
e-mail: thanhliemvo30@gmail.com

1 Introduction

A sinkhole is a natural or human-induced cavity formation in the ground. Sinkholes vary in sizes, with depths up to 500 m [1, 2], and can be induced by underground mining, tunnelling, explosive testing, leaking sewers, etc. Sinkholes cause ground subsidence and collapse in many regions of the world.

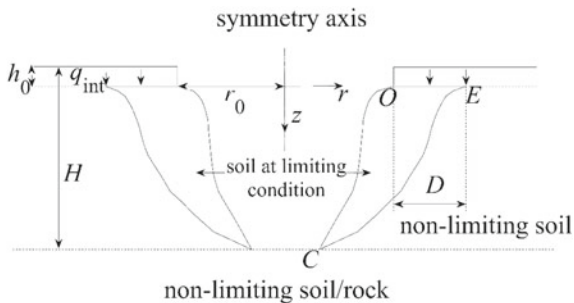
Different types of sinkholes have been identified [3]. Buried, dropout and suffosion sinkholes are formed in a soil layer overlying bedrock. Buried sinkholes are depressions in thin layer of soil and evolve over a period of 10,000 years or more and are comparatively less hazardous than dropout and suffosion sinkholes. Dropout sinkholes, which have characteristic overhanging arches, are more likely to form in cohesive soils. Suffosion sinkholes do not have overhanging arches and are more likely to form in non-cohesive soils. Experiments show that a sinkholes' geometry is related to its stability [4–6]. Mechanistic analyses of sinkhole in the literature focus on dropout sinkholes rather than on suffosion sinkholes.

This article reports an analysis of the limiting geometry of collapsed suffosion sinkholes obtained by the slip line theory in axial symmetry. The analysis considers, for the first time, nonhomogeneous soils as well as curvilinear profiles of the sinkhole sidewalls. The geomaterial surrounding the sinkhole satisfies static equilibrium, may be partially saturated and have a suction that contributes to the stability, and has a shear strength governed by the Mohr-Coulomb failure criterion. Results, presented in dimensionless charts, show the size of a sinkhole, the shear strength of soil and the ground condition govern the geometry of sinkhole sidewall. Applications of the results are demonstrated using an example.

2 A Boundary Value Problem Relating the Shape of the Sinkhole to Strength of Materials Around It

The geometry of a curvilinear axisymmetric sinkhole is shown in Fig. 1. The radius of the cavity at ground surface is r_0 . The sinkhole is formed to a depth H , which may be the thickness to a layer of underlying soil or bedrock. A “curvy” soil wedge forms a surface of revolution and is at limiting condition i.e. on the verge of failure. Outside of this volume the soil and rock are not at a limiting condition. A surcharge load q_{int} , being the weight of a layer that is h_0 thick plus any external loads acting on top of that layer, acts across the surface.

Fig. 1 Geometry of a sinkhole



2.1 Static Equilibrium of Cohesive-Frictional Materials at Limiting Condition of Stability (on the Verge of Failure)

The static equilibrium equations of cohesive-frictional materials on the verge of failure according to the Mohr-Coulomb failure criterion and including the effect of suction in unsaturated soils formulated by Vo and Russell [7] (based on the effective stress concept for unsaturated soils) are adopted here. They also include the case when cohesion (c') and the contribution of suction to the effective stress (χs) vary linearly with depth by the functions:

$$c' = c'_0 + k_c z \tag{1}$$

$$\chi s = (\chi s)_0 + k_{\chi s} z \tag{2}$$

where c'_0 , $(\chi s)_0$ are cohesion and the contribution of suction to the effective stress at $z = 0$, respectively, and k_c , $k_{\chi s}$ are constants. For a soil that is saturated all the way to the soil surface, $(\chi s)_0$ may be interchanged with $(u_w)_0$, that is the negative of the pore water pressure at the ground surface, and $k_{\chi s}$ may be interchanged with $k_{u_w} = \partial(-u_w)/\partial z$. For hydrostatic conditions, $k_{u_w} = -\gamma_w$. In Eqs. (1, 2), k_c and $k_{\chi s}$ have the unit of stress/length.

With reference to a coordinates system where r is the radial axis and z is the vertical axis, the governing equations of limiting equilibrium can be expressed as:

$$\langle \xi \rangle \equiv \begin{cases} d\bar{r} = \tan(\psi - \mu) d\bar{z} \\ -d\bar{\sigma}'_m + 2 \tan \varphi' \bar{\sigma}'_m d\psi = \frac{L}{S} A \left[-\frac{\sin(\psi + \mu)}{\cos^2 \varphi'} d\bar{z} + \frac{\cos(\psi + \mu)}{\cos^2 \varphi'} d\bar{r} \right] \end{cases} \tag{3}$$

$$\langle \eta \rangle \equiv \begin{cases} d\bar{r} = \tan(\psi + \mu) d\bar{z} \\ d\bar{\sigma}'_m + 2 \tan \varphi' \bar{\sigma}'_m d\psi = \frac{L}{S} B \left[\frac{\sin(\psi - \mu)}{\cos^2 \varphi'} d\bar{z} - \frac{\cos(\psi - \mu)}{\cos^2 \varphi'} d\bar{r} \right] \end{cases} \tag{4}$$

where

$$A = \sin(\psi + \mu) \left[\gamma + \frac{\partial(\overline{c' \cot \phi' + \chi s})}{\partial \bar{z}} - \frac{\overline{\sigma'_m} \sin \phi' \sin 2\psi}{\bar{r}} \right] + \cos(\psi + \mu) \left[\frac{\overline{\sigma'_m}(1 - \sin \phi' \cos 2\psi) - \overline{\sigma'_m}(1 - \sin \phi')}{\bar{r}} \right] \quad (5)$$

$$B = \sin(\psi - \mu) \left[\gamma + \frac{\partial(\overline{c' \cot \phi' + \chi s})}{\partial \bar{z}} - \frac{\overline{\sigma'_m} \sin \phi' \sin 2\psi}{\bar{r}} \right] + \cos(\psi - \mu) \left[\frac{\overline{\sigma'_m}(1 - \sin \phi' \cos 2\psi) - \overline{\sigma'_m}(1 - \sin \phi')}{\bar{r}} \right] \quad (6)$$

σ'_m is effective mean stress, ψ is angle between the vertical axis and the effective major principal stress direction, γ is soil total unit weight. $\bar{z} = \frac{z}{L}$, $\bar{r} = \frac{r}{L}$, $\overline{\sigma'_m} = \frac{\sigma'_m}{S}$, $\overline{c'} = \frac{c'}{S}$, $\overline{\chi s} = \frac{\chi s}{S}$ are non-dimensional quantities, $\mu = \pi/4 - \phi'/2$, and ζ , η denote families of stress slip lines. From Eqs. (1, 2), $\frac{\partial(\overline{c' \cot \phi' + \chi s})}{\partial \bar{z}} = k_c \cot \phi' + k_{\chi s}$, choosing $L = D$ (where D is as shown in Fig. 1) and $S = q_{\text{int}} + c'_0 \cot \phi' + (\chi s)_0$, the dependency between $(\overline{\sigma'_m}, \psi, \bar{z}, \bar{r})$ and governing dimensionless variables is:

$$(\overline{\sigma'_m}, \psi, \bar{z}, \bar{r}) = f \left\{ F \equiv \frac{D(\gamma + k_c \cot \phi' + k_{\chi s})}{q_{\text{int}} + c'_0 \cot \phi' + (\chi s)_0}, \phi', \frac{r_0}{D} \right\} \quad (7)$$

where f denotes a functional dependency. Equation (7) shows that it is convenient to present the limiting sinkhole geometry in terms of combinations of F , ϕ' , r_0/D .

2.2 Boundary Conditions and Solution Procedure

The surcharge on the soil surface at the top of the slope (q_{int}) can be derived from the condition of non-overlapping stress field [8] to be:

$$q_{\text{int}} = \frac{2[(\chi s)_0 + c'_0 \cot \phi'] \sin \phi'}{1 - \sin \phi'} \quad (8)$$

The corresponding thickness of the surcharge layer is:

$$h_0 = \frac{(\chi s)_0(1 - K'_a) + 2c'_0 \sqrt{K'_a}}{\gamma K'_a + k_{\chi s}(K'_a - 1) - 2k_c \sqrt{K'_a}} \quad (9)$$

where $K'_a = \frac{1 - \sin \varphi'}{1 + \sin \varphi'}$. Along the soil surface OE, the following two boundary conditions are satisfied:

$$\psi = \psi_{OE} = 0 \tag{10}$$

$$\bar{\sigma}'_m = \frac{1}{1 + \sin \varphi'} \tag{11}$$

where ψ_{OE} is the angle between the vertical axis and the effective major principal stress direction along OE. At the slope surface OC, the following two boundary conditions are satisfied:

$$\frac{d\bar{r}}{d\bar{z}} = \tan \psi_{OC} \equiv \tan \alpha_s \tag{12}$$

$$\bar{\sigma}'_m = \frac{\gamma s + c' \cot \varphi'}{(1 - \sin \varphi') [q + (\gamma s)_0 + c'_0 \cot \varphi']} \tag{13}$$

where ψ_{OC} is the angle between the vertical axis and the effective major principal stress direction along OC. At point O, the following boundary conditions are satisfied:

$$\psi = \psi_O = 0 \tag{14}$$

$$\bar{z} = 0 \tag{15}$$

$$\bar{r} = \frac{r_0}{D} \tag{16}$$

The governing equations (Eqs. 3–6) and boundary conditions (Eqs. 10–16) were solved by the finite difference method.

3 Profiles of Suffosion Sinkholes at Limiting Condition

Profiles of suffosion sinkholes at limiting condition are shown in Fig. 2 for typical combinations of F , φ' , r_0/D . Each profile is a curve OC (Fig. 1) in $(z/r_0, r/r_0)$ plane.

Figure 2a shows that given certain r_0/D and φ' , a higher F corresponds to a less steep profile. Figure 2b shows that given certain r_0/D and F , a higher φ' corresponds to a steeper profile.

Given certain F and φ' , it is expected that the axisymmetric profile would approach the corresponding plane strain profile reported by Vo and Russell [8] as $\frac{r_0}{D} \rightarrow +\infty$. Figure 3 shows an example of this convergence for $F = 1$, $\varphi' = 30^\circ$.

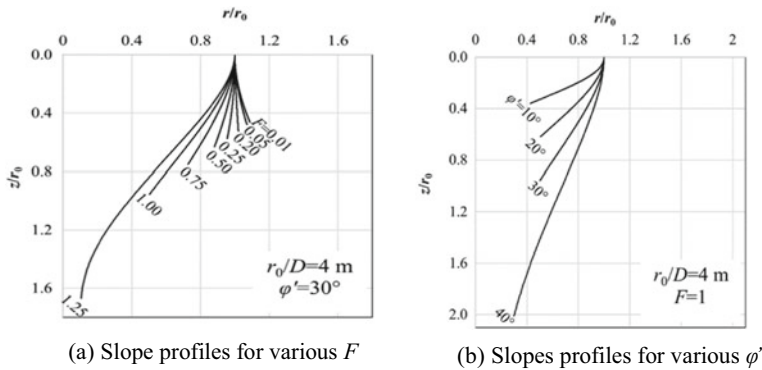
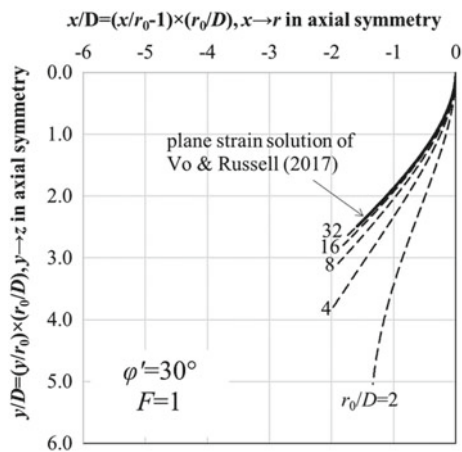


Fig. 2 Slope profiles for various F and various ϕ' . **a** Slope profiles for various F . **b** Slopes profiles for various ϕ'

Fig. 3 Curvilinear profiles for $F = 1$, $\phi' = 30^\circ$ when $\frac{r_0}{D} \rightarrow +\infty$



4 An Example of Application

Central Florida in the USA presents a karst topography of clays and sands overlying marine calcareous sediments in which sinkholes develop due to aquifer withdrawal. Most sinkholes are small, of a few meters depth and up to 10 m in diameter. Occasionally larger sinkholes form, such as the Winter Park sinkhole having 106 m diameter, 30 m depth [9].

The aquifer in the area of the sinkhole had a piezometric level of +14 meters Mean Sea Level (MSL). The Winter Park sinkhole formed in a surficial sand/silty sand from +29 m (MSL) to +14.5 m, and clay from +14.5 m to -24 m. As the piezometric level was at +14 m, the sandy layer is in an unsaturated state.

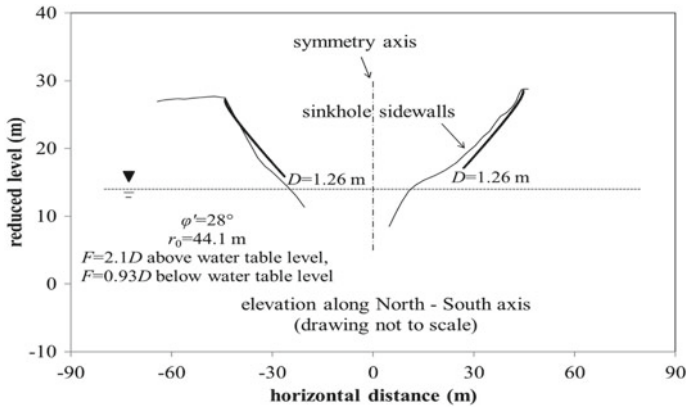


Fig. 4 Profile of Winter Park sinkhole (North–South axis) compared by to prediction

Based on SPT records of boreholes drilled in the vicinity of the Winter Park sinkhole and other CPT data in Florida [10, 11], a friction angle $\phi' = 28^\circ$ was estimated for the surficial soil. The surface stratum of the sinkhole was described as silty sand so it is assumed that $c_0' \cot \phi' + (\chi_s)_0 = 3 \text{ kPa}$ at $z = 0 \text{ m}$ (which corresponds approximately to 0.3 m of desiccated overburden) and $k_c = 0 \text{ kPa/m}$, thus the χ_s profile adopted for the sandy layer above the water table is $\chi_s = 3 - 0.208z \text{ (kPa)}$. Below the water table $k_{\chi_s} = -9.81 \text{ kPa/m}$. Given a typical $\gamma = 17.5 \text{ kN/m}^3$, it was found that $F = 2.1D$ above the water table level and $F = 0.93D$ below the water table. The corresponding profiles are shown on Fig. 4 for $D = 1.26 \text{ m}$.

5 Conclusion

Sinkholes are observed in many regions of the world. Researchers have reported that the geometry of sinkholes formed in soil overburden are linked to their stability. Geotechnical literature focuses on dropout sinkhole, few researchers analyse suffosion sinkhole. The geometry of a sinkhole is an input into stability analyses and is often idealised or back-calculated from empirical data. Suffosion sinkholes would expand if their sidewalls are unstable.

This paper reports on the limiting geometry of collapsed suffosion sinkholes obtained by the slip line theory. In particular, the work of Vo and Russell [8] is extended to axial symmetry, and the governing equations are solved by the finite difference method. Results illustrate the influence of 3 parameters governing the geometry of sinkhole sidewall at limiting equilibrium: r_0/D (accounting for the relative size of sinkhole), ϕ' (accounting for the frictional strength of the surrounding geomaterial) and a dimensionless parameter F (accounting for the ground condition). Applications of results are illustrated via an example.

References

1. White WB (1988) *Geomorphology and hydrology of karst terrains*. Oxford University Press, Oxford, UK
2. Ford D, Williams P (2007) *Karst hydrogeology and geomorphology*. England, Wileys
3. Waltham T, Bell F, Culshaw M (2005) *Sinkholes and subsidence: karst and cavernous rocks in engineering and construction*. Springer, Berlin
4. Howell FT, Jenkins PL (1984) Centrifuge modelling in flow prediction studies of granular materials. In: *Symposium on application of centrifuge modelling to geotechnical design*. A. A. Balkema, Manchester, UK
5. Craig WH (1990) Collapse of cohesive overburden following removal of support. *Can Geotech J* 27:355–364
6. Abdulla WA, Goodings DJ (1996) Modeling of sinkholes in weakly cemented sand. *J Geotech Eng* 122(12):998–1005
7. Vo T, Russell AR (2016) Bearing capacity of strip footing on unsaturated soils by the slip line theory. *Comput Geotech* 74:122–131
8. Vo T, Russell AR (2017) Stability charts for curvilinear slopes in unsaturated soils. *Soils Found* 57(4):543–556
9. Jamal SE (1986) The Winter Park sinkhole and Central Florida sinkhole type subsidence. In *The 3rd international symposium on land subsidence*, Venice, Italy
10. Jammal and Associates I (1982) *The Winter Park sinkhole: a report to the city of Winter Park*. Florida, USA
11. Gray KM (2014) *Central Florida sinkhole evaluation*. Florida Department of Transportation, Florida, USA

Construction Materials

A Study on Tunnel Lining Concrete with Crushed Aggregate from NATM Muck



Thu-Hang Tran

Abstract The reduction of the waste products, and the waste recycling as alternative construction materials is essential in the practice of sustainable development in civil engineering. The utilization of excavated muck after rock tunnelling has been executed worldwide but not always in propitious circumstances in countries where the legal backbone of the waste recycling is not strong enough against the conventional use of raw materials. The study and publication of such application cases is considered as an effort for the propagation of sustainability in tunnel projects. With that aim, the paper focused on a case study in Vietnam where the muck after the NATM tunnelling had been used as coarse aggregate for the C25 tunnel lining concrete. Compared with an equivalent lining concrete using raw material, through the analysis of the test results at construction site, the possibility of using recycled muck for tunnel lining was proven.

Keywords Tunnel muck · Recycling · Lining concrete · Coarse aggregate · NATM

1 Introduction

Rock tunnelling heavily threatens the environment by the disturbance of the ground strata during the excavation phase, the negative impacts during the construction and the voluminous amount of excavation waste. Since 1 m³ rock blocks is blasted into 1.8 m³ mixed rock fragments [7], the muck overcharging at the dumping sites cannot be ignored. As a countermeasure toward the sustainability, the muck recycling as construction materials has been executed [6]. The muck utilization as concrete aggregates in the recent tunnel projects has been remarkable worldwide: 5 million tons in Gotthard Base tunnel [11]; 2.7 million tons in Löttschberg project [11]; 2.4 million m³ in Lyon-Turin high-speed railway line project with more than

T.-H. Tran (✉)

Faculty of Civil Engineering, University of Transport and Communications, Hanoi, Vietnam
e-mail: tranhuhang@utc.edu.vn

10 tons in Turin-Lyon Base tunnel [9] and 1.27 million tons in Chartreuse tunnel [1]; 6.4 million m³ in the railway tunnel between St. Jean-de-Maurienne (France) and Susa (Italia) [6], etc.

As the sustainable development practice in the civil engineering in Vietnam, the utilization of rock tunnel's muck has been executed in the highway tunnel and hydropower plant projects. However, such works have been kept as the project's internal practice with the limited public publications. Beside the blockages from the recycling technology, equipment, and workmanship, the lack of a promoting legal corridor for the muck utilization is the most challenge. The promulgation of the Vietnamese national standard TCVN 11969:2018 on recycled coarse aggregate for concrete has been recognized as an effort of the government toward the sustainable development in the civil engineering. Under that light, the paper focused on the use of crushed tunnel muck as the coarse aggregate for C25 lining concrete in a NATM highway tunnel project in Vietnam. The mix design was done for a recycled rock lining concrete and an equivalent new rock one. The performance of the two concretes was collated and checked following the current relevant technical requirements. The obtained results shown the suitability of the recycled tunnel muck as an alternative for the lining concrete coarse aggregate beside the raw material.

2 Use of NATM Muck as Crushed Aggregate for Tunnel Lining

The ability of tunnel muck to be recycled as the concrete coarse aggregate depends on the quality of the rock mass in the excavation zone, the excavation solutions, the tunnel parameters, the mucking, and the transport work. Using explosive for rock breaking, the NATM and D&B (Drill and Blast) provides the non-flat blasted fragments with a wide grain of sizes [11]. It has been considered as an advantage of the muck by NATM and D&B against the muck by mechanized technics [1]. The TBM's muck is less competitive due to the elongate shapes (flakes or chips) [6]. Three points to be checked before using recycled aggregates: (a) Rock hardness requirement of the raw material; (b) Petrographic requirements of the raw material; (c) Alkali aggregate reaction and sulphate attack [11]. Some authors required the minimal strength of the recycled aggregate, at least 75 N/mm² for a B40/30 concrete for instance [11] but others did not [1, 3].

Studying the utilization of the NATM muck as crushed aggregate for the tunnel lining concrete, the current Vietnamese technical specifications were checked. However, since no specifications for the lining concrete had been found, the equivalent documents for the normal concrete were taken place. The Vietnamese national standard for aggregates for concrete and mortar (TCVN 7570:2006) and the Vietnamese national standard for recycled coarse aggregate for concrete (TCVN 11969:2018) was consulted. However, when collating them, no clear differences in

the technical requirements and in the required grain size distribution were found. It was understood that there were no special decreases in the requirements of the recycled materials comparing to the raw ones. In the paper, the utilization of recycled coarse aggregate from NATM muck for a 300 mm thickness C25 tunnel lining concrete was studied. The Class 1 aggregate recommended by TCVN 11969:2018 with the maximal nominal grain diameter $D_{\max} = 20$ mm was chosen [12].

2.1 *Manufacture of Crushed Aggregate*

The tunnel excavation zone was formed by the hard-fractured light-weathered granite with the minimal saturated uniaxial compression strength 90 MPa, the minimal Brazilian tension strength 5 MPa, and the wet moisture 0.24%. After the excavation by explosive, the tunnel spoils were mucked. Based on the geological map along the alignment of the tunnel, only the muck excavated from the tunnel segments where the geotechnical conditions were favourable for the aggregate manufacture were collected. It helped to ensure the utilization ability of the muck before entering the recycle aggregate muck manufacture. The selected muck was transported to the manufacture site while the rejected muck was sent to the dump areas of the project. The in situ testing was done for every mucking shift and the technical parameters of the muck were checked following TCVN 7570:2006 and TCVN 11969:2018 (Table 1).

In the study case of the paper, the excavation zone of the tunnel stays in the same rock strata and not far from the location of the exploited rock pit for the project. It was considered as a special advantage that led to the muck utilization's proposal. Arriving at the manufacture site, the selected muck was undergone the recycling process. The details were as follows:

Table 1 Technical parameters of the recycled muck for C25 lining concrete

Parameter	Actual value	Requirement [5, 12]	Unit
Specific gravity	2670	2300	kg/cm ³
Water absorption	0.6	5	%
Crushing in cylinder	9.4	≤ 20	%
Los Angeles abrasion	18.6	≤ 50	%
Organic impurities	Lighter than standard colour	Not darker than standard colour	–

- Step 1: Selection of non-contaminated rock blocks passing through the 40 mm sieve.
- Step 2: Crushing of rock blocks with the aimed $D_{\max} = 20$ mm grain size distribution following two mentioned Vietnamese standards.
- Step 3: Elimination of rock grains passing through the 5 mm sieve.
- Step 4: Injection of water on crushed rock for washing away the mud, dust, clay, and organic impurities.
- Step 5: Checking of the qualified crushed rocks following two mentioned Vietnamese standards.

The final main product of the aggregate manufacture was the conformed $D_{\max} = 20$ mm recycled coarse aggregate and the by-product was the finer rock fragments smaller than 5 mm. The former was used as an alternative coarse aggregate for the lining concrete, and the latter was utilized for the land filling purposes. Although there has been a worry on the mica content in the crushed aggregate because of the bad effect on concrete [2], the relevant regulations are not found in the current Vietnamese standards.

2.2 Mix Design of C25 Lining Concrete

Gomez-Soberon [4] has mentioned about the higher water content in the concrete mixing due to the high water absorption of the recycled aggregate. Besides, an increase of cement (5–20% of the weight) in the concrete mix made with the recycled aggregate due to the 40% greater void of the recycled aggregate has been proposed [11]. Considering that the recycled rock was water injected during the manufacture process, the Gomez-Soberon's concern could be neglected and the normal proportion of water in the mixing was used for the design. The normal water/cement ratio of the conventional lining concrete was kept, so that the amount of cement was not changed. For that end, two C25 lining concrete mixes were prepared: one used the obtained recycled coarse aggregate (hereinafter called as *Recycled rock lining concrete* and abbreviated as RRC), and one used the new rock from the exploited pit of the project (hereinafter called as *New rock lining concrete* and abbreviated as NRC). The proportion of two mixes was shown in Table 2.

Table 2 Mix proportion of two C25 lining concretes (unit: kg/m³ concrete)

Lining concrete	Coarse aggregate	Fine aggregate	Water	Cement	Admixture
RRC	1074	817	168	366	4.37
NRC	1221	742	168	366	4.37

2.3 Performance of C25 Recycled Aggregate Lining Concrete

The concrete compositions were mixed, and the slumps of the fresh concretes were recorded. Two designed lining concretes were checked with the recommendations of RDA and JICA [10] for the 30 MPa at 28 day age lining concrete made by normal Portland cement for the tunnels on the expressways, and the conformed results were found as in Table 3.

Six 15 × 30 cm cylinder specimens were prepared following the Vietnamese national standard TCVN 3105:1993 for each lining concrete. Their 7 and 28 day age compressive strengths in conformation of the Vietnamese national standard TCVN 5726:1993 were determined. The testing data were analysed and the theoretical distribution curves following the normal law were found (see Table 4).

The normal law’s theoretical distribution curves of two lining concretes were not coincided and the compressive strengths of RRC were slightly lower than of NRC (see Fig. 1).

Table 3 Comparison of two designed lining concretes and the recommended values

Parameter	RRC	NRC	Recommended value [10]
D_{max} of coarse aggregate (mm)	20.00	20.00	20.25
Initial slump (cm)	12.5	12.5	15 ± 2.5
Water portion (kg/m^3)	168	168	≤ 175

Table 4 Parameters of theoretical distribution curves of the compressive strengths

Lining concrete	Age	Mean μ	Standard deviation σ	Standard error SE
RRC	7 day	26.81	0.71	0.29
	28 day	31.08	0.85	0.35
NRC	7 day	28.42	0.70	0.29
	28 day	31.28	0.74	0.30



Fig. 1 Frequency and equivalent theoretical distribution curves of the empirical compressive strengths at 7 and 28 days age of two designed lining concretes

However, the RRC's mean value of 28 days compressive strength with 99.7% of chance stayed within the range of [30.04; 32.12] (MPa), which was always higher than the target value of 30 MPa at 28 days. Meanwhile, the equivalent results of NRC were [30.37; 32.19] (MPa). The target value was 1.23 and 1.72 times of the standard deviation for the RRC and the NRC, respectively. It was found to stay in the 95% confidence interval. Hence, two designed lining concretes were concluded as qualified. The augmentation of cement in the RRC mix proportion after Thalmann et al. [11] was a solution for receiving the same compressive strength as NRC.

3 Conclusions

After the Ministry of Construction of Vietnam, about 140 million meter cubic of concrete were used in 2019 in the country, which consisted of 150 million tons of coarse aggregates, approximately [8]. While the recycling of construction materials in Vietnam has been always in the beginning, the fact shown the rapid exhaustion of the non-renewable natural resources. Targeting at replacing 60% of the new concrete aggregate by the recycled ones in the near future is one of the efforts from the government towards the sustainability in the civil engineering [8]. For obtaining the good fruits, many works are waiting, especially the preparation of a suitable legal corridor for the use of recycled construction materials. A clear distinction between the wasted materials and the usable products from the tunnel spoil is recommended by ITA [6]. The paper studied the recycling of the tunnel muck after the NATM tunnelling as the crushed coarse aggregate for the C25 lining concrete. The performance of the recycled rock lining concrete was found to be normal as the one of the equivalent new rock lining concrete. Even 100% of the coarse aggregate in the lining concrete proportion had been replaced by the crushed muck, no negative indications were detected. Hence, the possibility of replacing the raw material by the recycled ones for the tunnel lining concrete was proven. It was considered as a good sign for the propagation of the tunnel muck recycling in the future projects in Vietnam.

References

1. Aarstad K et al (2019) Local use of rock materials—production and utilization. State-of-the-art, Veidekke Entreprenør AS, Norway
2. Fookes P, Revie W (1982) Mica in concrete—a case study from Eastern Nepal. *Concrete (J Concr Soc)* 16(3):12–16
3. Gertsch L, Fjeld A, Nilsen B, Gertsch R (2001) Use of TBM muck as construction material. *Tunn Undergr Space Technol* 15(4):379–402
4. Gomez-Soberon JMV (2002) Porosity of recycled concrete with substitution of recycled concrete aggregate: an experimental study. *Cem Concr Res* 32(8):1301–1311

5. IBST (2006) TCVN 7570:2006 aggregates for concrete and mortar—specifications. Ministry of Science and Technology of Vietnam, Hanoi. (In Vietnamese)
6. ITA working group 14 and 15 (2019) Handling, treatment and disposal of tunnel spoil materials—ITA report No. 21. ITA, Chatelaine
7. Ministry of Construction of Vietnam (2007) Document 1784/BXD-VP dated 16/8/2007: Norms of construction materials. Hanoi. (In Vietnamese)
8. Nguyen Q (2020) Presentation of department of construction material (Ministry of construction of Vietnam) at annual meeting of Vietnam concrete association. VCA, Hanoi. (In Vietnamese)
9. Oggeri C, Fenoglio T, Vinai R (2014) Muck classification: raw material or waste in tunnelling operation. *Revista Minelor—Mining Revue* 20(4):16–25
10. RDA and JICA (2018) Guideline for design of road tunnel. Japan and Sri Lanka technical assistance for Improvement of capacity for planning of road tunnels, Sri Lanka
11. Thalmann C, Schindler C, Kruse M (2003) Aggregates for high quality concrete and shotcrete made out of excavated rock material—experiences gained on the Alptransit tunnel projects. Kelebek and Grafika grup, Istanbul
12. VIBM (2018) TCVN 11969:2018 recycled coarse aggregate for concrete. Ministry of Science and Technology of Vietnam, Hanoi. (In Vietnamese)

Effect of Nano-Silica Content on Compressive Strength and Modulus of Elasticity of High-Performance Concrete



Van Thuc Ngo, Tien Thanh Bui, Thi Cam Nhung Nguyen,
Thi Thu Nga Nguyen, and Thanh Quang Khai Lam

Abstract The nano-silica (NS) particles trigger hydration reactions reduce the less stable components (Calcium hydroxide), and produce better quality pozzolan gel products in concrete. This process gives the concrete have a dense structure, early strength growth, increase compressive strength, flexural strength, splitting strength, water anti-permeability, and corrosion resistance. This article aims to research the influence of NS on compressive strength and modulus of elasticity of high-performance concrete. Nano-silica particles are added into high-performance concrete mixture with the contents 0.5, 1, 1.5, 2, 2.5 and 3% by weight of the binder. The addition of NS resulted in enhancing compressive strength and modulus of elasticity up to 1.5% replacement level. When the NS content is 2–3%, the compressive strength and modulus of elasticity increases nonsignificantly and tends to decrease compared to NS's rate using 1.5%. The experiment results will build a relationship function between the modulus of elasticity and nano-silica content.

Keywords Modulus of elasticity · Compressive strength · Nano-silica · High-performance concrete

1 Introduction

Among mineral additives added to concrete, nano-silica (NS) has many prospects to be used popularly in the future. There are many studies effects of NS on properties of HPC have been presented in recent years. The effects of the fill-in voids, lower free-water, pozzolanic more Calcium–Silicate–Hydrate (C–S–H) gel, and consume

V. T. Ngo (✉) · T. Q. K. Lam
Mien Tay Construction University, Vinh Long, Vietnam
e-mail: nvthuc34@gmail.com

T. T. Bui · T. C. N. Nguyen
Faculty of Civil Engineering, University of Transport and Communications, Hanoi, Vietnam

T. T. N. Nguyen
University of Transport Technology, Hanoi, Vietnam

$\text{Ca}(\text{OH})_2$ have been clearly stated in the researches with many experimental data [1–4]. NS not only strongly activates the hydrate reactions to form quality C–S–H gels but also fills the pores with ultra-fine dimensions leading to increased strength and durability of concrete. The interface transition zone of mortar and aggregate was improved when incorporating NS in the cement matrix.

Using NS materials can improve the modulus of elasticity of concrete [1]. The reason may be that its pore and interface transition zone was enhanced. In general, pores, microscopic cracks, and the tendency to crystallize calcium hydroxide are relatively more common in the transition zone than cement mortar, so they are essential to the relationship between stress and deformation in concrete. The interface transition zone is cited as the main reason for the elastic modulus of concrete in the middle of the elastic modulus of the aggregate and cement matrix.

The research assesses the effect of NS on HPC's compressive strength and modulus of elasticity. NS content is considered as the binder which added to the concrete at the rates of 0, 0.5, 1, 1.5, 2, 2.5 and 3% by weight of binder.

2 Materials

The portland cement (PC) was used in the experiment with a specific gravity of 3.1 g/cm^3 , the average particle size of $18 \text{ }\mu\text{m}$, the chemical composition shown in Table 1. The coarse aggregate (CA) is basalt stone with D_{max} of 12.5 mm and density of 2.74 g/cm^3 . Sand with the fineness modulus of 2.73 and density of 2.66 g/cm^3 is the fine aggregate (FA). Nano-silica is utilized with average particle size of 13 nm, and the chemical composition is shown in Table 1.

The Scanning Electron Microscope (SEM) and X-Ray Diffraction (XRD) experiments were carried out to check NS particles. Observing that the peak width increased from 16° to 30° showed that the compounds were in nano form and 100% amorphous state from the XRD test results (see Fig. 1).

3 Mix Proportion

HPC using NS is calculated and designed based on the ACI method. These studies show that the range of NS ratios in concrete is about 0–3%. The material composition calculation results of HPC using NS are shown in Table 2.

Table 1 Chemical composition of cement and nano-silica (%)

Materials	SiO_2	Al_2O_3	Fe_2O_3	TiO_2	CaO	SO_3	MgO	Na_2O	K_2O
Cement	21.65	5.25	3.42	–	65.0	1.8	0.06	0.25	0.72
Nano silica	<99.8	<0.03	<0.003	<0.03	–	–	–	–	–

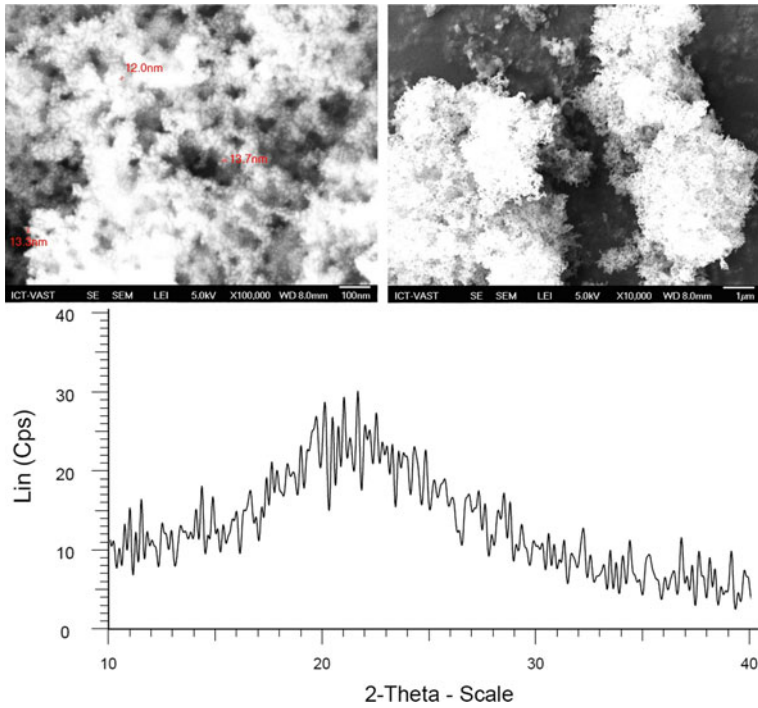


Fig. 1 Results of SEM and XRD scanning of nano-silica

Table 2 The material composition of HPC using NS

Mix code	Material compositions (kg/m ³)							
	PC	FA	CA	SF	NS	SP (l)	W	W/B
NS0.0	544.2	674.6	1049	28.6	0.00	5.44	154.6	0.27
NS0.5	541.3	673.6	1049	28.6	2.86	6.53	154.6	0.27
NS1.0	538.4	672.6	1049	28.6	5.73	7.35	154.6	0.27
NS1.5	535.6	671.6	1049	28.6	8.59	7.62	154.6	0.27
NS2.0	532.7	670.6	1049	28.6	11.46	8.71	154.6	0.27
NS2.5	529.8	669.6	1049	28.6	14.32	9.25	154.6	0.27
NS3.0	527.0	668.6	1049	28.6	17.19	9.80	154.6	0.27

4 Preparing for the Samples

The materials for a mixing batch was prepared as Fig. 2. The mixing procedure is proposed based on references to previous research and experience from mixing tests.



Fig. 2 Preparing the materials and curing process for the samples

5 Experimental Methods

The samples were tested for compressive strength by age (3 days, 7 days, 28 days, and 56 days) after curing. The compressive strength was tested base on ASTM C39 standard.

The modulus of elasticity of HPC using NS was tested according to ASTM C469. The cylinder has a diameter of 150 mm and a height of 300 mm. Each mix is prepared with six samples to serve the experiment.

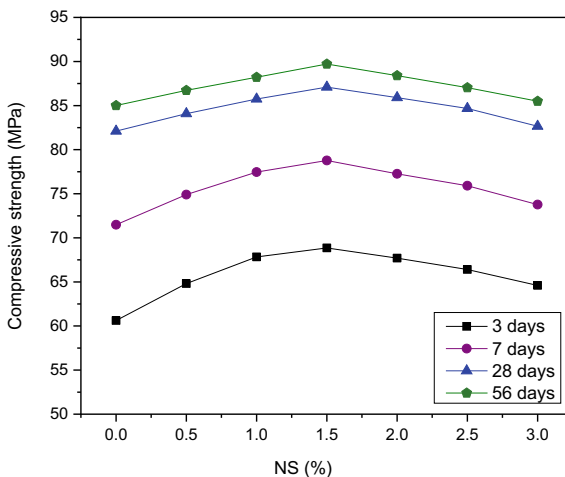
6 Results and Discussions

6.1 Compressive Strength

The compressive strength test results of HPC using NS are shown in Fig. 3.

Observing the effects of the NS ratio on compressive strength in Fig. 3, it can appear that for various age groups, the compressive strength increases when the rate of NS used is less than or equal to 1.5%. As the NS ratio increases from 2 to 3%, the

Fig. 3 Compressive strength of HPC using NS



compressive strength increases marginally and has tended to decrease compared to NS's ratio using 1.5. The cause can be mentioned as the uneven distribution of NS particles when the utilization rate exceeds the 1.5% threshold. Similarly, this phenomenon occurs in the studies of Chithra et al. [2], Khaloo [4].

On the other hand, the compressive strength of HPC at the period of 3 and 7 days of age is affected by NS more significant than the period of 28 and 56 days. Corresponding to 3 and 7 days of age, HPC's compressive strength using 1.5% NS improved by 13.58 and 10.18% relative to the 0% NS. For the period of 28 and 56 days, the rise was 6.09 and 5.53%. This result showed that it is possible to use NS in HPC.

6.2 Modulus of Elasticity

The results of the modulus of elasticity of HPC using NS are shown in the diagram in Fig. 4. The results show that when the NS ratio is less than or equal to 1.5%, the HPC modulus of elasticity increases steadily.

The correlation of modulus of elasticity and NS ratio to HPC is constructed by experimental results such as Eq. (1). The graph of the relationship between the modulus of elasticity and NS content is shown in Fig. 5.

$$E_{ns} = -1554NS^2 + 5233.9NS + 45476 \quad (1)$$

Fig. 4 Effect of NS on the modulus of elasticity of HPC

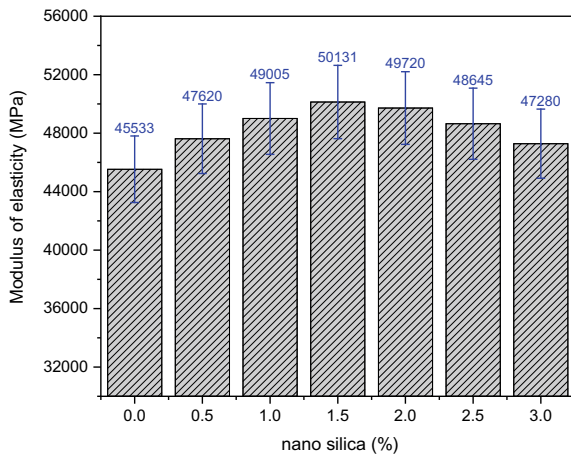
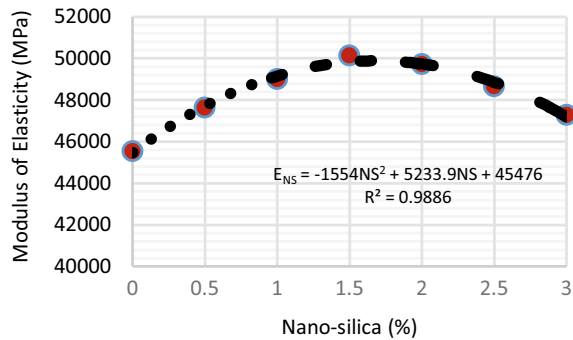


Fig. 5 Relationship between the ratio of NS and modulus of elasticity



7 Conclusions

Based on results of this study, some conclusions could be drawn as follows:

- The use of NS in the composition of HPC resulted in improved compressive strength at all periods of age. HPC's compressive strength during 3 and 7 days of age is higher than the period of 28 and 56 days when NS is affected. The combination of NS in the concrete composition improves the strength at early age due to its high hydration and pozzolanic activity.
- The modulus of elasticity of HPC was cured for up to 28 days also was improved when incorporating NS in the cement matrix. The increase is mainly due to improving the performance of the interface transition zone and increasing the density of C–S–H gel products.
- In the samples with 1.5% NS, the result obtained the optimum compressive strength and modulus elasticity. In addition, when the amount of NS exceeds 1.5%, the compressive strength, and modulus of elasticity decrease. The explanation is that in the HPC mixture, the amount of NS is higher than the amount of released lime that leading to the concentration of NS particles forming weak regions.

Acknowledgements This work was funded by Vingroup Joint Stock Company and supported by the Domestic Master/PhD Scholarship Programme of Vingroup Innovation Foundation (VINIF), Vingroup Big Data Institute (VINBIGDATA).

References

1. Sanchez F, Sobolev K (2010) Nanotechnology in concrete: a review. *Constr Build Mater* 24 (11):2060–2071
2. Chithra S, Kumar R, Chinnaraju K (2016) The effect of colloidal nano-silica on workability, mechanical and durability properties of high performance concrete with copper slag as partial fine aggregate. *Constr Build Mater* 113:794–804

3. Ngo T, Lam K, Do D, Nguyen C (2020) Increased plasticity of nano concrete with steel fibers. Magazine Civ Eng 93(1):27–34
4. Khaloo A, Mobini H, Hosseini P (2016) Influence of different types of nano-SiO₂ particles on properties of high-performance concrete. Constr Build Mater 113:188–201

Experimental Investigation of Fatigue Behavior for Polymer Modified Asphalt and Epoxy Asphalt Mixtures



Quang Tuan Nguyen and Thi Cam Ha Tran

Abstract Fatigue cracking is one of the main failures of the pavement structures. This paper presents the experimental investigation of the fatigue behavior for polymer modified asphalt and epoxy asphalt mixtures. One polymer modified asphalt mixture and epoxy asphalt mixtures at two different epoxy content in the binder are used in this study. The four point bending fatigue tests are conducted in strain-controlled mode at 10°C and 10 Hz. For each type of mixture, three levels of strain amplitude are applied in the test: 200, 300 and 400 $\mu\text{m/m}$. The test results allow determining the Wöhler curve for each tested mixture. The experimental results show a better fatigue resistance of epoxy asphalt mixtures in comparison with polymer modified asphalt mixture. The slope of the Wöhler curve is then obtained to evaluate the fatigue sensibility of each mixture. The nonlinearity phenomenon is also observed when analyzing the complex modulus and the phase angle at the beginning of the test.

Keywords Fatigue · Asphalt mixture · Wöhler curve · Epoxy asphalt · Polymer modified asphalt mixture · Four point bending test

1 Introduction

Fatigue phenomenon of asphalt mixtures is characterized by the decrease in complex modulus when the cyclic loadings are applied on the tested specimen. Three disparate phases can be considered when analyzing a fatigue test [1]. Phase I (or adaptation phase) is described by a rapid decrease in stiffness due to artifact effects (soft-heating, thixotropy...) [2]. While during phase II (or quasi-stationary phase), the role of cyclic effect (fatigue) is the most important [3]. The micro-cracks that appear during phase I and II propagate, form the macro-cracks and cause deterior-

Q. T. Nguyen (✉) · T. C. H. Tran
Faculty of Civil Engineering, University of Transport and Communications, Hanoi, Vietnam
e-mail: quangtuan.nguyen@utc.edu.vn

ration of the material in the phase III (failure phase). Fatigue is considered as one of most important failure of road pavement.

The fatigue test on asphalt mixtures can be performed on many different types of specimen shapes: cylindrical specimens, rectangular beams and trapezoidal beams. As the result of the test, the fatigue resistance is used as one of main criteria in the pavement design. In Vietnam, the four-point bending fatigue test is usually used. However, the four-point bending fatigue equipment is available in only a very few of research center. Some recent studies have been performed to investigate the fatigue life of classical asphalt mixtures in Vietnam [4, 5]. In this study, the four point bending fatigue tests were performed on high performance asphalt mixtures: one polymer asphalt mixture and two epoxy asphalt mixtures at two different epoxy contents. Some results of fatigue resistance, fatigue sensibility and nonlinearity phenomenon of these tested materials are presented and analyzed in this paper.

2 Materials and Four-Point Bending Fatigue Test

Three types of asphalt mixtures are used in this study: asphalt mixture prepared with polymer modified bitumen (called PMB), two asphalt mixtures prepared with epoxy asphalt where the proportions of epoxy/original 60–70 pen bitumen by weight are respectively 35/65 (called EA35) and 50/50 (called EA50). All three types of asphalt mixtures are designed with the same type and gradation of aggregate (Fig. 1a). The air void content of PMB, EA35 and EA50 mixture are respectively 4.8, 4.4 and 5.0%. The binder content of PMB, EA35 and EA50 are 5.2, 6 and 6% respectively.

The fatigue behavior of tested materials was studied using the four point bending test (Fig. 1b). The specimens of $380 \times 50 \times 50$ mm were cut from asphalt mixture slab of $400 \times 380 \times 50$ mm. The specimen is placed in the thermal chamber for at

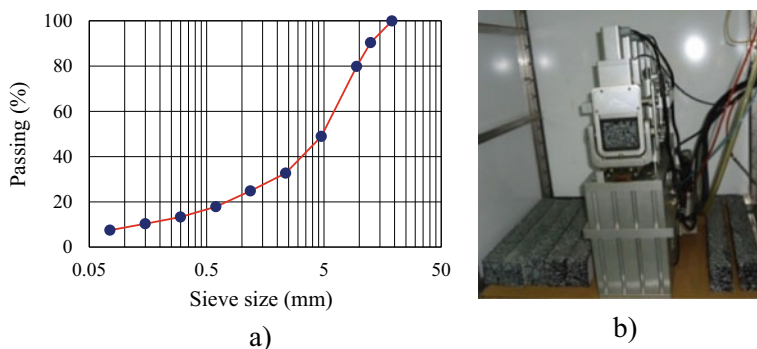


Fig. 1 a Aggregate grading curve of PMB, EA35 and EA50 mixture, b Four point bending fatigue test

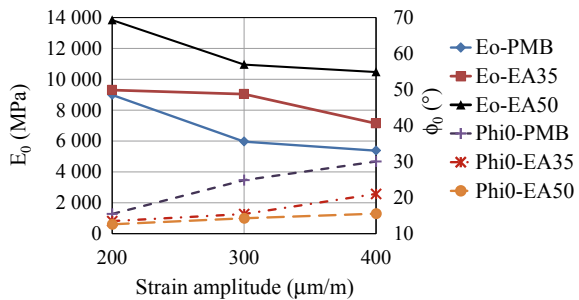
least 6 h before the fatigue test. All fatigue tests were performed in strain-controlled mode at the temperature of 10 °C and at the frequency of 10 Hz. Three levels of strain amplitude were used: 200, 300 and 400 $\mu\text{m/m}$. The norm of complex modulus ($|E^*|$) and the phase angle (ϕ) were collected during the fatigue test as a function of the number of loading cycles (N). The initial complex modulus (E_0) and phase angle (ϕ_0) of material at the beginning of the fatigue test were determined at the 100th cycle where the effect of loading, nonlinearity, heating... can be considered as negligible [2, 6, 7].

3 Test Results and Analysis

3.1 Nonlinearity Phenomenon

In this section, the nonlinearity phenomenon is analyzed. The nonlinearity is considered as the change in the complex modulus (both norm and phase angle) of material when the applied strain level increases or decreases. In order to analyze the nonlinearity phenomenon, the initial complex modulus (E_0) and phase angle (ϕ_0) of PMB, EA35 and EA50 mixture at the beginning of the fatigue test were presented as a function of strain amplitude in Fig. 2. The E_0 decreases and the ϕ_0 increases with the increase of the strain amplitude. A decrease of 23–40% in complex modulus and an increase of 3°–14° in phase angle were observed when the strain amplitude varied from 200 to 400 $\mu\text{m/m}$. This result indicated that the nonlinearity phenomenon has an important effect on the change of the complex modulus and should be carefully considered in the analysis. The linear viscoelastic domain of asphalt mixture is generally admitted smaller than 100 $\mu\text{m/m}$ where the chute of modulus is not exceeded 5% [8]. Thus, the behavior of tested asphalt mixtures cannot be considered as linear viscoelastic. The nonlinearity of PMB mixture was shown to be more important than one of EA35 and EA50 mixture. It can be observed that the initial complex modulus increases, and the initial phase angle decreases in the order: PMB, followed by EA35 and finally EA50. This obtained result showed that at 10°C and 10 Hz, the EA mixture is more rigid and elastic than the PMB mixture.

Fig. 2 Norm of complex modulus (E_0) and phase angle (ϕ_0) of PMB, EA35 and EA50 mixture as a function of the strain amplitude



3.2 Decrease in Complex Modulus During Fatigue Test

The decrease in complex modulus during fatigue tests was presented in Fig. 3. All fatigue tests were conducted until the complex modulus reaches 50% of the initial stiffness or the specimen was broken. It is shown that the chute of complex modulus at the beginning of the test (phase I) is more rapid than phase II. The three phase of fatigue test can be clearly observed for EA35 mixture at 200 $\mu\text{m/m}$ (Fig. 3a). While for other tests, up to 50% decrease of the initial complex modulus, the phase III is not clearly seen yet. The fatigue life is defined as the number of cycles where the 50% decrease in complex modulus is achieved or the specimen is at failure. The fatigue life is denoted as N_f . The fatigue life of all tested mixtures was summarized in Table 1. The result shows that the fatigue resistance of EA mixture is greater than PMB mixture. And the higher content of epoxy (from 35 to 50% in the binder) enhances the fatigue resistance of mixture. Combined with the results obtained in Sect. 3.1, both complex modulus and fatigue resistance were shown to be increased by using the epoxy asphalt.

The parameter $E_0 \times \sin(\phi_0)$ is generally considered as an indicator of fatigue resistance of asphalt mixtures [9]. The verification of relationship between $E_0 \times \sin(\phi_0)$ and fatigue resistance of tested asphalt mixtures was illustrated in Fig. 4. In order to compare the N_f at different levels of strain amplitude, the fatigue life N_f at each level of strain amplitude is normalized by N_f of PMB mixture, denoted as $N_f/N_{f(PMB)}$. The values of $N_f/N_{f(PMB)}$ as function of $E_0 \times \sin(\phi_0)$ were presented in Fig. 4. It can be seen that the parameter $E_0 \times \sin(\phi_0)$ can be used to evaluate the

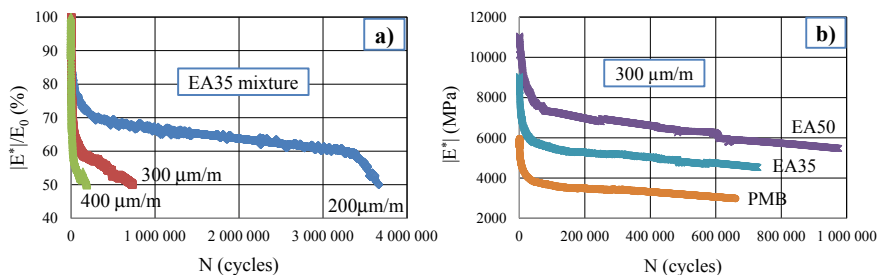
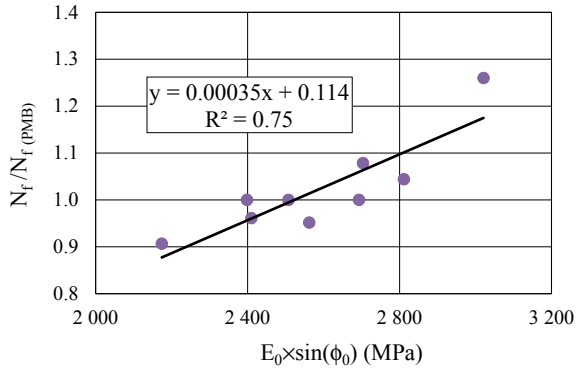


Fig. 3 Complex modulus as a function of number of cycle: **a** EA35 mixture, **b** all mixtures at 300 $\mu\text{m/m}$

Table 1 Fatigue life N_f of tested asphalt mixtures

Types of mixture	N_f at 200 $\mu\text{m/m}$ (cycles)	N_f at 300 $\mu\text{m/m}$ (cycles)	N_f at 400 $\mu\text{m/m}$ (cycles)
PMB	3,229,500	660,500	267,500
EA35	3,669,000	728,500	189,500
EA50	8,115,500	975,500	638,500

Fig. 4 Relationship between $E_0 \times \sin(\phi_0)$ and the fatigue resistance of asphalt mixtures



fatigue resistance of tested asphalt mixtures. The value of $N_f/N_{f(PMB)}$ increases with the increase of the parameter $E_0 \times \sin(\phi_0)$.

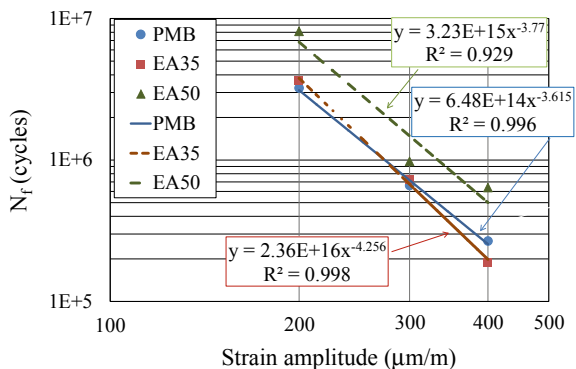
3.3 Wöhler Curves

Based on the fatigue life N_f obtained from previous section, the Wöhler curves of tested asphalt mixtures were presented in Fig. 5. The Wöhler curves illustrate the fatigue life N_f as a function of the strain amplitude ϵ in logarithmic axis. Equation (1) characterizes this relationship where A and B are two constants obtained from the fatigue test results.

$$N_f = A \times (\epsilon)^{-B} \tag{1}$$

The values of B for PMB, EA35 and EA50 are respectively 3.615, 4.256 and 3.77. These B values are in accordance with the values postulated for asphalt mixtures [1]. The results show a better fatigue resistance of EA50 mixture in comparison with two other mixtures. A small difference in N_f between EA35 and PMB mixture can be observed. At 200 and 300 $\mu\text{m/m}$, the EA35 mixture show higher N_f than PMB mixture while at 400 $\mu\text{m/m}$ the result is versa.

Fig. 5 Wöhler curves of tested asphalt mixtures



4 Conclusions

This paper presents the experimental investigation into the fatigue behavior of three types of asphalt mixture, including PMB, EA35 and EA50 mixtures using the four point bending tests. From the test results, some following conclusions were drawn.

- The initial complex modulus (E_0) and phase angle (ϕ_0), determined at the beginning of each fatigue test, change with the level of the strain amplitude. The nonlinearity phenomenon is clearly observed.
- The fatigue life of each asphalt mixture was determined at three levels of strain amplitude. The Wöhler curve for each tested mixture was obtained.
- The epoxy asphalt is shown to enhance the stiffness and fatigue resistance of asphalt mixture.
- The parameter $E_0 \times \sin(\phi_0)$ can be used to evaluate the fatigue resistance of tested asphalt mixtures.

References

1. Di Benedetto H, de La Roche C, Baaj H et al (2004) Fatigue of bituminous mixtures. *Mat Struct* 37:202–216. <https://doi.org/10.1007/BF02481620>
2. Di Benedetto H, Nguyen QT, Sauzéat C (2011) Nonlinearity, heating, fatigue and thixotropy during cyclic loading of asphalt mixtures. *Road Mater Pavement Des* 12(1):129–158
3. Nguyen QT, Di Benedetto H, Sauzéat C (2015) Effect of fatigue cyclic loading on linear viscoelastic properties of bituminous mixtures. *J Mater Civ Eng* 27(8). [https://doi.org/10.1061/\(ASCE\)MT.1943-5533.0000996](https://doi.org/10.1061/(ASCE)MT.1943-5533.0000996)
4. Tran TL, La VC, Nguyen XD (2015) Nghiên cứu thực nghiệm độ bền mỏi bê tông asphalt làm lớp mặt đường tại Việt Nam. *Tạp chí Giao thông Vận tải* 4. (In Vietnamese)
5. Vu PT, Bui XC, Nguyen QT (2014) Phân tích các thông số trong kết quả thí nghiệm uốn mỏi bốn điểm đối với vật liệu bê tông nhựa. *Tạp chí Cầu đường Việt Nam* 9:17–20. (In Vietnamese)
6. Nguyen QT, Nguyen ML, Di Benedetto H, Sauzéat C, Chailleux E, Hoang TTN (2019) Nonlinearity of bituminous materials for small amplitude cyclic loadings. *Road Mater Pavement Des* 20(7):1571–1585
7. Nguyen QT, Di Benedetto H, Sauzéat C, Nguyen ML, Hoang TTN (2017) 3D complex modulus tests on bituminous mixture with sinusoidal loadings in tension and/or compression. *Mater Struct* 50(1)
8. Perraton D, Di Benedetto H, Sauzéat C, Hofko B, Graziani A, Nguyen QT, Pouget S, Lily Poulidakos D, Tapsoba N, Grenfell J (2016) 3Dim experimental investigation of linear viscoelastic properties of bituminous mixtures. *Mater Struct* 49(11):4813–4829
9. Anderson D, Hir Y, Marasteanu M, Planche JP, Martin D, Gauthier G (2001) Evaluation of fatigue criteria for asphalt binders. *Trans Res Rec J Trans Res Board* 1766:48–56

Effect of Steel Fiber Content on the Shrinkage of Steel Fiber Reinforced Concrete in the Tropical Environment in Vietnam



Ngoc Tan Nguyen and Vinh An Le

Abstract Concrete shrinkage is one of the main causes of cracks occurred in reinforced concrete structures in the hot tropical environment. In this study, a series of test specimens was made of plain concrete and steel fiber reinforced concrete of strength grade C45 and with various contents of Dramix fibers ranging from 25 to 100 kg/m³. The shrinkage measurements were carried out on these specimens for more than 120 days. The experimental results show the total shrinkage of concretes tested and the effect of steel fiber content on the shrinkage.

Keywords Steel fiber reinforced concrete · Steel fiber content · Dramix fiber · Total shrinkage · Hot tropical environment

1 Introduction

Shrinkage of concrete is a phenomenon that reduces the volume of the material when it hardens in the air. The shrinkage depends mainly on three factors: (i) composition of concrete, (ii) the environmental conditions (e.g. temperature, humidity), and (iii) shape of the structure with regard to the ratio between volume and surface area [1, 2]. In fact, shrinkage of concrete happens early, and it is one of the reasons causing early cracks in the existing structures.

In the world, studies have been carried out to determine the factors affecting shrinkage of concrete and provide prediction models of shrinkage by time. In the 1950s, the studies concluded that shrinkage of concrete is directly proportional to the cement content and autogenous shrinkage of the cement mortar surrounding the aggregates [3, 4]. Water-cement ratio (w/c) is one of the factors affecting shrinkage of concrete [5, 6]. Meanwhile, other studies have shown that there is an unclear

N. T. Nguyen
National University of Civil Engineering, Hanoi, Vietnam

V. A. Le (✉)
Faculty of Civil Engineering, University of Transport and Communications, Hanoi, Vietnam
e-mail: levinhan@utc.edu.vn

relationship between w/c ratio and shrinkage of concrete [7, 8]. However, most studies agree that the increase of water or cement content leads to an increase in the shrinkage of the concrete. In addition, the coarse and fine aggregates and their properties significantly affect the shrinkage. With a constant mortar volume, increased aggregate reduces shrinkage. Aggregates with high elastic modulus also reduce concrete shrinkage [3, 8].

Environmental conditions as well as the curing method are the second group of factors directly related to shrinkage of concrete. In particular, the temperature and humidity of the air are two commonly mentioned factors in many scientific papers on shrinkage of concrete. Under the same conditions of humidity, temperature has little effect on shrinkage while moisture affects significantly on shrinkage of concrete. When concrete is maintained in an environment with a relative humidity of 65%, the drying shrinkage has a greater value than that of concrete stored in an environment where the relative humidity varies periodically from 40 to 90% [9]. For saturated concrete, volumetric expansion occurs albeit less prominent than shrinkage, thus shrinkage is generally reduced but still presents.

In Vietnam, due to the tropical climate, many existing structures after being completed, immediately cracked due to shrinkage of concrete. According to the design standard [10], the total shrinkage of the concrete can be identified through stress loss due to shrinkage, calculated values ranging from 266.7 to 400 microstrain. Recently, experimental studies for measuring the shrinkage of ordinary concrete on standard specimens in the laboratory have presented higher values from 1.2 to 2.1 times compared to the calculated values [11]. Currently, steel fiber reinforced concrete (SFRC) has been used in existing structures because of its advantages. Research works on shrinkage of SFRC in the tropical environmental conditions of is still limited, there are not many experimental data.

Therefore, in this study 12 prism specimens with the dimensions of $70 \times 70 \times 350$ mm were divided into four sample groups, which were built by plain concrete and SFRC with the steel fiber content ranging between 25, 75 and 100 kg/m^3 , respectively. The specimens were maintained in standard climatic conditions and determined to total shrinkage of concretes during 120 days. The experimental results allow the quantification of total shrinkage of SFRC, as well as the analysis of the effect of steel fiber content used on shrinkage.

2 Experimental Programs

2.1 Materials

Steel fiber reinforced concrete is a combination of a mixture of plain concrete and steel fibers evenly distributed in the concrete material as illustrated in Fig. 1. Table 1 presents the compositions of plain concrete used.

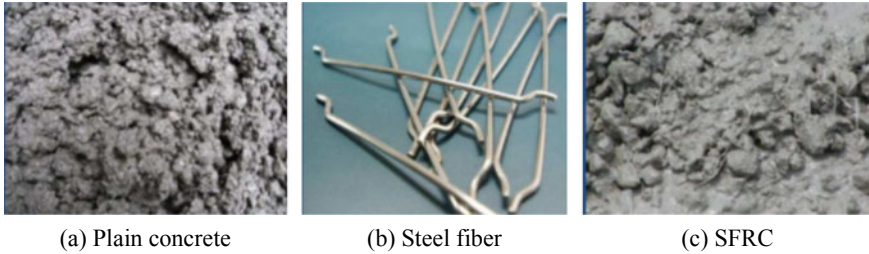


Fig. 1 Compositions of steel fiber reinforced concrete (SFRC)

Table 1 Plain concrete mix of 1 m³ volume

Cement PCB40 (kg)	Fly ash (kg)	Fine aggregates (kg)	Coarse aggregates (kg)	Water (liter)	Superplasticizer (liter)
480	85	760	965	147	5

In this study, the tested specimens were made of steel fiber reinforced concrete with different steel fiber contents ranging from 0, 25, 75 and 100 kg/m³. The steel fiber used is Dramix fiber denoted 3D 65/35 BG manufactured by Bekaert Company which is made of stainless steel, with a nominal diameter of $d = 0.55$ mm, length of $l = 35$ mm and tensile strength of 1100 MPa. The ratio between length and diameter is equal to 65 that is used to accommodate cement concrete. The steel fiber is bent at the ends as shown in Fig. 1b to enhance the bonding between the steel fiber and the concrete.

2.2 Testing Specimens

Shrinkage test specimen of plain concrete and SFRC is a prismatic specimen with the dimensions of 70 × 70 × 350 mm. On each test specimen, four stainless steel pins were mounted on opposite sides along the long side of the specimen. On one side, the distance between the two pins is fixed as 280 mm corresponding to four times of specimen width as shown in Fig. 2a. For each steel fiber content, a sample group consisting of three test specimens were fabricated in the same batch and cured under the identical environmental conditions. Specimens were kept moist for the first day, demolded and continued to be embedded in water for the next two days. From day 3, the test samples were taken out from the water, dried with a damp cloth, cured in a standard climatic chamber, controlled at 27 ± 2 °C and humidity $80 \pm 5\%$ (Fig. 2b), and perform the measurements of the total shrinkage.

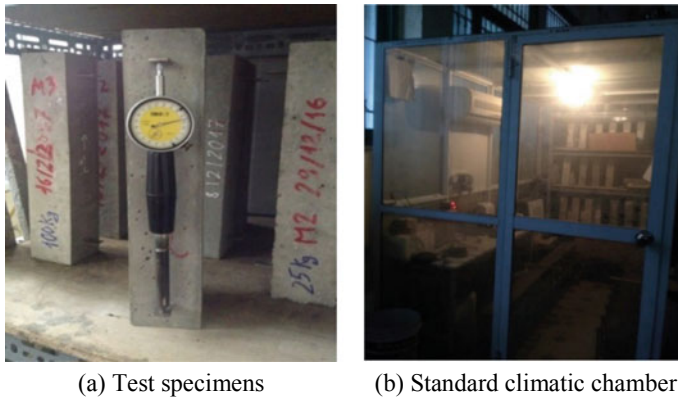


Fig. 2 Test specimens maintained in a standard climatic chamber

For each batch, three cubes with the dimensions of $150 \times 150 \times 150$ mm were also fabricated to determine the compressive strength of concrete at 28 days. The results of compression tests are synthesized in Table 2 for plain concrete named PC and steel fiber reinforced concrete with 25, 75 and 100 kg/m^3 Dramix fibers named SFRC25, SFRC75 and SFRC100, respectively. The results show that the average values of compressive strength range from 53.0 to 64.1 MPa. The average compressive strength of all test specimens is equal to 56.8 MPa corresponding to the strength grade C45. Moreover, the effect of steel fiber content on compressive strength of concretes is negligible.

2.3 Shrinkage Measurements

The measurements were carried out on the test specimens according to Vietnamese standard TCVN 3117: 1993 [12] to determine total shrinkage of plain concrete and steel fiber reinforced concrete over time. The first measurement was performed

Table 2 Compressive strength of concretes at 28 days

Cubic specimen	Compressive strength (MPa)			
	PC	SFRC25	SFRC75	SFRC100
Specimen 1	52.5	56.5	60.6	54.2
Specimen 2	50.4	66.5	53.5	53.1
Specimen 3	63.8	69.2	51.9	51.5
Average value (m)	55.6	64.1	55.3	53.0
Standard deviation (sd)	7.2	6.7	4.6	1.4

immediately after placing the specimen in a standard climatic chamber. Subsequent measurements were performed after 1, 3, 7, 14 days, respectively and then every two weeks until 120 days of age of the concrete.

To measure the shrinkage of concrete, a measuring device with an amplification of 1000 and an accuracy of 0.001 mm was used as shown in Fig. 2a. Total shrinkage of the concrete is determined on the gauge length of 280 mm corresponding to the distance between two fixed pins. For each test specimen, two measurements were carried out on two opposite sides to determine the average value of shrinkage. Measurements were performed sequentially on all test specimens of each sample group. Total shrinkage of each concrete tested is the average value of a sample group.

3 Experimental Results

The obtained experimental data are used to calculate the total shrinkage over time of plain concrete and steel fiber reinforced concrete with various fiber content. For plain concrete (PC), the total shrinkage after 120 days had an average value of 385×10^{-6} mm/mm. For steel fiber reinforced concrete with various steel fiber contents of 25, 75 and 100 kg/m³ (SFRC25, SFRC75 and SFRC100), the total shrinkage is equal to 333×10^{-6} , 265×10^{-6} , 244×10^{-6} mm/mm on average, respectively. These results show that the shrinkage of plain concrete is higher than that of steel fiber reinforced concrete. In addition, the shrinkage of SFRC reduced with increasing the steel fiber content in the concrete mixture.

Figure 3 shows the evolution of total shrinkage of tested concretes over time after 120 days. For all cases, the shrinkage increases rapidly from the initial measurement to the 14th day. During this time, when the steel fiber content increases, the shrinkage of the concrete decreases. As the results, total shrinkage of steel fiber reinforced concrete can be dropped to more than half value, from 245×10^{-6} mm/mm in plain concrete to 120×10^{-6} mm/mm in SFRC100.

From 14 to 28 days of measurements, the shrinkage continues to increase at a fast rate on plain concrete and concrete with a small steel fiber content (e.g. SFRC25), and at a slower rate on concrete with a higher steel fiber content (e.g. SFRC75, SFRC100). After 28 days, shrinkage tends to increase slightly on the tested specimens of concretes used. The total shrinkage of SFRC specimens with high steel fiber content tends to a stabilization with a slower rate for the measurements after 40 days. For all tested SFRC specimens, the total shrinkage changes negligible for the measurements after 90 days. Thus, it can be seen that the steel fiber content in material plays a significant role in limiting shrinkage during the hardening concrete stage and developing strength.

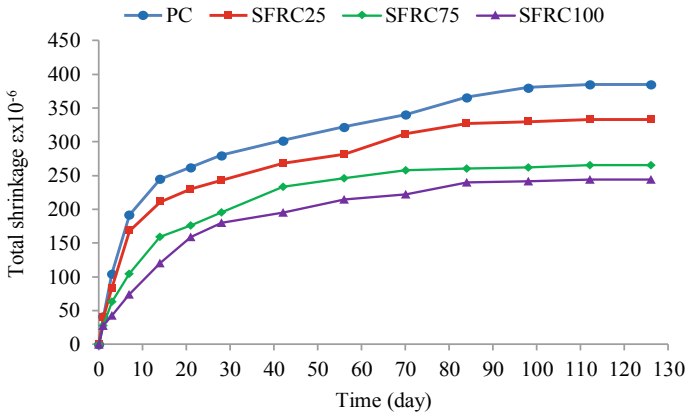


Fig. 3 Total shrinkage of plain concrete and steel fiber reinforced concrete over time

4 Conclusions

This study was carried out to determine total shrinkages of plain concrete and steel fiber reinforced concrete with various contents of Dramix fibers. The experimental results obtained allow some conclusions can be draw as follows:

- The steel fiber content plays a significant role in limiting shrinkage of high strength concrete during the hardening and strength development stage. The total shrinkage of plain concrete having strength grade C45 is equal to 385 microstrain, meanwhile that of SFRC decreases from 333 to 244 microstrain when increasing the steel fiber content between 25 and 100 kg/m³.
- For plain concrete and SFRC with a small steel fiber content (e.g. SFRC25), the shrinkage continues to increase at a fast rate over the period from the 14th day to the 28th day of measurements.
- For SFRC with a high steel fiber content (e.g. SFRC75, SFRC100), the shrinkage continues to increase at a slower rate from the 14th day of measurements, then tends to stabilize with a slower rate after 40 days. Thus, the shrinkage measurements can be ended shortly after 90 days for SFRC instead of 120 days that is usually recommended for ordinary concrete.

Acknowledgements This research is funded by the Ministry of Education and Training, Vietnam under grant number CT.2019.03.01.

References

1. ACI 224R-01 (2001) Control of cracking in concrete structures. American Concrete Institute
2. ACI 209.1R-05 (2005) Report on factors affecting shrinkage and creep of hardened concrete. American Concrete Institute
3. Pickett G (1956) Effect of aggregate on shrinkage of concrete and hypothesis concerning shrinkage. *ACI Proc* 52:581–590
4. Lyse I (1959) Shrinkage and creep of concrete. *Magazine of Concrete Research* 11(33): 143–150
5. Blanks RF, Vidal EN, Price WH, Russell FM (1940) The properties of concrete mixtures. *ACI Proc* 36:433–476
6. Smadi MM, Slate FO, Nilson AH (1987) Shrinkage and creep of high-, medium-, and low-strength concretes, including overloads. *ACI Mater J* 84(3):224–234
7. Haranki B (2009) Strength, modulus of elasticity, creep and shrinkage of concrete used in Florida. Master Thesis, The University of Florida
8. Deshpande S, Darwin D, Browning J (2007) Evaluating free shrinkage of concrete for control of cracking in bridge deck. *Structural Engineering and Engineering Materials SM report no 89*
9. Muller H, Pristl M (1993) Creep and shrinkage of concrete at variable ambient conditions. *Proceedings of the 5th international RILEM symposium on creep and shrinkage of concrete*, pp 859–872
10. Vietnamese standard TCVN 5574:2018. Design of concrete and reinforced concrete structures. (In Vietnamese)
11. Nguyen NB (2017) Study on the shrinkage of concrete in the standardized climatic conditions in Vietnam. PhD Thesis, National University of Civil Engineering, Hanoi
12. Vietnamese standard TCVN 3117:1993. Heavyweight concrete—method for determination of shrinkage. (In Vietnamese)

Research on Using Polymer Concrete for Portland Cement Concrete Airfield Pavement Repair—An Experimental Application of Noi Bai International Airport of Vietnam



Pham Huy Khang and Nguyen Trong Hiep

Abstract After long and effective exploitation time, the portland cement concrete (PCC) pavement, or rigid pavement area of Noi Bai International Airport (NIA) has been deteriorated, leading to the appearance of pavement distresses. Consequently, the maintenance activities have been intensively conducted for ensuring the safety and smooth conditions for airplane movements on airfield system. However, under the high dense air traffic conditions, strict regulations of activities including maintenance works on airfield area, and very high quality for repaired pavement area, there are lots of difficulties and specific requirements raising for maintenance work in practice. The paper presents the status of air transport development, PCC airfield pavement condition, typical distresses, causes analysis, and finally present primary result of pilot application of new material for PCC airfield pavement treatment of NIA.

Keywords Portland cement concrete pavement · Airport pavement · Deterioration · Distress · Repair · Treatment · Polymer concrete

1 Introduction

In last 10 years, Vietnam aviation market has been one of ten fastest growth markets in the World, with annual growth rate of 16.3% on passenger and 14.0% of cargo. In the year of 2019, Vietnam airport system served (by both domestic and international airlines) about 115.5 million of passengers and 1.5 million tons of cargo, at growth rates of 11.8 and 11.0%, respectively, comparing to that of 2018. There was about 700 international and 670 domestic flights taking place on the airport system per day, and domestic fleet was 229 aircrafts, increasing 54 (30.9%) airliners comparing to that of 2018 [1, 2].

P. H. Khang · N. T. Hiep (✉)
Faculty of Civil Engineering, University of Transport and Communications, Hanoi, Vietnam
e-mail: nguyentronghiep@utc.edu.vn

For Noi Bai International Airport (NIA), the second largest airport, total number of passengers also overloaded around 2017, and attained 29.2 million in 2019, excess of 4.2 million comparing to its current capacity. The high dense traffic, combining with adverse impacts of weather condition and other factors have led to the fast deterioration of airfield pavement system. Consequently, pavement defects, especially surface distresses of PCC, dominated pavement type in the airport, have been appeared at different severe and scale level (Fig. 1).

2 Present Condition of NIA Airfield Pavement

2.1 Airfield Pavement and Typical PCC Distresses

The airfield system of Noi Bai International Airport (NIA) presented in Fig. 2 comprises of two parallel runways 11L/29R (1A) and 11R/29L (1B); 1 parallel taxiways (S1) and 17 exit/connecting taxiways, turning pad; and the apron areas enough for 40 parking positions and taxilanes. Except Runway 1A and 4 connected exit taxiways were overlaid by asphalt, remaining airfield areas was PCC pavement. The typical PCC pavement structure is showed in Fig. 2, comprises of 3 layers: surface layer is Portland cement concrete grade M35; base layer is sand treated 8% cement; subbase is stabilized aggregate of crushed stone, laid on capping layer and subgrade. The thickness of the layers was presented in Table 1.

After a long exploitation time, PCC airfield pavement distresses have been appeared in a wide range of severity and scale by areas, depending on the pavement age, axle loading, traffic density, and environmental conditions. Beside some severe failures related to the base or subgrade such as settlement, faulting, pumping required large scale repair, the common defects related to surface distresses such as cracking, scaling, joint spalling, corner spalling etc. which can be treated by patching or partial depth repair.

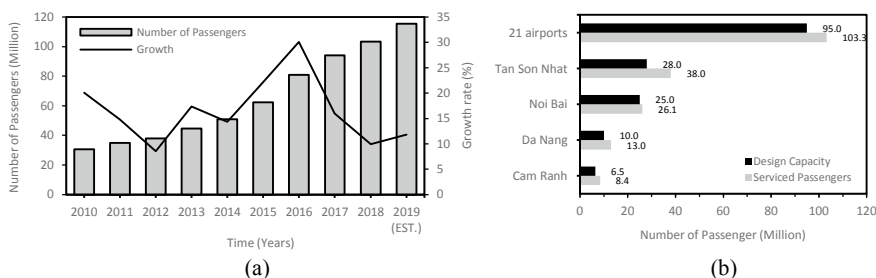


Fig. 1 a Vietnam aviation development, and b Exploitation condition of airport system 2018



Fig. 2 NIA’s master plan and typical PCC pavement structure

Table 1 Layer thickness of PCC pavement of NIA’s airfield components

Airfield components	Thickness (cm)/ Dimension (m)	Airfield components	Thickness (cm)/ Dimension (m)
Runway 1A	h1 = 40 cm; h2 = 18 cm; h3 = 28 cm Asphalt = 20 cm;	Apron A3	h1 = 28 cm; h2 = 20 cm; h3 = 28 cm Dimension: 78 × 280 m
	Dimension: 45 × 3200 m	Cargo terminal apron	h1 = 34 cm; h2 = 20 cm; h3 = 28 cm Dimension: 155 × 120 m
Runway 1B	h1 = 40 cm; h2 = 20 cm; h3 = 28 cm Dimension: 45 × 3800 m	Hangar apron	h1 = 40 cm; h2 = 20 cm; h3 = 28 cm Dimension: 93 × 28 m
T1 terminal Western Apron	h1 = 34 cm; h2 = 20 cm; h3 = 28 cm Dimension: 200 × 100 m	T1 terminal Eastern Apron	h1 = 40 cm; h2 = 20 cm; h3 = 28 cm Dimension: 152 × 292 m

2.2 Cause Analysis

There are many reasons causing airfield pavement distresses. For NIA, the deterioration of airfield pavement can be traced back to the factors: (1) High air traffic volume: From 2006 to 2018, the aircraft operations on NIA airfield system increased from around 74 to 456 operations per day on average. Currently, the number of takeoff/landing operations on Runways 1A and 1B exceed about 50 and 70% comparing to their capacity, respectively. This problem speeds up the deterioration of airfield pavement system, leading to appearance of distresses on airfield pavement system [1, 2]; (2) Heavy axle loading: The rapid development of domestic airliner fleet, with new joining of wide-body aircrafts such B787, A350 having high tire pressure (1.6–1.7 MPa) may induces high shear stress in pavement, leading to slab crack and other pavement distresses [1]; (3) Change of hydrothermal condition: Vietnam is one of the world's most vulnerable countries to the effects of climate change [3]. The increase of extreme weather events combining with characteristics of monsoon climate results in changes of pavement hydrothermal mode, which in turn inducing distresses on subgrade, base/subbase and also PCC slab or asphalt layers; (4) Local heat condition: Under heavy traffic condition, elevated temperature exhaust gases from aircraft engines coupled with high air temperature in heatwave time may increase the local temperature in airfield areas, and consequently inducing high temperature stress in PCC slab. This condition combining with heavy axle load may lead to failures on PCC pavement.

3 Requirements of Material Used for PCC Airfield Pavement Repair

Due to the strict regulations applied for operation including repair work and high requirement on quality pavement, there are specific properties that repair materials have to satisfy for used, including: (1) Curing time: This is the largest portion of total repair construction time. Therefore, the short curing time is the critical property for potential material used in repair work. For the busiest airports in Vietnam, the curing time of repair material less than 2 h is acceptable for most circumstances; (2) Compressive and flexural strengths: The properties of patching material should be least equal to that of the existing PCC pavement to keep the patching area not to be locally failure; (3) Bond strength: this material property plays two key functions. The first one is to keep patching material and PCC substrate working together as demonstrated in Fig. 3b, which is similar to the original working capacity of slab as showed in Fig. 3a, instead of separated layer as showed in Fig. 3c, therefore minimize risk that patching material and/or PCC substrate are damaged due to high induced stress under axle loading or environmental impact. The second function of the bond is to prevent FOD generation from patch to airfield; (4) Abrasion: small surface abrasion will keep patch area maintaining the

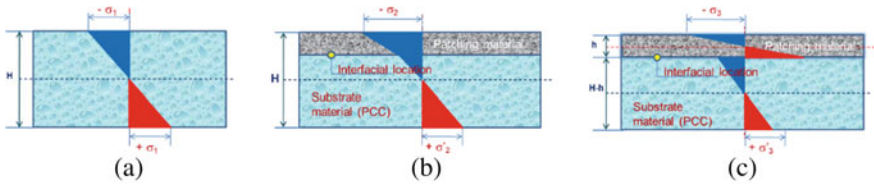


Fig. 3 The induced stress in PCC slab **a** normal working condition; **b** repair material completely bond to PCC substrate; **c** repair material loosely bond to PCC substrate [8]

Table 2 Proposing requirements for material used for PCC airfield pavement repair

Properties	Values	Note
Total construction time (h)	3.0–6.0	
Curing time (h)	≤ 2.0	
Compressive strength (MPa)	≥ 39.0	TCCS 24:2018/CHK
Flexural strength (MPa)	≥ 5.0	TCCS 24:2018/CHK
Abrasive (g/cm ²)	≤ 0.3	TCCS 24:2018/CHK
Bond strength (MPa)	≥ 0.41	TCVN 9491:2012
	Cohesive failure in existing concrete	

surface roughness, ensure the uniformity of skid resistance of overall pavement; (5) Construction procedure: a simple, and similar to other common pavement repair works, not require high skill of worker, or special tools or equipment in implementation would be easy to fit with real practice condition. According to the above requirements, and common properties PCC used for airfield rigid pavement construction [4], the main properties of the repair material are proposed as in Table 2.

4 Application of PC for PCC Pavement Repair in NIA

Polymer concrete (PC), a new construction material introduced in 1950s having many prominent properties such as fast curing, high compressive and flexural strength, perfectly bonding to substrate, resistance to chemical agents, PC is highly appropriate material for utilization in practice. From literatures, the material could be fit well with PCC airfield pavement work.

DOM 1-17 is a variation of polymer concrete, which was developed by researchers of University of Transport and Communications for PCC pavement repair. After a successive experimental process in laboratory with supports by related institutions, DOM 1-17 product was used for pilot application at NIA. The general performance indicators of the material in practice is presented in Table 3.

The practical application DOM 1-17 at NIA showed that the construction process was conducted in total time of 3 hours, including all steps in proposed

Table 3 Physical and mechanical properties of new polymer concrete DOM 1-17 used for PCC pavement repair at NIA

Indicators	Values	Notes
Total construction time (h)	3.0	
Curing time (min)	60	
Compressive Strength (MPa)	76.4	Sample test in laboratory
Flexural Strength (MPa)	13.0	Sample test in laboratory
Abrasive (g/cm ²)	0.09	Sample test in laboratory
Bonding (MPa)	0.996 (Failure in existing PCC pavement)	Test at patching area

construction procedure [5–7] smoothly implemented. The curing time of PC spent 60 min. The fast test results using concrete pocket penetrometer at that time showed that the strength on top of patch varying in range of 50–65 MPa, about 10–20 MPa higher than the control points in adjacent areas of existing PCC pavement. The average compressive and flexural strengths of samples molding by material using for the site construction were 76.4 MPa and 13.0 MPa, respectively. The average surface abrasion was 0.09 g/cm² on average. The adhesion of PC to PCC substrate was checked by a pull-off test. The average bond strength was of 0.996 MPa, with failures of three samples occurring in PCC pavement.

5 Conclusions and Recommendations

The repair of PCC airfield pavement is a challenging and complicated subject. It plays an important role in ensuring the safety conditions and improving smoothness movement of aircraft operation on the airfield at Vietnam airport system. The successful results of pilot application at NIA showed that the polymer concrete material DOM 1-17 was primarily satisfying the requirements of PCC pavement repair work in real condition, and for widely applied for other airports. Beside science and technology development meanings, the product promisingly showed high cost effectiveness comparing to other products.

The study demonstrates a strong and consent cooperation among research establishments, enterprises, and administrative agencies. It is the initial solid steps for further collaboration, which may contribute to sustainable development of air transport infrastructure of the country in future.

Acknowledgements The study was conducted by Department of Highway and Airport, Faculty of Civil Engineering, and Center of Transport Science and Technology of University of Transport and Communications, collaborated with Noi Bai International Airport, and financed by Vietnam Ministry of Transport under Research Project Code DT204-048.

References

1. Civil aviation authority of Vietnam (CAAV) (2020 June) Report on the first haft year of air transportation market
2. General Statistics Office of Vietnam (GSO) Homepage. <https://www.gso.gov.vn/>
3. Wiki website. https://en.wikipedia.org/wiki/Climate_change_in_Vietnam
4. TCCS 24:2018/CHK (2009) Standard of specification for portland cement concrete constructions and acceptance of aerodrome. Civil Aviation Authority of Vietnam
5. Advisory Circular 150/5380-6C (2014) Guidelines and procedures for maintenance of airport pavements. Federal Aviation Administration, U.S. Department of Transportation
6. National Cooperative Highway Research Program Report 281 (1985) Joint repair methods for Portland cement concrete pavements. National Research Council, Washington DC
7. Federal Highway Administration Report FHWA-RD-99-152 (1999) Materials and procedures for rapid repair of partial-depth spalls in concrete pavements. Federal Highway Administration, U.S. Department of Transportation
8. Khang PH (2017) Modern airport pavement. Transport Publishing House, Hanoi, Vietnam

Strength, Water Porosity and the Shrinkage of Self-Compacting Concrete in Hot Climate



Vinh An Le, Ngoc Tan Nguyen, Xuan Cay Bui, and Tuan Anh Bui

Abstract This paper presents an experimental program for assessing several physical and mechanical properties of self-compacting concrete (SCC) that was manufactured and cured in hot climate conditions. Two SCC mixtures were tested incorporating either OPC or slag cement. The slump-flow which was maintained constant whatever the initial temperature to be 20 or 50 °C by the addition of water at the end of mixing. SCC properties such as compressive strength, water porosity and shrinkage were determined on the cylindrical specimens of 11 × 22 cm. The obtained results on SCC mixed in hot temperature (50 °C) and relative to the control mixture (20 °C) showed that (i) concrete compressive strength is not altered with increasing the initial temperature, (ii) SCC with OPC/filler/slag presents better performances than OPC/filler based SCC.

Keywords Self-compacting concrete · Strength · Porosity · Shrinkage

1 Introduction

The utilization of self-compacting concrete was considerably developed during the last years. The mixtures have typically a high paste volume, high content of mineral admixtures, less coarse aggregate and high sand-to-coarse aggregate ratio linked to their specific self-compacting properties in the fresh state. Meanwhile, in the hardened state, they should have mechanical and durable performances very similar to those of traditional vibrated concrete. Many studies have shown that this requirement is almost achieved in mild weather conditions [1]. To maintain this requirement under hot weather concreting in the context of control specimens

V. A. Le · X. C. Bui · T. A. Bui
Faculty of Civil Engineering, University of Transport and Communications/UTC,
Hanoi, Vietnam

N. T. Nguyen (✉)
National University of Civil Engineering/NUCE, Hanoi, Vietnam
e-mail: tannn@nuce.edu.vn

manufacturing, recommendations are clearly established [2] and justified during the production, in case of vibrated concretes [3]. In this study, an experimental program was carried out on the 11×22 cm cylindrical specimens that were made of SCC mixed at hot temperature (50 °C) and at the control temperature (20 °C). Several mechanical and physical properties of SCC were determined such as compressive strength, porosity, shrinkage. The obtained results allow to assess the effect of the initial temperature and the compositions on the SCC properties.

2 Materials

For SCC design, the Portland cement CEM I 52.5N denoted C1 and blast furnace cement CEM III 52.5N denoted C2 were used. Table 1 presents the physical characteristics of the cements used according to European Standard EN 197-1 [4].

In this study, a limestone filler (LF) 0/90 μm manufactured by Carmeuse Company and according to the French standard NF P 18-508 [5] was used.

A superplasticizer (SP) used was a polycarboxylate type available as a commercial solution (specific gravity = 1.05; active solid content by weight = 21.6%).

Siliceous rounded coarse aggregates (G) 4/10 mm (density = 2670 kg/m^3) and sands (S) 0/4 mm (density = 2670 kg/m^3) were used.

The self-compacting concrete (SCC) mixtures tested in this study are presented in Table 2 for two cases of the initial temperature of 20 °C and 50 °C.

3 Experimental Program

The initial temperature of the concrete mixture was varied between 20 and 50 °C. The temperature of 50 °C was considered as a sufficient upper limit, reached in hot climate when concrete is cast with aggregates exposed to solar radiation. Accordingly, the cement, the limestone filler and the aggregates were heated to 80 °C in order to bring the mixture to 50 °C.

The slump-flow value was kept constant whatever the initial temperature may be (20 or 50 °C). In order to compensate the adverse effect of the temperature increase on workability, the slump flow was maintained by the addition of water (SCC-50-W), at the end of 4 minutes of mixing. Table 3 presents the values of workability for each SCC mixture, which were immediately measured after mixing

Table 1 Characteristics of the cements used

Designation	Type	Specific gravity (g/cm^3)	Clinker (% by wt)	Addition (% by wt)
C1	CEM I 52.5N	3.11	98.5	1 (Limestone)
C2	CEM III 52.5N	3.01	59.4	40 (Slag)

Table 2 Concrete mixtures (kg/m³)

Mix notation	C1	C2	F	S	G	SP	Water	W/ C + F
SCC1-20	350	–	87.5	808	889	4.375	190.3	0.43
SCC1-50-W	350	–	87.5	808	889	4.375	190.3 + 12.1	0.46
SCC2-20	–	370	92.5	795.4	875	4.625	187.8	0.41
SCC2-50	–	370	92.5	795.4	875	4.625	187.8	0.41

Table 3 Properties of fresh SCC mixtures

Property		SCC mixture			
		SCC1-20	SCC2-20	SCC1-50-W	SCC2-50
Density (kg/m ³)		2370	2400	2381	2400
Actual water content (l/m ³)		194.7	195.0	194.6	185.7
Slump	Average diameter	72.0	72.5	72.8	73.0
	T ₅₀ (s)	1.5	1.6	1.9	1.5
L-Box	T ₄₅ (s)	1.8	1.3	1.4	1.5
	H ₂ /H ₁ ratio	0.85	0.92	0.80	0.85
Sieve segregation test (%)		9.1	19.5	16.8	10.2

(t_0) according to the following order: slump flow ($t_0 + 1$ min); L-box ($t_0 + 5$ min); sieve stability (sample of concrete taken from the mixer at t_0 and tested at $t_0 + 15$ min).

All the cylindrical specimens were cured in the specified conditions according to the French standard NF P 18-404 [6], such as storage at 20 °C without any hydric exchange for the first 24 hours, then storage at 20 °C and 100% relative humidity until the time of tests.

The compressive strength of cylindrical specimens was determined at different ages of 1, 7 and 28 days according to the European standard NF EN 12390-3 [7]. The compressive strength at each tested age is determined as the average value of three specimens.

Porosity to water of the concrete mixtures was measured with the testing conditions recommended by AFPC-AFREM [8]. Specimens were placed in a primary vacuum for four hours, then they were totally immersed in water at 20 °C and saturated by maintaining the vacuum for 20 hours. The immersed mass was determined with a hydrostatic balance. Next, the specimens were wiped in order to remove the surface excess water, and the saturated mass was measured. Finally, specimens were dried at 105 °C for 48 hours and weighted after cooling in a desiccator.

The experimental protocols for endogenous and total shrinkage measurements follow the recommendations of the Standardized Tests Methods for Creep and Shrinkage (RILEM—TC 107-CSP) [9]. The endogenous shrinkage and total shrinkage were measured on three specimens. After demolding at 24 hours, the specimens for endogenous shrinkage are covered with a double thickness of

adhesive aluminum paper to prevent any water exchange, while those used for total shrinkage are only covered at their ends to favor radial water exchange.

4 Results and Discussion

4.1 Fresh Concrete

When the initial temperature of the concrete mixture was 50 °C, the addition of water enabled the self-compacting ability to be maintained for concretes incorporating cement CEM I. The SCC2 mixtures made of cement CEM III required no addition of water and remained self-compacting. In addition, the stability of SCC2 mixed at 50 °C was significantly increased.

4.2 Hardened Concrete

The compressive strength of SCC1 at 28 days ranges from 45 to 55 MPa with increasing the initial temperature from 20 to 50 °C as shown in Fig. 1a. Meanwhile, it is equal to 55 MPa for SCC2 for both cases of the initial temperature as shown in Fig. 1b. The results show that, the initial temperature of the mixture did not adversely affect the compressive strength. For SCC1, whatever the age of concrete, the compressive strength was not reduced, or even significantly increased with increasing the initial temperature. For SCC2, the evolution of compressive strength was not affected by the initial temperature ranging from 20 to 50 °C. The complementary addition of water was not required at 50 °C since it is the low reactivity of cement CEM III in comparison with cement CEM I.

Figure 2 presents the total porosity for each mixture. For SCC1, when the consistency was kept constant by water addition at 50 °C, the values of porosity did not increase. Concerning SCC2, the increase of the initial temperature did not affect

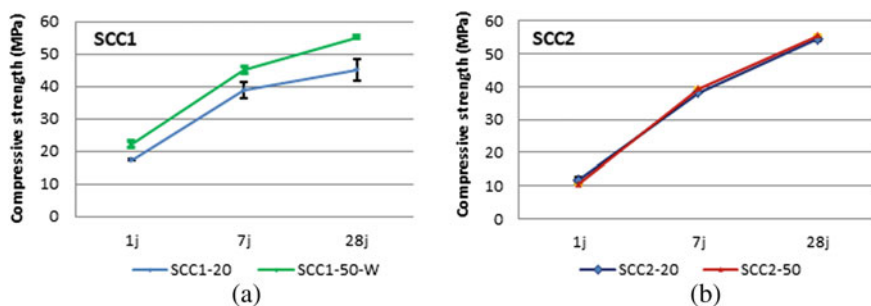


Fig. 1 Evolution of concrete compressive strength: (a) SCC1, (b) SCC2

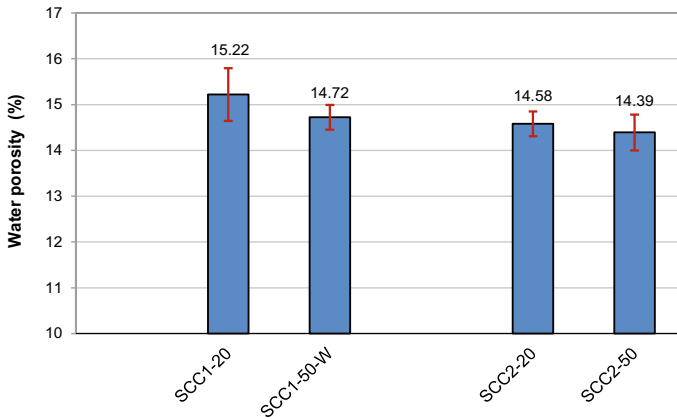


Fig. 2 Water porosity for SCC mixed at 20 and 50 °C

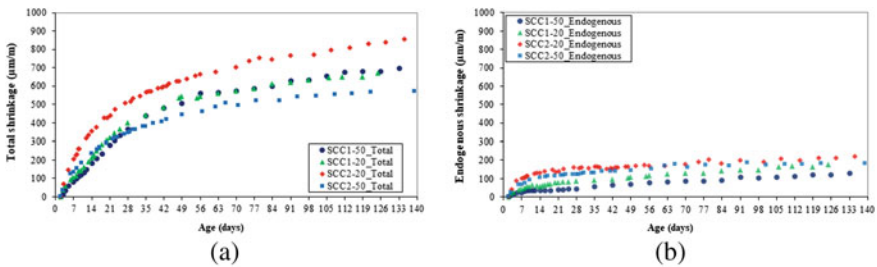


Fig. 3 Shrinkage of SCC: (a) total shrinkage, (b) endogenous shrinkage

the porosity. Hence, the obtained results show that the total porosity in the SCC hardened concrete does not raise with increasing the initial temperature of the mixture.

The shrinkages of SCC1 and SCC2 were measured during 140 days and presented in Fig. 3. It can be seen that SCC1 exhibits identical shrinkage whether mixed at 20 °C or at 50 °C. It seems that the initial temperature does not affect the shrinkage of SCC1. On the other hand, with regard to the ternary matrix material based on slag (SCC2), the results show that the total shrinkage of SCC2-20 mixed at 20 °C is greater than that of SCC2-50 mixed at 50 °C. The difference of the total shrinkage of SCC2 at different temperatures can be explained by the sensitivity of the material to desiccation because few variations in the endogenous mode is observed. The modification due to the movement of water from the matrix is generally associated with the variability in the porous network.

5 Conclusions

The difference in the SCC design was essentially based on the OPC/limestone filler combination or the cement nature. The consistency of fresh concrete was tested after mixing to control the self-consolidating ability. For hardened concrete, the measurements of compressive strength, water porosity and shrinkage were performed to assess the effect of the mixture initial temperature on these properties. The obtained results allow to draw the conclusions as follows:

- The increase in the mixture temperature from 20 to 50 °C required no addition of water for the slag cement/limestone filler combination in order to maintain the self-compacting ability.
- The compressive strength of SCC mixed at high temperature is similar or greater than that mixed at the control temperature.
- The water porosity is unchanged or slightly improved with increasing the mixture temperature for SCC mixtures tested.
- The total shrinkage of self-compacting concrete incorporating slag cement raises significantly with increasing the mixture initial temperature.

References

1. Persson B (2001) A comparison between mechanical properties of self-compacting concrete and the corresponding properties of normal concrete. *Cem Con Res* 31:193–198
2. ACI 305R-10 (2010) Guide to hot weather concreting. American Concrete Institute
3. Mouret M et al (2003) Strength impairment of concrete mixed in hot weather: relation to porosity of bulk fresh concrete paste and maturity. *Mag Con Res* 55:215–223
4. EN 197-1 (2000) Cements—Part 1: composition, specifications and conformity criteria for common cements
5. NF P 18-508 (1995) Additions pour bétons hydrauliques—additions calcaires—spécifications et critères de conformité
6. NF P 18-404 (1981) Bétons—Essais d'étude, de convenance et de contrôle—Confection et conservation des éprouvettes
7. NF EN 12390-3 (2003) Essai pour béton durci—Partie 3: Résistance à la compression des éprouvettes
8. AFPC-AFREM (1997) Durabilité des bétons, méthodes recommandées pour la mesure des grandeurs associées à la durabilité. INSA-LMDC, Toulouse, pp 11–12
9. RILEM—TC 107-CSP (1998) Creep and shrinkage prediction models: principles of their formation. *Materials and structures*, vol 31, pp 507–512

The Influence of Aggregate Size and Blocking Materials to the Water Infiltration Rates of Pervious Concrete



Hung Viet Vu and Soo Yeon Seo

Abstract The purpose of this study is to identify the differences in porosity and infiltration rates when the mixing ratio of aggregates is different and to present the mixing ratio satisfying the compressive strength requirement specified in Korean standard for sidewalks, bicycle roads and other civil facilities without consider the traffic loads. Three mix ratios were suggested by considering various aggregate sizes and three cylinders were made for each ratio. The porosities of those cylinders were evaluated through compression and water infiltration rate test, measuring the weight of specimens in underwater and analysis of pictured Computed Tomography (CT) image. Experiments have shown that it is best to mix 50% for 5–10 mm aggregates, 45% for 2–5 mm aggregates and 5% for sand in terms of strength and infiltration rates. In addition, as the proportion of fine aggregates increased, the porosity and infiltration rates decreased. Moreover, the effectiveness of maintenance method was also examined in this study.

Keywords Porosity • Infiltration rate • Mixing ratio • Aggregate size • Compressive strength • Blocking

1 Introduction

Pervious concrete, known as no-fines concrete or permeable concrete, is an environmentally friendly paving material, which has been well recognized as one of the key elements of low-impact sustainable development [1]. In general, it consists of

H. V. Vu (✉)

Campus in Ho Chi Minh City, University of Transport and Communications,
No. 450-451 Le Van Viet Street, Tang Nhon Phu A Ward, Thu Duc City,
Ho Chi Minh, Vietnam
e-mail: hungvv_ph@utc.edu.vn

S. Y. Seo

Department of Architectural Engineering, Korea National University of Transportation,
Chungju, South Korea

cement, water, uniform/single-sized coarse aggregate, and little or no fine aggregate, resulting in a large, open pore structure. As a result, pervious concrete shows better permeability than conventional impermeable pavements due to the porosity between aggregates [2]. Generally, the permeability of pervious concrete is due to its macropore structure. However, as the use of pavement concrete becomes longer, the pores of pervious concrete are easily clogged by various small particles [3, 4]. The permeability of pervious concrete helps to reduce heat island phenomena, traffic noise and provides better condition for recharging the underground water source. In addition, it has the advantage of ensuring the driver's safety by preventing water splash and reducing/eliminating the water film phenomenon on driving surfaces [5]. However, when the sediments, such as leaves, soil, and dust, penetrate the pores, it can be easily noticed that the pores may be blocked and the water permeability decreases. Therefore, continuous or regular maintenance of the pervious concrete is necessary to maintain the permeability performance [6].

The purpose of this study is to compare and analyze the differences between porosity and infiltration rates by varying aggregate mixing ratio of pervious concrete, and to present a mixing ratio that meets the criterion of compressive strength and secures permeability as well. Moreover, in order to investigate the effect of blocking materials to the infiltration rates, experiments on the maintenance of pervious concrete and recovery of permeation performance are carried out by conducting experiments on the pore blocking phenomenon. In addition, pores were identified using CT scanning method and compared with experimental results.

2 Experiment

The pervious concrete was designed with a water-to-cement ratio (w/c) of 0.3, Type I Ordinary Portland cement, which was supplied by a local company in South Korea, was used as a binder with a specific gravity of 3.15 and a poly-carboxylate high-range water-reducing admixture was applied in this research. The mix ratios of concrete considered in this study are shown in Table 1. Three-cylinder specimens with $\varnothing 100 \text{ mm} \times 200 \text{ mm}$ were manufactured for each mixing ratio and their permeability as well as the compressive strength were measured. For Mix 1, one more cylinder was made for CT scanning and three block specimens with $200 \text{ mm} \times 200 \text{ mm} \times 150 \text{ mm}$ for blockage testing.

Table 1 Mixing ratio of pervious concrete (kg/m^3)

Mix	Cement	Water	Aggregate		Sand
			D5–10	D2–5	
Mix 1	358	107	1,595 (100%)	–	–
Mix 2	431	129	1,222 (80%)	229 (15%)	76 (5%)
Mix 3	431	129	764 (50%)	687 (45%)	76 (5%)

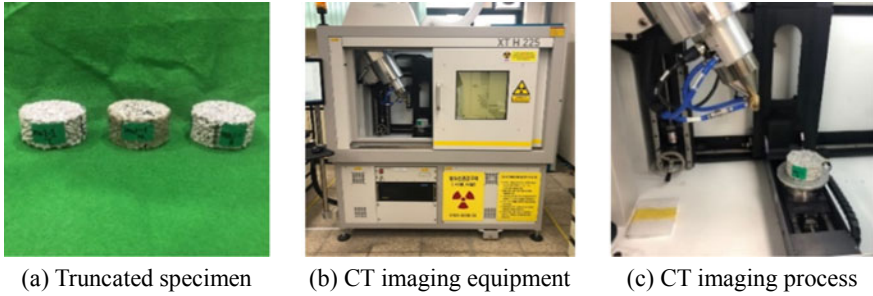


Fig. 1 Truncated specimens and CT imaging

The porosity for each cylinder specimen was measured by using the volume displacement method: the underwater mass and the dry mass of concrete were measured in accordance with ASTM C1754. Furthermore, CT scans were conducted to evaluate pores more accurately. Figure 1a shows the specimens for CT scan after cutting the cylinder specimen to a height of 50 mm, making it into three specimens. Figure 1b and c represent the equipment for CT scan and CT imaging process, respectively. To obtain the porosity of each image, the pixel of the area where void portion was deleted was calculated through Photoshop and converted to the entire void.

In accordance with ASTM C1701, the water infiltration test was performed in which the sides of the specimens were wrapped with tape and rubber packing to block the water flowing horizontally out of the specimens, and the specimens were fixed on the pipe top in Fig. 2a. The experiment was carried out while keeping the water of 1.2 L constant at a height of 10–15 mm. In this process, the total time of 1.2 L water passing through the specimen was measured, and the infiltration rate was calculated.

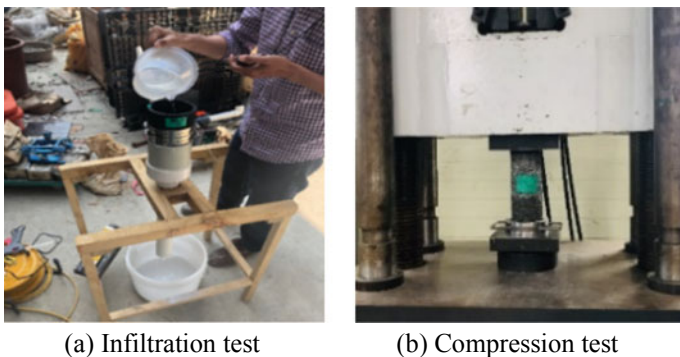


Fig. 2 Infiltration rate and Compressive strength test set up

In order to know the compressive strength of the pervious concrete for each mix case, the cylinder specimens of $\varnothing 100 \text{ mm} \times 200 \text{ mm}$ size were cured for 28 days and then tested according to the KS F 2405–2005 test method for cylinder specimens as shown in Fig. 2b.

Moreover, in this study to verify the effectiveness of the maintenance method of pervious concrete, infiltration tests were carried out by accumulating 8.3 g/L of contaminant substance of 0.15 mm or less four times assuming the sandy soils. After that, high pressure water and vacuum cleaning were performed to recover the permeability. This process was repeated three times to examine the infiltration rates of pervious concrete block.

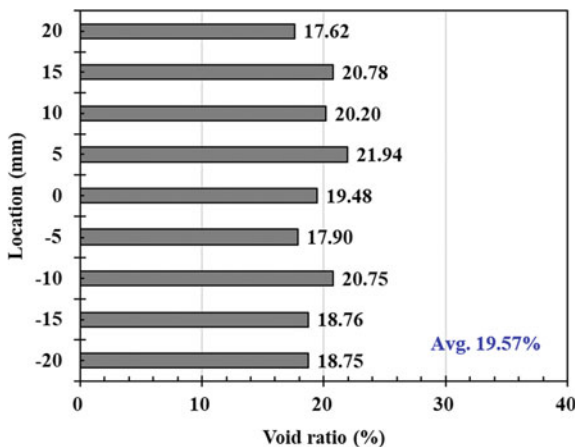
3 Experiment Results

3.1 Porosity of Hardened Pervious Concrete

The average porosity for Mix 1, 2 and 3 was measured at approximately 22.2, 13.7 and 11.6%, respectively. It was observed that the porosity decreased as the proportion of fine aggregates increased. The reason for this is that when the amount of fine aggregate increases, the surface area in which the aggregates contact each other increases. Figure 3 shows the porosity graph for each position obtained by analyzing CT images of Mix 1 case.

It can be seen that the porosity ranged from 17.62 to 21.94% and the average was 19.57%. The porosity obtained from the ASTM C1754 test was 17.1%, which is 87% of the CT scan result. The reason for this difference is that isolated pores inside the specimen, which could not be measured in the underwater mass, can be identified by CT scan.

Fig. 3 Void ratio at each truncated section from CT image



3.2 Water Infiltration Rates of Pervious Concrete

The average infiltration rates for each mix case is 2.72 mm/sec for Mix 1, 0.85 mm/s for Mix 2 and 0.16 mm/s for Mix 3, respectively. It can be seen that all the mix ratios satisfy the infiltration rate of 0.1 mm/s or more according to LH Guide Specifications [7]. In addition, as the proportion of fine aggregates increased, the porosity and permeability decreased. It can be explained that when the blended aggregates of different sizes were used in pervious concrete mixture, the initial porosity between aggregates after compaction is smaller than that of single size due to particle packing effect. Therefore, the water infiltration rate decreases.

3.3 Compressive Strength

The average compressive strengths of Mix 1, Mix 2 and Mix 3 were 11.0, 13.3 and 18.4 MPa, respectively. Among them, the average compressive strength of the specimens of Mix 3 satisfied 18 MPa that can be applied to sidewalks, bicycle roads and other civil facilities without consider the traffic loads (Korean Standards). By substituting smaller and appropriate-sized aggregates in blended aggregate system, it is believed that the void content becomes lower due to further particle contacting effect, resulting in higher compressive strengths.

3.4 Void Clogging Test Results

The average infiltration rate, which was 1.72 mm/s before the test without blocking materials, decreased to 0.77 mm/s after 1 cycle, and recovered 1.11 mm/s after the internal cleaning as shown in Table 2.

The infiltration is reduced by 55% compared to before the test in the first cycle. After completing the second and third cycles, the infiltration rates were 0.65 and 0.68, respectively. These values represent 38 and 40%, respectively, as ratios of the

Table 2 Variation of infiltration rates corresponding to accumulation of blocking material

Test cycle		No. of test				
		1	2	3	4	5
1st cycle	Infiltration rate (mm/s)	1.72*	1.42	1.21	0.93	0.77
	Ratio (%)	100	83	70	54	45
2nd cycle	Infiltration rate (mm/s)	1.11+	0.93	0.83	0.73	0.65
	Ratio (%)	65	54	48	42	38
3rd cycle	Infiltration rate (mm/s)	0.98+	0.81	0.78	0.72	0.68
	Ratio (%)	57	47	45	42	40

*Before adding blocking material; + After cleaning the blocking materials of previous cycle

infiltration rate drawn from the infiltration test without blocking materials. The experimental results show that the vacuum cleaning and high-pressure watering methods are effective in the recovery of infiltration capacity.

4 Conclusions

The mixing ratio of pervious concrete Mix 3 was considered as the most appropriate ratio that can satisfy the infiltration rate of 0.1 mm/s, the porosity of 8%, and the strength of 18 MPa.

Comparing the porosity through the experiment of mass underwater and the CT image analysis, it can be seen that the porosity by CT image is to be 115% higher. This is because, it is difficult to measure the pores isolated inside in the case of the test of underwater mass, but it is possible to measure all the pores inside in the case of CT imaging.

From the infiltration test results, it can be concluded that by blending smaller and appropriate-sized aggregates into concrete mix, the porosity of hardened concrete decreases resulting in the reduction of water infiltration rate of pervious concrete. Moreover, the water infiltration rate of pervious concrete was restored at a constant rate when the permeation performance was reduced and then cleaned by vacuum cleaning and high pressure spraying. However, it was not possible to restore the original infiltration performance.

References

1. Singh A, Sampath PV, Biligiri KP (2020) A review of sustainable pervious concrete systems: Emphasis on clogging, material characterization, and environmental aspects. *Constr Build Mater* 261:120491
2. Zhong R, Leng Z, Poon C (2018) Research and application of pervious concrete as a sustainable pavement material: a state-of-the-practice review. *Constr Build Mater* 183:544–553
3. Lin W, Park DG, Ryu SW, Lee BT, Cho YH (2016) Development of permeability test method for porous concrete block pavement materials considering clogging. *Constr Build Mater* 118:20–26
4. Yuan J, Chen X, Liu S, Li S, Shen N (2018) Effect of water head, gradation of clogging agent, and horizontal flow velocity on the clogging characteristics of pervious concrete. *J Mater Civil Eng* 30(9)
5. Chandrappa AK, Biligiri KP (2016) Pervious concrete as a sustainable pavement material—research findings and future prospects: a state-of-the-art review. *Constr Build Mater* 111:262–274
6. Kia A, Wong HS, Cheeseman CR (2017) Clogging in permeable concrete: a review. *J Environ Manage* 193:221–233
7. Korean Standard: LH guide specifications (2012) (in Korean)

Research on the Reinforcement of Basalt Soil Using Natural Pozzolan, Cement, and Lime for Building Rural Roads in Dak Nong Province, Vietnam



Truong Son Bui, Ba Thao Vu, Thi Nu Nguyen,
and Thanh Duong Nguyen

Abstract The paper presents the utilization of local natural pozzolan in combination with cement and lime to reinforce local basalt soil for building rural road structure in Dak Nong province. The research results showed that it is necessary to use lime in combination with cement and pozzolan for soil reinforcement. With the cement content ranging from 0 to 12% and 4% lime, the compressive strength of the reinforced soil reached the maximum value when the pozzolan content was 10%. The test results of a mixture of 10% pozzolan, 4% cement, and 4% lime indicated that the mechanical parameters (compressive strength, tensile strength, and elastic modulus) increase rapidly in the first 28 days and tends to grow slowly after 28 days. Additionally, the research results also found that the strength properties of reinforced soil after submerging in water insignificantly decreased.

Keywords Rural roads · Natural pozzolan · Basalt soil · Soil reinforcement

1 Introduction

The use of finely ground natural pozzolan in combination with binders to reinforce local soil has been widely studied in the world. In which, there are some studies regarding the use of natural pozzolan in combination with lime to improve the soft ground [1–4]. In general, the research results and application abroad have confirmed that natural pozzolan can combine with lime to improve the physical and mechanical properties of the soil for building the foundation and surface of the road.

In Dak Nong province, about 28% of the road surface has not been hardened. Additionally, it mainly goes through the weathered basalt soil which is often sat-

T. S. Bui (✉) · T. N. Nguyen · T. D. Nguyen
Hanoi University of Mining and Geology, Hanoi 100000, Vietnam
e-mail: buitruongson@hmg.edu.vn

B. T. Vu
Hydraulic Construction Institute, Vietnam Academy for Water Resources,
Hanoi 100000, Vietnam

urated with water in the rainy season, reducing the load capacity, increasing the deformation ability, increasing the soil erosion, and leading to damage of road surface structures, especially for the roads without hard surfaces. Therefore, the demand for hardening the rural road surface in Dak Nong province as well as in the Central Highlands is very necessary. Dak Nong now has 05 mines of natural pozzolan located in Quang Phu and Buon Choah communes, Krong No district. Thus, the study regarding the utilization of natural pozzolan in Dak Nong province is of great significance for sustainable economic development in this region. This paper introduces the results of research and application of natural pozzolan in combination with some binders to build rural road structure in Dak Nong province, Vietnam.

2 Materials and Methods

2.1 Materials

The soil used in this study is weathered soil from basalt and taken from the road surface. The physical and mechanical properties of the soil were determined at the Geotechnical lab—Hydraulic Construction Institute and are presented in Table 1.

According to the standard of soil reinforcement with the binder for roads—TCVN 10379: 2014, soils with liquid limit, $W_L > 45\%$, plasticity index, $I_p > 27$, and clay particle content $>30\%$ should not be used to reinforce with cement. Moreover, as recommended by the Association of American Military Engineers, soil with $W_L > 40\%$, plasticity index, $I_p > 20$ should not be used to reinforce with cement. Comparing the testing results of basalt soil above, the soil properties exceeded the recommended soil reinforcement threshold with cement of the two criteria, i.e., $W_L = 52.4\% > [40.0\%]$, $I_p = 20.2 > [20.0]$, clay particle content $31.1\% > [30.0\%]$. It can be seen that, the soil in the study area is not suitable for reinforcement with cement.

Natural pozzolan in the study area has a total content of $\text{SiO}_2 + \text{Al}_2\text{O}_3 + \text{Fe}_2\text{O}_3 = 72.9\% > [70\%]$ (Table 2). This material has no cementitious properties. However, it is suitable for using as a mineral admixture of F class according to ASTM C618-03. The lime absorption of pozzolan is of medium

Table 1 Physico-mechanical properties of soil used

No.	Index	Values	No.	Index	Values
1	Soil particles P, %		2	Liquid limit, W_L , %	52.4
	– Gravel (>2.0)	20.3	3	Plastic limit, W_p , %	32.2
	– Sand ($2.0-0.075$)	11.5	4	Plasticity index, I_p , %	20.2
	– Silt ($0.075-0.05$)	37.1	5	Maximum dry density, γ_{Kmax} , kN/m^3	15.9
	– Clay (<0.005)	31.1	6	Optimum water content, W_{opt} , %	26.0

Table 2 Compositions and physical properties of natural pozzolan

No.	Chemical composition, %		No.	Physical properties	
1	SiO ₂	46.6	1	Lime absorption, mg CaO	75.4
2	Fe ₂ O ₃	12.9	2	Milling coefficient	1.15
3	Al ₂ O ₃	13.4	3	Unit weight, kN/m ³	18.1
4	CaO	8.77	4	Specific gravity	2.85
5	MgO	8.72	5	Porosity, %	38.3

activity. The natural pozzolan samples meet the technical requirements for active additives, semi-active in cement production. According to similar studies on soil-reinforced natural pozzolan [1–4], this pozzolan can serve as a binder for soil improvement.

Cement used in this study is Portland cement PCB40 Ha Tien produced in Dak Nong with the percentage of 0% limestone, 6% colored stone, 4% gypsum, 74% clinker, and 16% pozzolan. This is the most common type of cement in this study area.

Lime used in this study is finely ground, packed in moisture-proof bags, taken from Khanh Ha Company—Ninh Binh. Experimental results show that the total content of CaO and MgO is 89.36%, classified as type II according to TCVN 10379-2014, ensuring the quality of soil reinforcement.

2.2 Experimental Scenario

From practical and economical view, the binder dose used for soil improvement should be less than 20% of the dry weight the soil [5]. Refer to the results of domestic and foreign studies on soil reinforcement, the binder contents were selected as follows: Natural pozzolan (P): 0, 5, 10, 15, 20%; cement (C): 0, 3, 5, 10, 12%, and lime (L): 0, 4, 8%; the gradation is denoted as PxCyLz, where x, y, z are percentages of adhesive compared to the dry weight of soil.

2.3 Methods and Standards

Experiments are conducted as follows: (1) Compaction of soil reinforced with natural pozzolan, cement, and lime with different proportions to determine the maximum dry density (MDD) and optimum moisture content (OMC) of the reinforced mixture. The compaction tests were carried out according to Vietnamese standard 22TCN 333-06; (2) Preparing cylindrical samples with an inner diameter $d = 110$ mm, a height $h = 120$ mm at MDD and OMC; (3) Conducting

compression tests for reinforced soil mixture at 14 days of age with the saturated condition (samples were wrapped in a plastic bag and cured at the room temperature of 25 °C for the first 7 days and soaking in water for the next 7 days); (4) Based on the compressive strength in the saturated condition at 14 days of curing (R_n^{14bh}), the reasonable mixture was selected; (5) For the reasonable selected mixture, the compressive strength, splitting strength, elastic modulus, and CBR were determined at 7 days, 14 days, 28 days, and 90 days of curing. The mechanical properties at 28 days of curing in saturated condition (cured at the room temperature of 25 °C for the first 7 days and soaking in water for the next 21 days) were also determined.

3 Test Results and Discussions

3.1 Effects of Pozzolan on Compaction Characteristics of Reinforced Soil Mixture

When the soil mixture was compacted, the soil porosity decreases, shear strength increases, and permeability and compressibility decreases. For embankment materials, the MDD and OMC are two important parameters that need to be determined for sample preparation and field construction. The results of compaction tests of some grades are shown in Fig. 1. It can be seen that the maximum dry density of reinforced soil mixture decreases and the optimum moisture content increases as the pozzolan content increases. This is because the specific gravity of pozzolan (2.85) and cement (3.18) is greater than the specific gravity of the soil (2.78).

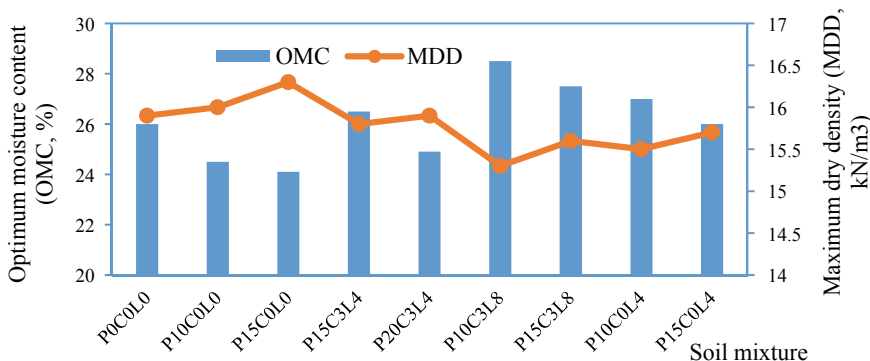


Fig. 1 Effect of the pozzolan content on the compaction characteristics

3.2 Selecting the Appropriate Proportions

The appropriate mixing ratio is the ratio of pozzolan that can replace the content of cement to achieve the strength of reinforced soil according to TCVN 10379:2014. To simplify the experimental scenario, this study conducted a test to determine the saturated compressive strength at 14 days of curing for all the designed proportions. Experimental results show that the compressive strength of the reinforced soil mixture when using 20% pozzolan, 12% cement or 4% lime or a combination of two types of cement—lime adhesive, pozzolan—cement or pozzolan—lime do not meet the requirements of compressive strength according to TCVN 10379: 2014. Non-reinforced soil samples (P0C0L0) and pozzolan reinforced soil (P10C0L0) were completely disintegrated in the presence of water, indicating that pozzolan is an inert additive and has no chemical reactions if there is a lack of a suitable catalyst. With the same amount of cement, soil reinforced with pozzolan-cement mixture has a lower compressive strength than a soil sample reinforced with only cement, which indicates that the reinforcement of soil with pozzolan and cement is inefficient. Therefore, to ensure the compressive strength of the mixture satisfies TCVN 10379: 2014, it is necessary to use pozzolan in combination with cement and lime. Experimental results of determining the correlation between the mixing ratios of pozzolan—cement—lime with compressive strength at 14 days of curing in saturated condition are shown in Fig. 2.

When reinforcing soil using a mixture of pozzolan—cement—lime with the lime content of 4%, the compressive strength of the reinforced soil reached the maximum value when the pozzolan content was 10%. The compressive strength of the mixture decreases as the pozzolan content increases exceeding 10%. The increase of pozzolan may lead to a lack of water for pozzolanic reactions. Additionally, the natural pozzolan is a non-plastic material and has no cementitious properties, so the increase of pozzolan can lead to a decrease in the cohesion force and results in a decrease in compressive strength. The appropriate proportions of pozzolan and

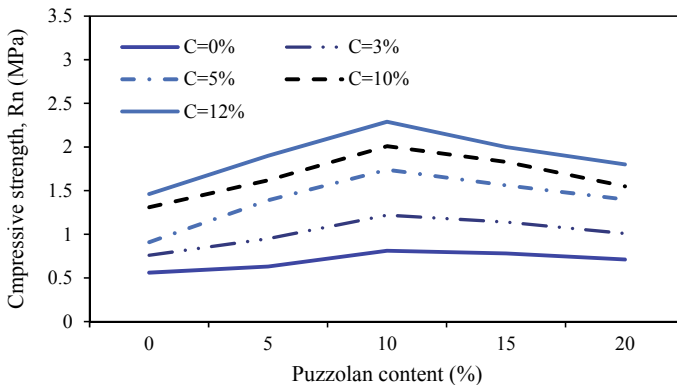


Fig. 2 Effect of pozzolan-cement-lime (4%) on the compressive strength (Rn) of reinforced soil

Table 3 Test results of mechanical properties of P10C5L4 mixture

No.	Mixtures	Index	Curing days				
			7	14	28	28st (saturated)	90
1	P10C5L4	R_n , MPa	1.70	2.01	2.16	1.90	2.32
2	P10C5L4	R_{ss} , MPa	0.19	0.27	0.34	0.29	0.35
3	P10C5L4	E , MPa	193	279	366	304	407
4	P10C5L4	CBR , %				137	

inorganic binder for soil reinforcement are P10C5L4 (10% pozzolan, 5% cement, and 4% lime). Experimental results of mechanical properties, including compressive strength, splitting tensile strength, elastic modulus, and CBR of the P10C5L4 mixture at different ages are shown in Table 3.

Experimental results show: (1) the reinforced soil has a stable structure when interacting with water, which means it can withstand flooding conditions; (2) soil reinforced with pozzolan—cement—lime has mechanical parameters (R_n , R_{ss} , and E) increasing rapidly in the first 28 days and tends to grow slowly after 28 days; (3) compressive strength and elastic modulus achieve the durability of grade II according to TCVN 10379: 2014; tensile strength only reaches the durability of grade III; CBR values show that the soil after reinforcement equals to type I of crushed stone. In general, there is no big difference between the two proportions in terms of compressive strength, tensile strength, and elastic modulus.

4 Conclusions

- (1) Basalt soil in Dak Nong has quite a high content of dust and clay particles. The liquid limit values and plasticity index greater than the recommended values for soil reinforcement with cement. Laboratory results also show that basalt soil has a very high disintegration in the presence of water, the compressive strength of reinforced soil with cement is not significantly increased compared to that of non-reinforced soil. Therefore, to ensure the quality of reinforcement, it is necessary to combine cement with other binders to reinforce basalt soil.
- (2) In combination with cement (0–12%) and lime (4%), the increase of pozzolan content increased the compressive strength of reinforced soil and it reached the maximum value at 10% pozzolan. The increase of pozzolan exceeding 10% led to a decrease in compressive strength. The mechanical parameters (compressive strength, tensile strength, elastic modulus) of P10C5L4 increased significantly in the first 28 days and tent to slowly increase after 28 days of curing. Additionally, the research results also found that the reinforced soil can be stable when interacting with water which means that it can withstand in flooding conditions

References

1. Harichane K, Ghrici M (2009) Effect of combination of lime and natural pozzolana on the plasticity of soft clayey soils. Near East University, Nicosia, North Cyprus
2. Harichane K, Ghrici M, Kenai S (2011) Effect of the combination of lime and natural pozzolan on the compaction and strength of soft clayey soils: a preliminary study
3. Vakili AH, Selamat MR, Moayedi H (2013) Effects of using Pozolan and Portland cement in the treatment of dispersive clay. *Sci World J* 2013
4. Mfinanga DL, Kamuhabwa ML (2008) Use of natural pozzolan in stabilising lightweight volcanic aggregates for roadbase construction. *Int J Pavement Eng* 9(3):189–201
5. Farouk A, Shahien MM (2013) Ground improvement using soil-cement columns: Experimental investigation. *Alex Eng J* 2013:1–9

Pavement and Construction Management

Evaluation and Recommendation for Management and Maintenance Specification of Rural Bridge in Vietnam



Xuan Tung Nguyen and Tuan Dung Pham

Abstract Vietnam area is more than 320,000 km² and three—fourth are mountainous area. In order to connect people between mountainous areas, Vietnamese Government has been investing fund for building and improving the infrastructure for these areas. Due to the mountainous geography, geotechnical and hydraulic conditions, the road, and bridge were designed at low level (A, B, C and D level according to TCVN 10380:2014 of Vietnamese specification. However, during the service life of those infrastructure system, there is a lack of management and maintenance specification for those road and bridge in the rural area. In this paper, the existing specification of exploitation and maintenance will be evaluated and the suggestion for exploitation and maintenance specification of rural bridge will be recommended.

Keywords Management · Maintenance · Specification · Rural bridges

1 Introduction

Transportation system is a vital matter to accelerate socio-economic development in rural and mountainous areas, in order to remove barriers between regions, to shorten the gap between the rich and the poor between regions and contribute to bring new face to the mountainous region also promoting socio-economic integration and development. However, the capital arrangement for development of mountainous transport infrastructure is always a difficult problem and depends on the state budget that is still limited and has not met the demand. Besides, due to the mountainous geography conditions, the bridge was designed at low level (A, B, C and D level according to TCVN 10380:2014 of Vietnamese specification) with expected life cycle of 20 years.

X. T. Nguyen (✉) · T. D. Pham
Faculty of Civil Engineering, University of Transport and Communications, Hanoi, Vietnam
e-mail: ngxuantung@utc.edu.vn

Along with the low level of bridge, the lack of specification of management and maintenance of those bridge is also a trouble that shorten the serviced life of bridges. Vietnamese government, with the Ministry of Transport on behalf had issued a circular no 12/2014/TT-BGTVT about guidance for management and operation for bridge in rural area but it only covers the concrete bridge with span larger than 50 m and suspension bridge with span larger than 7 m which is insufficient for all rural bridges. In this paper, the detail of management, operation and maintenance of rural bridge will be discussed, and the management and operation specification of rural bridges will be recommended.

2 Bridge Scenario of Rural Bridge in Vietnam

Local bridge which is located on the rural road system for transportation purpose of pedestrians, wagons, bicycles, motorcycles, motorbikes and other rudimentary vehicles. Recently, local bridges had special attention of government. There were many projects have been established with the aim of building more bridges for rural and mountainous area such as Program 135; LRAMP project and 186 project The plan for building local bridges in mountainous has also mentioned in the Decision 622/QĐ—BGTVT of Ministry of Transport that described in Table 1.

The national program 135 issued by government with the aim of using capital sources, mainly from state budget for poverty alleviation by building the necessary infrastructure for mountainous area. In phase II of Program, investment in building

Table 1 Summary of the number of bridges expected to be built in the northern mountainous region according to the Decision 622/QĐ-BGTVT on March 2nd, 2016 by The Ministry of Transport

No.	Province	Number of local bridges	Length (m)
1	Bac Giang	35	2163
2	Bac Can	57	1639
3	Cao Bang	52	1583
4	Đien Bien	63	4335
5	Ha Giang	69	2283
6	Hoa Binh	41	1892
7	Lai Chau	90	5405
8	Lang Son	63	3872
9	Lao Cai	130	3300
10	Phu Tho	65	2066
11	Son La	56	2765
12	Thai Nguyen	34	1906
13	Tuyen Quang	47	3409
14	Yen Bai	49	1757

such infrastructure as electricity, roads, schools, has focused and changed the rural appearance. The concrete bridges that built by Program help local people travel conveniently especially in rainy season.

LRAMP, Local Road Assets Management Project, the 385 million USD—ODA project of World Bank supports for the development of infrastructure in rural area of Vietnam by building the local bridges in the rural transportation system. Up to now, there are more than 1800 local bridges have been built by this project. The popular types of bridge are cast in place concrete bridges with length from 8 to 100 m and 2.5, 3.5, 4 m of width, respectively [1].

Project 186 is the initial investment stage to invest in the construction of 186 suspension bridges in order to ensure traffic safety in 28 Northern mountainous provinces, the Central and the Central Highlands, to quickly meet the transportation demand and socio-economic development, contributing to poverty reduction for ethnic minorities. Once completed, the bridges will be a premise for households that are often isolated when floods come back to feel secure in life, economic development and convenient transportation, ensuring children go to school safely; support for common development, improve people's lives.

3 Evaluation the Current Management and Maintenance Specification

In Vietnam, there are several guidelines for management, operation and maintenance such as Circular No 12/2014/TT-BGTVT of Ministry of Transport: guidelines for management and operation of bridge on rural road [2]; Circular No 52/2013/TT-BGTVT about regulations on the management, operation and maintenance of road works [3]; Decree No114/2010/NĐ-CP of Government about maintenance of construction works [4]; Decree No 15/2013/NĐ-CP of Government about Quality control of construction works [5].

Circular 12/2014/TT-BGTVT of Ministry of Transport: guidelines for management and operation of bridge on rural road including beam, truss, arch bridges that build on the rural road system. However, this guideline use for suspension bridge with span larger than 70 m and girder bridge with span larger than 50 m or bridge from level II according to Circular No 10/2013/TT-BXD of Ministry of Construction.

Circular 52/2013/TT-BGTVT about regulations on the management, operation and maintenance of road works focus for road only.

Decree No114/2010/NĐ-CP of Government about maintenance of construction works does not mention clearly about bridge.

From the above circular and decree that were issued recently, there is no guideline or decree that specify on management, operation and maintenance of local bridge in rural or mountainous area. It is necessary to propose such a guideline or specification for those typical local bridge.

4 Recommendation for Management and Maintenance Specification

Bases on the current guidelines and decree for bridge management and maintenance, and type of bridges in mountainous area of Vietnam, some recommendations have been proposed. The proposed guidelines expect to apply in management and maintenance of concrete and prestressed concrete bridges. The recommendations are as follow:

4.1 Receiving Finished Bridge and Put It in Operation

- The management unit, investor, contractor, supervisor and related organizations inspect and review the items together: reinforced concrete beam (prestressed concrete beam), abutment, pier, connecting roads, signs, corridors and lighting systems.
- After putting into the operation, management unit should notify to the local government about operation time, loading, speed limit
- During the warranty period, the investor and contractor are responsible for repairing the damaged, defects, and damaged parts according to the law.

4.2 Define the Scope of Management and Protection of the Bridge Include

- Superstructure: Concrete (prestressed concrete) beam, deck, handrail, barrier
- Substructure: Abutment, pier, foundation.

4.3 Establish, Recording the Bridge Management and Maintenance Documents

Before operation 10 days, the investor must have hand over the following documents to management unit:

- Maintenance procedure.
- Management and operation procedure.
- Construction drawing documents, finished construction drawing ...

- List of equipment, spare parts and materials not installed in the investment stage (if any).
- Traffic safety verification file and initial status of the bridge (if any).
- Elevation and bridge construction coordinates, landmarks serving observation (if any).

During the management process, the management unit is responsible for preparing all types of documents as follow:

- Bridge status monitoring;
- Profile of the bridge;
- Technical inspection and bridge assessment documents;
- Documents related to periodical repair, irregular repair, load test (if any).
- Documents related to traffic safety and vehicle counting data (if any).

4.4 Signs for Bridge Management and Operation

For bridges allowing cars, the following signs should plug in: name, load restriction, speed limit.

For bridges that only allow rudimentary vehicles and pedestrians, the following signs should plug in: name, no-car.

For bridges that only allow pedestrians only, the following signs should plug in: name, no-car, no-cart signs.

4.5 Traffic Organization

People and vehicles participating in traffic comply with the transportation law, signs and instructions of bridges.

The bridge management unit is responsible for organizing and guiding people in traffic to comply with regulations, guiding people to understand and comply with regulations while in traffic.

4.6 Patrolling and Monitor Bridge Conditions

The patrolling and monitoring of the bridge is organized by the bridge management unit.

The contents of the patrol include checking and detecting damage (if any) of structure (reinforced concrete or prestressed concrete beams), bridge deck, handrail, drainage system, bearing ...

When detecting damage, the detector should repair or report immediately to ensure traffic safety and report to the management unit and local government.

The bridge status patrol diary includes time, operator, detecting damage, repairing damage during patrol, damage that cannot repair during the patrol and suggested switching to regular, periodic maintenance, commenting on the possibility of ensuring traffic safety.

Number of bridge patrols, the combination between patrol and maintenance: not less than 01 time/week for bridges that operated less than 5 years, 02 times/week for bridges that operated over 05 years. The patrol is done independently or in combination with bridge maintenance.

4.7 Bridge Technical Inspection

The bridge technique checking can be checked visually or by specialized equipment.

For normal reinforced (prestressed) concrete girder span: Check the behavior of the beam through measurement, load test, record cracks and other activities to assess the bearing capacity of normal reinforced (prestressed) concrete beam.

Technical inspection with abutment, piers: assess erosion of flow to abutment, bridge pier; inspect settlement, displacement of foundation body, top of abutment, checking for crack appearance on concrete abutment.

At the end of a technical inspection, the organization or individual participating in the implementation must prepare an inspection report including: name of the bridge, inspection time, organization, individual, inspection consultant, test results and comments suggestions, reviews and recommendations.

4.8 Dealing with Deterioration in Quality and Safety of the Bridge Which Is Being Operated

When detecting or receiving a notice of deterioration in quality a bridge showing signs of the safety is not assured, the bridge management unit must comply with the following regulations: inspect the bridge quality, suspend the operation in case of danger, report on the local media, residential community and immediately report to the local government and superior agencies; repairing damage that may affect operation safety, applying protective measures to ensure safety, and limit the risk of bridge collapsing.

5 Conclusions

From the discussion and recommendations above, there are several conclusions as follow:

The current situation of management and maintenance specifications of Vietnam were evaluated.

The lack of the specification for mountainous bridge and it need to be research and issue officially for meeting the need of management and maintenance bridge of the remoted and rural areas.

Based on the current guidelines and the evaluation results of management and maintenance specifications, the basic guideline for management and maintenance of concrete and prestressed concrete bridges at rural areas has been proposed.

References

1. Local Bridge Construction and Road Asset Management (LRAMP) (2017)
2. Circular 12/2014/TT-BGTVT of Ministry of Transport: guidelines for management and operation of bridge on rural road
3. Circular 52/2013/TT-BGTVT about regulations on the management, operation and maintenance of road works
4. Decree No114/2010/NĐ-CP of Government about maintenance of construction works
5. Decree No 15/2013/NĐ-CP of Government about Quality control of construction works

Low Traffic Road Pavement Deterioration in Vietnam



Thi Kim Dang Tran

Abstract Low traffic road understood as district and commune roads take 82.61% of total road network and 94.4% local road network length. Road data bank for low traffic road were developed during Rural Transport Project No. 3 for pilot provinces namely VPROMPs includes major data of pavement age, traffic range, and condition of pavement, of shoulder, and of drainage. Roughness was collected in one pilot province using MERLIN equipment. The paper discusses on the low traffic road pavement deterioration using data from VPROMPs

Keywords Low traffic volume road · LVR · Road deterioration · VPROMPs · IRI · Fuzzy number · Fuzzy regression analysis

1 Introduction

1.1 Low Traffic Volume Road (LVR)

There is not unified concept and definition of the LVR for countries. Under SEACAP (South East Asia Community Access Programme), Laos classification gives concept of LVRs which are the roads with maximum 4-wheeled motorized vehicles of 150 per day and maximum axle load limit is 4.5 tons [1] while Vietnam classified the LVRs under SEACAP are the roads with maximum total vehicle of 200 per day. Under AFCAP (African Community Access Programme) at the same time, it is defined in the Guideline issued by SATCC for the SADC region [2] LVR are roads which may be primary, secondary or tertiary/access roads and typically carry less than 200 vehicles per day, including up to 20% commercial vehicles, and often include non-motorised traffic, particularly near

T. K. D. Tran (✉)

Faculty of Civil Engineering, University of Transport and Communications, Hanoi, Vietnam
e-mail: tranthikimdang@utc.edu.vn

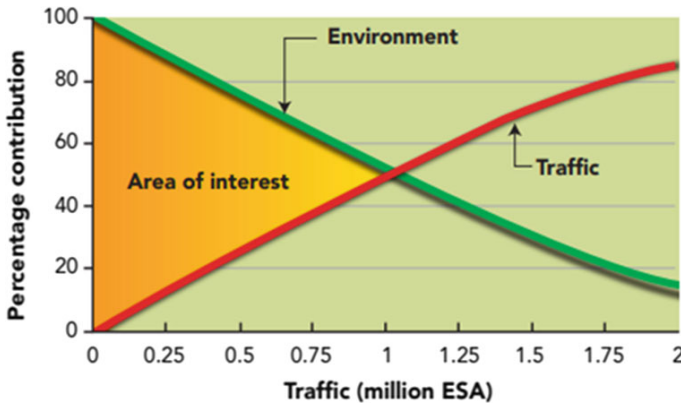


Fig. 1 Environment, traffic and road performance [3]

populated areas. LVRs as defined in [3] are Annual Average Daily Traffic (AADT), estimated for the middle of the design life, of 300 motorised 4 or more wheeled vehicles per day.

Common understanding of LVRs are the roads whose deterioration impacted by environmental factors much more than traffic, and as considering area under SEACAP, AfCAP and AsCAP, are the roads with accumulated traffic during service life of 10^6 ESALs (Fig. 1).

1.2 Overview of Deterioration of the LVRs

The deterioration of the LVRs possibly depends on environmental factors more than traffic. Road deterioration prediction could be made follows two basic approaches [4] which consist four types of road condition projection methods [5].

The first is probabilistic where the condition is predicted as probability function of a range possible conditions. The second is deterministic where the condition is predicted as a precise value on the basic of mathematical functions of observed or measured deterioration. Beside the probabilistic, regression is the most popular method for road condition prediction among the second approach.

It is particularly applicability for the deterioration prediction of the LVRs where the mechanic factor of traffic takes less important role. A typical road pavement prediction by probabilistic is given in Fig. 2 and formula (1) is an example for the regression method.

$$RCI = -5.998 + 6.870 * \ln RCI_B - 0.162 * \ln(AGE^2 + 1) + 0.185 * AGE - 0.084 * AGE * \ln RCI_B - 0.093 * \Delta AGE \quad (1)$$

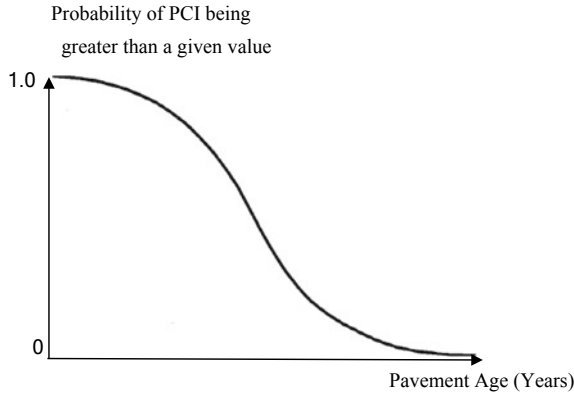


Fig. 2 Probability distribution of pavement condition index [4]

The deterioration monitoring of LVRs, medium term of 5-year program or long-term of 10 or more years program has been carrying out in AfCAP, SEACAP then ReCAP. The observed or measured data is for multi-purposes of pavement design guidance, construction and technology specifications, and pavement maintenance planning or even in long-term or medium expenditure planning for road works. The observed and measured data from monitoring trial surfacing sections in Vietnam under SEACAP—Rural Road Surfacing Trial (RRST) (2005–2012) provides a view of deterioration progress of the trial surfaces (Fig. 3) [6]. Checking LVR trial sections in Vietnam in 2019 under World Bank fund provided as long-term monitoring deterioration (Fig. 4).

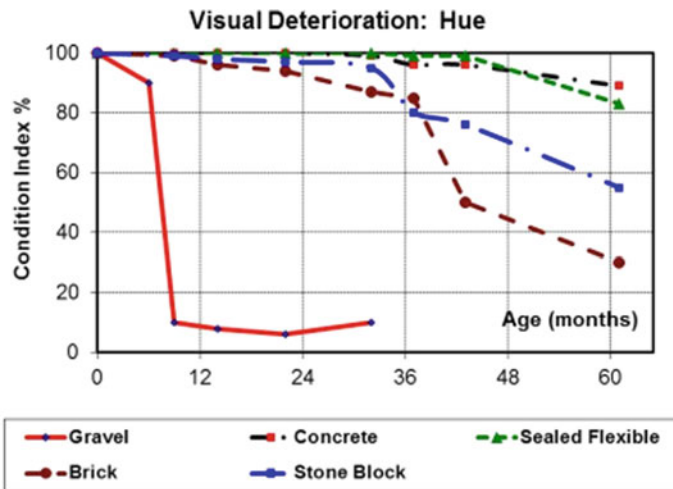


Fig. 3 Performance of different options on a single trial road (Thua Thien—Hue province, Vietnam): visual assessment of condition index (2006–2012)

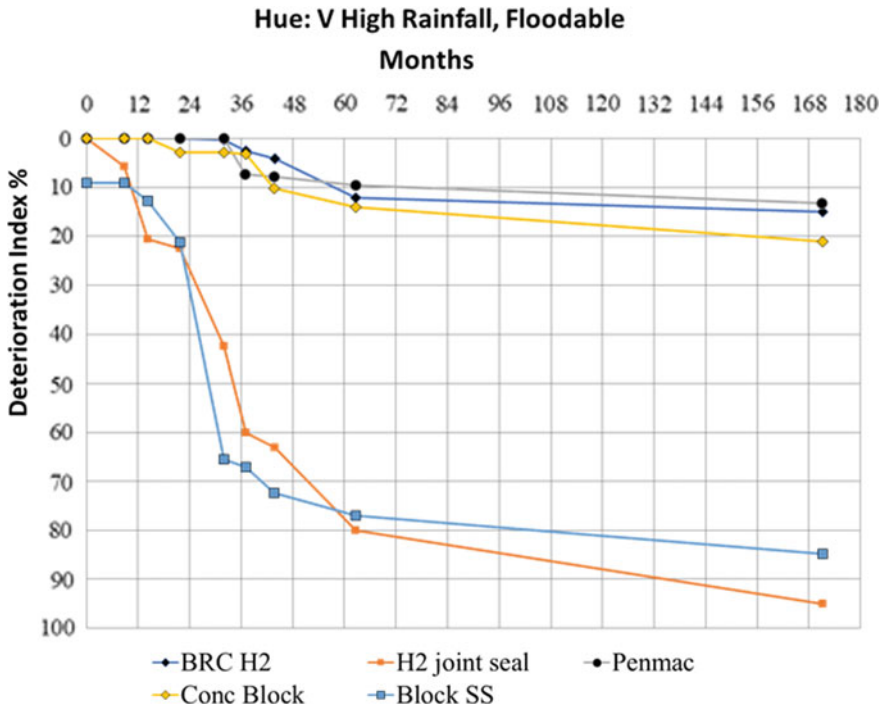


Fig. 4 Performance of different options on a single trial road (Thua Thien—Hue province, Vietnam); visual assessment of deterioration index (2006–2019)

2 Study Area and Methodology

2.1 Study Area

VPROMPs is a road data system for local road network was created under RTP3-AF World Bank in Vietnam. It was developed based on PRoMMS (Provincial Road Maintenance Management System) which provides a tool for local road inventory and assistances in prioritizing, planning and budgeting maintenance activities of roads and structures.

Beside technical data of the roads, the condition data includes Surface Condition; Drainage Condition; Shoulder/sidewalk Condition (Paved Road); Structure Condition; Accessibility; Access Constraint; and Pavement Roughness (Paved Road).

Pavement Roughness of IRI (International Roughness Index) measurement is the most challenged task of road data collection during RTP3-AF (2013). It was supposed for IRI measuring by Merlin equipment. However, there was limited numbers of Merlin equipment for only Ha Tinh province in 33 provinces under RTP3 have IRI data in VPROMPs.

Table 1 IRI estimate for unpaved pavement—the modified method

IRI	Assessment	Descriptions
Less than 3	Very good	Ride comfortable over 120 km/h. Not any defect is noticeable
3–4.5	Good	Ride comfortable up to 100 km/h. At 80 km/h, moderately perceptible movements or large undulations may be felt
4.5–8.0	Fair	Ride comfortable up to 70–90 km/h, strongly perceptible movements and swaying
8.0–12.0	Poor	Ride comfortable at 50–60 km/h, frequent sharp movements or swaying
More than 12.0	Very poor	Necessary to reduce velocity below 50 km/h. Many defects and severe disintegration (e.g.40–80 mm deep with frequency 8-16 per 50 m)

2.2 Methodology

A methodology has been developed for IRI estimation depends on riding quality namely Roughness Estimation by Subjective Evaluation [7], called original method from now on and modified to apply for different types of pavement in Ha Tinh and Thanh Hoa province during 2014 for MTEF (Medium Term Expenditure Framework) project under World Bank in Vietnam. Both original and modified methods provide “adjective (and some quantitative) descriptions of the road surface conditions and ride sensations representative for several points on the IRI roughness scale. These descriptions enable an observer traveling in a vehicle, and occasionally stopping to inspect the road, to recognize the conditions and to estimate the roughness.” [7]. Following table is example of modified method for IRI estimation of low traffic concrete road (Table 1).

IRI estimation versus relevant data from VPROMPs was analyzed using Minitab software.

3 Results and Discussion

3.1 Linear Regression Analysis

The regression equations for concrete pavement IRI estimate versus pavement age and traffic depends on the matrix of section topographic zone code, section surface condition code, and section drainage condition code. Difference between the equations is the constant which ranges from 3.4027 to 8.4160. An example of resulted equation for Flat topography, Fair surface condition and Fair drainage condition is:

Model Summary				Analysis of Variance					
S	R-sq	R-sq(adj)	R-sq(pred)	Source	DF	Adj SS	Adj MS	F-Value	P-Value
0.0843709	99.64%	99.63%	99.59%	Regression	10	1035.03	103.503	14540.18	0.000
				ADT	1	0.06	0.060	8.41	0.004
				Age of pavement	1	0.47	0.468	65.72	0.000
				Section Topographic Zone Code	2	0.08	0.040	5.55	0.004
				Section Surface Condition Code	3	132.20	44.065	6190.27	0.000
				Section Drainage Condition Code	3	7.69	2.563	360.12	0.000

Fig. 5 Variance analysis result

$$\text{Measured IRI (m/km)} = 4.4021 + 0.000181 \text{ ADT} + 0.01714 \text{ Age of pavement}$$

with Estimated IRI is at (m/km), the Pavement Age is at (years), and Traffic is at daily traffic at (Vehicles/day).

Variance analysis and Model Summary show very closed relationship and significant impact of the analyzed factors (Fig. 5).

3.2 Fuzzy Roughness Index and Approach Methodology of Regression for LVRs Deterioration

LVRs of very widespread network. District and commune roads in Vietnam which could be considered as LVRs take 82.61% of total road network and 94.4% local road network length. IRI measurement is challenges with overloaded works and budget for local road management institution. Even with new technology of Smartphone applications as RoadLab on IOS or Android, it still needs much labor and cost for IRI measurement.

The subjective evaluation as describe in Tables 1 as example make IRI estimation uncertain. A fuzzy set which could be used for dealing with classes of IRI namely fuzzy IRI. The fuzzy IRI could be described by symmetric triangular fuzzy numbers (Fig. 6).

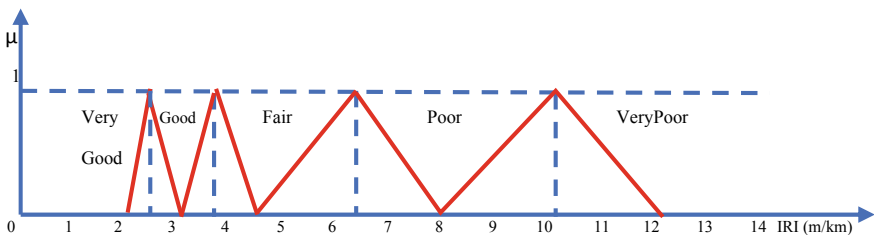


Fig. 6 The triangular IRI fuzzy numbers correspond to the descriptions of IRI estimation of concrete pavement

There are two methods of fuzzy regression analysis. The first is based on possibility concept namely possibilistic regression analysis and the second method is minimizing errors between the given outputs and the estimated outputs namely fuzzy least square method.

Having $\mu_i, i = 1, \dots, m$ presents possibility of success, $\mu_i = Poss(Y_i \approx 1)$. μ_i could be defined as a linguistic term of $\tilde{\mu}_i \in \{VeryGood, Good, Fair, Poor, VeryPoor\}$. Ratio of $\frac{\tilde{\mu}_i}{1-\mu_i}, i = 1, \dots, m$ is the possibility odds of the i th case and could be presented in model of

$$\tilde{W}_i = \ln \frac{\tilde{\mu}_i}{1-\mu_i} = A_0 + A_1X_{i1} + \dots + A_nX_{in} \quad i = 1, \dots, m$$

where $A_0, A_1, \dots, A_n \ni E$ indicates fuzzy relationship [8].

For analyzing IRI fuzzy data, a relation between a set of both crisp and fuzzy independent variables and IRI fuzzy variable is developed.

4 Conclusions

This study can be conclusion as follows:

- (i) LVRs take high proportion of road network and of local road network as well. The LVRs are road whose deterioration is impacted by environmental factors rather than traffic. The deterioration could be defined by changes of different criteria of pavement/road condition index, deterioration index, IRI which could be measured or estimated by subjective evaluation.
- (ii) A local road database with comprehensive data system of road, traffic and environment could be used for road deterioration process development. It depends on daily traffic volume (veh./day), pavement age (years), and lightly different for different set of environmental factors of topography and drainage condition, but with very high determination factor of R^2 .
- (iii) IRI could be described as symmetric triangular fuzzy number. Fuzzy regression analysis should be applied for local road deterioration. The response of IRI and most of predictors are fuzzy numbers presented by linguistic terms. IRI fuzzy number and changing IRI due to factors of traffic and environment should be defined using fuzzy regression analysis. It provides basic for local road maintenance planning for cost and benefit analysis.

Acknowledgements This research is funded by the Ministry of Education and Training, Vietnam under grant number T2020-CT-006TD

References

1. Cook J, Rolt J (2008) Low volume rural road standards and specifications. TRL Limited
2. Greening PAK, Rolt J (2003) Low volume sealed road guideline. TRL Limited
3. ERA low volume road manual—Ethiopian roads authority (2016)
4. Robinson R, Danielson U, Snaith M (1998) Road maintenance and management concepts and systems, 1st edn. MacMillan Press Ltd, Great Britain
5. Haas et al (1994) Modern pavement management. Krieger, Malabar Fa
6. Cook J, Pham GT (2014) Rural road pavement and surfacing designs options—public disclosure authorized—improving vietnam sustainability
7. Archondo-Callao RS (1999) Unpaved roads' roughness estimation by subjective evaluation, Transport No. RT-2
8. Pourahmad S et al (2011) Fuzzy logistic regression based on the least squares approach with application in clinical studies. *Comput Math Appl* 62:3353–3365

Numerical Analysis of the Influence of Shield-Gap Pressure on the Volume Loss and Surface Settlement of the TBM Tunneling



Thach Bich Nguyen, Thanh Le Le, and Phuong Duy Nguyen

Abstract Safely tunneling in the urban area by Tunnel Boring Machine (TBM) is assuring by maintaining the front face pressure and a suitable grout backfilling method to minimize the volume loss due mainly to the effects of over cutting and lining assembling inside the shield. However, the phenomenon is a three dimensional and complex interaction problem which seems could be solved only by a numerical approach. This paper presents a simplified 2D numerical model to analysis the effects of the balanced and compensated pressures of TBM to the volume loss and surface settlement. The numerical simulation was applied for the typical cross section of the Ho Chi Minh metro Line 1 and the results were confronted to the monitoring data during the construction. The simple numerical assessment allows a deeper understanding of the complex interaction between the face pressure, backfill grout injection pressure and the shield gap pressure and consequently the surface settlement.

Keywords TBM tunneling · Volume loss · Surface settlement · Earth balanced · Settlement monitoring

1 Introduction

During the past decade, earth balanced pressurized-face (EPB) tunnel boring machines (TBM) have recorded big step of progress and established it-self as a proven tunneling technic in adapting to divers ground conditions which were less applicable before. The technic is usually used in urban areas [1] for the construction of the shallow tunnel such as the metro system where the control of ground movement is in central important. Even thought, EPB shield tunneling unenviably

T. B. Nguyen (✉) · P. D. Nguyen
Faculty of Civil Engineering, University of Transport and Communications, Hanoi, Vietnam
e-mail: ntbich@utc.edu.vn

T. Le Le
Shimizu Corporation Vietnam, Ho Chi Minh City, Vietnam

causes some ground and underground-water disturbing leading to the ground movements in short and long term. Those unexpected ground movement could have adverse effects on both under and above-ground surface man-built structures [2]. Therefore, it is a major concern in urban area tunnel construction to evaluate tunneling-induced ground movements in preventing any risk of excessive surface settlement and damages to the surface structures.

Experiences with EPB shield machine show that these ground disturbances are strongly influenced by many parameters of machine: tunnel face support pressure, taper of the TBM shield (shield gap), backfill injection procedure, solidification of the grout and jacking forces but also the advancement speed. Due to this complex interaction between the different aspects along with the complexity of the soils behavior in urban area, the numerical approach seems to be the best suitable method for analyzing the problem. On another hand, Panet [3] and later on Benmebarek et al. [4] prove that by using the simple 2D models with the concepts of stress release and volume loss respectively at each stage of the tunneling construction, the ground-structure interaction behavior could be efficiently analyzed.

This paper presents the application of a simple 2D numerical model for analyzing the effect of lateral (shield gap pressure) in EPB tunnel-boring process. The model is referred to a typical cross section of Ho Chi Minh city metro line 1 (Ben Thanh—Suoi Tien). The underground section of the metro line had successfully completed in 2019. Sufficient experimental data, especially the monitored surface settlements were available [5].

2 EPB TBM Tunneling Numerical Simulation

2.1 TBM's Along Shield Pressure

Figure. 1 shows pressure balancing and grout injection arrangement on the contour of the shield TBM for HCM city line 1 metro. For assuring the minimum volume loss, during tunneling, any eventual gap should be fill-up with grout and the earth pressure at front face should be compensated by the balanced muck pressure (p_1).

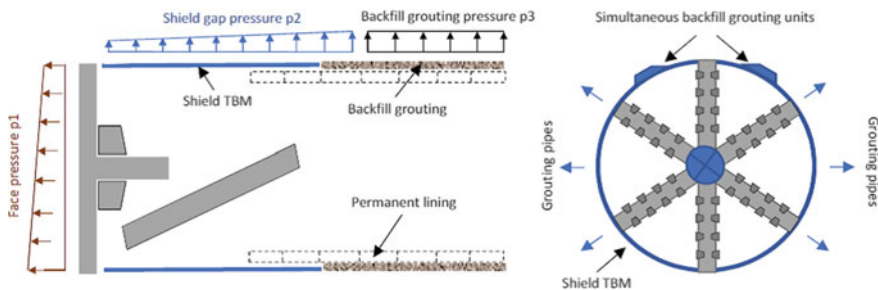


Fig. 1 Illustration of the shield TBM and grouting arrangement of HCM city line 1 metro

The pressures applied along the shield (p_2) and behind the shield-tail (p_3) are controlled through the grouting pressure at the injection pipes disposing around the shield (06 pipes), on the lining elements (06 pipes) and the backfill grouting unit (Fig. 1). However, during the tunneling, only front face pressures are monitored through four (04) earth pressure gages equipped on the back of the excavation chamber. The actual pressure acts on the excavation contour is then an unknown parameter for any numerical model.

Ring and Comulada [6] in their 3D numerical analysis show that the maximum settlement was calculated in the area of shield where only p_2 reacts against the ground movement toward the shield gap. That section should be considered as the most critical especially when the pressure p_2 greatly influences the relaxation of the ground and consequently the surface settlements. Just behind the shield-tail where greater injection pressure was applied, the vertical displacements were slightly reduced. The ground movement becomes stable in the area of lining as the grouting is settled and the installation of the stiff segmental lining prevents any large displacements to occur.

Since the existing shield gap between the shield and excavated profile extends from the cutter head to the ring gap, the magnitude of pressure p_2 is governed by face pressure p_1 through the pressurized mixture of excavated muck and conditioning agents that fill the shield gap and the backfill injection pressure, which are actively controlled by the shield operation process.

Reversely, considering the 2D configuration of the most critical section of the shield TBM, maximum surface settlement then could be predicted if we could determine the shield gap pressure p_2 based on p_1 and grout injection pressure. In the next part of the paper, we present an assessment of the shield gap pressure value in regard to the grout injection and face pressures by a numerical model in confronting with the available surface settlement monitoring data.

2.2 *Field Measurement and Monitoring Data*

Figure 2 presents the layout of surface settlement monitoring arrangement along shield tunneling from chainage KM1+400 to KM1+500. The section connects Opera House station where the two tunnels are in vertical superposition and Ba Son station where the two tunnels are in parallel horizontally.

Figure 3 shows the typical cross section of the tunnels and the settlement monitoring arrangement on the surface at chainage KM1+500.

For the shield TBM operation, Zizka and Thewes [7] prove that the target face support pressures and shield gap grouting pressures could be determined by analytical limit equilibrium methods for each ring. During shield tunneling operation, the minimum required face support pressures and ring injection pressures are provided for shield machine operating to ensure that the ground settlement remains within admissible ranges. Table 1 presents the shield TBM geometrical characteristics and operating balanced face pressure and ring injection pressure.

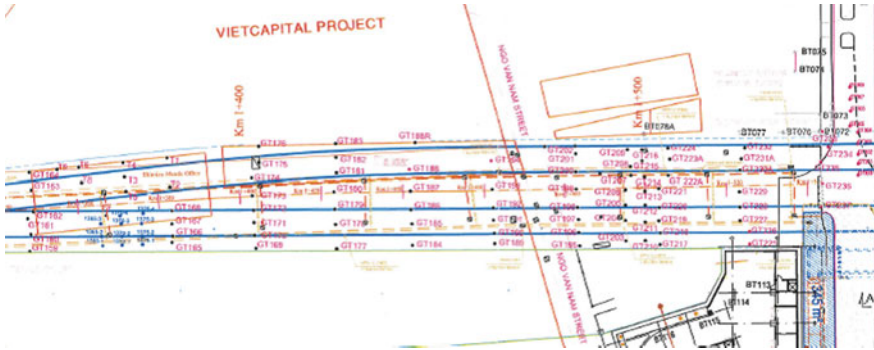


Fig. 2 Monitoring layout and TBM advancement scheme [5]

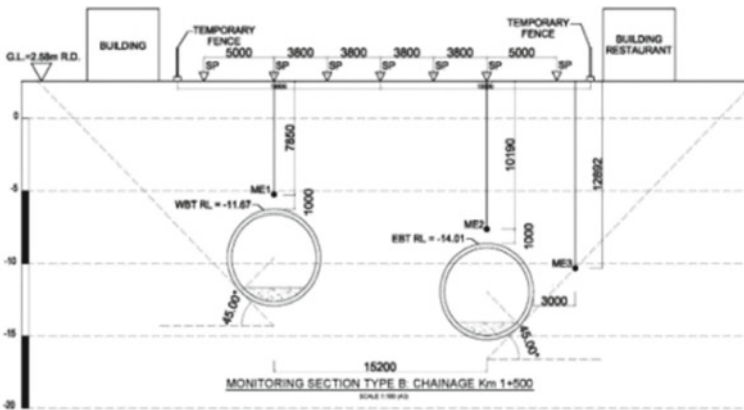


Fig. 3 Typical cross section at the Ba Son station

Table 1 Characteristics of the EPB shield TBM using for HCM metro line 1 [5]

Parameters	Unit	Value
Shield machine outer diameter	m	6.79
Segment outer diameter	m	6.65
Shield gap	mm	45
Skin plate length (excluding cutter head)	m	7.6
Balanced earth pressure (p_1)	MPa	0.18–0.22
Grouting Injection Pressure (injection pipes and backfill unit)	MPa	0.23

Table 2 Surface settlement monitoring data for section of chainage KM1+500 [5]

Monitoring point	Distance X (m)	Vertical settlement recorded (mm)				
		22/12/2018	05/01/2019	24/01/2019	23/02/2019	28/02/2019
GT216	-9	-26.5	-26.3	-25.2	-25.7	-25.2
GT215	-6	-22.8	-22.7	-22.1	-22.6	-22.1
GT213	-2	-6.5	-6.3	-5.4	-6.0	-5.4
GT212	4	2.9	3.2	2.4	3.1	3.0
GT211	8	2.8	3.1	2.3	3.0	2.9
GT210	14	-1.6	-1.9	-1.1	-1.8	-1.7

The monitored tunneling-induced surface settlements at the section of chainage KM1+500 are presented in Table 2. The vertical displacements are presented periodically from 22nd December 2018 to 28th February 2019 corresponding to the period after the passage of the first TBM (west tunnel—Fig. 3).

3 Numerical Model and Results

3.1 Numerical Model

A two-dimensional finite element model was used for the analysis of the selected cross section of chainage KM1+500. The analysis was performed with the software Plaxis-3D. The Mohr-Coulomb soil model was used for simulating the soils behaviour. The tunnelling was simulated in three main steps: initializing the stresses state, contour excavation and ring pressure application. Figure 4 presents the FEM numerical model meshes.

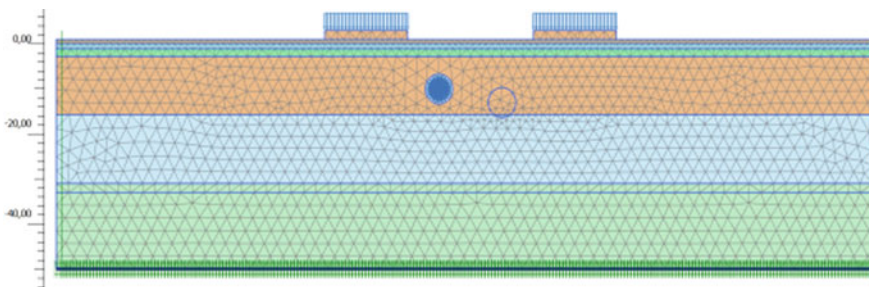


Fig. 4 2D finite elements model meshes in considering the road pavement and existing buildings

3.2 Numerical Results

The geotechnical data using for the numerical model is presented in Table 3. For assessment, the applied shield ring pressure was varied from 130 to 190 kPa. Those values were selected based on the vertical stress level at tunnel axis. Figure 5 compares the numerical calculation results of the surface settlements in regard to the monitoring data. The numerical results settlement curve seems to have a quit similar form but the uplift movements are more significant especially at high values of shield gap pressure.

Even the calculated surface settlement trough seems to be influenced by a more significant uplift movement, the maximum monitored values could agree with the case of numerical calculation when p_2 of 160 kPa was applied. This shield gap pressure value was much lower in comparing to the operational injection pressure of about 230 kPa and the face pressure of about 200 kPa (Table 1) and a little lower than vertical stress at the tunnel axis. The results show that the transfer of the shield gap pressure from the face pressure and the grout injection pressure is not a simple interaction.

Table 3 Soils condition parameters using for the numerical modelling

Geotechnical parameters	Unit	1st layer (Backfill)	2nd layer (Ac1)	3rd layer (As1)	4th layer (As2)	5th layer (Dc)
Layer thickness	(m)	1.1	1.7	14.0	17.0	16.0
Unit weight	(kN/m ³)	18.0	16.0	19.5	19.5	21.0
Young's modulus	(kPa)	1.8×10^3	1.8×10^3	4.2×10^3	13.9×10^3	20.5×10^3
Friction angle	(°)	28	15	31	17	34
Cohesion	(kPa)	8.5	14	4	1.1	22
Poisson's coefficient	–	0.35	0.48	0.33	0.33	0.35
Permeability	(m/day)	8.64×10^{-2}	8.64×10^{-5}	4.32	4.32	8.64×10^{-6}

Fig. 5 Calculated surface settlements resulted in comparing with the monitoring data

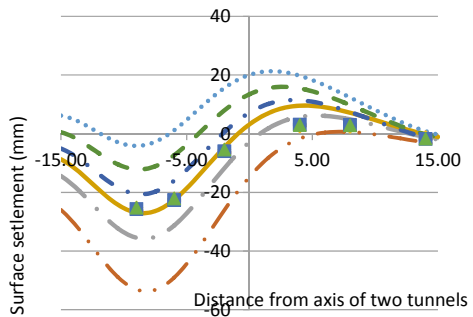
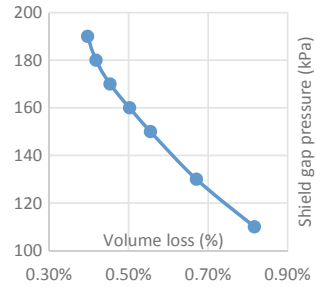


Fig. 6 Shield gap supported pressure influences to the volume loss



According to Peck [8], the volume loss could reflect directly the tunneling-induced settlement surface according to Eq. (1) where V_s is the volume of the settlement trough and D is the tunnel diameter. The volume loss then could be estimated and presented in Fig. 6 in regard to the shield gap pressure.

$$V_L = V_s / (\pi D^2 / 4) 100\% \tag{1}$$

We could observe that volume loss decreases when shield gap pressure increases. Above the value of 180 kPa, the volume loss changes slowly with pressure increasing.

4 Conclusions

Shield-gap pressure is considering as the critical operational TBM’s parameter for limiting the volume loss and the excessive surface settlements. For a deeper understanding of the shield-gap pressure transfer and the effect of face pressure and injection pressure on it, the simple 2D numerical analysis of a typical section of the HCM metro line 1 was performed. The result of surface displacements was compared with the available monitoring data for a reasonable shield-gap pressure assessment. The results show that the shield gap pressure could be lower than the face balanced pressure and the grout injection pressure. Based on the parametric numerical analysis results, the relationship between the volume loss and the shield gap pressure was established. The volume loss decreases when the pressure increases up to the value of 180 kPa when the change is slowdown.

References

1. Xie X, Yang Y, Ji M (2016) Analysis of surface settlement induced by the construction of a large-diameter shield-driven tunnel in Shanghai, China. *Tunn Undergr Space Technol* 51:120–132

2. Zhang Z, Zhang M, Jiang Y, Bai Q, Zhao Q (2017) Analytical prediction for ground movements and liner internal forces induced by shallow tunnels considering non-uniform convergence pattern and ground-liner interaction mechanism. *Soils Found* 57:211–226
3. Panet M (1988) Calcul de soutènement des tunnels a section circulaire par la méthode convergence-confinement—Tunnels et Ouvrages Souterrains, Vol 77, pp 228–232. *Ponts et Chaussées Press*
4. Benmebarek S, Kastner R, Ollier C (1998) Auscultation et modélisation numérique du processus de creusement a l'aide d'un tunnelier. *Geotechnique* 48(6):801–818
5. Shmz-Maeda JO (2019) Ground and building monitoring report for shield tunnel (TBMS). UMRLT1-CP1b-TBMS-MON-RPT-00568-A. HCM city
6. Ring B, Comulada M (2018) Practical numerical simulation of the effect of TBM process pressures on soil displacements through 3D shift iteration. *Undergr. Space* 3:297–309
7. Zizka Z, Thewes M (2016) Recommendations for face support pressure calculations for shield tunnelling in soft ground. In: *Deutscher Ausschuss für unterirdisches Baue (DAUB)—German Tunnelling Committee (ITA-AITES)*
8. Peck RB (1969) Deep excavation and tunnelling in soft ground. In: *Proceedings of 7th international conference on soils mechanics and foundation engineering, Mexico City, State of the Art*, pp 225–290

Developing the Success Index of Public-Private Partnership Transportation Projects in Vietnam



Thac Quang Nguyen, Dinh Thuc Le, and Duy Liem Nguyen

Abstract Like other construction projects, project success has always been the ultimate goal in Public-Private Partnership projects. However, it will be difficult for private and public sectors to define whether their projects have been successful or not if the success index is not considered. Thus, this study aims to construct a success indicator for Public-Private Partnership transportation projects in Vietnam via a case study. 15 success criteria were identified from a literature review and expert interview. Using factor analysis, four principal factors were grouped based on 15 identified success criteria, namely project objectives, reliable and quality service, effective output, and project management. Finally, the fuzzy synthetic evaluation (FSE) method computed the success index for Rach Mieu Bridge project is 4.15 which is considered as highly successful. This study might provide decision-makers with a quantitative tool to make the decision for implementing PPP projects effectively and assuring sustainable infrastructure development in Vietnam.

Keywords Success index · Public-Private partnership · Bridge project · Vietnam · Fuzzy synthetic evaluation

1 Introduction

Public-Private Partnership (PPP) emerged as an effective procurement in delivering infrastructure and public service. PPP schemes brought benefits in procurement for the parties. Nevertheless, not all PPP transportation projects are successful. The

T. Q. Nguyen (✉)

University of Transport and Communications, Campus in Ho Chi Minh City, Ho Chi Minh City, Vietnam

e-mail: ntquang@utc.edu.vn

D. T. Le

Department of Construction Management, Pukyong National University, Busan, South Korea

D. L. Nguyen

Ho Chi Minh City University of Technology and Education, Ho Chi Minh City, Vietnam

© The Author(s), under exclusive license to Springer Nature Singapore Pte Ltd. 2021

229

T. Bui-Tien et al. (eds.), *Proceedings of the 3rd International Conference on Sustainability in Civil Engineering*, Lecture Notes in Civil Engineering 145, https://doi.org/10.1007/978-981-16-0053-1_29

Sydney Cross City Tunnel were examples of the failure of PPP procurement [1]. In fact, it will be difficult for private and public sectors to define whether their projects have been successful or not if the success index is not considered [2]. Therefore, this study aims to assess the success of PPP transportation projects in Vietnam by evaluating a success index for Rach Mieu Bridge project as a case study. This result will help both practitioners and researchers to be more depth understanding of the success model in PPP transportation projects in Vietnam for good investment decision making.

2 Literature Review

PPP nature is complex due to the huge amount of investment and long-term contractual periods [3]. Determining whether a PPP project is successful or not has still remained an ambiguous perception [4]. To select criteria for evaluating the PPP project success, it is essential to satisfy the general criteria of project success in the construction industry. Therefore, many authors have sought different ways to gain success for PPP projects, such as Tam [5], Yuan et al. [6], Kusljic and Marenjak [7], Villalba-Romero and Liyanage [8], Osei-Kyei and Chan [2]. Whereby, fifteen success criteria were identified from prior related studies.

3 Research Methodology

The process of research methodology is presented in Fig. 1.

4 Data Analysis and Result

A questionnaire survey is constructed based on fifteen success criteria for PPP transportation projects. The pre-test of the questionnaire was carried out with five experts who had many experiences regarding PPP transportation projects in Vietnam. As a result, fifteen success criteria were agreed upon by the consensus of five experts, and no criteria were suggested to add to the list. 21 valid questionnaires have received for one month. The obtained sample size is small. The low number could be explained as (1) PPP model in Vietnam is still a new model and (2) respondents who are working in PPP projects hold a conservative perspective towards sharing information leading to fewer practitioners are willing for participating in this investigation. However, the reliability of investigation is high because 42.9% of respondents had at least 10 years of experience regarding PPP transportation projects, 47.6% of the respondents had more than 5 years of experience and the remaining percentage had less than 5 years. Apart from this, the number of

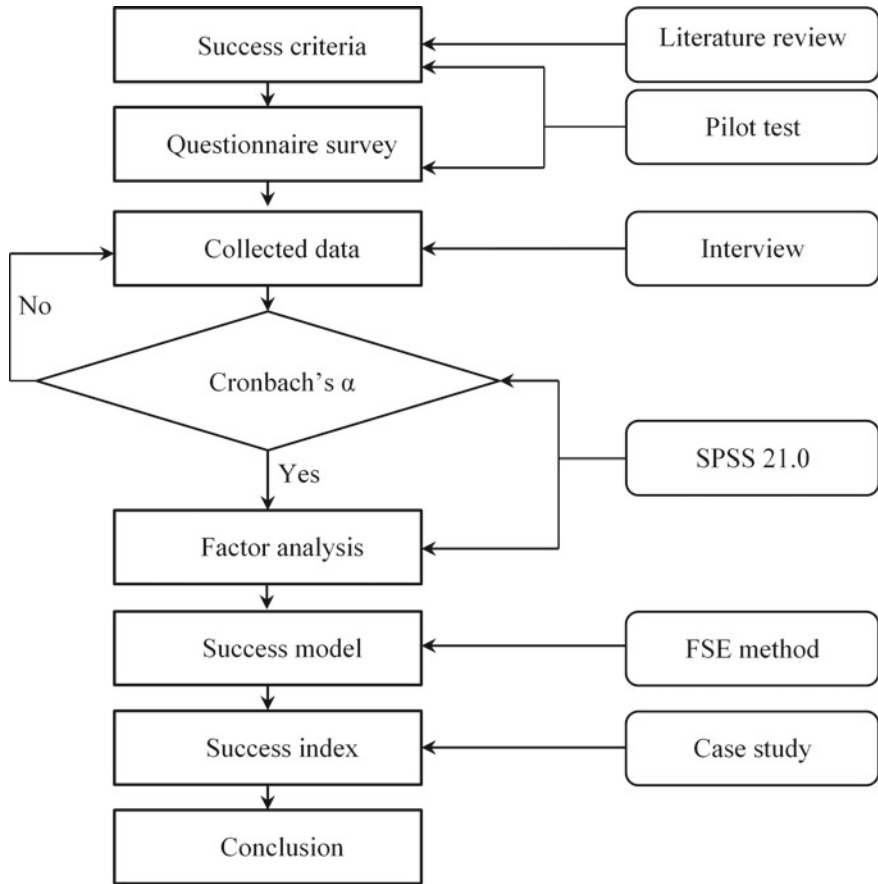


Fig. 1 Research methodology framework

respondents from the public sector accounts for 52.4% and the private sector of 47.6%. Majority of respondents is engineering with 38.1%, team leader of 33.3% and director accounts for 28.6%.

Cronbach’s Alpha was utilized to consider the reliability and internal consistency of the obtained data. Cronbach’s α value of the present study is 0.896 which greater than 0.70 [9]. Hence, the data of this investigation ensures for further analysis.

The factor analysis method is employed to group interrelated sub-variables into small groupings from a large number of factors. The value of Bartlett’s test of sphericity is significant with the Chi-Square value of 218.647 and the associated significant level (p) is 0.000. In addition, the obtained KMO value is 0.610 which greater than 0.50 [10]. Therefore, the collected data is suitable for factor analysis. The principal component analysis using varimax rotation was adopted to extract the

principal factors. Four principal factors were established with eigenvalues greater than 1.0, explaining 78.756% of the total variance with factor loadings of success criteria exceed 0.50. Four principal groups are presented in Table 1.

FSE method is then used to establish a project success index from identified success criteria. FSE was a developed method from fuzzy set theory (FST). As a branch of FST, FSE is considered as a prominent method for multi-criteria synthetic evaluation in complex and uncertain environment [11]. The process of the FSE

Table 1 Weight (W) and membership function of success criteria and success groups

Factor groupings	W	MF of level 2	MF of level 1
G1. Project objectives	<i>0.405</i>		[0.00, 0.04, 0.18, 0.44, 0.35]
Local development	0.167	[0.00, 0.05, 0.14, 0.48, 0.33]	
Long-term partnership	0.165	[0.00, 0.05, 0.14, 0.52, 0.29]	
Contract disputes	0.161	[0.00, 0.00, 0.33, 0.38, 0.29]	
Equitable legal system	0.189	[0.00, 0.00, 0.05, 0.29, 0.67]	
Stakeholder satisfaction	0.167	[0.00, 0.00, 0.14, 0.62, 0.24]	
Environment impact	0.150	[0.00, 0.14, 0.29, 0.33, 0.24]	
G2. Reliable service	<i>0.191</i>		[0.00, 0.09, 0.22, 0.43, 0.26]
Service quality	0.335	[0.00, 0.10, 0.24, 0.38, 0.29]	
Productivity	0.318	[0.00, 0.14, 0.19, 0.52, 0.14]	
Technology transfer	0.347	[0.00, 0.05, 0.24, 0.38, 0.33]	
G3. Product output	<i>0.259</i>		[0.00, 0.03, 0.24, 0.42, 0.31]
Health and safety	0.216	[0.00, 0.10, 0.52, 0.29, 0.10]	
Profitability	0.246	[0.00, 0.05, 0.14, 0.48, 0.33]	
Achieving VfM	0.280	[0.00, 0.00, 0.10, 0.43, 0.48]	
Risk management	0.258	[0.00, 0.00, 0.24, 0.48, 0.29]	
G4. Project management	<i>0.145</i>		[0.00, 0.00, 0.17, 0.29, 0.55]
Completion in budget	0.494	[0.00, 0.00, 0.19, 0.29, 0.52]	
Completion on time	0.506	[0.00, 0.00, 0.14, 0.29, 0.57]	

Table 2 Coefficient of success index for PPP bridge and tunnel projects

Factor grouping	Index	Ranking	Coefficient*	Linguistic
Project objectives	4.10	2	0.251	Very important
Reliable service	3.85	4	0.235	Important
Product output	4.01	3	0.245	Very important
Project management	4.38	1	0.268	Very important
Total	16.34			

*Coefficient = DI of each group/ΣDI of all groups

method is described as detail in research of Osei-Kyei and Chan [12]. Using FSE method and mean score, the weight and membership function (MF) of each success criterion (level 2) and success criteria groups (level 1) is presented in Table 1.

Then, the success index of each group is computed by normalizing the MF of level 1 with a set of corresponding grade E = (1, 2, 3, 4, 5). For example, the group of project objective is calculated as follows:

$$\text{Index of project objectives} = [0.00, 0.04, 0.18, 0.44, 0.35] \times (1, 2, 3, 4, 5) = 0.00 \times 1 + 0.04 \times 2 + \dots + 0.35 \times 5 = 4.10.$$

Similarly, the remaining groups and the coefficients of factor groupings are summarized in Table 2.

Finally, success index is expressed as follows [12]:

$$\begin{aligned} \text{Success index} = & (0.268 \times \text{Project management}) + (0.251 \times \text{Project objectives}) \\ & + (0.245 \times \text{Product output}) + (0.235 \times \text{Reliable service}) \end{aligned} \tag{1}$$

4.1 Calculating the Success Index for Rach Mieu Bridge Project

In order to illustrate the suitability of the above mentioned model, this section investigated and assessed the success of the Rach Mieu Bridge project which has implemented by the BOT model. This investigation relies on the information of the government’s website, investor’s website and the respondents who have involved in the Rach Mieu Bridge project. The average score of each criterion is computed according to the judgment of 16 respondents. The respondents were requested to rate based on a five-point Likert scale: 1—not reached; 2—fairly reached; 3—moderately reached; 4—highly reached; 5—extremely reached [12]. The result of the investigation is shown in Table 3.

Finally, by calculating the average score of each success criteria group, the success index for Rach Mieu Bridge project is defined by Eq. (1):

$$\text{Success index of Rach Mieu Bridge project} = (0.268 \times 4.50) + (0.251 \times 4.04) + (0.245 \times 3.89) + (0.235 \times 4.17) = 4.15.$$

Table 3 Average score of each success group in Rach Mieu Brige project

Code	Success criteria	Average score
G1.	Project objectives	4.04
G2.	Reliable service	4.17
G3.	Product output	3.89
G4.	Project management	4.50

Using the success evaluation model, the success index of Rach Mieu Bridge project is 4.15, mean that it is assessed as highly successful. Basically, this project has satisfied the expectations of stakeholder as well as selected criteria.

5 Conclusions

The previous studies noticed that there is no consensus in the perception of project success in the construction industry. In order to enrich refer to this knowledge, this study attempted to develop a success index for PPP transportation projects in Vietnam by a case study with the support of 15 identified success criteria and 4 success criteria groupings. This finding will help the government and private sector more depth understand in the success of PPP model in Vietnam, whereby the decision-makers might assess the success of other PPP projects in specific circumstances via the proposed model.

References

1. Davies A, Moore M (2005) No way out of tunnel torture. Sydney Morning Herald, 21 Oct
2. Osei-Kyei R, Chan APC (2017) Comparative analysis of the success criteria for public-private partnership projects in Ghana and Hong Kong. *Project Manage. J.* 48(4):80–92
3. Zhang S, Chan APC, Feng Y, Duan H, Ke Y (2016) Critical review on PPP Research—a search from the Chinese and International Journals. *Int. J. Project Manag* 34(4):597–612
4. Ahamd U, Ibrahim YB, Bakar ABA (2018) Malaysian public private partnership projects: project success definition. *Int J Eng Technol* 7:33–37
5. Tam CM (1999) Build-Operate-Transfer model for infrastructure developments in Asia: reasons for successes and failure. *Int J Project Manage* 17(6):377–382
6. Yuan J, Zeng AY, Skibniewski MJ, Li Q (2009) Selection of performance objectives and key performance indicators in public–private partnership projects to achieve value for money. *Constr Manage Econ* 27(3):253–270
7. Kusljic D, Marenjak S (2013) Critical PPP/PFI project success criteria for public sector clients. *Tehn Vjesn* 20(6):947–954
8. Villalba-Romero F, Liyanage C (2016) Evaluating success in PPP road projects in Europe: a comparison of performance measurement approaches. *Transp Res Procedia* 14:372–381
9. Field AP (2005) *Discovering statistics using SPSS*, 2nd edn. Sage Publications, London
10. Ismail S (2013) Critical success factors of Public-Private Partnership (PPP) implementation in Malaysia. *Asia-Pacific J Bus Adm* 5(1):6–19

11. Singh D, Tiong RLK (2005) A fuzzy decision framework for contractor selection. *J Constr Eng Manage* 131(1):62–70
12. Osei-Kyei R, Chan APC (2018) Evaluating the project success index of public-private partnership projects in Hong Kong. *Constr Innov* 18(3):371–391

River, Coastal, Environmental and Water Resources Engineering

Applicability of Duct-Type Devices to Erosion Tests of Sediments



Dake Chen, Jinhai Zheng, Chi Zhang, Yigang Wang, and Yuan Li

Abstract Methods of determining sedimentary bed shear stress in duct-type erosion testing devices were investigated by a series of erosion threshold tests. Results show that the smooth-wall assumption method under-estimates the actual shear stress. The Colebrook equation method can be applied to estimate the shear stress provided a suitable overall roughness height is applied. The side-wall correction method over-estimates the actual shear stresses for rough samples, but accurately estimates the shear stress for relatively smooth samples. A modified side-wall correction method proposed in this study accurately estimates the shear stress for both rough and smooth samples. It provides a universal approach to determining bed shear stress on sediment samples for different duct-type erosion testing devices.

Keywords Erosion test · Duct-type erosion testing device · Shear stress · Erosion threshold

1 Introduction

The erosion properties of sediments play a significant role in various domains, e.g., bridge failure, bathymetry evolution, marsh contraction, water environment and water ecology [2, 9]. However, due to the complicated interactions between the

D. Chen · Y. Wang

Key Laboratory of Ministry of Education for Coastal Disaster and Protection,
Hohai University, Nanjing, China

J. Zheng (✉) · C. Zhang · Y. Li

State Key Laboratory of Hydrology-Water Resources and Hydraulic Engineering,
Nanjing, China

e-mail: jhzheng@hhu.edu.cn

D. Chen

State Key Laboratory of Coastal and Offshore Engineering, Dalian University of Technology,
Dalian, China

State Key Laboratory of Estuarine and Coastal Research, Shanghai, China

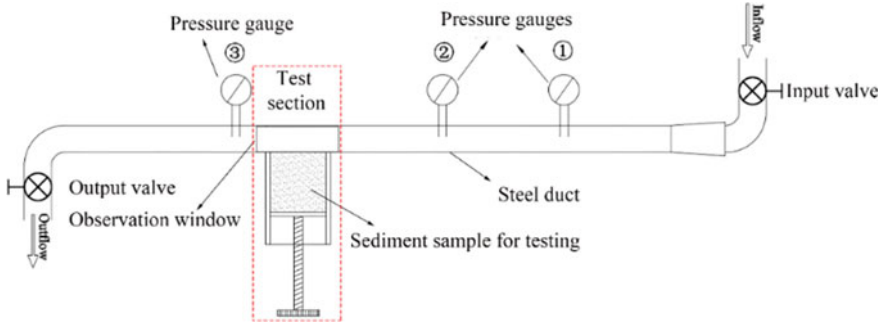


Fig. 1 Schematic diagram of a duct-type erosion testing device

hydraulics and the sedimentary bed, it remains a significant challenge to accurately quantify the erosion properties of sediment [3].

In the past decades, different kinds of erosion testing devices have been employed to investigate the erosion properties of sediment, including straight open flumes, rotating annular flumes, duct-type devices, rotating cylinder devices, submerged jet-type devices and benthic in situ devices. This study focuses on the duct-type device, which is a kind of apparatus consisting of a duct system and an injector-like tube with a piston assembly. The schematic diagram of a typical duct-type device is shown in Fig. 1. A typical duct-type device usually consists of a duct system and an injector-like tube assembled at the test section of the duct. A moving piston sits inside the tube for protruding the testing sediment sample into the duct. Water is made to flow over the sample, and as the sample erodes, it is raised to keep its top-surface flush with the bottom of the duct, so that erosion is caused by shear stress.

When using the duct-type device, the erosion rate of the sediment can be easily obtained by recording the piston movement. However, it is difficult to determine the bed shear stress (i.e., the shear stress acting on the surface of the sediment sample), as direct measurement is usually impracticable in the enclosed duct. Therefore, some indirect methods have been adopted to estimate the bed shear stress in duct-type devices, including the smooth wall assumption, Moody diagram, pressure drop (which has been proved unreliable) and side-wall correction method. However, the applicability and accuracy of most of these methods remain unclear. In this study, methods of determining bed shear stress in duct-type erosion testing devices are investigated based on a series of erosion tests of uniform sand.

2 Existing Methods of Determining Bed Shear Stress in Duct-Type Devices

2.1 Smooth Wall Assumption

In developing the duct-type devices named the Sediment Erosion at Depth Flume (Sedflume), McNeil et al. [7] assumed the wall of the duct and the surface of the sediment sample are both hydraulically smooth, and adopted the Darcy equation along with the Prandtl equation to estimate the shear stress on an eroding sample:

$$\tau_b = \frac{1}{8}f\rho U^2 \quad (1)$$

$$\frac{1}{\sqrt{f}} = 2.0 \log_{10}(\text{Re}\sqrt{f}) - 0.8 \quad (2)$$

where τ_b is bed shear stress; ρ is water density; f is friction factor; U is depth-averaged velocity; Re is Reynold number, which is defined as $\frac{UD_h}{\nu}$, with ν being kinematic viscosity of water; D_h is hydraulic diameter.

2.2 Moody Diagram (or Colebrook Equation)

Briaud et al. [1] also adopted the Darcy equation to calculate bed shear stress in the duct-type device namely the Erosion Function Apparatus (EFA). Instead of assuming hydraulically smooth conditions, they took account of bed roughness by adopting an overall roughness height for the wall of the duct and the sample. They estimated the friction factor using the Moody diagram which can be described by the Colebrook equation:

$$\frac{1}{\sqrt{f}} = -2.0 \log_{10} \left(\frac{k_s/D_h}{3.7} + \frac{2.51}{\text{Re}\sqrt{f}} \right) \quad (3)$$

where k_s is roughness height. Briaud et al. [1] recommended a roughness height of 0.5 times the sediment particle diameter because it was assumed that the top half of a particle in the surface of the sample protrudes into the duct flow whereas the bottom half is buried in the sediment mass. Crowley et al. [4] evaluated the roughness height as 0.7654 times of the sediment diameter for the SERF, based on measurements from the shear sensor in high-speed duct flows. However, Crowley et al. [5] re-evaluated the roughness height as 1.47 times the particle diameter using CFD simulations.

2.3 Side-Wall Correction Method

Dey and Debnath [6] introduced a side-wall correction procedure from an open rectangular flume when they used a duct-type device to measure the erosion rates of uniform sand. According to the side-wall correction procedure, the total flow area is divided into two sub-areas corresponding to the bed and the sidewalls, respectively. The average flow velocity and the hydraulic gradient in these areas are assumed equal. This method adopts the Darcy equation to calculate bed shear stress, but estimates the friction factors of the wall and of the sediment surface respectively by different formulas. The Blasius equation (Eq. 5) was adopted to calculate the friction factor of the wall which was assumed hydraulically smooth; and the Colebrook equation (Eq. 6) was used to compute the friction factor of the sediment sample:

$$f_w = \frac{0.3164}{\text{Re}_w^{0.25}} \quad (5)$$

$$\frac{1}{\sqrt{f_b}} = -2.0 \log_{10} \left(\frac{k_{s,b} U}{3.7 \nu \text{Re}_b} + \frac{2.51}{\text{Re}_b \sqrt{f_b}} \right) \quad (6)$$

where f_w and f_b are friction factors related to the wall and the sediment sample, respectively; Re_w and Re_b are the Reynolds number of flow associated with the wall and the sedimentary bed regions, respectively; $k_{s,b}$ is the roughness height of the surface of the sample, which was arbitrarily equated with the sediment diameter.

The relationship between the Reynolds number associated with the wall and the Reynolds number associated with the sample, and the relationship between the friction factor related to the wall and the friction factor related to the sample, were obtained from the continuity equation and the assumption of the same hydraulic grade line for the wall and sedimentary bed regions. The two relationships read:

$$\text{Re}_w = \frac{4UA}{\nu \chi_w} - \frac{\text{Re}_b \chi_b}{\chi_w} \quad (7)$$

$$\frac{f_w}{\text{Re}_w} = \frac{f_b}{\text{Re}_b} \quad (8)$$

where A is the flow area of the duct; χ_w and χ_b are the wetted perimeters of the wall and of the sediment sample surface, respectively.

The side-wall correction method solved the closed equations (Eqs. 5–8) to obtain the friction factor of the sediment sample. Then the Darcy equation was used to calculate the shear stress at the sample from this calculated friction factor.

2.4 Modified Side-Wall Correction Method

A modified method is proposed here based on the side-wall correction method. In this modified method, the roughness height of the sample is equated to half of the sediment diameter instead of the sediment diameter, following the recommendation of Brauid et al. [1]. This is more reasonable as only the top half of a surface particle protrudes over the bottom of the duct. In addition, the roughness of the wall is accounted for by using the Colebrook equation:

$$\frac{1}{\sqrt{f_w}} = -2.0 \log_{10} \left(\frac{k_{s,w} U}{3.7 \nu \text{Re}_w} + \frac{2.51}{\text{Re}_w \sqrt{f_w}} \right) \quad (9)$$

where $k_{s,w}$ is the roughness height of the wall.

3 Evaluation Methodology and Experimental Setup

Erosion threshold tests were performed on six groups of well-sorted uniform sand with median diameter ranged from 0.183 to 1.09 mm, using a duct-type erosion testing device. Critical velocities of these six groups of uniform sand were measured and from them critical shear stresses were estimated by each method described above (except the pressure drop method). These estimates of the critical shear stresses were compared with the classic Shields threshold criterion. If the critical shear stresses estimated by a certain method fitted the Shields threshold curve well, the method was assumed useful.

The procedure for each erosion threshold test was as follows. After the tube carrying the prepared sand sample was fixed to the duct, the duct was filled with water slowly and the sample was positioned to be flush with the bottom of the duct. The flow rate was increased slowly and step by step from a very low value. For each step increase in flow rate, the velocity was measured and the sample surface was observed. Four different intensities of sand particle movement were defined and observed during the tests. Slight movement was defined as when occasional grains are moving in some locations of the bed; moderate movement was defined as when grains are moving frequently in many locations; general movement was defined as when grains are moving frequently at most locations; strong movement was defined as permanent grains are moving at all locations all the time. The four kinds of movement can be seen as different criteria of incipient motion. Though the tests, the critical velocities of six groups of uniform sand for the observed four kinds of motions can be measured. Then the alternative methods described above are applied to calculate the critical shear stresses corresponding to the four criteria.

4 Results and Analyses

The critical shear stresses estimated from the above methods were compared with the Shields threshold criterion (see Fig. 2). The classic Shields curve, representing mean threshold values, along with the upper limit and lower limit of the threshold values, were plotted using the formulas of Paphitis [8].

From Fig. 2a, it can be seen that the smooth wall assumption method under-estimates the shear stress on the relatively rough sample. For the sand of

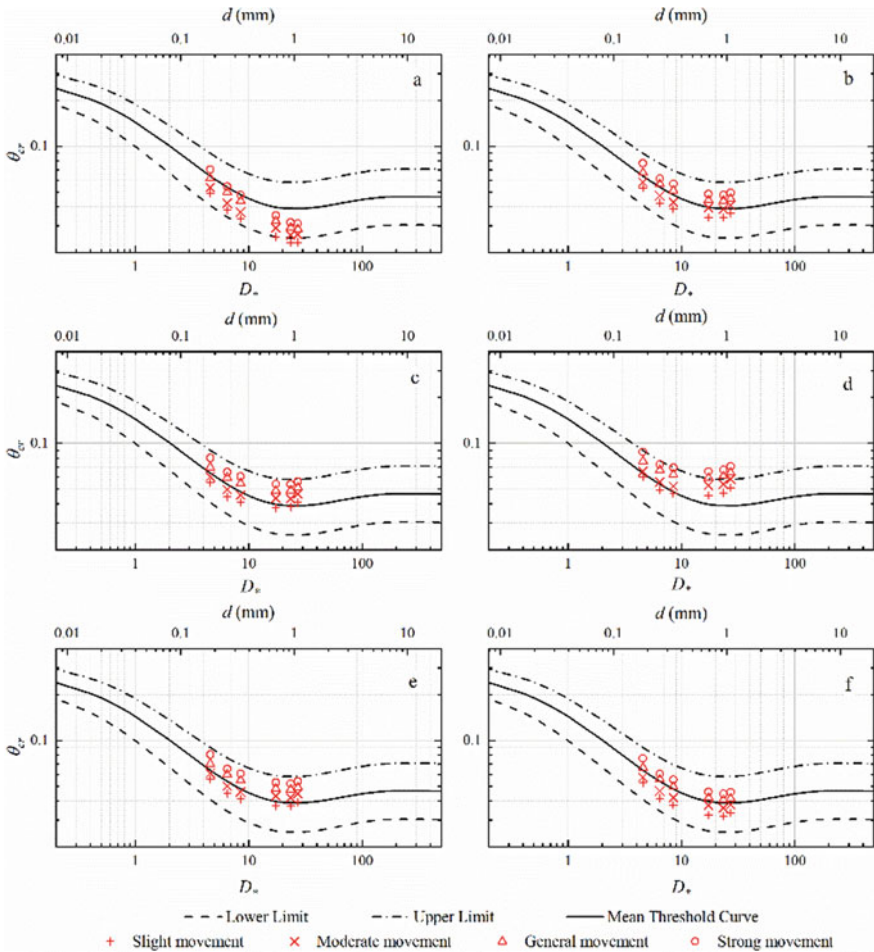


Fig. 2 Comparison of the Shields threshold criterion and critical shear stresses of six groups of uniform sand estimated by: **a** Smooth wall assumption method; **b** Colebrook equation method with an overall roughness height of $0.5d$; **c** Colebrook equation method with an overall roughness height of $0.7654d$; **d** Colebrook equation method with an overall roughness height of $1.47d$; **e** Side-wall correction method; **f** Modified side-wall correction method

median size of 0.183 mm, the estimated shear stresses for incipient motions agree well with the classic Shields threshold values. However, with increasing sediment particle size, the estimated threshold shear stresses become lower than the classic Shields threshold criterion and the discrepancies between the estimated threshold shear stresses and the mean Shields threshold values rapidly amplify.

When the overall roughness height is valued as half of the sediment diameter, the estimated shear stresses for incipient motions by the Colebrook equation method approximately match the mean Shields threshold curve (see Fig. 2b). The mean Shields curve is between the threshold values for general movement and for moderate movement when the sediment diameter is no larger than 0.336 mm; the mean Shields threshold curve is between the threshold values for moderate movement and for slight movement when the sediment size is 0.692 mm or larger. When the overall roughness height is assumed 0.7654 times the sediment diameter, the Colebrook equation method seems to produce accurate threshold values for the sand of diameter equaling 0.336 mm, but over-predicts the threshold values for rougher samples (see Fig. 2c). When the overall roughness height is assumed to be 1.47 times the sediment diameter, the Colebrook equation method over-estimates the threshold shear stresses for the six groups of uniform sand (Fig. 2d).

The side-wall correction method proposed by Dey and Debnath [6] performs similarly to the Colebrook equation method with the overall roughness height set to 0.7564 times the sediment diameter (see Fig. 2c and e).

The modified side-wall correction method proposed in this paper performed well in estimating bed shear stress. The estimated bed shear stresses for each stage of incipient motion generally follow the form of the mean Shields curve (Fig. 2f), with the classic Shields threshold curve between the threshold values for general movement and for moderate movement.

5 Conclusions

Existing common methods of determining sedimentary bed shear stress in duct-type erosion testing devices were investigated by conducting a series of erosion threshold tests with a duct-type device. The following conclusions and suggestions were obtained.

1. The smooth wall assumption generally under-estimates the actual shear stresses. The coarser the sediment sample, the larger the error of the estimated shear stress.
2. The Colebrook equation method can be applied to estimate the bed shear stress provided a suitable overall roughness height is applied (however which is “device specific”).
3. The side-wall correction method over-estimates the actual shear stresses for rough samples (sediment diameter larger than 0.336 mm), but accurately

estimates the shear stress for relatively smooth samples (sediment diameter no larger than 0.336 mm).

4. The modified side-wall correction method accurately estimates the actual shear stress and provides a universal approach of determining the bed shear stress on the sediment sample in different duct-type erosion testing devices. In these devices it is more reasonable for the roughness height of the sediment sample to take the value of half of the sediment diameter than the sediment diameter.
5. When the sample is smooth enough, all of the evaluated methods, i.e., the smooth wall assumption method, the Colebrook equation method, the side-wall correction method and the modified side-wall correction method, tend to provide similar estimates of shear stress.

Acknowledgements This work was supported by the Open Research Fund of State Key Laboratory of Coastal and Offshore Engineering, Dalian University of Technology (LP2020); the Open Research Fund of State Key Laboratory of Estuarine and Coastal Research (SKLEC-KF202003); the Fundamental Research Funds for the Central Universities, Hohai University (B200202052); the Open Research Fund of Key Laboratory of Ministry of Education for Coastal Disaster and Protection, Hohai University, Nanjing 210098, China (201914); the National Natural Science Foundation of China (51879096); the National Science Fund for Distinguished Young Scholars (51425901). Also, the valuable suggestion from Prof. Bruce Melville and Mr. Graham Macky are highly appreciated.

References

1. Briaud JL, Ting F, Chen H, Cao Y, Han SW, Kwak K (2001) Erosion function apparatus for scour rate predictions. *J Geotechn Geoenviron Eng* 127(2):105–113
2. Chen D, Wang Y, Huang H, Chen C, Yuan C (2017) A behavior-oriented formula to predict coastal bathymetry evolution caused by coastal engineering. *Cont Shelf Res* 135:47–57
3. Chen D, Wang Y, Melville B, Huang H, Zhang W (2018) Unified formula for critical shear stress for erosion of sand, mud, and sand-mud mixtures. *J Hydraul Eng* 144(8):04018046
4. Crowley RW, Bloomquist D, Hayne JR, Holst CM, Shah F (2012) Estimation and measurement of bed material shear stresses in erosion rate testing devices. *J Hydraul Eng* 138(11):990–994
5. Crowley RW, Robeck C, Thieke RJ (2013) Computational modeling of bed material shear stresses in piston-type erosion rate testing devices. *J Hydraul Eng* 140(1):24–34
6. Dey S, Debnath K (2001) Sediment pickup on streamwise sloping beds. *J Irrig. drain. Eng.* 127(1):39–43
7. McNeil J, Taylor C, Lick W (1996) Measurements of erosion of undisturbed bottom sediments with depth. *J. Hydraul. Eng.* 122(6):316–324
8. Paphitis D (2001) Sediment movement under unidirectional flows: an assessment of empirical threshold curves. *Coast Eng* 43(3):227–245
9. Zheng J, Zhang C, Demirbilek Z, Lin L (2014) Numerical study of sandbar migration under wave-undertow interaction. *J. Waterw. Port Coast. Ocean Eng.* 140(2):146–159

Experimental Measurements of Wave Transformation on Coral Reefs



Pham Thi Thuy, Le Hai Trung, and Nguyen Manh Linh

Abstract Extensive laboratory experiments were carried out to investigate the wave transformation on coral reefs in the East Sea of Vietnam. These coral reefs usually have very high fore-reef slopes and followed by a wide coral platform which is very different from gently-sloping beaches. The process takes place in two parts including from deep water to the reef edge and from the edge to the submerged reefs. The experiments were designed into measure wave spectrum, broken waveforms, and wave attenuation on the shallow reef part. Remarkably, extreme wave scenarios were generated to confirms the broadening of wave spectrum and the appearance of low-frequency waves during propagation. The wave spectrum shape in the platform is similar to those after undergoing repeated wave break, changing from sharp to obtuse.

Keywords Wave transformation · Coral reef · Extreme waves · Infragravity waves

1 Introduction

The East Sea of Vietnam has archipelagos, including many floating and submerged reefs. A cay always has a part above the sea water level, even at the highest tide. The topographic conditions of these cays usually have a very high fore-reef slope with the bottom changing sharply from very deep to very shallow, followed by a wide coral platform with a fairly large area extending into the reef's core (Fig. 1).

P. T. Thuy (✉)

Thuyloi University and Le Quy Don Technical University, Hanoi, Vietnam

e-mail: thuy39vtl@gmail.com

L. H. Trung

Thuyloi University, Hanoi, Vietnam

N. M. Linh

Vietnam Academy for Water Resources, Hanoi, Vietnam

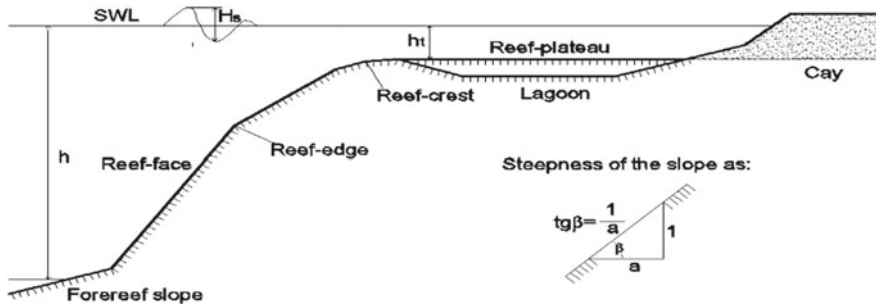


Fig. 1 A representative cross-section of a coral reef

Previous researches mainly focused on the wave transmissions for the gently-sloping beaches (steepness $< 1/20$) with gradual depth variation. Studies of wave propagation on the coral reefs were mostly observational based. The results showed that there was a significant decrease of the observed waves and a significant expansion of the spectrum wave during the wave transformation. Most of the energy loss comes from the vicinity of the spectral peak, and energy shifts to harmonics of the peak of the spectrum can be seen [1]. In addition, experimental studies also pointed out the wave hydrodynamic regime through steep submerged reefs ($\tan\alpha = 1/5$ and $1/10$). Tuan and Cuong [2] showed that the wave energy dissipation, wave transmission on the reef flat could be split into two regions: the reef-edge surfzone and the one behind the surfzone. Two experimental formulas of wave spectral parameters (H_{m0} and $T_{m-1, 0}$) were finally created for the wave breaking zones and the region behind the respectively wave break zone. Thus, quite a few studies exist for the wave transformation on coral reef with a high fore-reef slope have been studied in the world, and in Vietnam, they are still scattered. The purpose of this article is to point out the features of wave transformation over the reef such as variation of the wave spectra, breaker types, breaker indices, the decrease in wave heights and the formation of infragravity waves. Physical model experimental data were collected in the design of extreme wave condition with a fore-reef slope $m = 1/2$ based on topographic simulation for a cay.

2 Experimental Conditions

The simulated topography of wave transmission is based on topographic documents of the SC cay of Viet Nam. The slope of 08 directions of SC island is calculated ranging from $1/1.8$ to $1/20$. The steep slope directions are North ($1/1.8$) NorthEast ($1/2$); East ($1/2.3$); NorthWest ($1/5.2$) and SouthEast ($1/7.8$). While the South, SouthWest, and West have the slope of $1/17$; $1/19.5$ and $1/20$, respectively.

In the model, the section in the Northeast direction with a slope of $1/2$ was selected as this direction, based on many years' observations in the Spratly islands

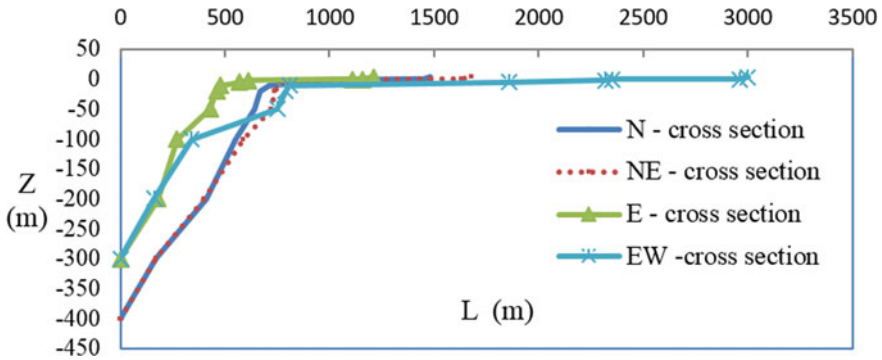


Fig. 2 Some cross sections of the reef by directions (chart altitude)

and wave statistics shows the most affected direction of the wave regime (NorthEast waves) with the longest maintenance time. In this section, the reef-crest is located at an elevation of -7.88 m, followed by reef flat of 600 m long (Fig. 2).

The experimental design water level data calculated based on the global tidal database for the extreme water level value with the test frequency of $P = 3.33\%$ which is $Z_{tk} = +2.00$ m. The data of deep water waves for these area was based on data of water level and deep water waves from following sources: Refer to 14TCN 1613 - 2012 and using global wave model database WaveWatch III and the design wave parameters of European Meteorological Organization Furgo with a 100-year period at a depth of 93 m [3]. The experiment was conducted by 04 scenarios: 01 topographic scenario $m = 1/2$; 01 scenario with water level $H = +2.0$ m; 04 variations of deep water wave: $P = 3.33\%$; 5% ; 10% and Furgo100 years.

3 Laboratory Experimental

The scale model experiments were conducted in the 37 m long and 1.0 m wide wave flume of the Vietnam Academy for Water Resources. The test waves were JONSWAP spectra with the peak enhancement factor $\gamma = 3.30$ as found most suitable for storm waves at the deep-sea region off the coast of Vietnam. Each of experiments were carried out, lasted approximately 700 waves to sufficiently cover the main frequency domain of desired wave spectra and allow for stable statistical properties of wave heights.

Due to the wave flume capacity and boundary condition parameters to select the model ratio: $N_L = 75$ (long scale) and $N_t = 8.66$ (rate of time). The experiment arranged 04 wave gauges WG1, WG2, WG3 and WG4. Of which, WG1 measured deep-water waves (17.4 m); WG2 measured waves at the top of the reef (9.3 m); WG3 measured waves on the reef flat (8 m), and WG4 measured near-shore waves

Table 1 The matrix of experimental program

Wave frequency	Fore-reef slope $\tan\alpha$ (-)	Prototype		Model	
		Wave height H_s (m)	Wave period T_p (s)	Wave height H_s (m)	Wave period T_p (s)
P 3.33%	1/2	12.68	13.8	0.169	1.59
P 5%	1/2	12.38	13.6	0.165	1.57
P 10%	1/2	11.78	13.3	0.157	1.54
Furgo 100 years	1/2	7.875	11.9	0.105	1.37

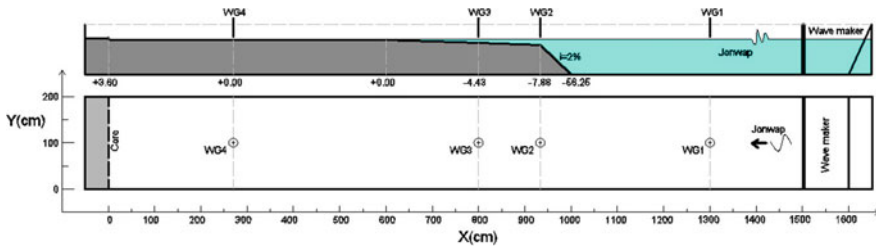


Fig. 3 Reef profile geometry and gauge locations

(2.67 m) from the shore. The matrix of experimental program is shown in Table 1 and diagram in Fig. 3

During the reliability test, the gauges are calibrated to minimize errors. Carry out 03 identical tests with regular and irregular waves. For regular waves, H_i and T_p measurements show typical errors below 1.5 and 0.1% respectively. For irregular waves, the error of the parameters from the three tests is less than 1%.

4 Results and Discussion

4.1 Wave Spectrum Variation Across Submerged Reefs

The variation of wave spectrum across submerged reefs according to experimental results at locations WG1, WG2, WG3 and WG4 through 4 experimental plans was analyzed by Mike Zero model/WS Wave Analysis Tools modular/WS Linear Spectral Analysis. Since in all 4 experimental scenarios, the shape of the wave energy spectra diagrams were quite similar, for example, the wave energy spectra of $P = 3.33\%$ at four locations are shown in Fig. 4.

Considering the direction of wave transformation, the wave spectral density peaks varies as the waves transmit. The wave spectral density peak energy at WG2 (the reef-crest) was greater than that in deep-water area WG1 (0.0076 and 0.0059 m^2/Hz), and when wave transmitted into shallow-water area on the reef flat

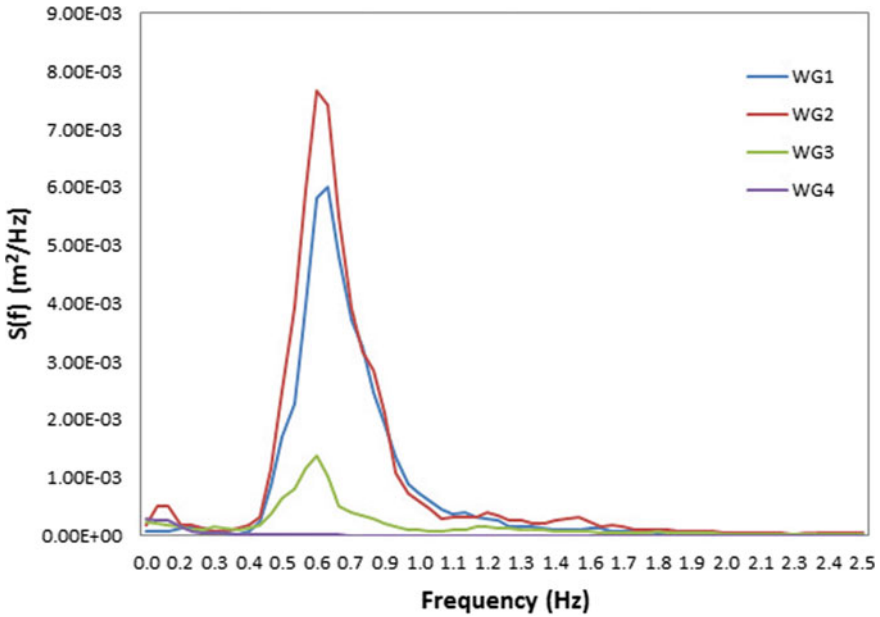


Fig. 4 Wave energy spectra at various positions, scenario of P = 3.33%

at WG3 and WG4, the spectral peak energy decrease significantly (0.0014 and 0.00028 m²/Hz).

4.2 Wave Spectrum Variation Across Submerged Reefs

Since in all 4 experimental scenarios at WG4 (in shallow water area), there is no great difference in energy of the spectrum. The wave spectrum shape in the platform is similar to those after undergoing repeated wave break, changing from sharp to obtuse. In the surfzone with high relative wave energy the distribution shape, particularly at the middle part, is most complex and evolves considerably. Behind the surfzone the shape becomes rather simple and stable [4]. Remarkably, the appearance of infragravity waves (IG)—waves with very low frequency or long period (greater than 25 s [5]). Analysis spectral peak periods had a remarkable change, especially at WG4 had spectral peak periods ranging from 22 to 28 s corresponding to four options.

The wave transformation on coral reef where having a sudden transition in depth across a steep slope, it is impossible not to consider the classification of breaking types and its evaluation criteria. The applicable standard is Iribarren $\xi = \frac{\tan \alpha}{\sqrt{H/L_0}}$.

Table 2 Preliminary classification of breaking waves on submedged crest of SC island

Options	Fore-reef slope	$\tan\alpha$	ξ_i	Type of breaking
P3.33%	$\frac{1}{2}$	0.5	2.29	Plunging
P5%	$\frac{1}{2}$	0.5	2.30	Plunging
P10%	$\frac{1}{2}$	0.5	2.30	Plunging
Furgo 100 years	$\frac{1}{2}$	0.5	2.49	Plunging

When waves transmit from deep-water with the small wave steepness ($H/L = 0.036 \div 0.043$) and face with the coral slope, with the height of SC island reef-crest is of -7.88 m, deeply submerged below the transmitted wave level (-2.0 m), the height of wave was increased in order to conserve energy. The wave transformation has a rather high speed of $C = 18.6\text{--}21.5$ m/s, the waves pass over the reef-crest, due to the shortage of falling waves. The relative water depth over the reef crest is a dominant factor affecting the breaking characteristics. The relative crest submergence is reduced, there is a considerable increase in the intensity of wave breaking over the reef and a corresponding decrease in wave transmission and reflection as the submergence is reduced [6].

Depending on the fore-reef slope ($\tan\alpha$) and the steepness of the incident wave (H/L_o), it could be preliminarily classifies and determines the breaking type (according to Iribarren parameter ξ) on the submedged crest as follows (Table 2).

Thus, the Iribarren number (ξ_i) calculated at the top of the edge reef ranges from 2.29 to 2.49 in the above 4 plans. According to the surf-similarity standard, the breaking type on on submedged crest is plugging. In this form, the wave crest is asymmetrical, but curled up to embrace the air sacs in the wave, which then collided with the slope and bounces forward perpendicular water jets.

When waves propagate from deep water into the shallow water, the deep water wave undergo many physical dissipation processes dissipates wave, the wave height decreases significantly. The effect of wave reduction on the reef is illustrated in Fig. 6. The wave reduction effect index: $\varepsilon = (1 - K_t) \times 100\%$, within $K_t = H_{s,i}/H_{t,i}$ is a ratio of wave height in the reef flat to the wave heights in the reef crest. When passing on the shallow reef part to a position 200 m from the shore, the wave height decreases by 83–87% and continues to reduce when entering the core (Fig. 6). It is this feature of the cays that greatly decrease the wave height from the offshore to the reef's core. Another reason is that the reef flat are quite long, and the bed friction on the platform is quite large, which also plays a significant role in the reduction in the wave height and the great dissipation of the wave energy. This is also a natural feature that helps to stabilize floating reefs over time, together with measures to prevent erosion for the floating reefs (Fig. 5).



Fig. 5 Experimental model of breaking wave on the steep

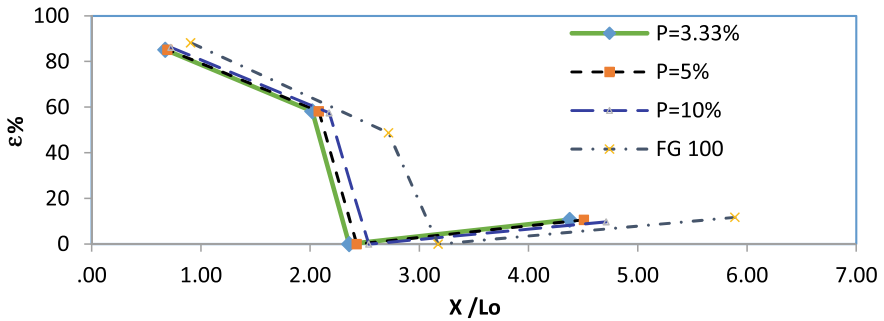


Fig. 6 Effect of wave reduction on the reef by options

5 Conclusions

This study can be conclusion as follows:

1. The energy of spectral peaks varied as the waves transmitted. The maximum spectral peak energy density at the WG2 section at the reef-crest and when entering the shallow water area on the coral platform, the peak spectral density decreased markedly. The energy density in shallow water area did not vary largely, changing from sharp to obtuse
2. Occurrence of waves with period from 22 to 28 s, called infragravity waves. The energy of the short waves is largely dissipated, while the long wave energy remains quite large.
3. The broken wave pattern at the slope-edge was plugging. After breaking, waves continue to propagate to the island, under the impact of bed friction the reef flat, the wave height decreased (200 m from the core, $\epsilon = 83-87\%$). However, studying the effect of bed friction in this study has not be done yet because the model ratio is 1/75 and the roughness is extremely difficult to be shown in this model.

References

1. Gourlay MR (1994) Wave transformation on a coral reef. *Coast Eng* 23(1-2):17–42
2. Tuan TQ, Cuong DQ (2019) Wave transmission across steep submerged reefs. In: *International conference on asian and pacific coasts*. Springer, Singapore, pp. 687–694
3. Institute of technical Engineering (2015–2019) National level independent research; Research on solutions to prevent erosion of a cay in Spratly Islands
4. Lugo-Fernández Alexis, Roberts Harry H, Suhayda Joseph N (1998) Wave transformations across a Caribbean fringing-barrier coral reef. *Cont Shelf Res* 18(10):1099–1124
5. Baldock TE (2012) Dissipation of incident forced long waves in the surf zone-Implications for the concept of “bound” wave release at short wave breaking. *Coast Eng* 60:276–285
6. Battjes JA (1975) Surf similarity. In: *Coastal engineering 1974*

Investigation the Influence of Cua Tien Urban Area on Flood Drainage Capacity of Vinh River, Vinh City, Nghe an Province by Numerical Model



Nguyen Viet Thanh, Hoang Nam Binh, and Bui Vinh Phuc

Abstract Cua Tien urban area is located in Vinh riverside, Vinh City, Nghe An province. The New urban area was constructed in flood plain of Vinh river may reduce the flood drainage capacity. This research used numerical model to investigate the flood distribution, water depth change and current speed during history flood based on the bathymetries measured in May 2005 and November 2019 in the Vinh river. The results show that, the highest water depth before and after construction of Cua Tien urban area increased only 7.5 cm and the largest current speed reached to 1.58 m/s. These results indicated that the construction of Cua Tien urban area only causes a very small impact on the increasing of water level in upstream and does not change the flood drainage capacity of Vinh River in the rainy season.

Keywords Vinh river · Flood current · Flood drainage capacity · Flood water depth

1 Introduction

Vinh River is a natural small river in Vinh City, Nghe An province, Vietnam. The Vinh river starting from the Duoc intersection where the Thap river is end and divided into Vinh river and Gai river. The Vinh river flowing through the territory of Cua Nam, Vinh Tan, Trung Do wards, Vinh city flows into Ca River (local name Lam River) in Ben Thuy and the to the East Sea of Vietnam. Vinh river has a length of 5.8 km, width of 19–60 m. The main function of Vinh river is to provide additional water sources for pumping stations No. 11, 12, 13 on Hoang Can canal,

N. V. Thanh (✉) · H. N. Binh · B. V. Phuc
University of Transport and Communications, Hanoi, Vietnam
e-mail: vietthanh@utc.edu.vn

N. V. Thanh · H. N. Binh
Viet Trung Research and Development Center, University of Transport and Communications,
Hanoi, Vietnam

to drain water for 19,450 ha of area in Kenh Thap—Lam Tra—Hoang Can and Vinh river basin during the flood season through Ben Thuy sewer combined with waterway transport. The two sides of the river currently have ring dikes, some sections are eroded, encroached to build houses, narrowing the river bed cross section [1].

Cua Tien new urban area is one of the key areas in Vinh City, Nghe An province. The North of the Cua Tien urban area is adjacent to the Vinh River, connected to the city center of Vinh through the Cua Tien No. 1 Bridge and Cua Tien Bridge No. 2 (Fig. 1). Due to the lowland terrain and located next to the sea, it is affected by strong storms and heavy rain, it is often flooded in the rainy season. The construction of Cua Tien new urban area can also affect safety, and flood drainage capacity of Vinh River under the impact of flood. Recently, the media has reported that the urban area of Cua Tien built in the dyke protection corridor, potentially affecting flood drainage of Vinh River [2, 3]. This study used numerical models to investigate the influence of Cua Tien New Urban Area on the safety and flood drainage capacity of the Vinh River and the safety of stone embankment when implementing the project of Cua Tien New Urban Area, Vinh City, Nghe An Province.

2 Data and Methodology

2.1 Input Data

Hydrology data such as water level and current was observed from 10th to 18th, November 2019 from Railway bridge and Cua Tien No. 2 bridge.

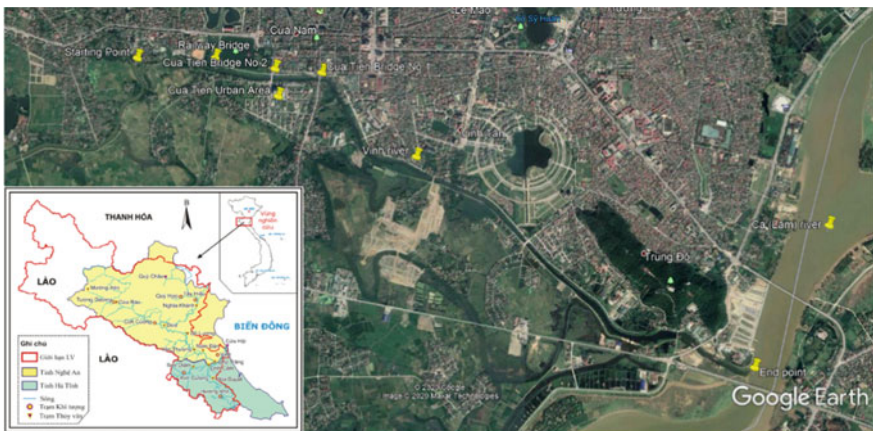


Fig. 1 Study area and Vinh river

Bathymetries use in the simulation were surveyed in May 2005 and November 2019 [4].

Flood river discharges in 1978 (equal 1%) and 1988 (equal 5%) were selected for representative flood in Vinh river. The 1978 flood has two flood peaks (double flood) while flood 1988 is a extreme flood with only one peak [4]. Based on the results of 1D hydraulic model, the flood discharges in Sep 1978 and Oct 1988 at Bien Thuong Luu, Bien Cau Duoc and Bien Cua Tien presented in Fig. 2.

2.2 Numerical Model Setup

MIKE 21 HD model was setup with the domain is plotted in Fig. 3. Upstream boundary called Bien Thuong Luu located in Thap river where is far from Duoc intersection 650 m. Boundary in Gai river called Bien Cau Duoc is located at Duoc bridge far from the intersection 450 m and the boundary in downstream of Vinh river call Bien Cua Tien far from Cua Tien No. 1 about 100 m.

Discharges were applied for Bien Thuong Luu and Bien Cau Duoc boundaries, the water level was applied for boundary at Cua Tien bridge No. 1.

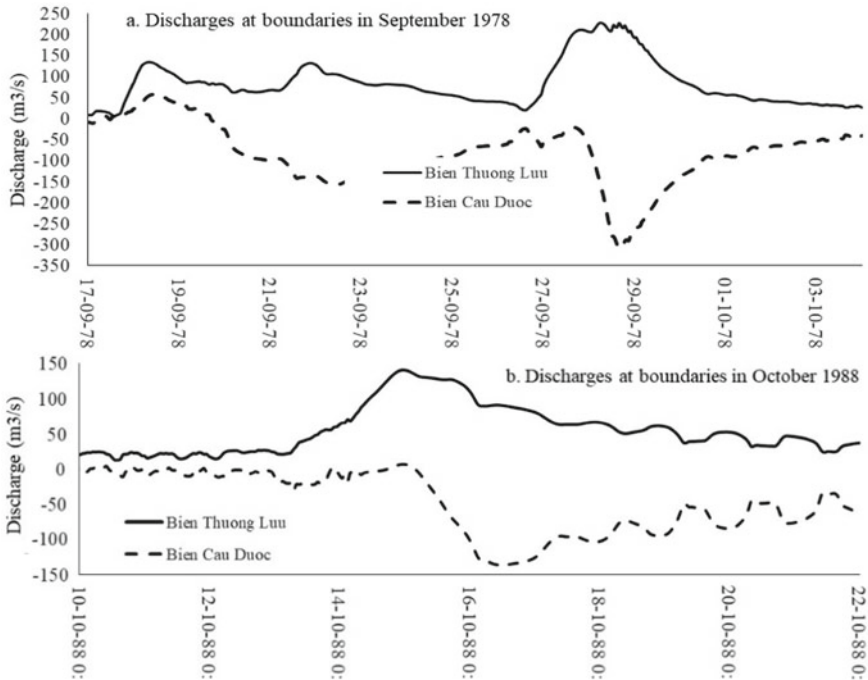


Fig. 2 Hourly river discharges at boundaries in September 1978 and October 1988



Fig. 3 Domain of Mike 21 HD—2D model

2.3 Modelling Scenario

In order to investigate the influence of Cua Tien New Urban Area on the safety and flood drainage capacity of the Vinh River when implementing the project of Cua Tien New Urban Area, this study model 05 scenarios as following:

- Scenario 0 (KB0) modelling with observation data in Nov, 2019 to calibrate and verified model.
- Scenario 1 (KB1) modelling the historic flood in September 1978 with the bathymetry surveyed in May 2005.
- Scenario 2 (KB2) modelling the historic flood in September 1978 with the bathymetry surveyed in November 2019.
- Scenario 3 (KB3) modelling the extreme flood in October 1988 with the bathymetry surveyed in May 2005.
- Scenario 4 (KB4) modelling the historic flood in October 1988 with the bathymetry surveyed in November 2019.

3 Results and Discussion

3.1 Model Calibration and Verification

Observation of water level, current velocity and direction measured from 11th to 15th November 2019 were used to calibrate the Mike 21 HD model. The current data measured from 15 to 18 November, 2019 were used to verified model. Absolute Mean Different (AMD) and Root Mean Square Error (RMSE) proposed to

use for evaluating the accuracy of the model. The results of calibration and verification show in Table 1 and indicated that the Mike 21 HD model consistency with the observation data and the Maning number, M ($m^{1.3}/s$) was selected range from 8 to 35.

3.2 Variation of Water Depth

Water depths of historic flood Sep 1978 simulated in KB2 is plotted in Fig. 4 and the maximum water depths at 3 selected locations t6, t5 and t2 showed in Fig. 5.

The simulation result in the historic flood Sep, 1978 in both of KB1 and KB2 showed that the flood peak discharge time occurred in the study area from 6:00 to 7:00 on September 28, 1978 but the highest flooding level occurred at 15:00 on the same day. This can be explained by the fact that the high flood discharge cannot be escaped due to the closure of the Ben Thuy sluice, causing the increase of water level. After the flood recedes for 9 h, the water level tends to decrease gradually. The flood depth in natural ground increased from 1.0 to 1.5 m while in the ponds increased from 4.0 to 5.0 m.

The maximum water depth at 3 locations t6, t5 and t2 in KB3 and KB4 indicated that when constructed of Cua Tien urban area, the water depth of flow from Duoc intersection to the Railway bridge increases slightly from 1.7 to 2.5 cm and then starts to climb downstream of Cua Tien 2 bridge, with an increasing height of 7.5 cm (Fig. 4).

Water depths of extreme flood Oct 1988 simulated in KB3 is plotted in Fig. 6, the result in both of KB3 and KB4 showed that the flood peak discharges time occurred in study area as same as the flood Sep 1978. The flood depth in natural ground increased from 0.2 to 0.5 m while in the ponds increased from 3.0 to 4.0 m.

The maximum water depth at 3 locations t6, t5 and t2 in KB3 and KB4 indicated that when constructed of Cua Tien urban area, the water depth of flow from Duoc intersection to the Railway bridge increases slightly from 1.2 to 2.0 cm and then starts to climb downstream of Cua Tien 2 bridge, with an increasing height of 5.0 cm (Fig. 7).

Table 1 Results of Mike 21 HD model calibration and verification

OBS station	RMSE	RMSE (%)	AMD	AMD (%)
<i>Model calibration</i>				
Water level (m)	0.06	4.79	0.05	3.69
Current velocity (m/s)	0.08	14.01	0.06	10.89
Current direction (°)	17.69	4.93	14.86	4.14
<i>Model verification</i>				
Current velocity (m/s)	0.06	13.04	0.04	9.7
Current direction (°)	8.28	33.19	6.82	27.32

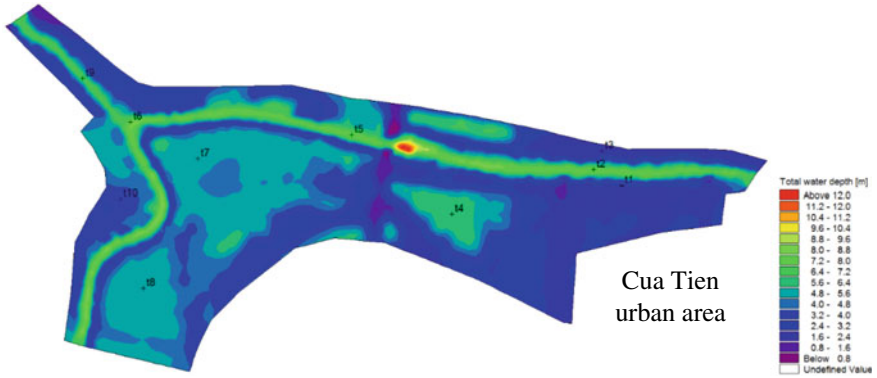


Fig. 4 Total water depth in flood Sep 1978 with bathymetry in Nov, 2019 (KB2)

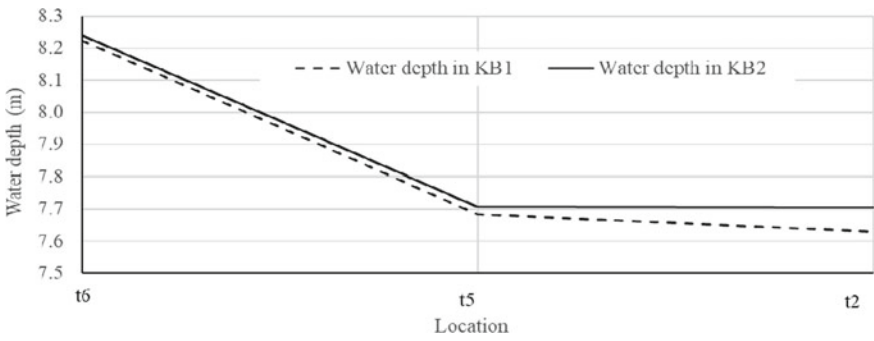


Fig. 5 Variation of total water depth a long the Vinh river in the flood Sep, 1978

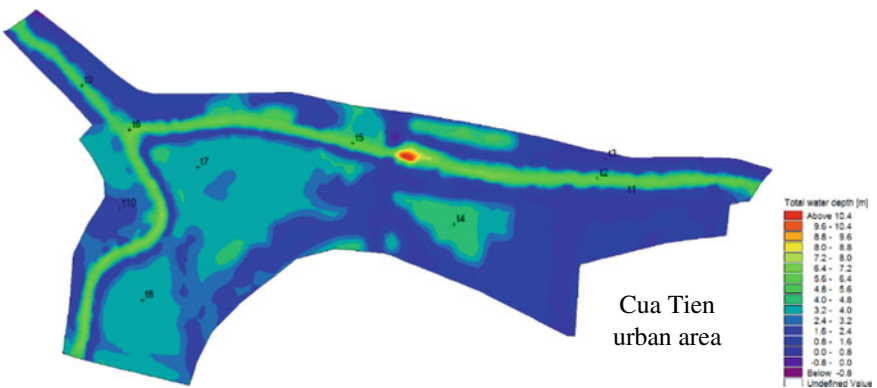


Fig. 6 Total water depth in flood Oct 1988 with bathymetry in May, 2005 (KB3)

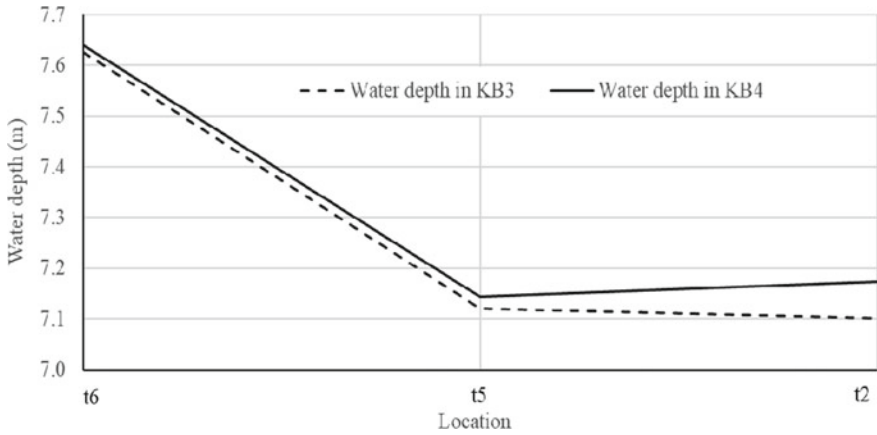


Fig. 7 Variation of total water depth a long the Vinh river in the flood Oct, 1988

3.3 Flood Current Speed

Flood current speed field of KB1 and KB2 are presented in Fig. 8, it showed that the maximum current speed is fairly evenly distributed along the river. At the toe of the embankment, the current speed is quite small, the maximum in KB1 is only 0.12 m/s and in KB2 is only 0.35 m/s. This is understandable because with the construction of Cua Tien urban area the flow in upstream will have a certain degree of openness, then focus on the banding section of Vinh river in Cua Tien Bridge No. 1 induced increasing of speed and due to cross section of river is partly narrowed, the speed increases steadily throughout this river section.

Flood current field of KB3 and KB4 are plotted in Fig. 9. The result indicated that the maximum current speed at the Cua Tien bridge No. 2 reached to 0.62 m/s in the KB3 and 0.72 m/s in KB4. This result showed that the construction of Cua Tien urban area the flood current speed increases 16.3%.

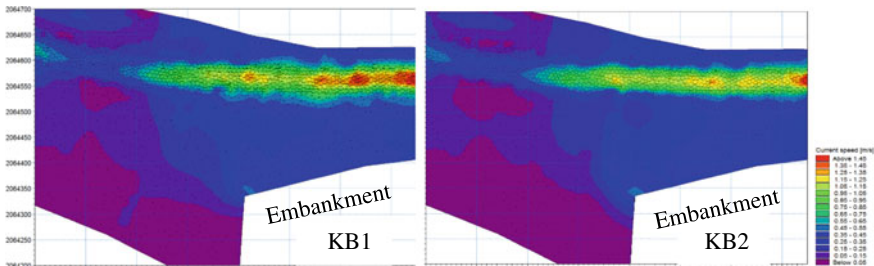


Fig. 8 Current speed field in KB1 and KB2

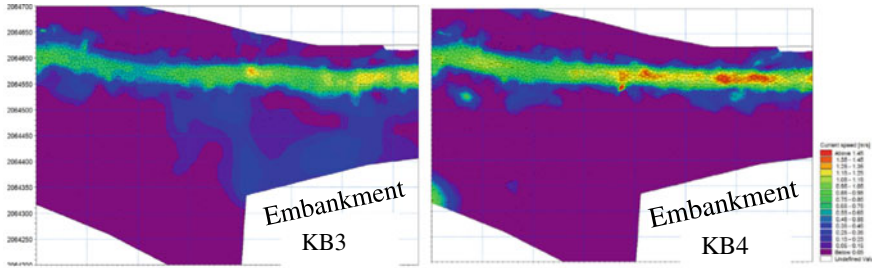


Fig. 9 Current speed field in KB3 and KB4

4 Conclusions

Cua Tien urban area induced the increasing water level only 5.3 and 7.5 cm in the historic flood in September 1978 and extreme flood in October 1988, and increasing of flood current speed to 16.3% and the maximum current speed reached to 1.58 m/s in the downstream of Cua Tien bridge No. 2.

The results indicated that embankment structures will safe under the flood seasons because the design flood current is 3.5 m/s.

References

1. Institute of Water Resources Planning (2012) Planning for flood drainage in the Southern of Hung—Nghì region and Vinh city, Nghe an province. Hanoi, Vietnam
2. Pham T, Pham H (2019) Vinh City flooded a meter of water in heavy rain, the traffic paralysis. <https://news.zing.vn/tp-vinh-ngapca-met-nuoc-trong-dot-mua-nhu-trut-giao-thong-te-liet-post1002138.html>. Accessed 04 Nov 2019
3. Tjep D (2019) Nghe an: do not let Vinh citadel “fall” when it rains. <https://baotainguyenmoitruong.vn/nghe-andungde-thanh-vinh-that-thu-khi-mua-lon-294725.html>. Accessed 04 Nov 2019
4. Nguyen VT (2020) Research on evaluation of the effects to safety and service capacity of Vinh river when Cua Tien new urban area project constructed in Vinh city, Nghe An province. University of Transport and Communications, Hanoi, Vietnam

Field Measurement of Wave Overtopping Frequency and Intensity at Sea Dike Using Shore-Based Video Images



Shanhang Chi, Chi Zhang, Zhubin Cao, and Jinhai Zheng

Abstract A tentative field measurement of wave overtopping over a rubble mound sea dike using video images was carried out during two storms in the summer of 2018 at Rizhao Coast, Shandong Province, China. A shore-based video monitoring system was mounted at the top of a lighthouse behind the sea dike to collect coastal images with a sample frequency of 1 Hz in the beginning 10 min of each hour during daylight. Image georectification, describing the transformation from the pixel coordinates to world coordinates, was calibrated following the two-step calibration methodology. The number, location, width and duration of overtopping events were extracted in the rectified time-stack images and the process of extraction was performed automatically using 150 virtual pixel sensors distributed along the sea dike crest. Finally, a total of 7120 individual overtopping events were detected. Temporal and spatial variations of overtopping intensity, defined as the product of width and duration to estimate the dimension of an individual overtopping event, were analyzed. Using the EurOtop 2018 and JTS 145-2015 formulas, overtopping volume was also calculated based on the measured offshore wave parameters and tidal level at the nearby Rizhao ocean station. The correlation coefficient between the calculated results and the observation was 0.66 and 0.64, respectively. During storm AMPIL, the alongshore variation of overtopping intensity was revealed to be dominated by the alongshore variation of surf zone width. While during the moderate storm JONGDARI, it was affected by the surrounding coastal structures. The present study suggests the feasibility of shore-based video monitoring technique to capture the main features of wave overtopping at coastal dikes, providing new possibilities to monitor wave overtopping in the field and to improve our calculation method and tools.

Keywords Wave overtopping · Coastal video monitoring · Field measurement · Temporal and spatial variations · Storm events

S. Chi (✉) · C. Zhang · Z. Cao · J. Zheng
College of Harbour, Coastal, and Offshore Engineering, Hohai University, Nanjing, China
e-mail: chishhang@hhu.edu.cn

© The Author(s), under exclusive license to Springer Nature Singapore Pte Ltd. 2021
T. Bui-Tien et al. (eds.), *Proceedings of the 3rd International Conference on Sustainability in Civil Engineering*, Lecture Notes in Civil Engineering 145,
https://doi.org/10.1007/978-981-16-0053-1_33

263

1 Introduction

Under the influence of global climate change, more frequent severe storms combined with sea level rise lead to more wave overtopping, that sea dikes which were built to protect coastal areas may be not safe and capable any more. With the continuously increasing population, economic and recreation activities in coastal zones, it is vital to reduce and prevent the occurrence of overtopping disasters.

A common strategy used to study overtopping is physical model tests. The relationship between mean overtopping discharge and different structure configurations under regular waves or irregular waves [1, 2], and solitary waves [3, 4] have been investigated. Extensive empirical formulas based on physical model tests have been widely used to predict wave overtopping for the design of coastal structures [5–7]. As the high flexibility of hydrodynamic and structure shape, numerical models are also used to simulate wave overtopping process extending the application scope of empirical formulas [8–10]. Field observation on overtopping is of great practical interest but very difficult to implement and has been rarely done. Existing measuring methods can't capture the temporal and spatial variation of overtopping at the same time. Thus, a more effective field measurement method is needed.

Since 1980s, shore-based video monitoring techniques [11, 12] have been proved to be adequate in detecting and quantifying temporal and spatial variation of coastal areas. Under the condition of stable power supply and good fixation, shore-based video monitoring system can sample continuously with a high frequency and can be used in severe weather conditions, which is difficult to be achieved by other means. A range of image data products and a series of image processing methods [13] can be applied to analyze and quantify coastal morphology and wave parameters [14]. However, no application of the system to monitor wave overtopping has been reported so far.

In this study, we investigate the feasibility of using shore-based video images to observe and quantify wave overtopping at a sea dike during two storms in the summer of 2018. The continuous images collected by four cameras were used to analyze both the temporal and spatial variations of wave overtopping characteristics.

2 Study Area

The study area is located on the east coast of Rizhao, China (Fig. 1). The area is open to the Yellow Sea. Tides are mainly semi-diurnal and the mean tidal range is 3 m. The wave climate is dominated by prevailing waves from east/southeast with the significant wave height of 0.46 m and the extreme wave height during storms ranging from 1.4 m to 3.3 m.

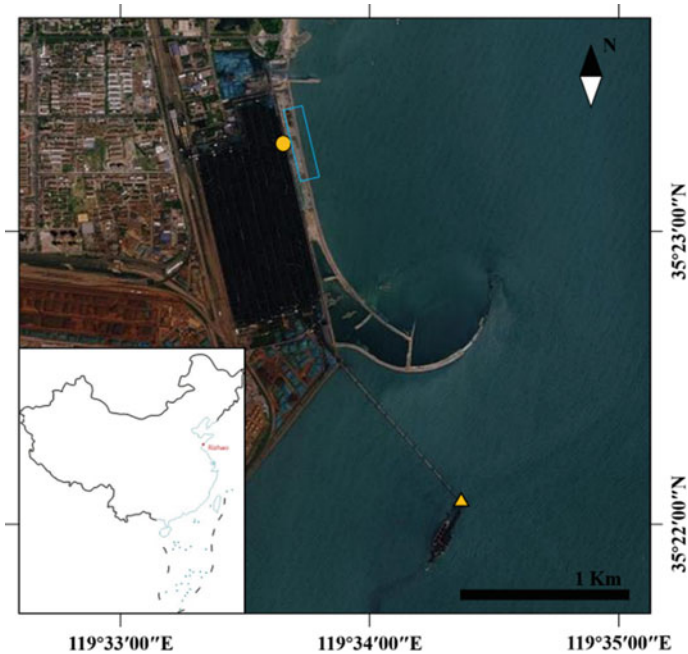


Fig. 1 Sketch of the study area

The rubble mound sea dike has a cemented rock wave wall. The crest height of the wave wall is +7.5 m LNLW (lowest normal low water), slightly higher than the armour crest (+7.1 m LNLW). The seaward design slope is 1:1.5 and the slope is armoured with Accropode I stone. At the north and south end of the sea dike, a groyne was built respectively. And an arcuate breakwater stretches into the deep water at the south of the area.

3 Methods

3.1 Image Acquisition and Image Georectification

Four MOBOTIX cameras were mounted on a 33 m high lighthouse (the yellow dot in Fig. 1) about 110 m behind the breakwater on June 18, 2018, acquiring imagery with a resolution of 1280 * 960 pixels in the beginning 10 min of each hour during daylight.

The intrinsic and extrinsic parameters of each camera were calibrated following the two-step calibration methodology. Intrinsic parameters were determined using the method of Zhang [15]. Twenty-four ground control points (six GCPs for each camera) were used to calibrate the extrinsic parameters. Finally, images obtained by

the monitoring system could be rectified into a local space coordinate system, whose original point (0,0,0) was at the ground point right below the camera center, x-axis was pointing eastward and y-axis was pointing northward (length unit: m), with an accuracy of $5 \sim 17$ cm.

3.2 Overtopping Event Extraction

Coastal imagery recorded by the monitoring system covered the whole process of AMPIL, from 5:00 to 17:00, on July 23, 2018, and part of the process of JONGDARI, from 5:00 to 12:00, on August 4, 2018. From the image sequence, the type of overtopping (spray or green water) could be identified directly. To quantify the overtopping events, time-stack images of the pixels in rectified images corresponding to the crest of the breakwater were generated. In time-stack images, the location, width and duration of each individual overtopping event could be extracted and the frequency of overtopping in the period could be determined. Virtual pixel sensors, identifying overtopping events by the gray threshold method, were used to extract overtopping automatically.

4 Results

4.1 Coastal Dynamics

Figure 2 shows the hydrodynamics measured at the nearby Rizhao ocean station (yellow triangle in Fig. 1) from July 1 to August 15. The significant wave height is much larger than usual during AMPIL and relative moderate during JONGDARI.

4.2 Temporal Variation of Overtopping Parameters

The variation of accumulated overtopping frequency and intensity, average width and duration among different hours during the two storms is shown in Fig. 3. Significant temporal variation of overtopping frequency and intensity during AMPIL can be found, with two peak values marking the violent overtopping at 6:00 and 13:00, which is synchronized with the temporal variation of offshore tidal level. And an additional peak value of overtopping frequency appears at 11:00, due to the large significant wave height at that time (Fig. 3b). The hourly variation of overtopping frequency and intensity during JONGDARI is different to AMPIL. The curves are unimodal, which is consistent to the change of offshore tidal level during the storm process, with the peak value of frequency and intensity appears at 9:00

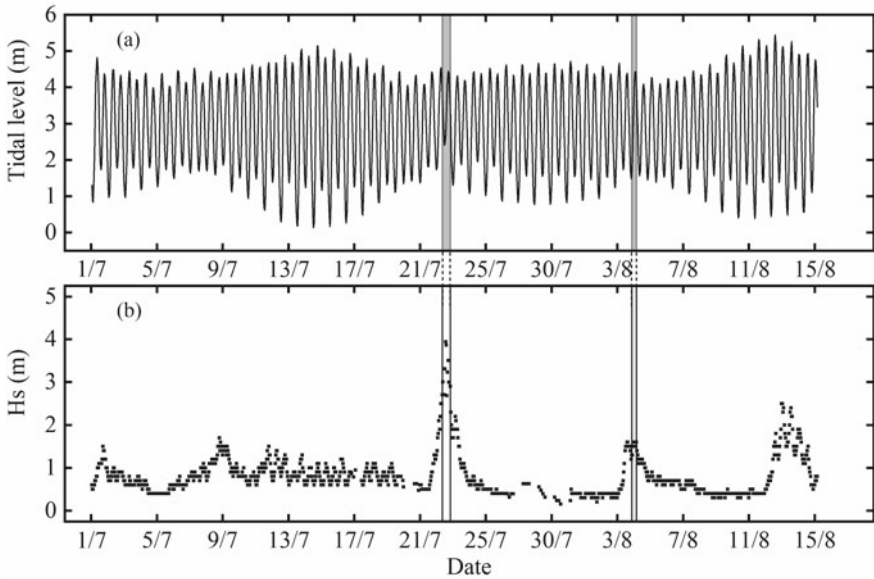


Fig. 2 Measured tidal level (a) and significant wave height (b) at 13 m water depth from July 1 to August 15, 2018, with duration of two storm events indicated with vertical lines

and 10:00, respectively. And much smaller values of both parameters were observed compared to those of AMPIL, owing to the moderate wave condition during JONGDARI (Fig. 3d). The temporal variation of average duration is similar to overtopping intensity, with a maximum of 1.85 s and a minimum of 1.26 s. While the change of average width with time is not obvious (Fig. 3a, c).

A comparison between normalized observation data and overtopping volume calculated using EurOtop 2018 and JTS 145-2015 formulas at each hour was conducted (Fig. 4). The correlation coefficient between the calculated results and the observation was 0.66 and 0.64, respectively.

4.3 Spatial Variation of Overtopping Parameters

The study area was divided into ten sections on average (numbered from north to south) and overtopping parameters were counted, respectively.

As for AMPIL, the spatial variation of overtopping parameters is shown in Fig. 5. The average width and duration are found to be shorter in the middle part than that in the south and north parts of the seawall, at 6:00 and 9:00 (low tidal level). While at 12:00 and 15:00 (high tidal level), the difference between the average width in the middle part and that in the sides narrows down. The along-shore variation patterns of the accumulated frequency and intensity are similar to

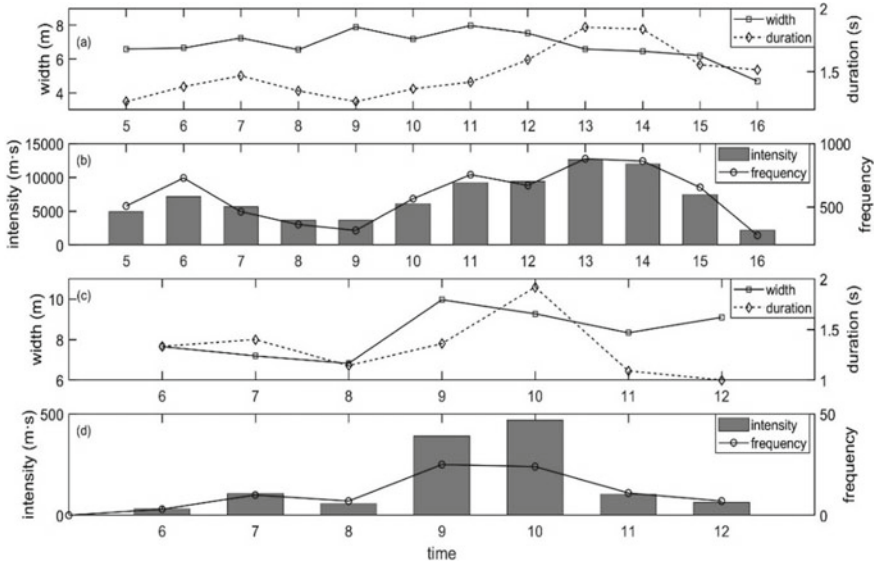


Fig. 3 Hourly variation of average width and duration during AMPIL (a) and JONGDARI (c), accumulated frequency and intensity during AMPIL (b) and JONGDARI (d)

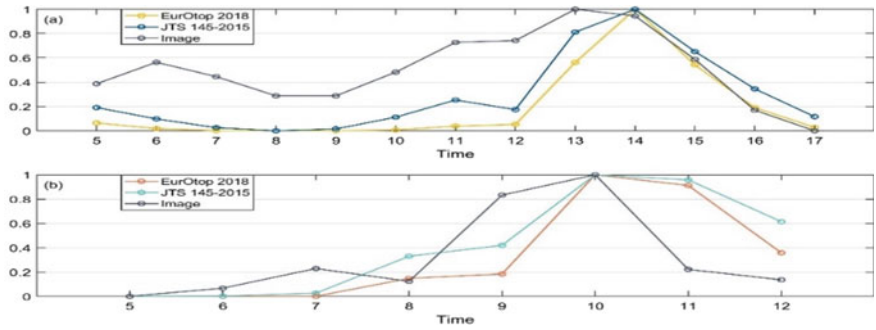


Fig. 4 Comparison between normalized observation data and formulae results during AMPIL (a) and JONGDARI (b)

each other. The maximums of them appear at Sect. 1, the minimums can be found in the middle part, and the south part is considered as moderate. As shown in Fig. 6 overtopping events during storm JONGDARI are concentrated in the middle part, and few events occurred in the south part of the seawall owing to the protection of the arcuate breakwater against southeast waves, which are dominant during JONGDARI.

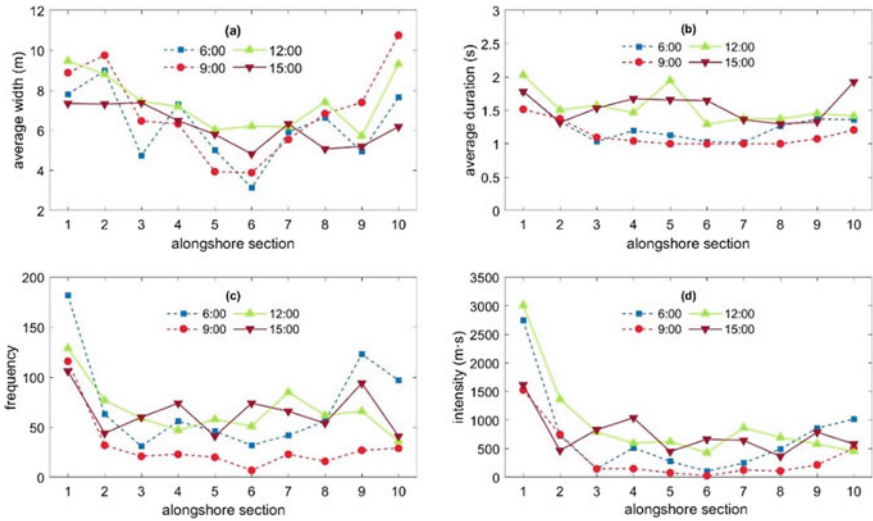


Fig. 5 Spatial variation of **a** averaged width, **b** averaged duration, **c** accumulated frequency, **d** accumulated intensity of overtopping events during typhoon AMPIL

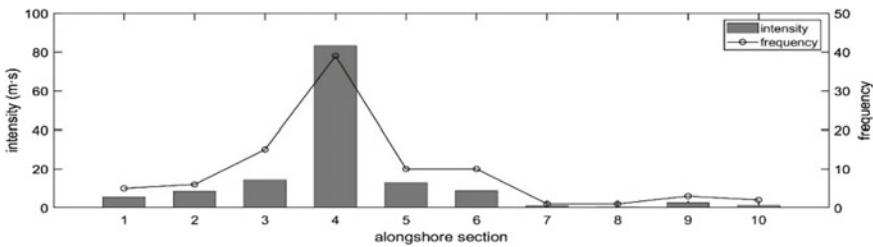


Fig. 6 Spatial variation of accumulated overtopping frequency and intensity during JONGDARI

5 Conclusions

The present study suggests the feasibility of shore-based video monitoring technique to capture the main features of wave overtopping at coastal dikes, providing new possibilities to monitor wave overtopping in the field and to improve our calculation method and tools. The temporal and spatial variation of overtopping characteristics can be captured at the same time, which is difficult by other means. It is found that the temporal variation of overtopping intensity is synchronized with the tidal level. And high energy waves lead to an increase of overtopping frequency. Besides, the nonuniform spatial distribution of overtopping parameters is revealed to be dominated by the surf zone width and surrounding structures which are rarely considered in existing models.

References

1. Goda Y (1975) Laboratory investigation on the overtopping rates of seawalls by irregular waves. *Ports and Harbour Res Inst* 14(4):3–44
2. Kobayashi N (1994) Irregular wave overtopping of revetments in surf zones. *J Waterway Port Coast Ocean Eng* 120(1):56–73
3. Grilli PT (1994) Characteristics of solitary wave breaking induced by breakwaters. *J Waterway Port Coast Ocean Eng* 120(1):74–92
4. Hsiao SC (2012) An experimental observation of a solitary wave impingement, run-up and overtopping on a seawall. *Coast Eng* 57(1):1–18
5. Van der Meer J (2014) New physical insights and design formulas on wave overtopping at sloping and vertical structures. *J Waterway Port Coast Ocean Eng* 140(6). [https://doi.org/10.1061/\(asce\)ww.1943-5460.0000221](https://doi.org/10.1061/(asce)ww.1943-5460.0000221)
6. Hedges TS (1998) Random wave overtopping of simple seawalls a new regression model. *Water Marit Energy J* 157:113–122
7. Van der Meer J, Allsop N, Bruce T (2018) *EurOtop, 2018. Manual on wave overtopping of sea defences and related structures*. In: An overtopping manual largely based on european research, but for worldwide application. Available www.overtopping-manual.com
8. Hubbard ME (2002) A 2D numerical model of wave run-up and overtopping. *Coast Eng* 47:1–26
9. Zou Q (2011) Evolution of wave shape over a low-crested structure. *Coast Eng* 58(6):478–488
10. Shao SD (2006) Simulation of wave overtopping by an incompressible SPH model. *Coast Eng* 53(9):723–735
11. Holman RA (2007) The history and technical capabilities of Argus. *Coast Eng* 54:477–491
12. Voudoukas MI (2012) Coastal vulnerability assessment based on video wave run-up observations at a mesotidal, steep-sloped beach. *Ocean Dyn* 62:123–137
13. Plant NG (2007) The performance of shoreline detection models applied to video imagery. *J Coastal Res* 233(3):658–670
14. Splinter KD (2018) Remote sensing is changing our view of the coast: insights from 40 years of monitoring at Narrabeen-Collaroy, Australia. *Remote Sens* 10(11):1744
15. Zhang Z (2000) A flexible new technique for camera calibration. *IEEE Trans Pattern Anal Mach Intell* 22(11):1330–1334

Designing the Paradigm that Treats the Wastewater of Concrete Batching Plants



Vu Phuong Thao

Abstract The paper presents the technological scheme to treat wastewater of concrete batching plants, design calculation the paradigm with 1:5 scale. Using physical and chemical technology combined biology, wastewater goes through oil separating tanks, clarifiers, mixing tanks, contact tanks to remove grease, insoluble substances, suspensions, etc. The performance results show stable TSS (Turbidity and Suspended Solids) performance, COD (Chemical Oxidation Demand), BOD₅ (Biological Oxygen Demand) processing and other pollution indicators are standard follow National Technical Regulation on Industrial Wastewater, coded QCVN 40: 2011/BTNMT. This proves that the model works well and perfectly suitable to propose the construction of a treatment system for wastewater from concrete mixing stations in the future.

Keywords Wastewater • Wastewater treatment • Wastewater treatment paradigm • Concrete batching plants

1 Introduction

Wastewater produced from concrete mixing plants mostly contains a large portion of residual products such as cement, sand, additives from commercial concrete production, waterproof concrete ... [1]. When the untreated wastewater source contains a high component of these excess products, it will have a significant impact on the environment, such as: causing blockage of drainage canals due to the curing of cement, sand; The quality of irrigation water for agriculture is degraded, due to the fact that the wastewater contains many toxic additives; The habitat of the aquatic plants and animals is affected [2]; Impacted soil environment, soil containing cement, and freezing additives will make it difficult to

V. P. Thao (✉)

Faculty of Civil Engineering, University of Transport and Communications, Hanoi, Vietnam
e-mail: vpthao@utc.edu.vn

cultivate crops. The odor of concrete wastewater is unpleasant, affecting the health and quality of the surrounding air; loss of landscape and aesthetics of the surrounding environment [3].

Wastewater from concrete mixing plants usually has a large pH [4]. The suspended solids have a very high content, even after the sedimentation process, the amount of suspended solids is not below the permitted level follow the National Technical Regulation on Industrial Wastewater, coded QCVN 40: 2011/BTNMT (column B) [5].

In general, commercial concrete mixing plants only use mechanical sedimentation to treat wastewater. Obviously, a treatment that only separates TSS by mechanical sedimentation is ineffective for COD, Grease [6].

2 Objective

The main objective of this research presented in this paper was to design a laboratory-scale wastewater treatment (WWT) to propose a treatment plan include the color, COD, TSS, Grease of the output wastewater sample is within the allowed threshold. The model achieves high productivity and processing efficiency. Treatment methods include the following steps:

- Adjust pH by acidification (using dilute sulfuric acid or hydrochloric acid) [7];
- Because the suspended residue content is derived from carbonate residue, which exists in the conditions of high pH level and is difficult to settle, the research proposed to use the flocculation method not only improving the sedimentation efficiency but also reducing the color of wastewater [8];
- COD: using chemical methods with strong oxidizing agents;
- Grease: using the Oil separation-Detention Basin on the principle of gravity separation.

3 Design the Wastewater Treatment Paradigm

Design parameters for the actual wastewater treatment system of concrete mixing plant A. After that, choose the appropriate design rate for the experimental model, draw up and model machining. During the operation, the value of parameters will be monitored and considered to change which be compared to the previous calculation, to choose the most optimal values: such as retention time, stirring speed, stirring time, sedimentation speed etc. to get the highest treatment efficiency for the paradigm.

3.1 Wastewater Treatment Process

Wastewater from the concrete mixing plant is put into Oil separation—Detention Basin. The combination of forced air blowing and surfactants in the mixture of wastewater will produce air bubbles floating on the surface of the tank. Air bubbles will lead the grease to overflow into the oil compartment. Oil separating wastewater will be pumped into a horizontal depositing tank. At this point, the majority of the sand and insoluble matter will settle to the bottom and then will be collected by blowdown valves. Water after sedimentation is collected at the water collecting compartment at the end of the tank and pumped into the flocculant tank. H₂SO₄ 10% will be added to the pipe that is connected to the flocculant tank, followed by 2% PAC (Poly Aluminum Chloride) solution [9]. In the flocculant tank, the paddle works continuously to mix the acid, the PAC and the wastewater. The coagulation reaction takes place, water is led to the clarifier tank. Deposition velocity 0.0002–0.0006 m/s. At the clarifier tank, the flocculants after flocculation will settle to the bottom of the tank, clear water overflows water inlet and flows to the chlorine mixing tank. Sludge is discharged periodically at the blowdown valve. Javen 2% will be filled into the water pipe from the clarifier tank to the chlorine mixing tank. At this point, the paddle will mix Javen with wastewater and flows to the contact tank to increase mixing efficiency. Water from the contact tank flows to the reservoir after treatment for reuse as a source of water for concrete production and other activities. The treated wastewater meets column B in National Technical Regulation on Industrial Wastewater, coded QCVN 40: 2011/BTNMT.

3.2 Design the Wastewater Treatment Paradigm

Data input is shown in Table 1.

Average hourly wastewater flow:

$$Q_h^{tb} = \frac{Q_{ng}^{tb}}{24} = \frac{80}{24} = 3.33 \text{ (m}^3\text{/h)}$$

$$Q_{max} = 80. \quad k = 160 \text{ (m}^3\text{/day) (with } k = 2)$$

Table 1 Input pollution criteria

No.	Criteria	Unit	Value
1	Volumetric flow rate	m ³ /day	80
2	pH		12–13
3	TSS	mg/l	25,000
4	COD	mg/l	300
5	BOD ₅	mg/l	20
6	Grease	mg/l	500–700

$$Q_h^{\max} = \frac{Q_{ng}^{\max}}{24} = \frac{160}{24} = 6.7 (\text{m}^3/\text{h})$$

Because of the model in the laboratory scale, the design of technical drawings for the model with the ratio B, L, H = 1:5 compared with the calculated size with the actual flow. Then, the operating flow of the model will decrease 125 times compared to the previously calculated flow. Flow rate model is:

$$Q_{vh} = \frac{Q_{ft}}{125} = \frac{80}{125} = 0.64 \text{ m}^3/\text{day} = 271/\text{h}$$

Then, the design dimensions of the treatment works in the experimental model will be shown in the Table 2.

3.3 Calibration of the Wastewater Treatment Paradigm

Operate wastewater treatment model, then compare the results with QCVN 40: 2011/ BTNMT (column B). Experimental results through analyses shown that the parameters of COD, TSS, Grease all met the limited value in QCVN 40: 2011/BTNMT

Table 2 Design parameters of the model

No.	Parameters	Unit	Value
<i>The oil separation-detention basin</i>			
1	Length of detention/collecting oil compartment	mm	300/100
2	Width of detention/collecting oil compartment	mm	300/300
3	Height of detention/collecting oil compartment	mm	400/100
4	Protection height	mm	100
<i>The horizontal depositing tank</i>			
1	Length of sedimentation zone	mm	630
2	Width of sedimentation zone	mm	250
3	Height of sedimentation zone	mm	250/100
5	Sedimentation zone slope	%	1–2
6	Top/Bottom of the collecting hole	mm	280/100
8	Height of the collecting hole	mm	150
9	Slope of the collecting hole	degree	40–50°
<i>The flocculant tank</i>			
1	Length	mm	300
2	Width	mm	200
3	Operation height/protection height	mm	200/100
<i>The clarifying tank</i>			
1	Length	mm	300
2	Height of deposition area/protection height	mm	250/50
3	Height of cone	mm	200

Table 3 Experimental results on pollution criteria after treatment

Criteria	Unit	Method	Before processing	After processing	QCVN 40: 2011/BTNMT (column B)
pH		TCVN 6492: 2011	12.8	7.81	5.5–9
Color	pt/Co	TCVN 6185: 2015	245	108	150
TSS	mg/l	TCVN 6625: 2000	20,394	78.5	100
COD	mg/l	TCVN 6491: 2000	483	112	150
Grease	mg/l	TCVN 7369: 2004	279	8.1	10

Table 4 Processing performance of the model

Date of sampling	Processing performance (%)	Color	COD	Grease
	TSS			
7/23/2018	99.6	55.9	76.8	97.1
7/27/2018	99.5	54.8	76.4	97.0
8/05/2018	99.6	57.7	75.9	96.9

(column B). This result proves that the operating conditions of the model are completely suitable for the production wastewater treatment of the concrete mixing plant (Table 3).

Table 4 shows the processing performance of the model with indicators TSS, color temperature, COD, grease.

4 Conclusion

Monitoring results, analysis of color criteria, COD, TSS, grease of the output effluent samples which are referred to the report are in the allowed threshold of National Technical Regulation on Industrial Wastewater, coded QCVN 40: 2011/BTNMT (column B). Stable TSS performance with over 99% efficiency; color level processing at 54.8–57.7%; COD processing at 75.9–76.8%; Grease processing at 97%. This shows that the model works well and is completely suitable for proposing the construction of wastewater treatment systems from concrete mixing plants.

References

1. Klus et al (2017) The properties of waste water from a concrete plant. In: 1st International conference on advances in environmental engineering, AEE 2017
2. Mehta PK (2000) Reducing environmental impact of concrete. *Concr Int* 23(10):61–66
3. Shekarchi M, Yazdian M, Mehrdadi N (2012) Use of biologically treated wastewater in concrete. *Kuwait J Sci Eng* 39:97–111

4. Shahidan S, Senin MS, Kadir ABA et al (2017) Properties of concrete mixes with carwash wastewater 2017. MATEC Web Con 87
5. National technical regulation on industrial wastewater, coded QCVN 40: 2011/BTNMT
6. Triet LM (2008) Industrial and urban wastewater treatment. Vietnam National University, Ho Chi Minh city
7. Metcalf L, Eddy HP (1991) Wastewater engineering: treatment, disposal and reuse. McGraw-Hill Education
8. Bratby J (2006) Coagulation and flocculation in water and wastewater treatment, 2nd ed. IWA Publishing, UK
9. Thao VP, Pham VH, Nguyen TBM (2018) Research to determine optimal chemical dosage of PAC as a database for designing wastewater treatment system for concrete mixing plant. Sci J Transp 63, 04/2018

Research on Automated Monitoring to Access the Port Structure Inspection in Operating Offloading Vessel Test



Duong Thi Bach Nguyen, Van Hien Le, and Duc Cong Tran

Abstract Nowadays, the fleet structure has a significant change in deadweight, size and age in the world and in Vietnam. This significantly affects port infrastructure and equipment. The policy of the Ministry of Transport, the Vietnam Maritime Administration and relevant state management agencies shall consider, create conditions and allow ports to receive larger ships than the designed (large deadweight vessels are reduced) to improve and develop sustainable the capacity of Vietnamese seaports. In order to implement this policy, the port structure assessment, evaluation of stability conditions and transposition of the must be conducted fully and accurately. In particular, the automatic monitoring of the stability of the port during the test operation process take on large vessel offloading is very important and necessary. The paper goes into GPS/RTK application research of this automatic monitoring work in the port structure inspection.

Keywords Offloading vessel · Fleet · Automatic monitoring · Port structural assessment · Port structure evaluation · Stability · Transportation

1 Introduction

The fleet structure has a significant change in weight, scale, and age globally and Vietnam. According to UNCTAD, the tonnage of the world fleet has increased by 2.4 times since 2001. In 2018 the total tonnage of ships had reached 1.91 billion DWT; 64% increase compared to 2010; in which the bulk cargo fleet has the most growth, up about 79%, followed by container ships by 49%; tanker fleet increased by 25%, these three types of vessels currently account for about 85 ~ 92% of the total tonnage of the world fleet.

According to Equasis, the number of very large ships (ships with a tonnage of more than 60,000 DWT) in 2018 increased by nearly 2.8 times compared to 2005;

D. T. Nguyen (✉) · V. Hien Le · D. C. Tran
Faculty of Civil Engineering, University of Transport and Communications, Hanoi, Vietnam
e-mail: ntbachduong@utc.edu.vn

the number of large vessels (larger than 25,000 DWT and smaller than 60,000 DWT) in 2018 increased by almost 2.1 times compared to 2005, medium and small ships in 2018 increased by nearly 1.4 times in 2005.

In Vietnam, the following statistics show that over four years, the fleet size has been considerable, with ships more deadweight than the design ships of the ports have been increasing [1]. In recent years, the trend of ships with large tonnage (>20,000 DWT) arriving at Vietnamese seaports has increased by 11%/year, equivalent to tens of thousands of ships/year. This characteristic affects port infrastructure and equipment. The actual berths have accepted offloaded large vessels to the port [2] (Table 1).

The scientific basis of the port structure’s calculation theory to satisfy the offloading vessel is mainly on the structure’s calculation with technical conditions as in the initial design, not to mention the structural deterioration over time. It is a concern for regulators when consider allowing port structures to receive offloaded large ships. In many cases, it is necessary to conduct the test operation process with maritime safety. To assess specific structural stability conditions through the horizontal displacement, regular and continuous monitoring is required.

2 Research on Automatic Monitoring System for Port Structure Inspection

The Global Positioning System (GPS) technology has successfully used to measure displacements of oscillating flexible civil engineering structures, such as suspension bridges and high-rise buildings [3]. A GPS includes two kinds of station: (1) base

Table 1 Statistic table of berths received large off-load vessels

No.	Name of port area	Type	Design vessel (10 ³ DWT)	Max forecast vessel (on plan) (10 ³ DWT)	Max actual vessel (10 ³ DWT)
1	Lach Huyen terminals	General		50–100	
		Container	50–100	(6000–8000) TEU	132
		Specialized port		10–25	
2	Dinh Vu and Nam Dinh Vu terminals	General and container	20–30	10–20	65 and 38.7
		Liquid	10–15	10–20	20
3	Buoy, float, transfer		20–30	50	65
4	Sai Gon port	General	20–30	60	60
5	CMIT port	Container	80	160	192

station that is located at a stable position and unable to move overtime of monitoring; and (2) rover station that is located on the structure and move due to the frame moving. There are some advantages of GPS technology to monitor the displacements civil structural; e.g., it overcomes climate limitation. It can also measure the structural displacements in the three-dimensional directions at centimeter-level accuracy [4].

Monitoring structures by the traditional method, the total station is well known as a high accuracy method mentioned on the technical criteria. However, this traditional method could not define structural displacement in real-time.

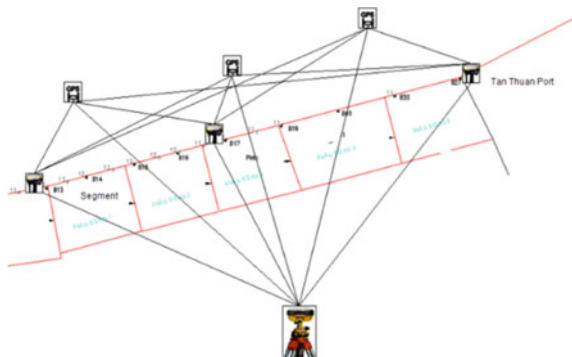
Real-Time Kinematic (RTK) is a method that allows providing the 3D coordinates of the rover point in real-time, especially, the field of super-structure monitoring. Satellite reception data at fixed stations (base stations) and mobile stations (rover stations) on the attached dedicated data processor. The GPS-RTK measurement method includes 1 or 2 machines located at the point with the coordinates (base station) and one or more mobile stations (rover station), communicating between the base station and the rover station with Radio Link transmitters or by data cable. When measured by the GPS-RTK method, the measured data are affected by the satellite orbit's errors, satellite clocks, error due to the ionosphere and ion layer, multi-path ... Causing signal attenuation and the spatial relationship of these errors depends much on data transmission (Fig. 1).

To check the transverse and longitudinal displacement of the pier, monitoring with GPS-RTK machines fitted with benchmarks on the pier, GPS-RTK Technology (i.e., real-time dynamic measurement) ensures accuracy determined on request. The measured results compare with the previously observed results.

GPS-RTK measurement method can measure data continuously, automatically for each specific cycle (measuring time per cycle depends on the time from when large ships enter port until large ships leave).

Bases for choosing the location of benchmarks to track and install GPS-RTK equipment:

Fig. 1 A diagram illustrating the monitoring method using GPS-RTK technology



- Carry out field survey and inspection with the naked eye, combine length measuring equipment, crack, transfer device to predict the feasibility of installing automatic monitoring equipment, to plan to monitor.
- The installation location an airy, sufficient viewing angle to space according to the satellite positioning measurement requirements.
- The installation location of the equipment is required to ensure a sufficient and continuous supply of power to operate the system continuously 24 h a day;
- Equipment installation location to ensure safety and safety for equipment during operation.

3 Automatic Monitoring Application on the Test Operation Process of Port Structure Inspection

The research team applies automatic displacement monitoring using GPS-RTK technology that has been applied by testing berths on Saigon, Vietnam. It is the first time to apply this technology. A harbor on the Saigon River has built since 1999, according to the original design for ships of 20,000–30,000 DWT. As the vessel size structure on the transport channel has increased in recent years (Table 1), the larger vessels have reduced the deadweight on entry and exit. The verification by theoretical calculation has confirmed the infrastructure. Floors and port equipment ensure to meet operation. The State's policy, the Ministry of Transport, and the Maritime Administration facilitate exploitation to improve the port owner's operation capacity. Before allowing the announcement of the port meeting the 60,000 DWT vessel offloading, the management units requested a test operation. During the trial operation, it is very important to monitor the harbor's stable conditions. It is necessary to monitor the horizontal and vertical displacement of the pier, preferably, and it must be essential to monitor automatically.

Based on the calculation and marine safety methods receiving the 60,000 DWT offloaded vessel, the research team determined the most dangerous horizontal displacement positions when subjected to horizontal forces caused by the ship (anchors, collision). The most hazardous horizontal displacement positions are bow anchor, steering (or nearby collision), where the anchor force is greatest (impact force can be small due to docking with tugboats, tugboats). These are the locations where GPS-RTK equipment is mounted.

The automated monitoring system is installed to measure the port in real-time during specific monitoring time. Besides, the large ships arrive at the port during the monitoring time to consider analyzing the monitoring points' displacement. The schedule for large vessels to the harbor is shown in Table 2.

According to the initial design documents, the permissible horizontal displacement of the pier segment is 32.7 cm.

Figure 2 shows the location of selected monitoring point at the port.

Table 2 Schedule for large ships to port

Name of vessel	Daily	Arrival time	Leave time	DWT
DIMI	MACS	11-May-20 18:00	12-May-20 10:00	57,034
LORENTZOS	OCEANIC	02-Jun-20 11:40	04-Jun-20 05:00	53,688
EMELDA	AGE LINES	15-Jul-20 12:20	17-Jul-20 03:20	55,638
COS PROSPERITY	SUNRISE	30-Jul-20 00:50	31-Jul-20 02:00	55,550



Fig. 2 The selected location for installing automatic monitoring equipment

4 Results and Discussion

Figures 3, 4, 5, 6 show the deflecting data in real-time of one point with three dimensional coordinates. Figures 7 and 8 shows a case of large ship (DIMI) arriving the port.

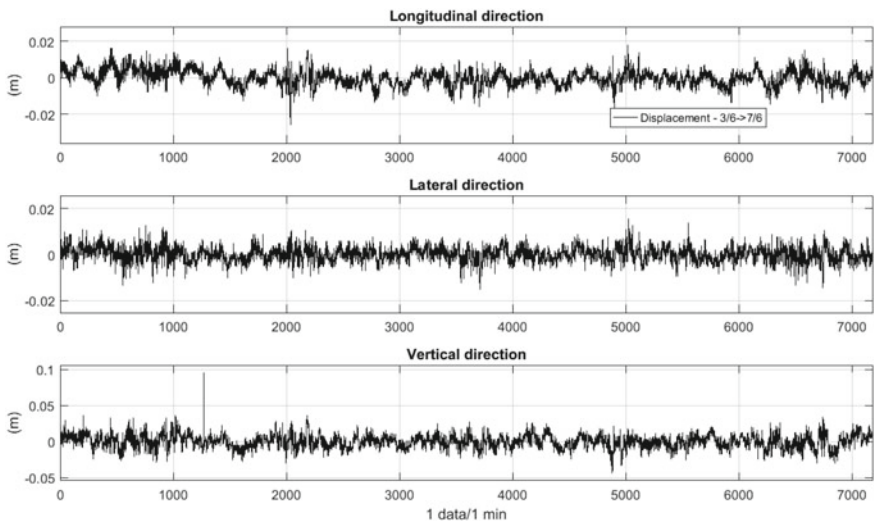


Fig. 3 The data from Jun 3rd to 7th

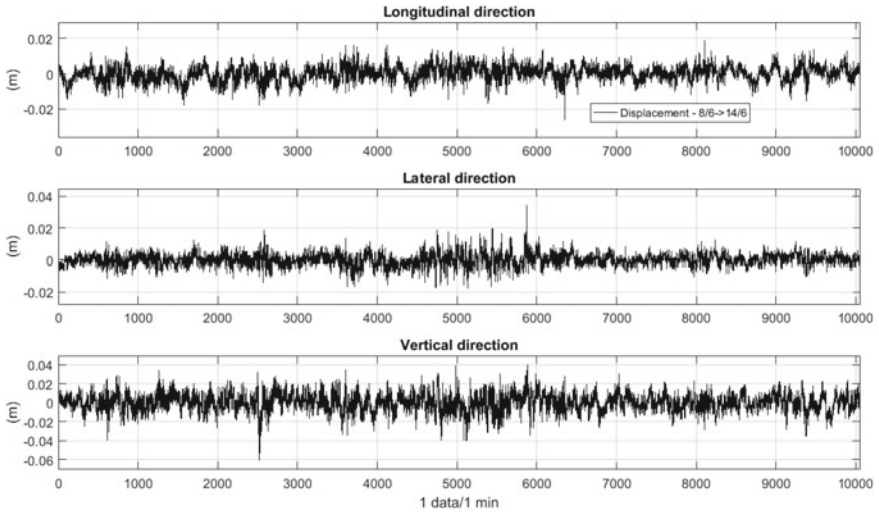


Fig. 4 The data from Jun 8th to 14th

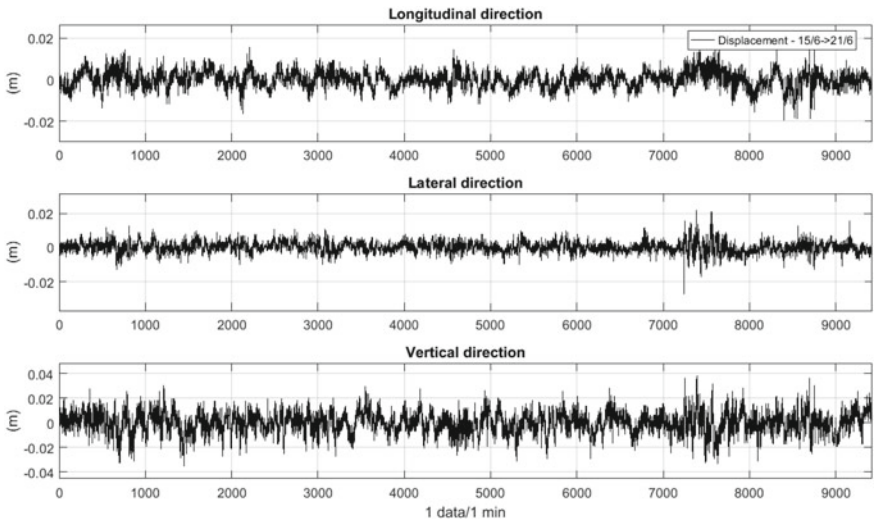


Fig. 5 The data from Jun 15th to 21st

Diagram of displacement by different directions and statistics of typical displacement value during the time of big vessels' arrival.

The monitoring system operated stably during the test observation period. Monitoring data were received at 1 Hz continuously and calculated and converted to each pier's vertical, horizontal, and vertical directions. In general, the observed

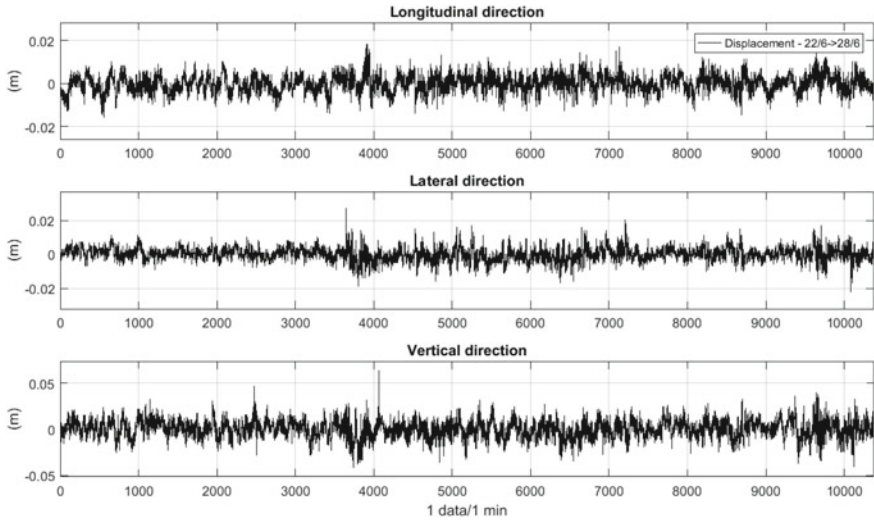


Fig. 6 The data from Jun 22nd to 28th

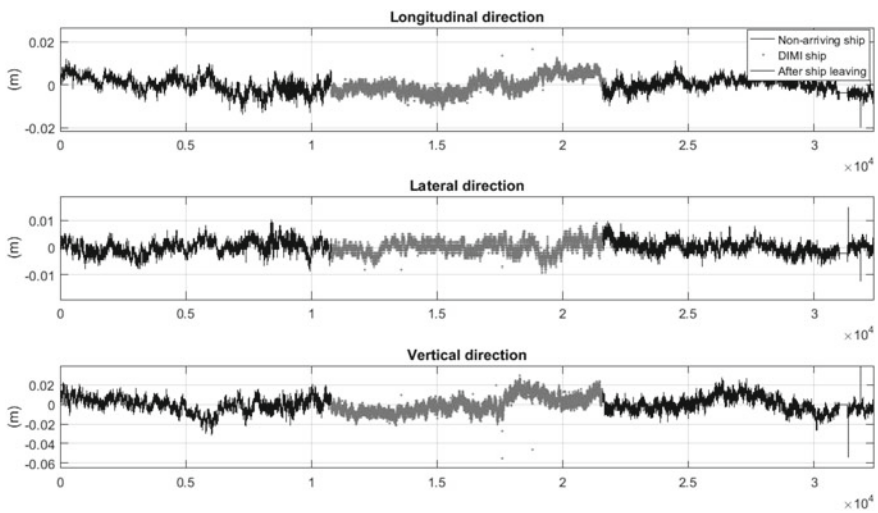


Fig. 7 Displacements on berthing DIMI

data correctly reflected the displacement of the characteristic points (the critical point of monitoring bridge) in different cases: no load and when a large vessel anchored).

Comparing the piers' transverse displacement value with the design displacement threshold value shows that the piers' actual displacement value is horizontal (in both cases: large ships moored and without load) has a much smaller amount

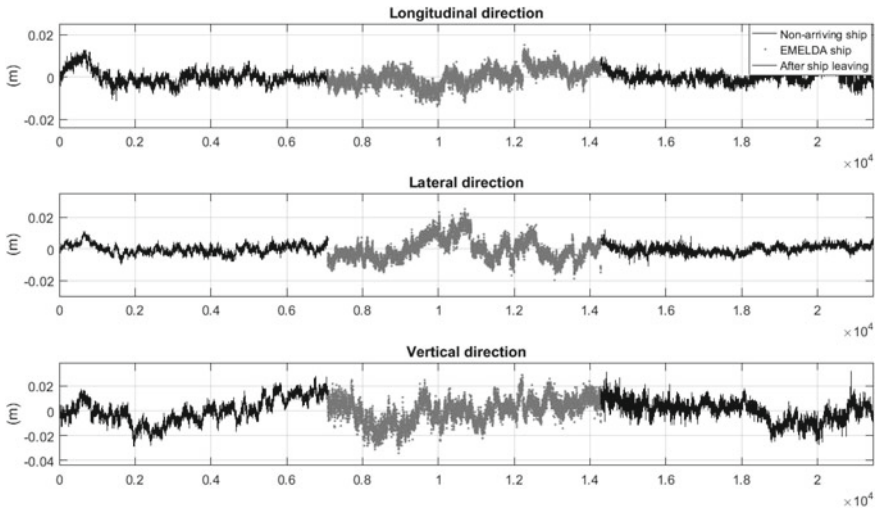


Fig. 8 Displacements on berthing EMELDA

Table 3 Statistics of characteristic displacement values of port structure

Cases	Displacement by different directions (m)					
	Longitudinal		Horizontal		Vertical	
	Max	Min	Max	Min	Max	Min
Before the berthing vessel	0.033	-0.004	0.047	-0.013	-0.017	-0.169
Berthing vessel	0.104	-0.032	0.196	-0.057	0.351	-0.353
After the berthing vessel	0.051	0.01	0.129	0.046	0.169	0.012
None load	0.01	-0.008	0.009	-0.007	0.021	-0.02

than the displacement threshold. Table 3 shows the amplitude of acquired displacements by different directions.

This result shows that the above berth structure ensures stable control when receiving offloaded 60,000 DWT ships.

5 Conclusions

The GPS-RTK automatic monitor is a new tool that is easy to apply for accurate, immediate results. Users can follow up regularly and continuously. It is entirely applicable to Vietnam.

Safety alert conditions can be set during monitoring to prevent structural breakdowns from damage to property and people.

GPS-RTK technology is a useful tool in monitoring the berth stability conditions and verifying the quality of the pier structure.

Apply this technology for stable monitoring of the pier under new operating conditions, which can be used in situations where the ability to reduce berth structure or the structure's bearing capacity is deactivated. Especially when evaluating the quality of the jetty receiving larger loads than designed.

References

1. Nguyen DT et al (2019) Researching port infrastructure and equipment when operating vessels with reduced tonnage on navigational channels in Hai Phong and Group 5. Research Project of Ministry of Transport, Code no. 184061, Vietnam
2. Nguyen DT (2019) Overview research on fleet, technical characteristics of channel, infrastructures, equipment of sea ports on main Hai Phong channel. In: The international conference on water resources- and coastal engineering. ISBN: 978.604.82.2698.5, Vietnam
3. Nguyen DT (2019) Researching port infrastructure and equipment when operating vessels with reduced tonnage on navigational channels in Ho Chi Minh fairway. *J Transp*, ISSN 0866–7012 (2354–0818), No. 7/2019, Hanoi, Vietnam
4. Le HV, Mayuko N (2015) Time-series analysis of GPS monitoring data from a long-span bridge considering the global deformation due to air temperature changes. *J Civil Struct Health Monit* 5(4):415–425

Sand-Spit Evolution and Inlet Dynamics Derived from Satellite Images: A Case Study for Tien Chau Inlet, Vietnam



Tran Thanh Tung, Nguyen Quang Chien, and Do Xuan Tinh

Abstract The Tien Chau inlet, where the Ky Lo river discharges into the southern part of Xuan Dai Bay, belongs to the An Ninh Dong ward, Tuy An district. This place has been a shelter area for over 400 vessels of Tuy An and other districts of Phu Yen province. The inlet is frequently accreted and shifted, causing difficult and unsafe navigation of vessels on their routes to seek for shelter and sell fishing products. This paper presents the results of a research on the evolution patterns of a sand-spit to the north of Tien Chau inlet as well as the analysis on the linkage between river dynamic factors to the past evolutions of the sand-spit and the inlet, using collected Landsat images from 1988 to 2019 and Sentinel images from 2016 to 2020. The results highlight strong relationships between geometries of both the Tien Chau inlet and the northern sand-spit, and the peak discharge Q_{\max} of the Ky Lo river.

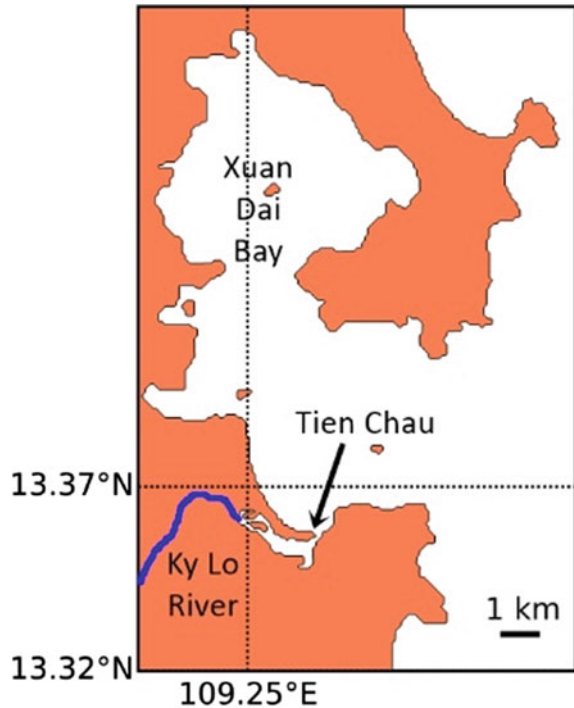
Keywords Sand-spit · Satellite images · Fishing harbor · Shoreline detection · Tien Chau Vietnam

1 Overview of the Study Area

Along the 3260-km coastline of Vietnam, many economic activities have been taking place. Of which, fishing brings substantial benefits to local people, especially in the Central Vietnam. Two key infrastructural factors for fishing are an efficient navigation route and a capable port. However, the situation is very challenging in some locals where the harbours and channels are shoaling rapidly and the elongated sand spits are severely intruding into the inlet. This study focuses on the Tien Chau inlet, which is located at the end of the Ky Lo river (Fig. 1).

The inlet (13.36° N, 109.26° E) leads to a fishing port and also serves as a shelter for over 400 vessels from storms. In recent years, the inlet has been narrowed

T. Thanh Tung (✉) · N. Quang Chien · D. Xuan Tinh
Thuyloi University, Hanoi, Vietnam
e-mail: t.t.tung@tlu.edu.vn

Fig. 1 Study area

remarkably, due to extension of the northern sand spit. At times, the basic maneuvering lane reduced to only just over 20 m.

The evolution of this sand spit is examined through a series of satellite images. Some results of analysis for the time period 1988–2020 are shown in Sect. 3. On the other hand, the factors responsible to the evolution of this sand spit are also discussed. Section 4 elaborates on the relation between the major river dynamic factor (discharge) and the geometries of the sand spit (length, area) and the inlet (width).

2 Materials and Methods

2.1 Data Collection

In recent years there has been an increase in number of researches using satellite images to analyze shoreline changes, due to improvements in image quality and availability of free image sources. For this study, the Landsat and Sentinel images since 1975 with a reasonable resolution are valuable data sources to monitor coastline changes at Tien Chau inlet. For a long-term, synchronized analysis, the Landsat images are chosen. The Sentinel images are used as an auxiliary source or

for analysis during hazards (storms, floods) and adverse effects (clouds in Landsat image).

Landsat-4 and 5 satellites, being launched by NASA in 1982 and 1984, respectively, incorporated the Thematic Mapper™ sensors with a maximum resolution of 30 m. The Landsat-7 was launched in Apr-1999, achieving a spatial resolution of 30–15 m with an improved ETM (Enhanced Thematic Mapper) sensor. The Landsat-8 was launched in 2013, with a maximum resolution of 15 m, using advanced imaging techniques. The imagery data can be downloaded from the Earth Explorer webpage [3], with the specific location: Path 123 and Row 51. There are 68 images collected (from 1975 to 2020). Only images with little cloud coverage, or no clouds, covering the Tien Chau area, are selected.

A newer source of satellite image is Sentinel-2 or ‘S2’ [1], which has been available since 2015 (S2-A) and 2017 (S2-B). The Sentinel-2 MSI (Multispectral Instrument, Level-1C) provides a resolution up to 10 m for visible bands (red, green, and blue) as well as near infrared and other bands, and therefore is suitable for detecting shorelines. The repeat cycle is 10 days (only five days since Oct-2017). S2 images for the study area have been retrieved from the online Access Hub [2], since 15-Nov-2015. The CoastSat [4], a web-based Python toolbox, has been used. Totally 120 relatively cloud-free images are selected for shoreline detection.

In terms of hydrographic data, it is ideal to use local water level measurement at Tien Chau. However, this data is only available from 04-Sep-2019 to 14-Sep-2020. Therefore, the data is lengthened based on data collected from the nearby Quy Nhon station (1988 to 2020), which shows very good correlation ($R^2 = 0.98$).

In addition, the water-level and river discharge time series has been collected for Ha Bang station on Ky Lo river (period 1975–2020), and the An Thanh environmental monitoring station (on Ngan Son bridge crossing Ky Lo river) (period 2012–2020).

2.2 Analysis Method

The Landsat and Sentinel 2 images are collected, then preprocessed to eliminate geometric distortions and converted to the WGS-84 coordinate system. Therefore, these images do not need further corrections for distortion, but only to be converted into the VN-2000 coordinate system. For Landsat images, the task has been accomplished using ArcGIS software, and some of the shoreline polygons are shown in Fig. 2.

Shoreline detection is based on the contrast level between the beach and the seawater quantified with MNDWI (Modified Normalized Difference Water Index) which involves two spectral bands (for Landsat MSS, bands 2 and 4; for Landsat TM and ETM+, bands 2 and 5). For the Sentinel images, an automatic MNDWI threshold between ‘water’ and ‘sand’ is applied [4]. The detected coastline is further processed with linear tidal correction based on a local beach face slope of 0.05.

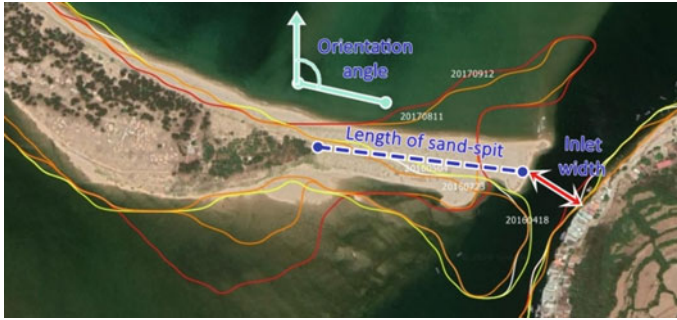


Fig. 2 Shorelines extracted from the satellite images. The geometries of the sand-spit (length, area, and orientation) are also shown

The extracted shoreline polygons (in the form of X–Y coordinates) are then used to calculate the geometries of the sand-spit and the Tien Chau inlet. First, a fixed point (the ‘Origin’—where vegetation exists) is identified ($X = 311,612$ m, $Y = 1,477,289$ m, UTM projection, Zone 49). The tip of the sand-spit is the furthest point from ‘Origin’. The length of the sand-spit is measured alongshore between these two points. Its orientation is measured from the vector connecting ‘Origin’ to ‘Tip’. The area is calculated for the part of polygon bound between the two tips (Fig. 2). The inlet width is measured from ‘Tip’ to the opposite shore of the inlet. All these geometries can be determined from the coordinate data.

3 Results and Discussion

The evolution of the sand-spit during 1988–2020 period can be reflected through the change of the inlet width, B . Figure 3 shows the evolution pattern of B since 1997. During 1997–2007, there was a stable fluctuation in B , around 90 m. Then B increases up to 340 m, due to a major river flood occurred on 2-Nov-2009. Remarkably there was a recovery time period (Jan-2010 to Oct-2016), during which the inlet became narrower.

Using Landsat data, we can find the regression Eq. (1) of B versus time, with a correlation coefficients R^2 of 0.90793:

$$B = 329.51 - 0.1344t \quad (1)$$

where t [days] the time starting from 28-Jan-2010.

The Sentinel data source has augmented since Mar-2016 and they provide a basis for forecasting the trend of sand-spit evolution. Specifically, after the flood on 9-Nov-2016, there existed a similar recovery period, which is characterized by the following Eq. (2) with $R^2 = 0.71725$:

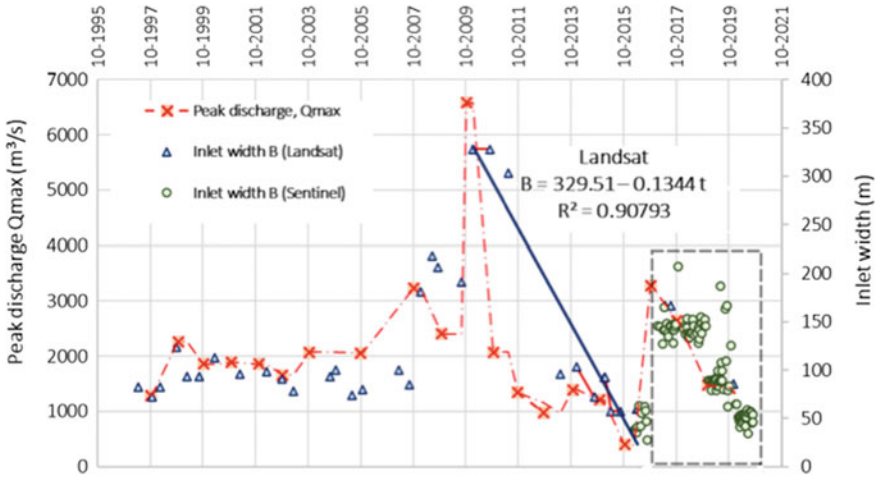


Fig. 3 Time evolution of the inlet width, B

$$B = 148.55 - 0.0967t \tag{2}$$

where t [days] is the time starting from 9-Nov-2016.

The time variations of sand-spit area, its length and orientation are not remarkable. The area varies from ~ 8.5 ha to ~ 4 ha, and tends to decrease since 2018. The sand-spit length is more stable, about 700 m. The spit orients approximately between eastward and ESE-ward, making an angle from 80° to 105° with respect to the north.

There is however a relationship between the inlet width and sand-spit orientation, as shown in Fig. 4. In this case, the Sentinel-derived data points only include those with $B < 200$ m. However, they are still scattered, possibly due to the width measurement is done automatically and may not correctly reflects the sand-spit curvature.

4 Relationship with the Peak River Discharge

There exists a clear relationship (Fig. 5) between the peak river discharge of the river, Q_{\max} (m^3/s), and the inlet width, B (m):

$$B = 0.0449Q_{\max} + 21.137 \tag{3}$$

Using Sentinel data only adds four data points corresponding to annually maximum discharge (period 2016–2019). However, the trend of these points generally follows the correlation between Q_{\max} and B derived from Landsat images.

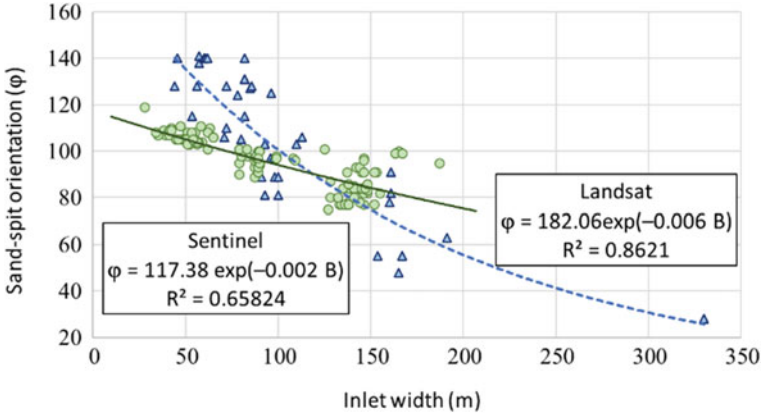


Fig. 4 Correlation between the sand-spit orientation, ϕ , and inlet width, B

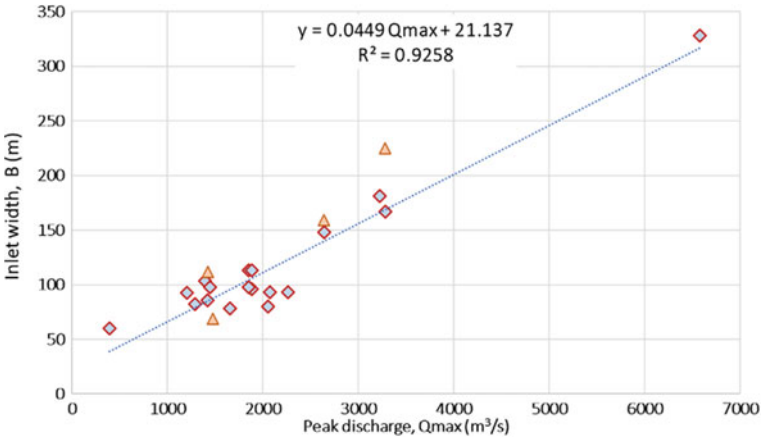


Fig. 5 Correlation between the peak discharge, Q_{max} , and inlet width, B

The shoreline data obtained from Sentinel-2 images are not only more abundant but also more consistent in time, thus provide a good basis to predict B from Q_{max} .

5 Conclusions

With an increasing availability of free satellite images, it is possible to monitor the evolution of coastal features such as the sand-spit north of Tien Chau inlet, Phu Yen province. Landsat images dated from 1988 to 2019 have been collected, with a spatial resolution of 15–30 m, and repeat cycle of 16 days but in reality many

images cannot be used for shoreline detection, due to cloud coverage. Sentinel-2 images have been additionally collected with better resolution (~ 10 m) and shorter repeat cycle (5 days). The development of the sand-spit length, the correlation between sand-spit orientation and inlet width, and between the inlet width and the river discharge have been formulated. By using the Sentinel dataset, and newly developed analysis tools such as CoastSat, the recent evolution of the sand-spit is tracked in more details and prediction for future evolution due to e.g. peak river flood discharge would be possible using machine learning techniques. Determining geometries of the sand-spit and the inlet would be necessary in estimating the stable width of the inlet, for stabilizing the inlet entrance to the fishing harbour.

Acknowledgements This study is funded by the Project “Research on training solutions, countering channel accretion for fishing ports and anchoring harbours of Phu Yen province and the vicinity, with a case study for Tien Chau inlet”, code DTDLCN.33/18.

Reference

1. ESA (European Space Agency) (2020) Sentinel-2 mission: Sentinel online. <https://sentinel.esa.int/web/sentinel/missions/sentinel-2>. Last accessed 2020/10/01
2. ESA (2020) Copernicus open access hub. <https://scihub.copernicus.eu/>. Last accessed 2020/09/16
3. USGS (2020) Earth explorer. <https://earthexplorer.usgs.gov>. Accessed 2020/07
4. Vos K, Splinter KD, Harley MD, Simmons JA, Turner IL (2019) CoastSat: a Google earth engine-enabled python toolkit to extract shorelines from publicly available satellite imagery. *Environ Model Softw* 122:104528

Wave Energy Assessment Along Chinese Coasts Based on a 40-Year Hindcast



Jiali Xu, Jian Shi, and Chi Zhang

Abstract A wave database has been built over the period of 1979–2018 using the third-generation wave model TOMAWAC. This database can provide wave parameters with high spatial (1 km along Chinese coast) and temporal (1 h) resolutions, which can be used to estimate wave power potential along Chinese coast areas. To better use of wave energy, appropriate wave energy collection devices and collection points need to be determined. The working costs of three types of wave energy collection devices: AquaBuOY, Pelamis, and Wave Dragon, are analyzed based on the wave energy density, annual average coefficient of variation, and extreme wave event. The most promising areas of wave energy harvesting are located at the southern part of the East China Sea and the northern part of the South China Sea near Taiwan Island. In addition, the Pelamis device is most suitable for the collection of wave energy in China offshore than the AquaBuOY and Wave Dragon.

Keywords TOMAWAC · Wave simulation · Wave energy density · Wave energy convertor

1 Introduction

With the global consumption of traditional energy, the rising cost of electricity generation and climate warming, the development of new green energy has become an urgent need for both economic and social development. Scientifically developing and utilizing ocean energy are of great importance to alleviate the energy crisis and

J. Xu · J. Shi (✉) · C. Zhang

State Key Laboratory of Hydrology-Water Resources and Hydraulic Engineering,
Nanjing 210098, China
e-mail: Jianshi@hhu.edu.cn

J. Xu · J. Shi · C. Zhang

College of Harbor Coastal and Offshore Engineering, Hohai University,
Nanjing 210098, China

environmental pollution. Wave energy is the most studied ocean energy. Since the 1970s, scientists have used limited ocean ship report data and buoy data to evaluate wave energy resources [1].

The assessment of wave energy resources based on observed data usually has a short test time and does not allow long-term sequence analysis of the wave energy resources of the entire demonstration site. In 2009, Rusu and Soares [2] studied the wave energy resources of Portugal's nearshore using buoy observation data and the results of WAM and SWAN wave model simulations. The average wave energy density was used as the criterion to determine the most potential development area. Iglesias et al. [3] used the results of the WAM and SWAN models every three hours from 1996 to 2005 to evaluate the wave energy potential in the waters near Galicia in northwestern Spain, based on annual estimated energy generation and annual average wave energy density. Folley and Whittaker [4] used the third-generation nearshore wave numerical model SWAN to investigate the wave energy resources in the shallow waters near the shore of the North Atlantic coast of Scotland, and analyzed the changes in the wave energy from the offshore deep water area to the shallow water near the shore. It was recommended to propose new indicators instead of using the total wave energy density to assess the availability of wave energy in the sea. In 2016, Gallagher et al. [5] used HARMONIE and WAVEWATCH III to track wind and wave data for 14 years from 2000 to 2013 in Ireland, and studied the spatial and temporal distribution of wave energy resources in the west, south, northwest and southwest of Ireland.

So far, the evaluation of wave energy resources in various regions of China is often not accurate enough, and the distribution of long-term wave energy resources in the studied area has not been analyzed. In addition, it is difficult to assess the wave energy potential in the study area and determine the optimal location for the construction of wave power stations. This paper analyzes the variation coefficient of wave energy at different time scales in China's sea areas, and the power generation cost of different wave energy collection devices. Considering both of them to determine the appropriate wave energy collection points and the corresponding wave energy collection device.

2 Assessment of Offshore Wave Energy Resource in China

2.1 Spatial Distribution of Wave Energy

Energy density, also known as wave power density, refers to the average value of wave power in a wave period, in kW/m. In the general analysis of wave energy resources, waves are treated as deep-water waves. The empirical formula proposed by EPRI [6] (Electric Power Research Institute) in the United States is applicable to a wide range of calculations and widely used by scholars at home and abroad.

The calculation formula is as follows:

$$P = 0.5 \times H_{1/3}^2 \times \bar{T} \tag{1}$$

where P represents the energy transport per unit crest length, $H_{1/3}$ represents the significant wave height, \bar{T} represents the mean wave period.

It can be seen from Fig. 1 that the energy density increased from north to south (except Beibu Gulf). The energy density of Bohai Sea was no more than 4 kW/m, and the energy density of the Yellow Sea did not exceed 6 kW/m. The energy density of East China Sea was between 12 and 18 kW/m. The energy density of the South China Sea except for Beibu Gulf was 10–18 kW/m.

2.2 The Annual Variation of Wave Energy

The stability of wave energy has always been an important factor in the selection of wave energy collection devices and the best site for installation. Stable wave energy output is even more important than high wave energy density. The annual variability index (AVI) is used to represent the stability of wave energy, which is given by

$$AVI = \frac{P_{A1} - P_{A2}}{P_{year}} \tag{2}$$

where P_{A1} represents average wave energy of the year with the largest wave energy in 40 years, P_{M2} represents average wave energy of the year with the smallest wave energy in 40 years P_{year} represents average wave energy of 40 years.

Fig. 1 Average wave energy density from 1979 to 2018

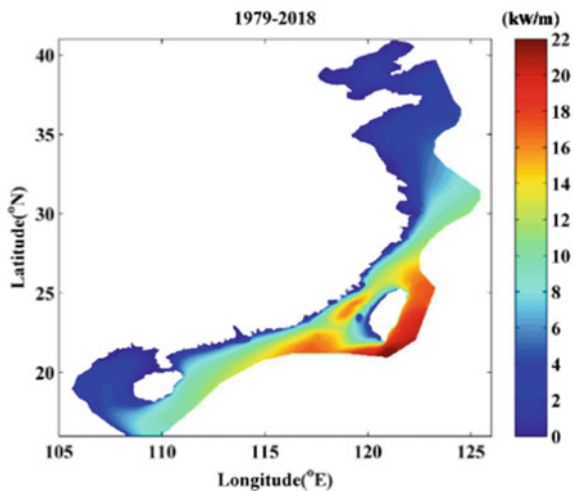


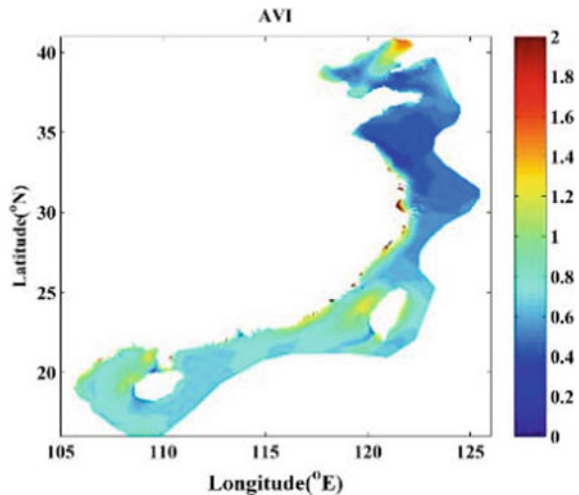
Figure 2 reflects the variation of wave energy with the year from 1979 to 2018. The smaller the value of AVI, the smaller the difference between the maximum and minimum annual mean values of wave energy from 1979 to 2018. That is, the wave energy does not change significantly with the years during the 40 years. A value of AVI exceeding 1.2 indicates a considerable change, and a value of AVI exceeding 1.5 indicates that the wave energy flow density changes dramatically with the year. From Fig. 3, it can be seen that the annual average coefficient of variation of the wave energy in China's coastal waters from 1979 to 2018 is mostly less than 1.2, indicating that the change of wave energy in China's coastal waters is not particularly large, but in the northeastern Bohai Sea, there is a sudden change in the annual average coefficient of variation of the wave energy up to 1.4. This is because although the wave energy in the Bohai Sea is generally small, the maximum value in the Northeast Sea is much higher than the minimum value, but the average value is not large.

2.3 Levelized Cost of Electricity According to Different WECs

There are three different WECs are discussed here: Point Absorbers (AquaBuOY), Terminators (Pelamis), Systolic wave-type wave energy collection device (Wave Dragon).

The levelized cost of electricity for the above three WECs are calculated as follows:

Fig. 2 Annual variability index (AVI) of wave energy for the period 1979–2018



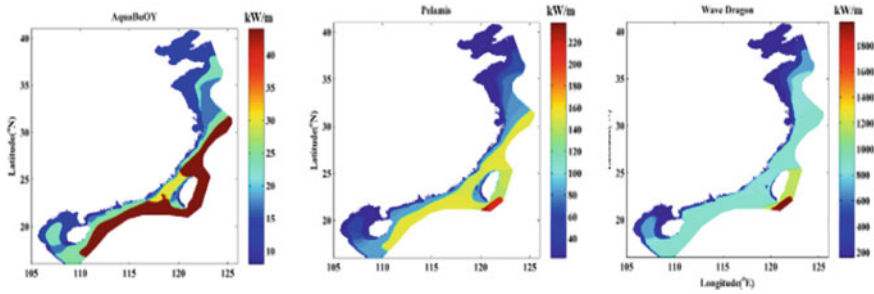


Fig. 3 Actual energy output of three different WECs

$$\begin{aligned}
 LCOE_{Device1} &= 76 + \frac{10.47}{k_{Device1}} \\
 LCOE_{Device2} &= 23 + \frac{30.00}{k_{Device2}} \\
 LCOE_{Device3} &= 53 + \frac{44.39}{k_{Device3}}
 \end{aligned}
 \tag{3}$$

where Device1 represents point absorbers, Device2 represents terminators, Device3 represents linear absorbers, $k_{Device1}$, $k_{Device2}$, $k_{Device3}$ refers to the efficiency coefficients of the three devices, respectively.

$$k = \frac{P}{P_{max}}
 \tag{4}$$

where P is the actual energy output of each device, P_{Max} is the maximum energy output of the device. Here P can be obtained by checking the worksheet of each device.

Figure 3 shows the actual wave energy output of three different WECs. In addition to the eastern area of the East China Sea, the sea area near Taiwan Island and the northern sea area of the South China Sea (except the Beibu Gulf), the three WECs can actually acquire the largest wave energy. However, according to the worksheet of the three WECs, the maximum wave energy that the AquaBuOY device can actually collect is 250 KW, Pelamis can actually collect 750 kW, Wave Dragon can actually collect 7000 kW.

Figure 4 shows the levelized cost of electricity of three kinds of devices in the coastal waters of China. The levelized costs of electricity of three devices in most areas of the Bohai Sea and the Western Yellow Sea are relatively high, which is due to the low working efficiency of these areas. In most of the sea areas of the East China Sea, the sea area near Taiwan Island and the sea area in the north of the South China Sea (except the Beibu Gulf), the levelized costs of electricity of the three devices are relatively low.

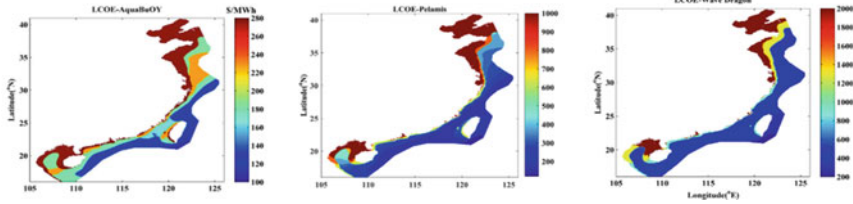


Fig. 4 The levelized cost of electricity of the three WECs (\$/MWh)

2.4 Selection of Hotspots for Wave Energy Utilization

For the purpose to select the optimum hotspots for wave energy utilization in China, jointly taken the average wave energy of 40 years P_{year} , AVI and LCOE into accounts, the Optimum Hotspots Identifier (OHI) defined as:

$$OHI = \frac{P_{year}}{AVI \cdot LCOE_{Device_i}} \tag{5}$$

where, $Device_i$ represents point absorbers, terminators, and linear absorbers, respectively. P_{year} represents average wave energy of 40 years. AVI refers to the coefficient of variability of wave energy in 40 years.

Figure 5 shows that the values of OHI in the Bohai Sea, the Yellow Sea and the Beibu Gulf of the South China Sea are relatively low, not more than 1×10^{-5} , indicating that the AquaBuOY device is not suitable for wave energy collection in these waters, because the wave energy density of these waters is not high, and the work cost of the AquaBuOY device in these waters is high, so it is not suitable for wave energy collection. However, the value of OHI in the East China Sea area near Taiwan island is up to 3.5×10^{-5} , and that in the South China Sea area near Taiwan island is up to 2.5×10^{-5} . The wave energy density is high in these areas, and the working cost of AquaBuOY device is not high in these areas, so it is more suitable to collect wave energy. Although the OHI index is the largest in the southeast of Taiwan Island, considering the study of extreme wave events by Shi et al. [1], the frequency of extreme wave events in the southeast of Taiwan island is large, the duration is strong, and the average intensity is large, which may damage the wave energy collection device. Therefore, the two sea areas (red frame sea area) close to the southeast of Taiwan Island and the north of South China Sea are still the most suitable sites for wave collection.

For Pelamis and Wave Dragon devices, the values of OHI index in the sea area framed red are larger, so they are more suitable for wave energy acquisition. As the same as the AquaBuOY device, considering the extreme wave events, these two sea areas are the most suitable sites for wave energy acquisition. In addition, Pelamis device has higher value of OHI in these two areas, which is more suitable for wave energy acquisition near the coast of China.

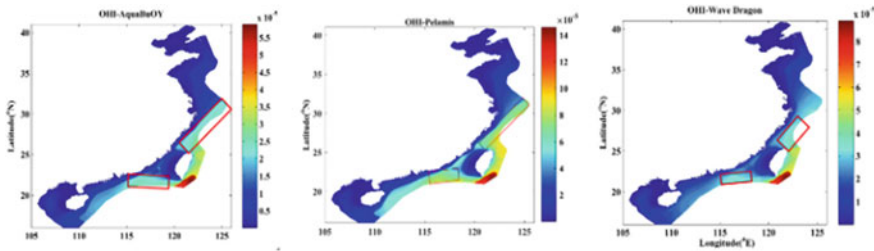


Fig. 5 OHI index distribution of the three WECs

3 Conclusions

In this paper, a high-precision and high-resolution wave database of long time series near the coast of China is established by using the TOMAWAC model, and the wave energy resources in various sea areas of China are evaluated. It is found that the distribution of wave energy density increases from north to south, and the average annual variability index is less than 1.2 in most areas, indicating that the variation of wave energy is not obvious. For AquaBuOY, Pelamis and Wave Dragon, the most suitable wave energy acquisition sites are in the sea area of the South China Sea and the South China Sea near Taiwan Island. In addition, Pelamis device has a larger OHI coefficient than AquaBuOY and Wave Dragon, and is more suitable for the acquisition of wave energy in China's offshore waters.

Acknowledgements This work is supported by the National Natural Science Foundation of China (41930538), the Postgraduate Research and Practice Innovation Program of Jiangsu Province (KYCX18_0613), the Fundamental Research Funds for the Central Universities (2018B653X14, B200202064) and the High Performance Computing Platform, Hohai University.

References

1. Shi J, Zheng JH, Zhang C et al (2019) A 39-year high resolution wave hindcast for the Chinese coast: model validation and wave climate analysis. *Ocean Eng* 183:224–235
2. Rusu E, Soares CG (2009) Numerical modelling to estimate the spatial distribution of the wave energy in the Portuguese nearshore. *Renew Energy* 34(6):1501–1516
3. Iglesias G, López M, Carballo R et al (2009) Wave energy potential in Galicia (NW Spain). *Renew Energy* 34(11):2323–2333
4. Folley M, Whittaker TJT (2009) Analysis of the nearshore wave energy resource. *Renew Energy* 34(7):1709–1715
5. Gallagher S, Tiron R, Whelan E et al (2016) The nearshore wind and wave energy potential of Ireland: a high resolution assessment of availability and accessibility. *Renew Energy* 88: 494–516
6. Sierra JP, White A, Mósso C et al (2017) Assessment of the intra-annual and inter-annual variability of the wave energy resource in the bay of Biscay (France). *Energy* 141(P1): 853–868

A Framework to Develop Intensity-Duration-Frequency Curves for Ungauged Sites in Vietnam: The Case of Hoa Binh Province



Noi Thi Doan, Thanh Tien Nguyen, and Son Hoang Nguyen

Abstract The Intensity-Duration-Frequency (IDF) curves play especially important role in water resources engineering or design of infrastructure. It is widely applied to quantify the probability of occurrence of extreme precipitation events. The IDF curves often based on the long-term historical precipitation observation at high spatial temporal resolution. However, it is difficult to gather the long records of short duration precipitation in most areas of developing countries like Vietnam. It is note-worthy that the satellite-based or reanalysis precipitation products are recently becoming available, providing the high-resolution estimations at regional or even global scales. Therefore, this study provides a framework to develop IDF curves based on the different precipitation data for ungauged sites in Vietnam and taking Hoa Binh province as a pilot. The products of satellite-based and reanalysis precipitation are investigated and evaluated. More importantly, the station-based precipitation is used to evaluate and correct the different products. The results illustrate an agreement, to a good extent, of IDF curves derived from the considered precipitation products.

Keywords IDF curve · Satellite-based precipitation · Reanalysis data · PERSIANN · ERA

1 Introduction

Precipitation in the tropics is characteristically uneven both temporally and spatially, which makes it challenging to design hydrograph for construction of transportation infrastructure. For most water engineering projects, rainfall intensity analyses, especially IDF curves for the different return periods, are of great

N. T. Doan (✉)

Faculty of Civil Engineering, University of Transport and Communications, Hanoi, Vietnam
e-mail: dtnoi@utc.edu.vn

T. T. Nguyen · S. H. Nguyen

Faculty of Water Resources Engineering, Thuyloi University, Hanoi, Vietnam

importance. Based on the available rainfall, the IDF curves can be developed and designed through the application of appropriate statistical distributions such as Gumbel Type I or Weibull. With an IDF curve, the time concentration of rains is fully interpreted [1–4]. To do this, the requests of precipitation information at high resolution of tempo-spatial are important. This, however, is hard difficult to collect rainfall data records for a long-term, especially in Vietnam, a developing country and Hoa Binh province as special region in northern Vietnam where topography is relatively complex with mountains.

For different regions worldwide, IDF formulae were developed at ungauged sites [3, 5]. The numerous distributions of Gumbel, Log Pearson III, and Log normal were applied to generate the empirical formulae to estimate the IDF curves for Riyadh region as an example [6]. In Vietnam, the IDF curves were developed for seven stations, and proposed a generalized IDF formula using base rainfall depth and base return period for a part of northern Vietnam [7]. More specially, the parameters of rainfall intensity duration frequency equations are then regionalized for ungauged areas to estimate rainfall intensity for various return period and rainfall duration. A way to construct IDF curves was proposed and applied based on the rainfall height but not intensity using the power function for central Vietnam [8]. The IDF curves then developed for sub-daily based on daily rainfall and relationship between hourly and daily rainfall at several stations.

Still, there have not yet studies in applying the satellite or reanalysis rainfall data in Vietnam where there are no available records of rainfall intensity or climate variables for gathering. At ungauged sites like Hoa Binh province of Vietnam as an example, it is of importance to generate satisfactory IDF curves for multiple purposes in the field of transportation infrastructure. Therefore, the purpose of this study attempt to depict a framework to develop IDF curves for this area based on the rainfall records from four stations in Hoa Binh province. Furthermore, the satellite and reanalysis rainfall data are corrected to generate IDF curves for return periods of 10, 20, 50, 100 and 200 years with an emphasis of 1, 2, and 3-maximum daily rainfall. The IDF curves generated from these rainfall data is also compared with IDF curves generated from the station-based rainfall data.

2 Materials and Methods

2.1 Materials

This study collects the data from different sources including: (i) Station-based hourly rainfall data is collected from the Vietnam Center of Hydro-Meteorological Data with a total of hour rainfall stations (i.e., ChiNe, Hoa Binh, Lac Son and Mai Chau (Fig. 1)). (ii) Satellite data of PERSIANN: PERSIANN (Precipitation Estimation from Remotely Sensed Information using Artificial Neural Networks) is a satellite-based precipitation retrieval algorithm, providing near-real time

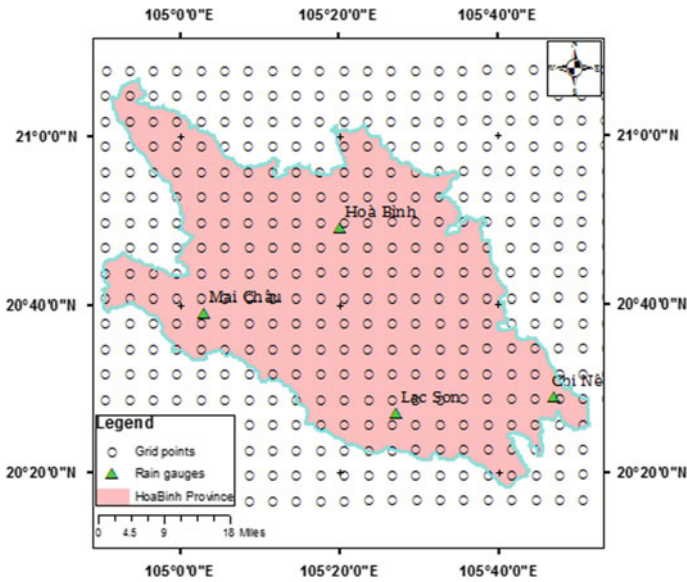


Fig. 1 Study area

precipitation products [9]. The original PERSIANN product has a temporal resolution of 1 h and a global spatial grid of 0.05° between 60° N and 60° S. (iii) Reanalysis data of ERA5. It is noted that there is several positive points of ERA5 data such as spatially and temporally complete data set of multiple variables at high spatial and temporal resolution; better able to resolve features like hurricanes than previous generations of the reanalysis [10].

2.2 Methodology

Before performing IDF construction, the satellite-based and reanalysis-based rainfalls are corrected using the bias correction. In this study, a simple bias is applied. It operates with monthly correction values based on the differences between station-based data and estimated data (i.e., satellite-based and reanalysis data). The daily estimated rainfall amounts are transformed into by multiplying with the monthly scaling factor. It is noteworthy that the drizzle effect is removed in time series by replacing daily rainfall accumulation values less than 1 mm with zero. Later, the data is assembled by all 12 months. This grouping removed seasonality from the raw time series; and therefore potentially improved the bias correction methods. The method is as shown in Eq. (1).

$$Rain_daily_{P,E} = \frac{Rain_{month(O)}}{Rain_{month(P,E)}} Rain_daily_{P,E} \tag{1}$$

where, *P* denotes PERSIANN, *E* denotes ERA5 and *O* refers station-based rainfall.

Later the construction of IDF curves follows the approach described in [8]. Generally, it is generated with three steps. Firstly, precipitation data for a number of precipitation durations (e.g., 1, 2, 3 days) is fitted by probability distribution function (PDF) or Cumulative Distribution Function (CDF). Then the maximum precipitation intensity for each time interval is related with the corresponding return period from the cumulative distribution function. Finally, from the known cumulative frequency and given duration, the maximum precipitation intensity can be determined using an appropriate fitted theoretical distribution function of Gumbel. A detailed description could be found in [8]. The flowchart described the step by step in this study is present in Fig. 2.

3 Results and Discussion

Performance of IDF curves is generated for each station but shown the results implemented for HoaBinh station. The probability distribution method is implemented to identify the rainfall and their corresponding return period. For various durations, IDF curves are plotted for various return periods. It is noted that the rainfall data is simply labeled for before and after correction. More specifically, the ERA5 product with and without correction is labeled by ERA5 and ERA5_Cor, respectively.

Similarly, the PERSIANN product with and without correction is labeled by PERSIANN and PERSIANN_Cor, respectively. Obs indicates the station-based data. In this study, an emphasis of analysis for HoaBinh is presented. Figure 3 shows intensity duration frequency curves for Hoa Binh station with different rainfall. It depicts the trends and curvature for each rainfall data and intensity values. IDF curves generated with ERA5 and PERSIANN are relatively different in

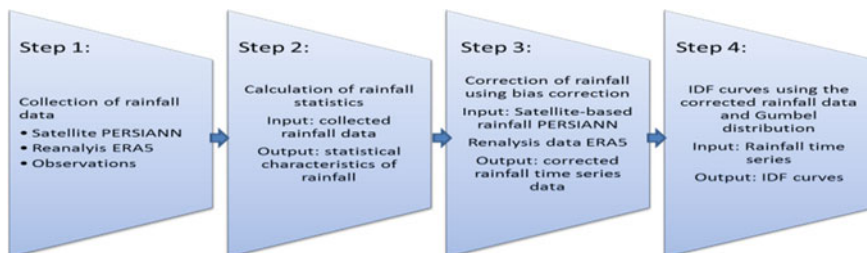


Fig. 2 Flowchart of methodology

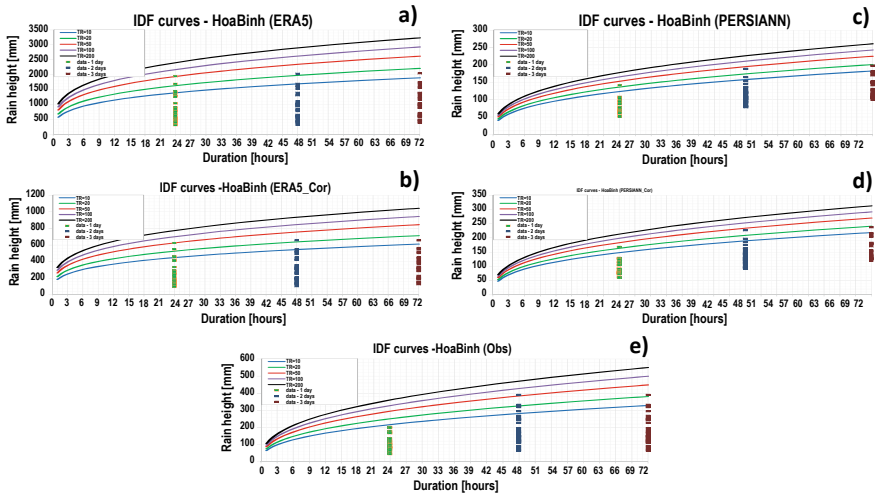


Fig. 3 IDF curves for Hoa Binh station with ERA5 (a), ERA5_Cor (b), PERSIANN (c), PERSIANN_Cor (d) and Obs (e)

comparison with that generated by Obs. Compared to the IDF curves generated by Obs, IDF curves generated by ERA5 product tend to reasonably overestimate (nearly 1000 mm within 3 days), whereas IDF curves generated by PERSIANN product tend to lightly underestimate (about 100 mm within 3 days).

It is special emphasized that performance of bias correction robust the accuracy of ERA5 and PERSIANN products used for development of IDF curves. To better visualization, Fig. 4 shows the time return periods for Hoa Binh station. The distance between the IDF curves generated by ERA5_Cor, PERSIANN_Cor and Obs

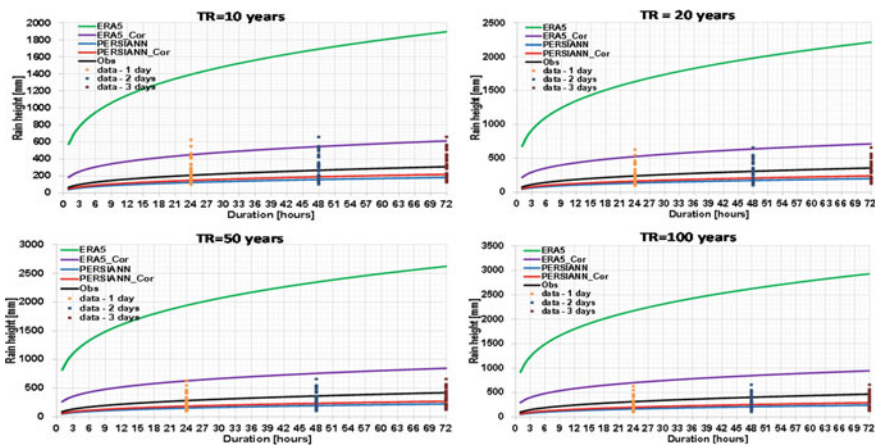


Fig. 4 Time return periods for Hoa Binh station

is significantly tiny, especially the IDF curves generated by PERSIANN_Cor. With a bias correction, the generated IDF curves are good some extent. The uncertainty of rain height is improved with approximately 40 mm within 3 days for time return periods of 10, 20, 50 and 100 years. It is can be seen from the Fig. 4, the authors also suggest a need to implement further investigations for an ensemble of rainfall products with bias correction. Using this approach, the IDF curves for ungauged sites could be generated using the grid points of satellite-based and analysis-based rainfall data.

4 Conclusions

The study provides a useful approach to generate IDF curves for construction of transportation infrastructure project in ungauged sites. A bias correction combined with the Gumbel distribution is applied to satellite-based and reanalysis-based rainfall data for developing the IDF curves in Hoa Binh province. The results show the generated IDF curves using the satellite-based rainfall data combined with bias correction are significantly closed to the IDF generated by station-based rainfall data. From that, IDF curves are completely constructed at grid points in which there is ungauged rainfall. Based on the IDF curves, it is recommended for the prediction of rainfall intensities and designs the projects in the region.

Acknowledgements This research is funded by The University of Transport and Communications, Hanoi, Vietnam under grant number T2020-CT-002TB.

References

1. Akan AO, Houghtalen RJ (2003) Urban hydrology, hydraulics, and stormwater quality: engineering applications and computer modeling. John Wiley & Sons
2. Jolliffe CJ, Janssen J (2007) Development of age-specific adolescent metabolic syndrome criteria that are linked to the adult treatment panel III and international diabetes federation criteria. *J Am Coll Cardiol* 49(8):891–898
3. Koutsoyiannis D, Kozonis D, Manetas A (1998) A mathematical framework for studying rainfall intensity-duration-frequency relationships. *J Hydrol* 206(1–2):118–135
4. Sivapalan M, Blöschl G (1998) Transformation of point rainfall to areal rainfall: intensity-duration-frequency curves. *J Hydrol* 204(1–4):150–167
5. Baghirathan VR, Shaw EM (1978) Rainfall depth-duration-frequency studies for Sri Lanka. *J Hydrol* 37(3–4):223–239
6. AlHassoun SA (2011) Developing an empirical formulae to estimate rainfall intensity in Riyadh region. *J King Saud Univ Eng Sci* 23(2):81–88
7. Nhat LM, Tachikawa Y, Takara K (2006) Establishment of intensity-duration-frequency curves for precipitation in the monsoon area of Vietnam. *Ann Disas Prev Res Inst* 93–103
8. Nguyen TT, Dutto ARL (2018) Projected changes of precipitation idf curves for short duration under climate change in central Vietnam. *Hydrology* 5(3):33

9. Hsu KL, Gao X, Sorooshian S, Gupta HV (1997) Precipitation estimation from remotely sensed information using artificial neural networks. *J Appl Meteorol* 36(9):1176–1190
10. Hersbach H, Bell B, Berrisford P, Hirahara S, Horányi A, Muñoz-Sabater J et al (2020) The ERA5 global reanalysis. *Q J Roy Meteorol Soc* 146(730):1999–2049

Assessment of Hydrodynamic Regime and Inundation Mode After Construction of Hydraulic Project in Quang Ngai Province



Nguyen Phuong Dung, Nguyen Thai Binh, and Tran Thi Hoai Phuong

Abstract Before the construction of any hydraulic project, the flow regime should be ensured to have little effect on the banks and on the civil constructions downstream. From the data of nearby projects, the authors have carried out the numerical simulation of a low-head dam project on Tra Khuc river using the International River Interface Cooperative (IRIC). The calibration is conducted by comparing the simulation of the river in its natural state with actual measurement from surrounding stations and the results are shown to be acceptable. The model is tested on several scenarios of flooding, with a combined spillway (piano-key weir and gated ones) or without the structure. It is shown that the flow regime behind the piano key is very complicated, however, after a certain distance, flow streams of various directions and velocities combine into a considerably stable and uniform stream. Furthermore, compared to the natural state of the river, the water level after the construction of the low-head dam does not rise significantly and at the same time, the task of increasing the upstream water level is fulfilled.

Keywords Low-head-water hydraulic project · Combined spillways · Hydrodynamic regime · Flood-routing

N. Phuong Dung (✉) · T. Thi Hoai Phuong
Thuyloi University/TLU, Hanoi, Vietnam
e-mail: nguyenphuongdungn@tlu.edu.vn

T. Thi Hoai Phuong
e-mail: phuongth63@wru.vn

N. Thai Binh
ICE/TLU, Hanoi, Vietnam
e-mail: binh19@ymail.com

1 Introduction

The construction of low-head dams on rivers near estuaries has been on the rise recently in Vietnam. Meanwhile, the data and research on the topic of low-head water dam in Vietnam is still rudimentary and as such, this study chooses to focus on examining the operation of a hydraulic project related to barrages via the numerical model IRIC. This research examines the operation of the planned complicated spillway (including piano spillway and sluice gates) on the Tra Khuc river [1] because of its potential applicability and on-site evaluation in the future. Specifically, evaluation of the downstream hydrodynamic regime and its impact on river banks with different operating scenarios are conducted after the calibration of the model is completed. The main objective of the paper is to assess the hydrodynamic regime and inundation mode after the construction of the hydraulic project in Quang Ngai through IRIC in order to obtain deeper understanding on the topics of barrages and piano-key weirs, especially their effects on flood prevention.

2 Methodology

2.1 Governing Equations and Numerical Method

In order to evaluate the hydrodynamic regime on the river, the governing equations of the continuity and momentum equations are used. In IRIC, water flow is transformed from the Cartesian coordinate system to a moving boundary-fitted coordinate system due to the deformation of side banks [2, 3]. The equations is written in the moving boundary-fitted coordinate system (ξ, η) .

The governing equations for water flow are solved numerically using the finite difference method in (ξ, η) coordinate systems with high-order Godunov scheme known as the cubic interpolated pseudo-particle (CIP) [4].

2.2 Model Configuration

The inflow at the inlet boundary is taken from the 1% AEP flood from 2 upstream reservoirs—Nuoc Trong and Dak-Drinh. This is the most extreme flood scenario available from the obtained data, which is used for most consultant or production projects in the surrounding areas. The outlet boundary adopts the free outflow condition as the research does not account for the negligible tidal effect on river flow. Two grid types (rectangular) are adapted in the model. The coarser one (Fig. 1a) with the size of 100×100 is used to determine the overall flood situation in the region, and the detailed one (Fig. 1b) 12.5×12.5 is for the purpose of figuring out the hydraulic regime in Tra Khuc river. The Manning roughness

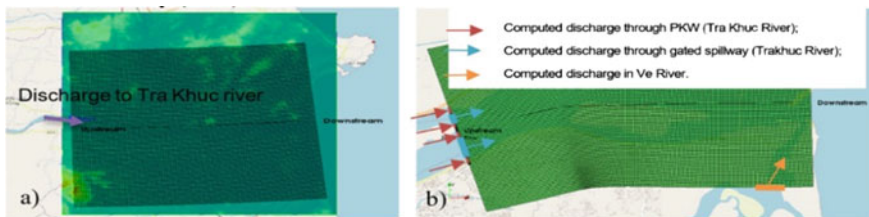


Fig. 1 Computation grid domain, a for inundation model, b for hydro-dynamic computation

parameter for the river bottom is $n = 0.03$. The initial water level of the river is taken from the hydrological data in the region. The time step is determined by satisfying the Courant–Friedrichs–Lewy (CFL) condition.

2.3 Relationship Between Flood Routing Scenarios and Hydrodynamic Regime

The distribution of the outflow discharge through complicated spillways is the special concern of this research. The outlet components have piano key weirs (PKW) to ensure free discharge and minimum ecological flow during the dry season or provide flood routing during the flood season. In the flood season, the flow is let-off through the sluices regulated by vertical-lifted gates, and this operating process will greatly affect the hydrodynamic regime on the downstream river. Thus, several scenarios related to the degree of opening are provided in Table 1.

The first 3 scenarios are proposed to simulate the river in its natural state, because currently there is no construction in this area. TH3 simulates the flood scenario where upstream reservoirs are working as intended and cut off part of the upstream flood. This scenario will be used for all cases from TH4 to TH8, where the

Table 1 Simulation scenarios

Case No.	Descriptions
TH1	The 1% AEP flood on the Tra Khuc and Ve rivers
TH2	The 1% AEP flood on the Tra Khuc river
TH3	The 1% AEP flood on Tra Khuc river (part of upstream flood is cut off)
TH4	After construction, with an even unit discharge through the spillway
TH5	The 1% (AEP) flood on the Tra Khuc river with sluice gate opening of 1 m
TH6	The 1% (AEP) flood on the Tra Khuc river with sluice gate opening of 1.5 m
TH7	The 1% (AEP) flood on the Tra Khuc river with sluice gate opening of 2.0 m
TH8	The 1% (AEP) flood on the Tra Khuc, flood regulation through PKW and few lateral sluices

construction of the barrage is included and the changing parameters are related to the spillway component. With the sluices, the total discharge is calculated based on submerged flow model over broad-crest weir and with the PKW, it is computed from the National Standard 12262:2018 [5]. Those discharge values (unit discharge values) are used as input parameters for the construction simulation.

2.4 Model Validation

Model validation: The original model was run for 120 h for the case TH1 and compared with the actual measurement at Tra Khuc station. To measure the predictive capability, the Nash–Sutcliffe model efficiency coefficient (NSE) is used and represented as followings:

$$NSE = 1 - \frac{\sum_{i=1}^n (O_i - S_i)^2}{\sum_{i=1}^n (O_i - \bar{O})^2} \quad (1)$$

The resulted NSE is estimated at approximately 0.86, which means the model can be used for further, more complex simulation.

3 Results and Discussion

3.1 Low-Head Hydraulic Work on Tra Khuc River

A hydraulic project is already planned for the research region and as such, this research will use the same setting of the project for the simulation. The planned hydraulic work is located on Tra Khuc river in Quang Ngai Province. Outlet work is consisted of 19 sluice gates and 2 piano spillways, located on the north and south banks of the Tra Khuc hydraulic work. The hydraulic work alignment is shown in Fig. 2 (highlighted in red). The functions that the project must fulfill are: (1) the ability to pass all normal and up to 100 year AEP flood flows without negatively affecting water levels upstream; (2) the ability to maintain a constant water level in the lake [1].

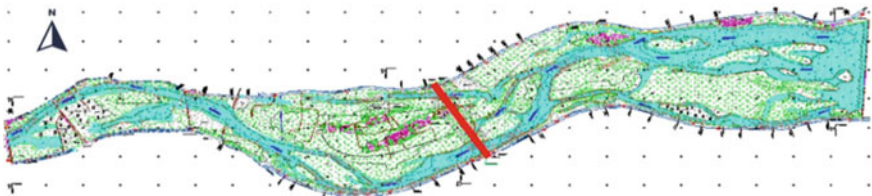


Fig. 2 The structural alignment in Tra Khuc river (highlighted in red)

3.2 Evaluation of the Hydraulic Regime

The flow simulation results for each specific case are listed in Table 2. Calculation results include water elevation profile, velocity profile and time series of simulations. There are three important timelines $t_1 = 36,000$ s, $t_2 = 162,000$ s, $t_3 = 396,000$ s, all of which correspond to the peak and trough of the inflow.

As can be clearly seen in TH8, a complex flow pattern develops due to the combination of both the PKW and sluice gate (Fig. 3). After a certain distance (100 m downstream), multiple directions of flow conjugate and form an almost uniform stream; the velocity becomes evenly distributed and its value is nearly 1.17 m/s. Turbulence effects are significant, particularly directly behind the spillway. In contrast, the flow field in the simulation of the natural state shows that the upstream flood is still divided into 2 branches due to the effect of the island in the middle, however, the flow velocity and turbulence intensity is not as high as the case with the construction. In general, the combination of PKW and sluice gate complicates the flow pattern in the river (the part behind the island) but does not have significant impact on the downstream hydraulic regime.

Due to the small capacity of the reservoir (the flood storage/surcharge is not large) and the complex topography of the Tra Khuc river bed, using both the sluices and PKW for the flood routing task is essential. In TH5, the duration of the peak storage in downstream areas is more than 120 h, which is the whole duration of the flood. Regarding the others scenarios (with opening more sluices), the peak storage period is shorten—the outflow discharge reaches the maximum value in about 1 day. Interestingly enough, the outflow hydrograph is very close to the natural inflow hydrograph. In simulated cases with structures, the velocity distribution (behind structure) in stilling basin reaches a maximum speed of 9.65 m/s, and its direction is almost parallel to the structural alignment. If only looking at the average parameter, the flow does not heavily affect the river bank. However, the maximum instantaneous velocity that occurs in the stilling basin is of great concern. Furthermore, at the location about 60 m away from the construction alignment, a velocity vortex is formed and thus, it is necessary to have appropriate reinforcement measures in this area.

Table 2 Calculation results

No.	TH1	TH2	TH3	TH4	TH5	TH6	TH7	TH8
V_{t1} (m/s)	0.83	0.81	0.82	0.81	0.82	0.81	0.83	0.80
H_{t1} (m)	2.32	2.12	2.12	2.10	2.10	2.10	2.12	2.09
V_{t2} (m/s)	1.53	1.53	1.50	1.50	1.71	1.74	1.67	1.61
H_{t2} (m)	8.18	7.94	7.97	8.07	8.37	8.30	8.21	8.43
V_{t3} (m/s)	1.09	0.91	0.92	0.90	0.90	0.91	0.91	0.80
H_{t3} (m)	4.09	3.94	4.08	3.98	3.87	3.97	3.90	3.88

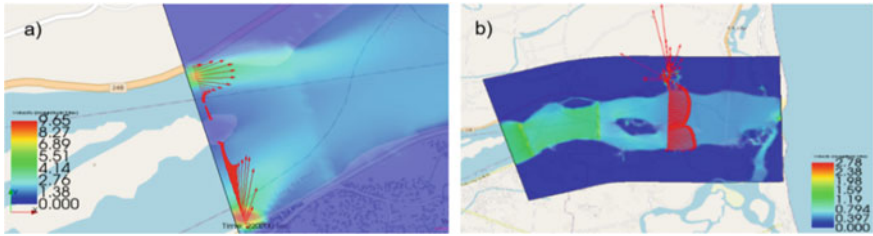


Fig. 3 Velocity profile along structure alignment corresponding to TH8 (flood regulation through PKW and few lateral sluices), **a** velocity distribution along structural alignment, **b** velocity distribution in section at 2.4 km from structural alignment



Fig. 4 Computed inundation map of Tra Khuc's downstream at two time instances

There are some civil buildings along the bank of the lower reaches of the Tra Khuc river, which may be threatened by the reservoir flood discharge. Under a high water level, a large volume of water would rush into the downstream river and river cannot release the flood in time. From the simulation results, it can be said that the maximum submerged area can reach 40,000 ha, and the highest water level can drown the house with 0.5–5 m of water (Fig. 4).

4 Conclusions

In this paper, a combination type of spillway (PKW and sluice gate) is proposed and simulated to evaluate its flood management ability. Preliminary results have shown that the proposed type of structure can satisfy both the flood management and the upstream storage purposes. However, with different operation scenarios, downstream flow regime is not the same and more detailed research needs to be conducted to have a deeper understanding on the matter. In addition, the assessment

of the hydrodynamic regime after the low-head-water structure as in Tra Khuc shows that the energy dissipation area behind the sluices should be wider, and thus the required reinforcement work could be more than anticipated.

References

1. HEC (2018) Calculation appendix of Tra Khuc hydraulic structure. Hanoi
2. Mathias Kondolf G, Piégay H et al (2016) Tools in fluvial geomorphology. John Wiley & Sons, 2nd edn
3. Nelson JM et al (2015) The international river interface cooperative: public domain flow and morpho dynamics software for education and applications. *Adv Water Resour.* <https://doi.org/10.1016/j.advwatres>
4. Yabe T, Ishikawa T, Kadota Y, Ikeda F (1990) A numerical cubic- interpolated pseudo-particle (CIP) method without time splitting technique for hyperbolic equations. *J Phys Soc Jpn* 59 (7):2301–2304
5. TCVN 12262:2018 (2018) Hydraulic structures—Spillway—Hydraulic calculation of Piano key weirs. Hanoi

River Water Level Prediction Based on Deep Learning: Case Study on the Geum River, South Korea



Xuan-Hien Le, Sungho Jung, Minh Yeon, and Giha Lee

Abstract At present, deep learning models have been widely applied in many studies related to the field of water resource management. In this study, several deep learning neural network models based on the Gated Recurrent Unit (GRU) architectures have been applied to the river water level prediction for a short-time period, from one hour to nine hours ahead. The input data of these models are hourly water levels which are observed at four hydrological stations on the Geum River, South Korea. Though the model does not require data such as topography, land cover, or precipitation data, the forecasted results indicate significant stability and performance. Compared to the observed water level data, the correlation coefficient NSE (Nash-Sutcliffe efficiency) is up to more than 99% in the case of a 1-hour forecast. The results of this study prove the potential of deep learning models in predicting water level and applicable to other river basins.

Keywords Deep learning · Gated recurrent unit (GRU) · Water level prediction · Geum river · Water resource management

1 Introduction

In the context of the rapid development of information technology in recent years, deep learning models have been widely applied in various fields to solve problems such as speech recognition, object detection, or natural language processing. Deep learning is attracting significant interest from academics and researchers are trying to apply deep learning in the field of water resource management [1]. However, according to [2], the application of deep learning models in the field of hydrology and water resources is modest compared with other fields.

X.-H. Le (✉) · S. Jung · M. Yeon · G. Lee
Kyungpook National University, Sangju 37224, South Korea
e-mail: hienlx@knu.ac.kr

X.-H. Le
Thuyloi University, Hanoi 10000, Vietnam

For the river streamflow prediction problem, [3] reviewed and evaluated in detail flood forecasting methods using machine learning models, however, this study has not mentioned the exploitation of deep learning models in streamflow prediction. In deep learning models, Recurrent Neural Network-based models (RNN) receive more interest from scientists because of their superiority in solving sequential data problems. There have been a few recent studies applying two special architecture kinds of the RNN, the Long Short-Term Memory (LSTM) and the Gated Recurrent Unit (GRU), in predicting the streamflow on the river [4, 5], as well as, tidal-affected water level prediction [6]. These studies have pointed out the potential of deep learning models in the river streamflow prediction. However, a common feature of these studies is that the input data of the models on a daily scale or every six-hour scale, whereas, the observed data with the hourly scale is not yet of interest.

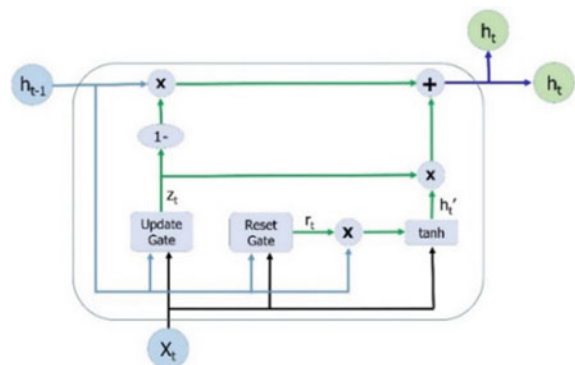
In this study, several GRU-based models were built to forecast the river water level in a short-time period, from one to nine hours ahead. The data used for this study are hourly water levels observed at hydrological stations in the Geum River basin, South Korea. The research results illustrate that the GRU model has achieved impressive performance when using the hourly data for short-term forecasting.

2 Methodology and Study Area

2.1 Gated Recurrent Unit (GRU) Neural Network

The GRU architecture is a special kind of the RNN model proposed by [7]. Along with the LSTM, these are two network architectures widely used in studies of sequential data problems, especially in the hydrological field [4–6, 8]. In this study, a GRU neural network model was constructed to forecast water level at Okcheon station on the Geum river basin. The architecture of a GRU cell is illustrated in Fig. 1.

Fig. 1 The structure of the GRU cell [6]



According to [9], GRU architecture does not have separate memory cells like the LSTM. The GRU architecture has only two gates for processing information, namely the reset gate (r_t) and the update gate (z_t). The output of each GRU cell (or hidden state- h_t) is used both for decision making and as input information for the next cells. The update gate (z_t) determines how much information from the previously hidden state (h_{t-1}) is passed to the current state (h_t). Next, the reset gate will determine the amount of information to ignore from the previous memories. When this value is close to 0, the role of the previous hidden state is negligible. In the final step, the output of a GRU cell is determined by the candidate of the hidden state value (h'_t) and the previous hidden state (h_{t-1}).

2.2 Study Area

The study area belongs to the Geum River basin, one of the four largest river basins in South Korea. Data collected in this study are hourly observed water level data at four hydrological stations, Sutong, Hotan, Songcheon, and Okcheon, respectively for 11 years, from January 2006 to December 2016. In particular, Okcheon station is the target-forecast station and also the hydrological station located downstream of the three stations mentioned above. Map of Geum River basin and location of hydrological stations are shown in Fig. 2. In this study, water level data were measured in meters (m).

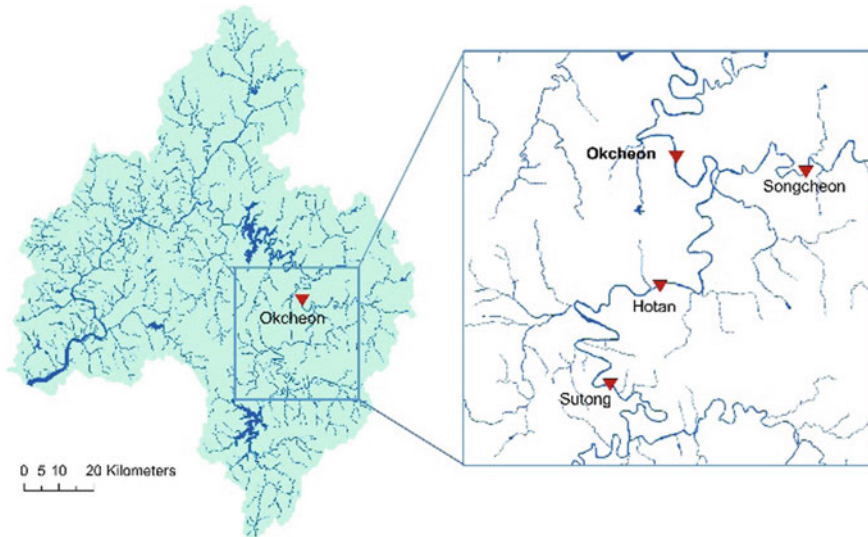


Fig. 2 Location of hydrological stations in the study area

2.3 Model Design

In this study, the 11-year hourly observed water level data from the four hydrological stations were divided into two datasets with different purposes. The first dataset is a series of 10-year water level data from 2006 to 2015 used for the purposes of training and validating model performance. Of which, training data set accounts for 80% (corresponding to 8 years, from 2006 to 2013), the remaining 20% of data is used for model performance validation purpose. The second dataset is the hourly observed water level data in 2016 used for the testing step to objectively evaluate the forecasted performance of the GRU model.

According to [5], the training and optimization process of a neural network model depends on the selection of parameters such as optimization function, optimization algorithm, learning rate, number of neurons, as well as, the number of hidden layers in the neural network. For this study, the GRU model using the Adam algorithm is the optimization algorithm with a default learning rate of 0.001. Besides, the model was built with only one hidden layer and the number of units in each GRU cell changed from 8 to 32. In addition, the maximum number of epochs is set to 5,000 times to ensure full recording of information during training.

3 Results and Discussion

The proposed GRU model is trained and validated with water levels observed for 10 years from 2006 to 2015, with data rates of 80% and 20%, respectively. The best results of the validation process are indicated in Table 1. Two criteria are selected for evaluation respectively NSE (Nash-Sutcliffe efficiency) and MAE (mean absolute error).

The figures in Table 1 indicate that the GRU model exhibits significant performance in all four forecast cases. In the case of 1-hour in advance, the NSE value is up to 99.8%, the corresponding figures for the forecast cases 3-, 6- and 9-hour ahead are 99.1%, 97.3%, and 94.2%, respectively. For each forecasted case, there

Table 1 The best results of water level forecast at Okcheon station in the validation step

Forecasted time (h)	Case	Number of units	Number of epochs	MAE (m)	NSE
1	1h_16	16	204	0.007	0.998
3	3h_32	32	212	0.013	0.991
6	6h_16	16	212	0.017	0.973
9	9h_16	16	314	0.020	0.942

was no significant difference in model performance when the number of units per GRU cell was varied from 8 to 32. In general, with the number of units per cell of 16, the GRU model tends to be more stable and efficient than the other cases (except for the case of 3-hour forecast ahead). In the cases of further forecast (3 to 9 h in advance), the model performance tends to decrease slightly in both the NSE and MAE values. MAE values corresponding to the case of 6 h and 9 h of water level forecast are 0.017 m and 0.020 m, respectively.

3.1 Testing Result

In order to objectively evaluate the predictability of the GRU model, an independent data set for 2015 was used. The results of the model corresponding to the four forecast cases are expressed in Table 2.

Overall, the results forecasted from the GRU model demonstrated steady performance in all four forecast cases and no difference from the validation period. In the case of a 1-hour forecast in advance, the MAE and NSE values are 0.010 m and 99.6%, respectively. NSE coefficients tend to decrease when forecasting for a longer time, the corresponding values for 6-hour and 9-hour predictions are 94.8% and 89.8%. The comparison between the predicted water level values and the actual measured water level values of the four forecast cases is shown in Fig. 3.

Figure 3 depicts the correlation between observed water levels and forecasted water levels for the testing period. These figures show the pairs of data that are paired between the observed data (horizontal axis) and forecasted data (vertical axis). The closer these data points are to the 45° diagonal, the higher the performance of the model. In addition, the NSE value is up to 99.6% when the forecast is one hour ahead and reaches 89.8% when the water level forecast is nine hours in advance. In the case of the 2016 flood forecast, the flood peak is forecasted to occur at the same time as the flood peak observed at 09:00 on July 6, 2016 (case 1h_16), the relative error value is less than 5%. This is an acceptable error value for a flood peak prediction. These results once again confirm that the GRU model can provide predictive results with high efficiency and stability.

Table 2 Results of water level forecast at Okcheon station in the testing step

Forecasted time	Case	Number of units	MAE (m)	NSE
1 h	1h_16	16	0.010	0.996
3 h	3h_32	32	0.018	0.986
6 h	6h_16	16	0.022	0.948
9 h	9h_16	16	0.029	0.898

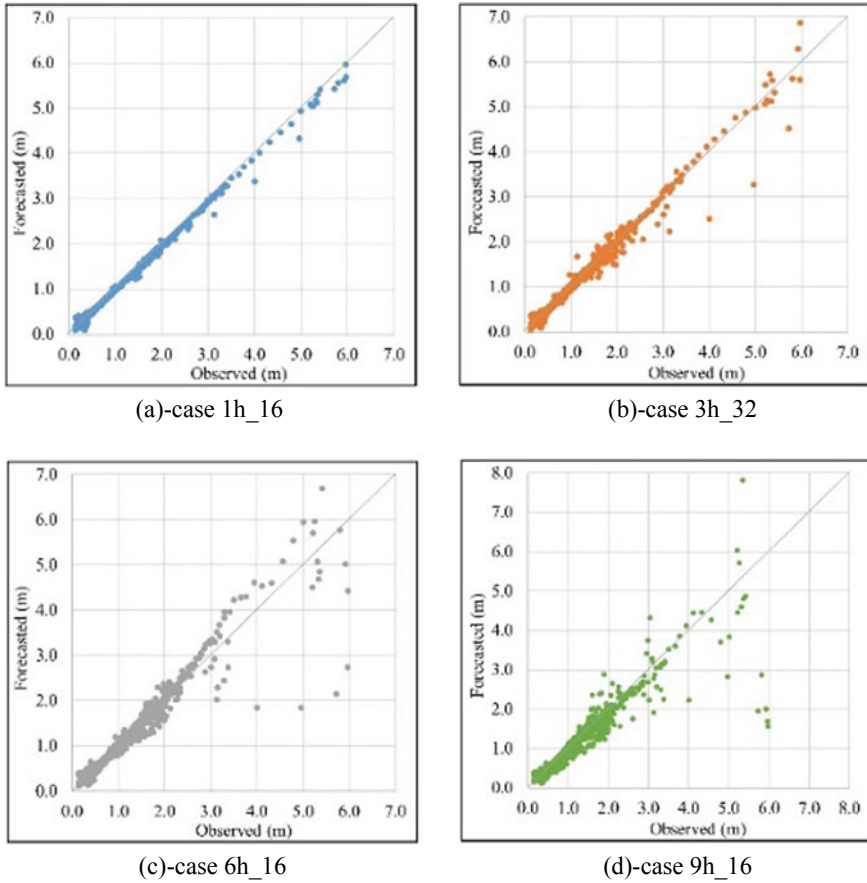


Fig. 3 Scatter plot for forecasting one-hour (a), three-hour (b), six-hour (c), and nine-hour (d) ahead in the testing step

4 Conclusions

In this paper, several models have been built based on a deep learning framework to forecast the water level at the Okcheon. The parameters of the GRU model have been experienced through a careful selection and evaluation process. Though using a modest amount of data, observed water level data at four hydrological stations and without requiring data on topography or land cover, the forecasted results are obtained high performance and stability.

The results of the validation and testing processes indicate a close correlation between the forecasted data and the observed data. The findings of this study have demonstrated the potential of deep learning models, especially the GRU model in predicting the streamflow. In addition, the GRU model belongs to the data-driven

model kind which has the advantage of not requiring many types of input data when compared with hydrological models. Besides, the GRU model could be applied to other river basins to address problems related to water resource management.

Acknowledgements This work was supported by the National Research Foundation of Korea (NRF) grant funded by the Korea government (MSIT). (No. 2020R1A2C1102758).

References

1. Le XH, Lee G, Jung K, An H, Lee S, Jung Y (2020) Application of convolutional neural network for spatiotemporal bias correction of daily satellite-based precipitation. *Remote Sens* 12(17):2731
2. Shen C (2018) A transdisciplinary review of deep learning research and its relevance for water resources scientists. *Water Resour Res* 54(11):8558–8593
3. Mosavi A, Ozturk P, Chau K-W (2018) Flood prediction using machine learning models: literature review. *Water* 10(11):1536
4. Le XH, Ho HV, Lee G (2019) River streamflow prediction using a deep neural network: a case study on the Red River, Vietnam. *Korean J Agric Sci* 46(4):843–856
5. Le XH, Ho HV, Lee G, Jung S (2019) Application of long short-term memory (LSTM) neural network for flood forecasting. *Water* 11(7):1387
6. Le XH, Ho HV, Lee G (2020) Application of gated recurrent unit (GRU) network for forecasting river water levels affected by tides. In: *APAC 2019 Proceedings*, pp 673–680. Springer
7. Cho K, van Merriënboer B, Gülçehre Ç, Bougares F, Schwenk H, Bengio Y (2014) Learning phrase representations using RNN encoder-decoder for statistical machine translation. *ArXiv*, abs/1406.1078
8. Kratzert F, Klotz D, Brenner C, Schulz K, Herrnegger M (2018) Rainfall–runoff modelling using long short-term memory (LSTM) networks. *Hydrol Earth Syst Sci* 22(11):6005–6022
9. Chung J, Gülçehre Ç, Cho K, Bengio Y (2014) Empirical evaluation of gated recurrent neural networks on sequence modeling. *ArXiv*, abs/1412.3555

Validation of Some Empirical Equations to Estimate Bridge Abutment Scour in Non-cohesive Soil Using Field Data



Huy Quang Mai, Phong Dang Nguyen, and Tuan Anh Tong

Abstract The scour under the bridge can cause very serious economic and social damages. The prediction of the maximum scour depth at the abutment is very important when assessing and warning the safety of the bridge. Recently, there have been many equations to predict local scour depth at bridge abutments. Most of them have been developed based on laboratory data. Validation of these equations using field data is necessary to make recommendations for the proper application of these equations. In this article, four design equations for the estimation of the equilibrium maximum scour depth at an abutment in non-cohesive soil were selected for validation by using field data in the United States. Based on the results of this analysis would allow to promote the highly accurate design of the abutment foundation to reduce construction and maintenance costs.

Keywords Local abutment scour · Non-cohesive soil · Field data

1 Introduction

Scour occurs at abutments when the abutment and roadway embankment obstruct the flow. Local scour at bridge abutments is one of the main causes leading to bridge failure. The failure of bridge due to scour will result in economical loss and may also result in the losses of human life. Recent surveys have shown that in the United States the damage to bridges and highways from major regional floods in 1964 and 1972 amounted to about \$100,000,000 per event [1]. The failure of bridges in Vietnam due to scour problems during flood is not published, so there is no local record to be used in this study.

Accurate estimation of the scour depth at the abutments is important for the safe design of the abutment foundations. Therefore, there have been a lot of intensive

H. Q. Mai (✉) · P. D. Nguyen · T. A. Tong

Faculty of Civil Engineering, University of Transport and Communications (UTC), Hanoi, Vietnam

e-mail: mqhuy@utc.edu.vn

studies to develop reliable methods to predict maximum scour depth at the abutments as well as to minimize the impacts of local scour on the bridge foundation. There are many estimation formulas for maximum local scour depth at abutments that have been developed by many authors. The development of these formulas is based on small scale studies in laboratories under various conditions. Therefore, the application of these formulas to determine scour depth in practice is uncertain because of simplified laboratory conditions. For example, the studies were carried in laboratory flumes with rectangular cross-sections and fixed walls which is different from the natural channels with non-rectangular cross-sections and movable beds and lateral flow distribution in non-uniform.

Validation of the proposed formulas using the field measurements data is essential to improve the estimation of the maximum scour depth at bridge abutments. This can reduce the unnecessary costs of scour countermeasures, making the bridge design process more efficient.

In this study, the field scour measurement data in the United States were used to validate four selected formulas for estimating local scour depth at bridge abutment sites. Statistical methods were used to recommend formulas with the smallest error when estimating local scour at bridge abutments.

2 Formulas for Predicting Scour Depths at Bridge Abutments

There are many formulas and models for predicting maximum local scour depth at abutment sites. Since the local scour is a very complex phenomenon resulting from the interaction between the flow around the abutment and the flow bottom, formulas for predicting maximum scour depth at bridge abutments are often derived from laboratory investigations. These formulas have not been verified by field data, raising some doubts when applying them in practice. Therefore, it is essential to validate these formulas using field measurements to find the uncertainty associated with applying these formulas to the field conditions. Four of the popular formulas were selected to evaluate their accuracy.

2.1 *Froehlich Equation*

The original Froehlich equation [2] was developed from a multiple linear regression analysis of 170 laboratory measurements of live-bed abutment scour in non-cohesive sediments. The laboratory data used in the analysis represented the component of abutment scour only, which was typically estimated by subtracting any observed contraction scour, outside of the abutment region, from the total scour measured at the abutment. Although the equation was initially derived for the analysis of live-bed abutment scour, HEC-18 [3] recommends its use for the

assessment of both live-bed and clear-water abutment scour. The regression equation predicts the maximum depth of local scour at an abutment and is defined below:

$$\frac{y_s}{y_a} = 2.27K_1K_2 \left(\frac{L}{y_a} \right)^{0.43} Fr^{0.61} + FS \quad (1)$$

where y_s = maximum abutment scour depth (in m); y_a = average depth of flow on the floodplain upstream from the abutment (in m); K_1 = dimensionless correction factor for abutment shape; $K_2 = (\theta/90)^{0.13}$ —dimensionless correction factor for the angle of the embankment to the flow; L = length of the embankment blocking flow (in m); Fr = Froude number of the approaching flow upstream from the abutment; and FS = factor of safety, which is set equal to 1 [4].

Without a factor of safety, the regression equation encompassed only 45% of the laboratory data, which was undesirable for design and safety purposes. Therefore, Froehlich [4] recommended a factor of safety equal to 1, which forced the equation to encompass 98% of the laboratory data.

2.2 HIRE Abutment Scour Equation

An equation based on field data of scour at the end of spurs in the Mississippi River (obtained by the USACE) can also be used for estimating abutment scour (FHWA 2001) [4]. This field situation closely resembles the laboratory experiments for abutment scour in that the discharge intercepted by the spurs was a function of the spur length. The modified equation, referred to herein as the HIRE equation, is applicable when the ratio of projected abutment length (L) to the flow depth (y_1) is greater than 25 [4]. This equation can be used to estimate scour depth (y_s) at an abutment where conditions are similar to the field conditions from which the equation was derived:

$$\frac{y_s}{y_1} = 4Fr^{0.33} \frac{K_1}{0.55} K_2 \quad (2)$$

where: y_s = Scour depth, ft (m); y_1 = Depth of flow at the abutment on the over-bank or in the main channel, ft (m); Fr = Froude Number based on the velocity and depth adjacent to and upstream of the abutment; K_1 = Abutment shape coefficient; K_2 = Coefficient for skew angle of abutment to flow calculated as for Froehlich's equation (above section).

2.3 Melville Abutment Scour Equation

Melville [2, 5–8] proposed a design method to estimate the scour depth at abutments based on empirical relationships containing different factors or coefficients. Each factor or coefficient represents the effect of flow depth, abutment size (K_{hl}), flow intensity (K_I), sediment characteristics (K_d), abutment shape (K_s), abutment alignment (K_θ) and channel geometry (K_G) on scour depth. The proposed equation is

$$d_s = K_{hl}K_IK_dK_sK_\theta K_G \quad (3)$$

He argued that for short abutments ($l/h \leq 1$), the scour depth scales with the abutment length; whereas for long abutments ($l/h \geq 25$), the scour depth scales with the flow depth. For all other abutments ($1 < l/h < 25$), the scour depth is proportional to $(hl)^{0.5}$ [2].

The abutment shape factor is assumed to be 1 for vertical-wall abutments and 0.75 for wingwall abutments. Spill-through abutments are assigned values of $K_s = 0.6$; 0.5 and 0.45 for 0.5: 1 (horizontal: vertical), 1: 1 and 1.5: 1 side slopes, respectively. These values of shape factor apply only to shorter abutments ($l/h \leq 10$). Shape effects were found to be unimportant for long abutments, and hence, $K_s = 1$ for $l/h \geq 25$.

The value of abutment alignment factor $K_\theta = 1$ for an abutment aligned across the flow, that is an angle of alignment $\theta_a = 90^\circ$. For $\theta_a < 90^\circ$, the abutment is pointed downstream and vice versa. For alignment angles $\theta_a = 30^\circ$; 60° ; 120° and 150° , the values of $K_\theta = 0.9$; 0.97; 1.06 and 1.08, respectively. Melville [7] recommended that the alignment factor can be applied only to longer abutments ($l/h \geq 3$). Alignment effects are negligible for short abutments, and hence, $K_\theta = 1$ for $l/h \leq 1$.

Channel geometry factor K_G is defined as the ratio of the scour depth at a given abutment sited in the compound channel to that at the same abutment sited in a corresponding rectangular channel of the same overall width as that of the compound channel and the same depth as that of the main channel of the compound section.

2.4 Richardson Equation

Based on the field data of scour at the end of spurs in the Mississippi river, Richardson et al. [4] proposed the equation below to estimate scour depth at an abutment for live-bed scour:

$$\frac{y_s}{h} = 7.27K_sK_\theta Fr^{0.33} \quad (4)$$

3 Validation of Selected Bridge Abutment Scour Formulas

In this study some of the commonly used formulas indicated above will be tested using field data. The formulas were Froehlich, Hire, Melville, and Richardson. Field scour measurements used for validation process were collected from bridges which had experienced local scour at abutments in the United States [3]. A comparison between the recorded field data and the computed scour depths are shown in Fig. 1. Statistical tests were conducted to validate the accuracy of computed local scour depths obtained from four formulas. The statistical tests are the mean absolute error (MAE) and root mean square error (RMSE). Their mathematical forms are shown in Eqs. (5) and (6) respectively.

$$MAE = \sum_{i=1}^n |e_i|/n \quad (5)$$

$$RMSE = \sqrt{\sum_{i=1}^n e_i^2/n} \quad (6)$$

where e_i is the error in the predicted scour depth for i event of the record from the application of the formula or model, and n is number of records.

Evaluation of the output obtained from the application of Eqs. (5) and (6) on the four selected formulas was made. The values of MAE and RMSE indicate accurate prediction. Table 1 shows the average values obtained from the statistical tests.

The comparison between the measured scoured depths and computed scour depths using four formulas showed low degree of accuracy and this also confirmed by using two different statistical tests namely mean absolute error, MAE, and root mean square error, RMSE. Table 1 shows the computed values of the above two statistical tests. The validation process and the statistical tests showed that the Froehlich's formula is the best among the four selected formulae, followed by Richardson, HIRE and Melville formulas. However, these four formulas all give conservatively predictive value of the scour depth, much larger than the observed scour depths.

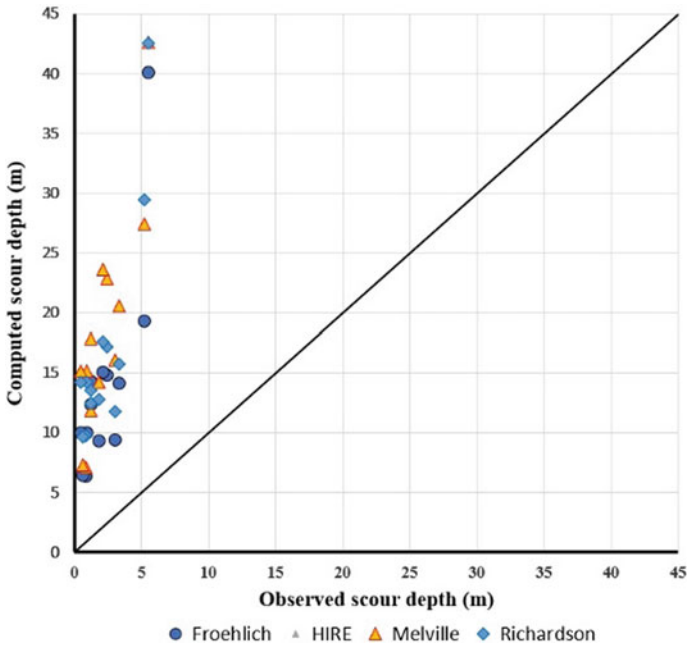


Fig. 1 Comparison of measured and computed scour depths

Table 1 Result of statistical tests conducted on the selected formulas

Scour equation	Mean absolute Error, MAE	Root mean square Error, RMSE
Froehlich	-9.56	11.38
HIRE	-12.60	14.10
Melville	-14.19	15.62
Richardson	-12.59	14.09

4 Conclusion

Four formulas for predicting local scour depth at the bridge abutment were tested based on scour measurements in the field. Statistical tests were also conducted to investigate the accuracy of the output from the validated formulae. With the field scour measurement data set is still limited, the validation process revealed that Froehlich’s formula is more accurate among the other three formulas.

References

1. Melville BW (1992) Local scour at bridge abutment. *J Hydraul Eng ASCE* 118(4):615–631
2. Froehlich DC (1989) Local scour at bridge abutments. In: *Proceedings of A.S.C.E. national hydraulics conference*, pp 13–18. Colorado Springs, Colorado, USA
3. U.S.Geological Survey (2001) National bridge scour database (<http://water.usgs.gov/osw/techniques/bs/BSDMS/index.html>)
4. Richardson EV, Davis SR (2001) Evaluating scour at bridges. HEC18 FHWA NHI-001, Federal Highway Administration, US Department of Transportation, Washington, DC
5. Melville BW (1995) Bridge abutment scour in compound channels. *J Hydraul Eng Am Soc Civ Eng* 121:863–868
6. Melville BW (1997) Pier and abutment scour: integrated approach. *J Hydraul Eng Am Soc Civ Eng* 123:125–136
7. Melville Bruce W, Coleman Stephen E (2000) Bridge scour. Water Resources Publications, LLC, P.O. Box 260026, Highlands Ranch, Colorado 80163-0026, USA
8. Melville BW, Etema R (1993) Bridge abutment scour in compound channels. In: *Proceedings of national conference hydraulic engineering*, pp 767–772. University of Iowa, Iowa City, Iowa

Transportation in General

A Neural Network Approach for Solving Traffic-Flow Forecasting Based on the Historical Voyage Datasets: A Case Study on Hai Phong Roads



Quang Hoc Tran, Van Truong VU, Quang LE, Thi Lan Huong HO,
and Van Hien LE

Abstract Traffic congestion is one of the most common issues in big cities in the world. Therefore, traffic warning and forecasting always play a vital role for traffic participants. Currently, in Vietnam, drivers only know the information and level of congestion through experience and some traffic information channels. Meanwhile, the journey data of vehicles participating in traffic has been stored and transmitted to a management center continuously. These data play an integral part but they are not fully exploited to provide useful information for road users such as average velocity information at each time interval or at each road. In this paper, the authors propose an approach to address this problem. There are two main steps: the first one is to convert raw data to a time series dataset that can provide moving status on each road section. The next step is to use neural networks to make a forecast of average velocity on each road at different times. Experimental results with data on Le Hong Phong and Nguyen Binh Khiem streets (Ngo Quyen District, Hai Phong City, Vietnam) show that the proposed approach gives feasible results that can be applied to many different areas in Vietnam.

Keywords Neural network · Traffic-flow forecasting · Traffic congestion warning · Traffic-flow prediction

1 Introduction

In recent years, the rapid development of surveillance technology has created a huge amount of traffic information data. In general, there are three traffic parameters relate to traffic congestion: traffic flow, occupancy, and traffic speed. Many solutions have been investigated to deal with the traffic congestion, in which the speed prediction is

Q. H. Tran (✉) · Q. LE · T. L. H. HO · V. H. LE

Faculty of Civil Engineering, University of Transport and Communications, Hanoi, Vietnam
e-mail: hoctq@utc.edu.vn

V. T. VU

Le Quy Don Technical University, Hanoi, Vietnam

importance and efficient solution. Accuracy of speed forecast information is essential. It provides drivers with estimated journey times, delayed times as well as alternative routes. Time series forecasting has been studied in previous studies in many areas such as currency exchange rate forecasting and consumer price index prediction [1]. Various approaches have been proposed for prediction of traffic speed time series. In general, these approaches can be categorized into two groups: model-based methods and data-driven methods [2]. The model-based approaches predict future traffic conditions based on traffic flow theory. They can be spitted into smaller groups: macroscopic, microscopic, and kinetic [3]. Meanwhile, data driven approaches relate observed traffic conditions with current and past traffic data. In general, these solutions can be divided into two main groups: the parametric and nonparametric methods. The typical parametric methods are the autoregressive integrated moving average (ARIMA) model [4]. These algorithms have the advantage of being easy to execute, but the disadvantage is that they are only suitable for stable and accurate data sets. However, in fact, with traffic data, they always fluctuate, therefore, these methods prove ineffective and difficult to give accurate and stable forecast results with real traffic datasets. An alternative solution to this problem is using non-parametric methods. Some popular nonparametric methods can be mentioned as the k-nearest neighbor approach [5], artificial neural network (ANN) model [6], and support vector regression (SVR) model [7]. Among them, the ANN is the most commonly used method. The ANN has a capable of learning how to associate and map non-linear input and output patterns. This makes them being a suitable approach for solving the complicated non-linear traffic prediction problem. In this paper, an average velocity time series prediction is presented based on the history data using the neural network. The objective of this study is to introduce a process for processing a big raw vehicle journey data into a time series dataset and investigate the short-term vehicle speed prediction with these datasets using a multilayer perceptron (MLP).

The structure of this paper is as follows: Sect. 2 presents the proposed method. Section 3 shows the experimental results. Finally, conclusions are presented in Sect. 4.

2 Proposed Method

The proposed algorithm model contains two 2 main phases as follows.

2.1 Phase 1: Using GIS Spatial Query Techniques to Generate Time Series Data from Raw Journey Data

Trip data is collected from many different devices with frequency in seconds. Therefore, it can be seen that the amount of data collected in a day by a receiver can be up to Gigabytes. These data are usually stored in JSON (JavaScript Object

Notation) or BSON (Binary JSON) format, which is read and processed computationally by MongoDB [8]—a document-oriented NoSQL database used for high volume data storage. Therefore, we can consider the problem to be solved here as a big data problem.

However, with the raw signal data received from the cruise device (see Table 1), we only have information about the x and y coordinates of each vehicle as well as the vehicle’s speed. We cannot know which road this vehicle is traveling on. Therefore, the first thing to do with this raw data is that we need to filter out which signals are on the road being considered. This can be done using Geospatial Queries in MongoDB. However, to be able to perform this query, we need to know the coordinates of the polygon’s vertices. A solution for this problem is using a vector-based road map. The implementation of polygon creation is done by buffering each segment under consideration. After that, we decompose the polygon into a point collection. All of these operations can be performed by a GIS programming tool. In this study, we use the Arcobject programming library [9].

After filtering the points in the polygon. The next step is to perform the calculation of average velocity over different time intervals. In this study, we divide a day into 96 equal intervals (15 min/segment). For each travel point, based on the time of collection (datetime field in Table 1), it will be included in each corresponding time interval. All points in the same timeframe will be calculated to give the average velocity of the segment within that time frame. The output of this process will be a time series data set. This is the input of the forecasting process using the ANN.

2.2 Phase 2: Using Machine Learning Algorithm (I.E. ANN) to Predict Average Speed on Each Road Segment

The mean velocity data set at each time interval is considered a time series. This data series continues to be normalized to [0,1] and divided into two sets: train and test dataset. In this study, we use the sliding window [10] technique to create a set of input and output datasets for the neural network. Assuming the window size is K, the first K values of the time series will be the K inputs of the ANN network; (K + 1)th value will act as the output value. In this way, by moving the sliding window by one unit, we get a new set of input and output values. In this study we use 70% of the datasets for training, the rest is used for testing. Detailed results will be presented in the experimental section.

Table 1 A sample of the raw data structure

Id	VehicleId	ProviderId	Datetime	Speed	X	Y
1	51G02821	1028	1580515219	53	107.42198	10.91535833

2.3 Model Performance Measures

The performance of the ANN model is compared with that of the ARIMA model under six different data collection. Three indicators [11] including the mean square error (MSE); the mean absolute error (MAE) and mean absolute percentage error (MAPE) are used for the comparison.

3 Results and Discussion

3.1 Data Description

Experimental data were collected in the area of Ngo Quyen district, Hai Phong city, Viet Nam. We choose two roads for experimentation: Le Hong Phong street and Nguyen Binh Khiem street. They are the two main roads in this area with high traffic volume. For this study, we split Le Hong Phong street into 2 main segments (Segment 1 and 2) and Nguyen Binh Khiem street is divided into Segment 3 and Segment 4. Twenty-six days (1 February to 26 February 2020) of speed data was extracted from the Vehicle Data System (VDS) system. The original speed data for each day is aggregated into 96 time-intervals (15 min/interval). At each of these intervals, the average vehicle velocity is calculated for each segment.

3.2 Parameter Setting

Details of the parameters are listed in Table 2. The number of inputs for each network is determined by trial and error based on the accuracy of the predictions of testing data.

Table 2 The parameters setting

Method	Parameters	Value	Parameters	Value
ANN	Input number	4	Learning rate	0.2
	Output number	1	Momentum	0.01
	Number hidden nodes	4	Iterations	500
	Testing rate	30%	Sigmoid value	2
ARIMA	Parameter P	2	Parameter Q	2

3.3 Results and Analysis

Experimental results are shown in Fig. 1. From the experimental results, we can draw the following two points: The first one is that the ANN algorithm outperformed the ARIMA algorithm on all measurements in all 4 test cases. This is predictable because the ARIMA algorithm often works well only on linear data. For data having nonlinear distribution, the neural network is more suitable. The second point is that two segments on Nguyen Binh Khiem street (Segment 3 and 4) give much better forecast results than those on the Le Hong Phong street (Segment 1 and 2). This can be explained by looking at the data distributions on these road segments. Obviously, on Le Hong Phong street, the data fluctuates and varies greatly between different time frames and between different days. This will be a challenge for any predictive model. Meanwhile, at two segments on Nguyen Binh Khiem street, the data fluctuates but is distributed in a more regular manner, which makes it easier for ANN to learn the rule of change. there. This helps the forecast results of ANN to be more accurate.

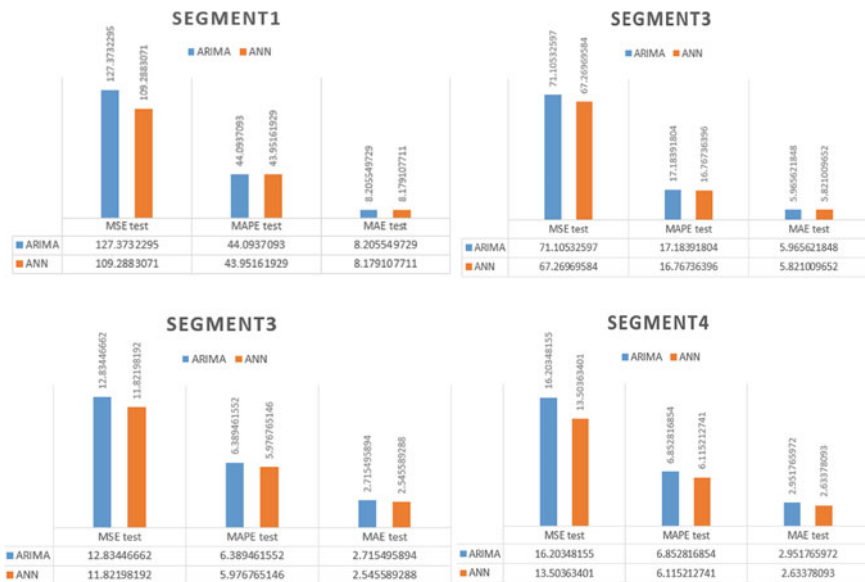


Fig. 1 Performance comparisons between the ANN and ARIMA on four test datasets

4 Conclusions

In this study, the authors presented a solution for processing big journey data and applying neural networks to training and predicting average velocity per segments. Specifically, the authors utilised the ArcObject programming library to handle geometry with spatial objects. At the same time, we also used spatial query methods with GeoJSON Objects in MongoDB to filter and calculate the average velocity in each time interval at each segment. By processing this, we have turned the original big raw data set into a much smaller time series dataset. The Neural network and ARIMA algorithms were applied to experiment on these datasets. Experimental results on four segments show that ANN network outperforms ARIMA and it fits perfectly with this type of dataset. This study is the initial step in our series of vehicle speed prediction. In subsequent studies, we will focus on improving the model to achieve even more impressive results.

Acknowledgements This research is funded by the Ministry of Education and Training, Vietnam under grant number CT.2019.05.02.

References

1. Bui LT, Dinh TTH (2018) A novel evolutionary multi-objective ensemble learning approach for forecasting currency exchange rates. *Data Knowl Eng* 114:40–66
2. Shen L (2008) Freeway travel time estimation and prediction using dynamic neural networks
3. Park J et al (2011) Real time vehicle speed prediction using a neural network traffic model. In: *The 2011 international joint conference on neural networks, IEEE*
4. van Hinsbergen CPIJ, Van Lint JWC, Van Zuylen HJ (2009) Bayesian committee of neural networks to predict travel times with confidence intervals. *Transp Res Part C Emerg Technol* 17(5):498–509
5. Nihan NL, Holmesland KO (1980) Use of the Box and Jenkins time series technique in traffic forecasting. *Transportation* 9(2):125–143
6. Chan KY et al (2011) Neural-network-based models for short-term traffic flow forecasting using a hybrid exponential smoothing and Levenberg–Marquardt algorithm. *IEEE Trans Intell Transp Syst* 13(2):644–654
7. Jeong YS et al (2013) Supervised weighting-online learning algorithm for short-term traffic flow prediction. *IEEE Trans Intell Transp Syst* 14(4):1700–1707
8. Banker K (2011) *MongoDB in action*. Manning Publications Co
9. Amirian P (2013) *Beginning ArcGIS for desktop development using, NET*. John Wiley & Sons
10. Yahmed YB et al (2015) Adaptive sliding window algorithm for weather data segmentation. *J Theor Appl Inf Technol* 80(2):322
11. Adhikari R, Agrawal RK (2013) An introductory study on time series modeling and forecasting. Preprint [arXiv:1302.6613](https://arxiv.org/abs/1302.6613)

ICD Concept: An Overview of the Development from an Original Purpose to a Global Viewpoint



Vu Quoc Hung, Vu Minh Tuan, and Nguyen Viet Phuong

Abstract The shortage of space, congestions in seaports and inland connectivity have primarily resulted in establishment of original ICDs as nodes in a multimodal transport. Progressively, the concept of ICD has been required to develop through new generations due to international logistics and global supply chain. This article focuses on analysing the development of ICD from its initial purpose to broader perspectives via numerous studies in literature. Moreover, the classification of ICDs based on relative distance from a seaport including near ICD (below 150 km), middle ICD (from 150 to 500 km) and distant ICD (above 500 km) to be appropriate for intermodal transports as an outcome of this research. Finally, a combination of these types of ICDs could be an alternative solution for their distributions in logistics transport.

Keywords ICD · Seaport · Logistics · Dry port · Multimodal transport · Hinterland · Inland

1 Introduction

Development of connection between seaports and their inland areas has been more important for supply chain in many parts of the world. In order to develop the market, seaports have attempted to increase their capacities. The inlands of seaports are able to significantly enlarge due to factors acknowledged such as: containerisation, door to door services, globalisation and multimodal transports [1, 2]. Nevertheless, the obstacle of seaport development is the increasing containerised transport and urbanisation. It leads to congestion on the access routes serving terminals, seaport gates and developing area shortage of seaports. Consequently, this factor had sparked to create an Inland Container Depot (ICD) concept, where many functions of seaports are outsourced at the reasonable hinterland locations [2].

V. Q. Hung (✉) · V. M. Tuan · N. V. Phuong
National University of Civil Engineering, Ha Noi, Vietnam
e-mail: hungvq@nuce.edu.vn

The idea of ICD as a multimodal transport node with connecting rails/roads/waterways and seaports, is certainly not new. Actually, ICD concept can cover more functions than its original purpose. Therefore, numerous definitions have been generated [3–6]. As a result, there was a consensus on the higher importance of ICD. It means that an ICD must be global perspectives with improving cost-efficiency, environmental issues, global logistics and supply chains [4, 7]. The main objective of the article is to analyse the expanding ICD concept from an original idea to the global perspectives and classify ICDs according to distance from seaport as a solution to redistribution of container cargo.

2 Methodology of Research

A methodology of this research is an analysis the ICD concepts from the literature with about 109 scientific articles and international proceeding reports regarding keyword: “ICD, dry port”, as an essential input part of the research mission. An extensive literature review is to provide good insight into the development of ICD concept. The literature methodology contains three-steps including: (1) definition of original ICD concept; (2) the development of ICD generations through global cases studies; (3) relatively classify ICDs following a viewpoint of distance from seaport.

2.1 *Overview of Conventional ICD Concepts*

In the literature, there are several different definitions of ICDs used for either the same hinterland terminal facilities or different facilities.

ICD is Inland Clearance Depot that is a common concept of hinterland infrastructure. It is preferred to associate with seaports or airports, with public authority status, equipped with fixed installation, and offering services for handling and temporary storage of any kind of goods [2].

ICD is Inland Container Depot that is focused on facilities for handling and temporary storage of import/export stuffed and empty containers [8]. India firstly introduced Inland Container Depots (ICDs) in 1983. Fundamentally, an ICD is a consolidation node for containers where are generally located outside the seaports.

ICD is Intermodal Freight Centre that is a concentration of economic independent companies working in freight transport and supplementing services on a designated area where a change of transport units between traffic modes can take place [3]. This concept is normally used in Euro.

ICD is Inland Freight Terminal that was defined by Eurocode [9]. Accordingly, ICD is often located inland, generally far from seaport terminals. ICD is an intermodal terminal where value-added services is given or a merging point for different traffic modes involved in distributing goods that comes from ports and is directly linked to seaports.

ICD is Dry Port that is a facility connecting between seaports or airports and hinterland in local and international trade. A dry port usually provides both local and international logistics and distribution services, including freight forwarding, customs brokerages, integrated logistics, and information systems [10].

Basically, most seaports are placed in cities or the gateway of economic areas, where requests the effective and safe goods transport. Simultaneously, space and facilities for loading, unloading, storage, terminals are also demanded to guarantee the development of the seaports. The conventional ICD concepts above cover all not enough aspects of hub's functions due to only common feature linking to seaports. Therefore, a more precise definition and category of the ICD concept is necessary to come up with broader perspectives.

3 Discussion About the Global Viewpoint of ICD Development

The global perspective of ICD concept has been developing from the application for many parts of the world such as Europe, North America, Africa and Asia. Generally, an ICD is planned in the proximity of an existing or potential production or economic centre. The number of ICDs depends on locations and economic activities. About 150 ICDs were established in North America, 130 in Europe and about 200 ICDs in the Asia-Pacific region by 2015 [11]. Many factors involved such as material flows, infrastructure, logistics and stakeholders were also indicated in the ICD development [11]. In which, logistics services are a key aspect providing on the planning, location and utilisation of ICDs. Thus, new ICD is much more than original one and should cover additional services to give support to maritime container logistics such as customs services, inspection services, empty container depot services and other added value logistic services such as stuffing and stripping or warehousing could be also integrated in ICDs. The other researchers revealed that the dynamics of price, cost and quality services are primary facets of improving ICDs. For example, the development of ICD in India was focused on providing better quality services and policy rather than offering low cost [12]. The development of ICDs in China has shown another aspect that ICD was known as a node in global supply chain. The ICD concept has only used in China since 2002. However, due to the economic strategies focusing on the extremely large hinterland with remarkable resources enhancing for ICD structures. According to the concept of new ICD in China, it is only node in the global supply chain and has close relations with seaports; it can collect and distribute cargoes for seaports. Thus, the efficiency of ICD has vital importance for a seamless global supply chain. The concept of ICDs has been developing from simple to complicated services through their new generations [14, 15]. Discussions among policy makers on ICD concepts primarily handled the step by step to improve from basic ICD to ICD with more services. As a result, there are numerous ICDs that were built to explore both domestic and

global market for multimodal transport. It has led to an increasing attraction for interconnection between nodes and improving logistics transport system. Clearly, the new generation of ICD concept has provided more benefits such as logistics efficiency, low environmental impact and improvement of quality services. However, there is no common formula for developing ICDs in general due to the significant difference in regional and local transport policies, as well as infrastructural logistics plans in specific countries. Thus, it is generally admitted that the development of ICDs is a global phenomenon with local characteristics [15].

Classifying ICD according to distance

Currently, there are three different types of ICD linking to seaports [16]. In which, a single ICD servicing one seaport, a single ICD servicing multi-seaport and multi-ICDs servicing the same seaport. Based on the location of an ICD in comparison to distance from seaports, they might be classified including distant, middle and near. Accordingly, a distant ICD has the longest distance of three ones.

Figure 1 indicated that a seaport linked to its ICD with a long distance. The advantages of distant ICD in relation to road and rail that caused reduction of congestion at the seaports and its surroundings. Moreover, the distant ICD is promoted in a broad hinterland due to low cost and high-quality services. Particularly, it might make more services even though seaports are reluctant to transport in containers unconnected to shipping. Nevertheless, road transport does not directly benefit by transporting containers from road to rail, but they are still in relation to the intermodal transport chains.

Moreover, geographical and demographical conditions primarily influence on the competitiveness of road and rail transport. The rail transport is generally competitive at distances above 500 km [17]. Mid-distance (from 150 to 500 km) is appropriate for road transport in hinterland as shown in Fig. 2. In this case study, it is necessary to establish mid-distant dry port in term of a middle ICD to connection seaports with conventional intermodel terminals or cities.

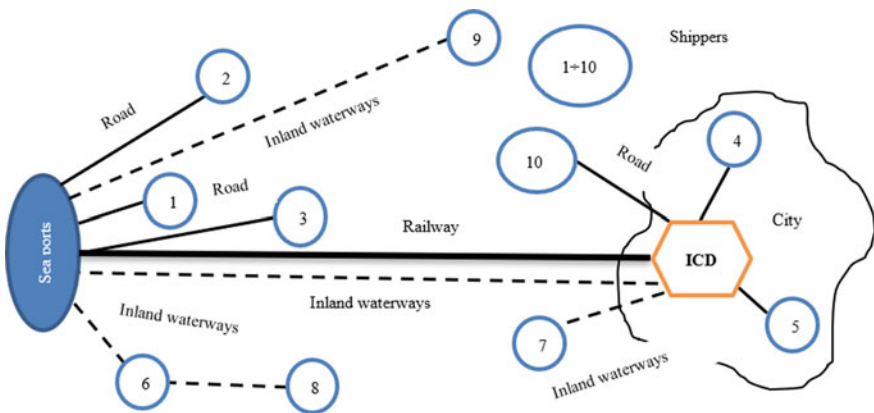


Fig. 1 Seaport with a distant ICD

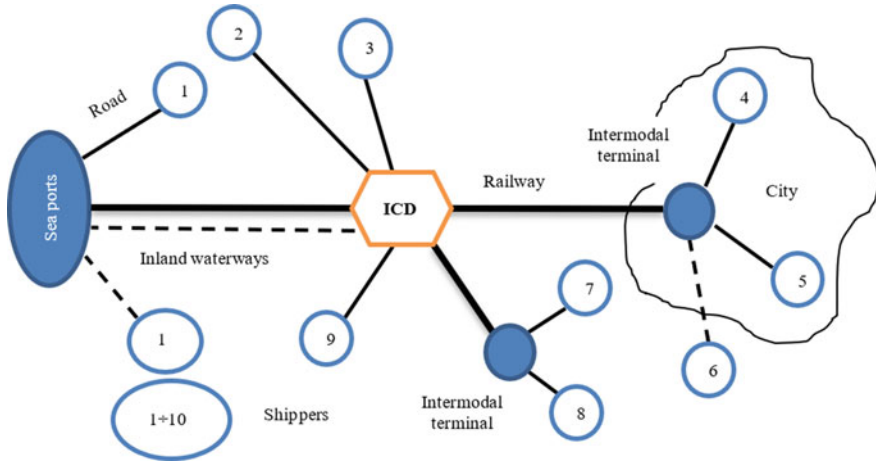


Fig. 2 A middle ICD in linking to the seaport

A near ICD is to describe an ICD placed at the edge of the seaport city. It supports for road transport from shippers outside the city area as shown in Fig. 3. Compared to the other types of ICDs, larger possibilities for buffering containers can be provided by a near ICD. Clearly, the risk of container vessels waiting is decreased significantly due to highly reliable rail service. A radius of less than 50 km from the seaport is relatively appropriate for setting up a close ICD [4].

A combination of the three types of ICDs could be alleviated drawbacks of road transport connecting between a seaport and its city area as shown in Fig. 4. In the case, the shippers closest to the seaport (1, 2, 9 and 10) connecting to a near ICD, shippers (7 and 8) linking to middle ICD through another intermodal terminal and the shippers (3, 4, 5 and 6) transporting to the distant ICD are used either railways

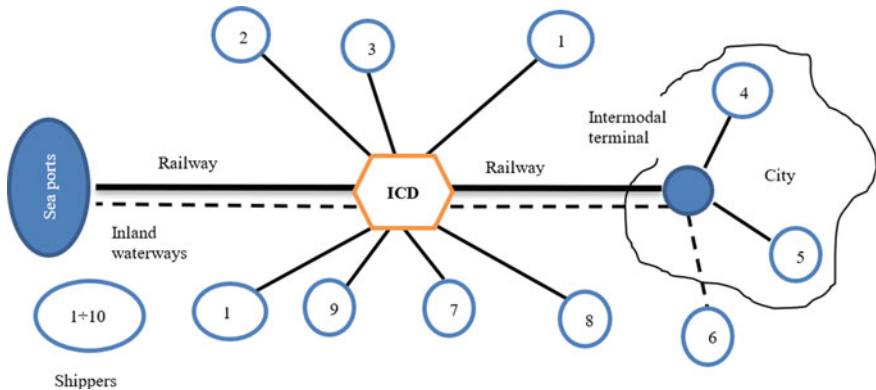


Fig. 3 An ICD in proximity with connection to the seaport

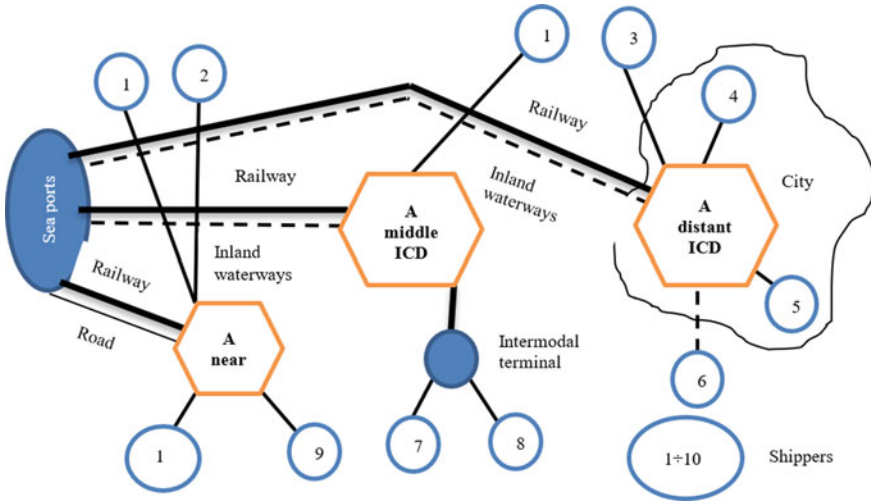


Fig. 4 A combination of intermodel connections with ICDs

or inland waterways to seaport. Consequently, gate congestion in the seaport is unavoidable. Therefore, the intermodel connections between seaports and shippers with ICDs is an answer this problem.

4 Conclusions

A conventional ICD concept is an initiative as a transport node to deal with a lack of capacity, efficiency issues and congestion in the seaports. Progressively, ICDs have confronted the high density of freight distribution, the augmented focus on multimodal transport infrastructures and capacity problems due to globalisation, containerisation, global logistics and supply chain. Thus, it is essential for ICDs to expand their functions to solve such problems. The development of ICDs is different from other countries due to local characteristics, but the global perspectives of ICD generations is the same way. This article proposes a combination of ICD's distributions based on their categories according to distance from seaports as one of solutions for dealing with the improvement of ICDs. For further research, other solutions will be considered such as the operational and tactical level to provide more studies in different regions.

References

1. Song D-W (2003) Port co-opetition in concept and practice. *Marit Policy Manag* 30(1):29–44
2. Jaržemskis A, Vasiliauskas AV (2007) Research on dry port concept as intermodal node. *Transport* 22(3):207–213
3. Rodrigue J-P, Debrie J, Fremont A, Gouvernal E (2010) Functions and actors of inland ports: European and North American dynamics. *J Transp Geogr* 18(4):519–529
4. Roso V, Woxenius J, Lumsden K (2009) The dry port concept: connecting container seaports with the hinterland. *J Transp Geogr* 17(5):338–345
5. Leitner SJ, Harrison R (2001) The identification and classification of inland ports. University of Texas at Austin. Center for Transportation Research
6. Walter CK, Poist RF (2003) Desired attributes of an inland port: shipper versus carrier perspectives. *Transp J* 42–55
7. Bergqvist R (2012) 13 Hinterland logistics and global supply chains. *Maritime logistics: a complete guide to effective shipping and port management*, p 211
8. Notteboom TE, Winkelmans W (2001) Structural changes in logistics: how will port authorities face the challenge? *Marit Policy Manag* 28(1):71–89
9. ECE U: UN/LOCODE–Code for Ports and other Locations (1998) Recommendation, pp 16:1–2
10. Fatimazahra B, Charif M, Alami S (2015) Dry port development: a systematic review. *J ETA Marit Sci* 3(2):75–96
11. Bergqvist R (2016) Dry port: the India experience and what the future holds—India needs to think out-of-the-box. In: *Dry ports—a global perspective*, pp 129–158. Routledge
12. Ng AY, Gujar GC (2009) Government policies, efficiency and competitiveness: the case of dry ports in India. *Transp Policy* 16(5):232–239
13. Monios J, Lambert B (2013) Intermodal freight corridor development in the United States. *Dry ports—a global perspective, challenges and developments in serving hinterlands*, pp 197–218
14. Kunaka C (2016) Dry ports and trade logistics in Africa. In: *Dry ports—a global perspective*. Routledge, pp 103–126
15. Bergqvist R (2015) *Hinterland logistics and global supply chains*, pp 67–88
16. FDT (2007) Feasibility study on the network operation of hinterland hubs (dry port concept) to improve and modernise ports' connections to the hinterland and to improve networking
17. Van Klink A (2001) Optimisation of land access to sea ports: beyond infrastructure. *Land access to sea ports ECMT report* 113

Fatigue Life Evaluation of Bogie Frame of Railway Covered Goods Wagons Using a Combined FEA/MDS Approach



Tuan Duc Do, Dat Tuan Vu, Toan Duc Nguyen, and Tu Anh Do

Abstract In this study, a combined method of the finite element analysis (FEA) and the multi-body dynamic simulation (MDS) was proposed to estimate the fatigue life of bogie frame of railway covered goods wagons. The multi-body dynamic (MBD) model of the wagon was built with the bogie frame body could be converted from the modal neutral file of FE model, which is obtained by using the ANSYS–ADAMS interface feature. The dynamic loads were obtained from the results of the MDS before being served as inputs in the structural dynamic analysis of bogie frame. From the results of structural dynamic analysis, the stress histories were determined and then used in the fatigue life analysis. The fatigue analysis model of the bogie frame was established based on the stress-life method. In addition, the effects of percentage probability of survival and reduction coefficient of material strength of were considered. The fatigue life of the bogie frame was estimated, then evaluated according to QCVN 87:2015/BGTVT.

Keywords Fatigue life · Bogie frame · Finite element analysis (FEA) · Multi-body dynamic simulation (MDS) · Stress-life method

1 Introduction

The bogie frames are the main load bearing components of railway vehicles and frequently subjected to dynamic loads, inducing cyclic stress that may lead to fatigue failures. In Vietnam, although the QCVN 87:2015-BGTVT [1] requires the

T. D. Do · D. T. Vu · T. D. Nguyen
Faculty of Mechanical Engineering, University of Transport and Communications,
No. 3 Cau Giay Street, Dong Da District, Hanoi, Vietnam

T. A. Do (✉)
Faculty of Civil Engineering, University of Transport and Communications,
No. 3 Cau Giay Street, Dong Da District, Hanoi, Vietnam
e-mail: doanhtu@utc.edu.vn

design service life of 30 years of bogie frames, but it does not specify what methodology should be used to evaluate fatigue life of bogie frame.

Under limiting conditions, the computer aided simulation method has been preferably used for fatigue life analysis of bogie frames [2–7]. In this paper, the combined analysis method of the FEA and MDS is proposed for fatigue life estimation of the bogie frame of railway wagon, which was locally manufactured in Vietnam. Fatigue analysis model was established based on stress-life method [8] with the effect of percentage probability of survival and reduction coefficient of ultimate tensile strength of material are considered.

2 Combinative Analysis Method

The proposed combinative analysis method for fatigue life calculation of a bogie frame with the implementation process includes the following steps:

1. Establishing FE model of the bogie frame in ANSYS as shown in Fig. 1. Using the ANSYS-ADAMS interface feature to create a modal neutral file (*.mnf).
2. Building MBD model of one railway wagon in ADAMS/View with the bogie frame as rigid body can be converted from the modal neutral file (*.mnf). The MBD model of the railway wagon is shown in Fig. 2 with the key specifications of wagon and the bogie frame are presented in Table 1.

When performing MDS, it is assumed that the vertical excitation of the left wheel (q_{iL}) and the right one (q_{iR}) are sinusoidal function, $q_{iL} = q_{iR} = A \sin[\omega(t + \Delta t_{i-1})]$, which is characterized by its amplitude $A = 0.012 \text{ m}$, angular frequency $\omega = 2\pi/T$ and period $T = L/V_{\max}$ with L is rail length, $L = 12.5 \text{ m}$, Δt_{i-1} is the time difference of the excitation between the i axle and 1st axle, $i = 2, 3, \text{ and } 4$. After performing the MDS, using the Export FEA Loads feature in ADAMS to export the dynamic loads acting on the bogie frame to a load file (*.lod).

3. Importing a load file (*.lod) to the FE model of the bogie frame and performing a structural dynamic analysis in the time-domain. Obtaining a result file (*.rst) includes the stress/strain histories.

Fig. 1 FE model of bogie frame

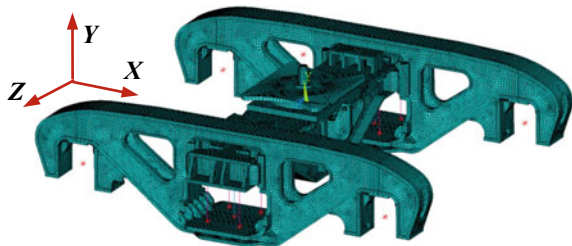


Fig. 2 Multi-body dynamic model of the railway goods wagon

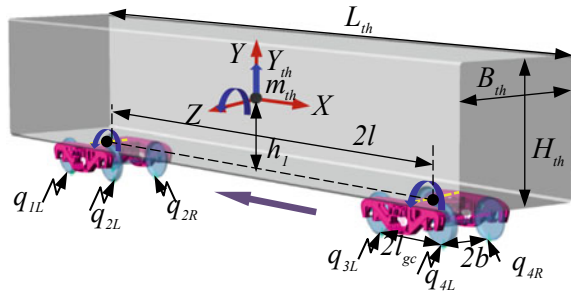
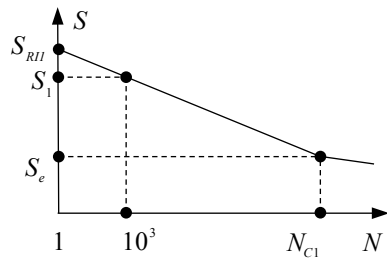


Table 1 The specifications of the wagon and bogie frame

Parameters	Values	Parameters	Values
Maximum designed operating speed of vehicle (V_{max})	100 (km/h) (≈ 27.78 m/s)	Distance between two axles in bogie frame ($2 l_{gc}$)	1.70 (m)
Distance between two centre plates of bogie frames ($2l$)	10.70 (m)	Distance between two wheel treads in wheel set ($2b_x$)	1.054 (m)
Height from body center of mass to centre plate (h_1)	1.341 (m)	Dimensions of wagon body: $L_{th} \times B_{th} \times H_{th}$	$15.0 \times 2.60 \times 2.565$ (m)
Mass of the wagon body (m_{th})	49,200 (kg)	Mass of wheelset (m_{wh})	916 (kg)
Mass of bogie frame (m_{gc})	1108 (kg)		

Fig. 3 S-N curve of material



4. Selecting the stress-life method [8] to establish a fatigue analysis model in ANSYS nCode DesignLife. In this model, the $S-N$ fatigue curve of the material, as shown in Fig. 3, was built with its parameters are calculated by Eq. (1) [9].

$$S_1 = 0.9\sigma_b; S_e = 0.357\sigma_b; S_{R11} = \frac{2S_e}{(N_{C1})^{b1}}; b_1 = \frac{(\lg S_e - \lg S_1)}{(\lg N_{C1} - 3)}; b_2 = \frac{b_1}{(2 + b_1)} \tag{1}$$

where S_{R11} is stress amplitude intercept corresponding to $N = 1$; S_1 is stress amplitude corresponding to $N = 10^3$; S_e is fatigue limit corresponding to transition point, $N_{C1} = 10^5 \div 10^7$; and b_1 and b_2 are first and second fatigue strength exponent; σ_b is ultimate tensile strength of the material.

In practice, the standard error (SE) of $\lg N$ is used to adjust the fatigue life predicted to any given probability of survival: $N_p(\%)$ is calculated based on the standard deviation (SD) of the mean (50%) life according to SE with the relationship between SD and $p(\%)$ is shown in Fig. 4 [9]. In addition, the Rainflow-counting algorithm [8] is used to count the number of cycles of different stress amplitudes. It allows the application of Miner’s rule [10] to calculate cumulative fatigue damage. With σ_b is chosen to be 490 N/mm^2 and $N_{C1} = 10^7$, the initial parameters of S - N curve are calculated using Eq. (1). The fatigue life of the bogie frame is estimated for the following cases:

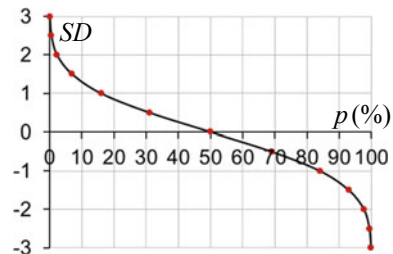
- The percentage probabilities of survival: $p(50\%)$; $p(90\%)$; $p(95\%)$; $p(99\%)$ and $p(99,9\%)$,
- Considering the impact of factors that reduces σ_b to k times. k is called the reduction coefficient of σ_b and is chosen with the values: $k = 1.0, 1.2$ and 1.4 .

3 Results and Discussion

3.1 Structural Dynamic Analysis

The Von-mises stress distribution of the bolster and the left side frame at the 70th load step as shown in Fig. 5.

Fig. 4 Relationship between SD and $p(\%)$



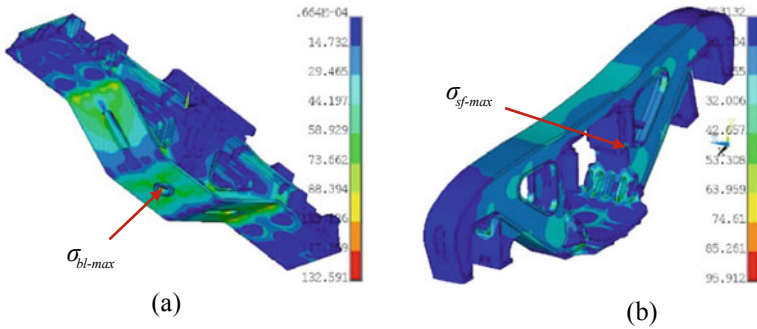


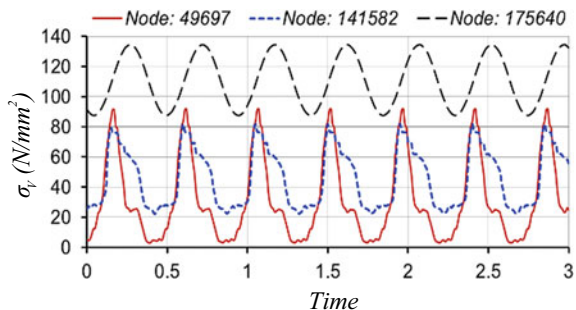
Fig. 5 Von-mises stress distributions of **a** bolster and **b** left side frame at the 70th load step

The stress concentration positions are at the interior edge of the hole on the bottom plate such as node 175640 on the bolster (σ_{bl-max}), and at the bottom corner of the interior slide plates such as node 49697 on the left side frame (σ_{sf-max}). The data of Von-mises stress time histories (σ_v) of some typical nodes in a period of three seconds with a time step of 0.01 s is shown in Fig. 6.

3.2 Fatigue Life Evaluation

The analysis results for different cases show that: the risk points are located at the contiguous corner between the slide plate and the bottom plate of the bolster such as node 141582, and at the node 49697 on the left side frame, as shown in Fig. 7. The fatigue life (N) of the risk points of the bogie frame were converted into years (N_{year}) of use as shown in Table 2. It can be seen that: in the cases of $k = 1.0$ and 1.2 with all the values of $p(\%)$, and in the case of $k = 1.4$ with $p(50\%)$, the fatigue life of the bogie frame is greater than the design service life of 30 years that meets the requirements of QCVN 87-2015-BGTVT [1].

Fig. 6 The data of Von-mises stress time histories of nodes



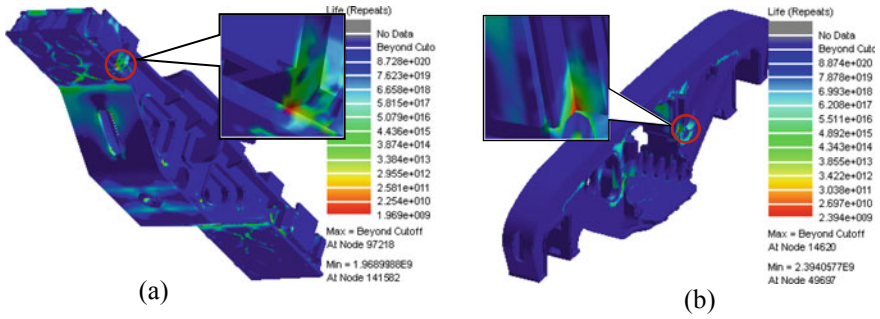


Fig. 7 Fatigue life distributions of **a** bolster and **b** left side frame

Table 2 The fatigue life of the bogie frame in different cases of $p(\%)$ and k

$p(\%)$	$k = 1$		$k = 1.2$		$k = 1.4$	
	N (cycle)	N_{year}	N (cycle)	N_{year}	N (cycle)	N_{year}
$p(50\%)$	8.62×10^{10}	8.20×10^3	5.48×10^9	5.21×10^2	5.16×10^8	4.91×10^1
$p(90\%)$	4.86×10^{10}	4.62×10^3	3.09×10^9	2.94×10^2	2.91×10^8	2.77×10^1
$p(95\%)$	4.13×10^{10}	3.93×10^3	2.63×10^9	2.50×10^2	2.47×10^8	2.35×10^1
$p(99\%)$	3.10×10^{10}	2.95×10^3	1.97×10^9	1.87×10^2	1.85×10^8	1.76×10^1
$p(99.9\%)$	2.37×10^{10}	2.26×10^3	1.51×10^9	1.44×10^2	1.42×10^8	1.35×10^1

4 Conclusions

A combined analysis method of FEA and MDS has been proposed to evaluate the fatigue life of bogie frame of railway covered goods wagons based on the stress-life method. In different cases of the percentage probability of survival ($p(\%)$) and reduction coefficient of ultimate tensile strength (k), the results of fatigue life estimation show that: in the cases of $k = 1.0$ and 1.2 with all the values of $p(\%)$, and in the case of $k = 1.4$ with $p(50\%)$, the fatigue life of the bogie frame is greater than the design service life of 30 years of bogie frame that meets the requirements of QCVN 87-2015-BGTVT [1].

The research methodology and results can be used to evaluate fatigue life of similar locomotive and wagon components, as well as to assist in design and manufacturing of such components.

Acknowledgements This research was supported by a grant from Di An Train Joint Stock Company in Socialist Republic of Vietnam.

References

1. QCVN 87:2015-BGTVT (2015) National Technical regulation on railway vehicles railway car's bogies—technical requirements. Vietnam Ministry Transp
2. Miao BR, Zhang WH, Zhang JH, Jin DCh (2009) Evaluation of railway vehicle car body fatigue life and durability using multi-disciplinary analysis method. *Int J Veh Struct Syst* 1(4):85–92
3. Bishop NWM, Sherratt F (2000) Finite element based fatigue calculations. *NAFEMS*
4. Kamal M, Rahman MM, Sani MSM (2013) Application of multibody simulation for fatigue life estimation. *Int J Automot Mech Eng* 7(1):912–923
5. Luo RK, Gabbitas BL, Brickle BV (1994) Fatigue life evaluation of a railway vehicle bogie using an integrated dynamic simulation. *Proc Inst Mech Eng Part F J Rail Rapid Transit* 208(2):123–132
6. Dietz S, Netter H, Sachau D (1998) Fatigue life prediction of a railway bogie under dynamic loads through simulation. *Veh Syst Dyn* 29(6):385–402
7. Ozsoya M, Pehlivanb K, Firata M, Ozsoya N, Ucara V (2015) Structural strength and fatigue life calculation of Y32 bogie frame by finite element method. *ACTA Physica Polonica Series A* 128(2B):B327–B329
8. Stephens RI, Fatemi A, Stephens RR, Fuchs HO (2000) *Metal fatigue in engineering*, 2nd edn. John Wiley & Sons, New York
9. HBM-nCode (2013) ANSYS 15.0 nCode DesignLife—DesignLife Theory Guide. HBM United Kingdom Limited
10. Fatemi A, Yang L (1998) Cumulative fatigue damage and life prediction theories: a survey of the state of the art for homogeneous materials. *Int J Fatigue* 20(1):9–34

Maximum Likelihood Estimation Method for Speed Prediction of Vehicles in Mixed Traffic Condition



Dang Minh Tan, Nguyen Hoang Tung, and Bui Xuan Cay

Abstract Overall objective of this study is to develop a traffic simulation model to realistically present the traffic flow in mixed traffic conditions. The simulation model can be used as applications in the fields of traffic operation and safety. This paper as a stage of the overall study presents a method to estimate speed of vehicles in mixed traffic condition in Ha Noi, Viet Nam. Several straight street segments in Ha Noi, Viet Nam were selected for observation. The traffic data includes vehicle types, speed that were extracted by using an image processing tool and other necessary data such as geometric conditions of streets. The result shows that there is a significant difference between free-flow speed of motorbikes and cars in different geometric conditions of the streets. The Maximum Likelihood Estimation method was used to develop a model for speed prediction of vehicles that takes into account types of vehicles and street geometric conditions. A Monte Carlo simulation method was also used to verify the developed speed model. It is concluded that the model can realistically represent the speed behavior of vehicles in the mixed traffic condition.

Keywords Mixed traffic · Traffic simulation model · Traffic safety and operation · Maximum likelihood estimation · Speed modeling

1 Introduction

Currently traffic simulation models have been used as effective tools for traffic safety and operation evaluation. However, several well-known prevalence models such as VISSIM, AIMSUN and so on still remain limitations for realistically presenting real various traffic conditions, such as mixed traffic conditions in Viet Nam. In which the rate of motorcycle accounts for around 70% and traffic condition in the city usually is very chaotic. The overall objective of the study is to develop a traffic

D. M. Tan (✉) · N. H. Tung · B. X. Cay
Faculty of Civil Engineering, University of Transport and Communications, Hanoi, Vietnam
e-mail: tandang@utc.edu.vn

© The Author(s), under exclusive license to Springer Nature Singapore Pte Ltd. 2021
T. Bui-Tien et al. (eds.), *Proceedings of the 3rd International Conference on Sustainability in Civil Engineering*, Lecture Notes in Civil Engineering 145,
https://doi.org/10.1007/978-981-16-0053-1_45

359

simulation model which is used to represent the mixed traffic condition in Viet Nam. At the beginning it is vital to understand behavior of road users such as speed of vehicles and factors influencing the speed behavior. Around the world, there have been several studies on the spot speed of vehicles at highway or street segments, in many different conditions and the purposes of safety and traffic organization such as [1, 2, 3, 4]. However, these studies still have limitation that does not reflect the randomness of speed of individual road users. The models are mainly used to predict an operational speed, such as 85 percentile speed. Thus, maximum likelihood estimation (MLE) method is used in this paper to model speed behavior of vehicles in mixed traffic condition that can realistically represent the randomness characteristics of vehicle speed. Several urban street segments in Ha Noi, Viet Nam were selected for data collection. The data includes geometric condition, traffic volume, vehicle types and speed. An image processing tool was used to collect data for empirical analysis. And finally, by using Monte Carlo simulation, the model is verified to ensure the reality.

2 Maximum Likelihood Estimation Methods for Modeling Speed Behavior

2.1 Methodology

MLE method is a very important method for probabilistic estimation of parameters of road user behavior models used for representing road traffic networks that can be integrated for developing traffic simulation model [5]. In detail, it is a technique used for parameter estimation of a given distribution, based on the observed data. This estimation method is widely used for presenting the randomness of natural phenomena as road user behavior. MLE methods are found in several studies in the transportation field, [6, 7, 8]. Taylor [7] presented a maximum likelihood method for parameter estimation of a path choice model for road traffic networks. His work indicated that the procedure is both convenient and quick, and model parameter estimation may be accurately obtained. Bunker [8] presented a MLE method for estimating traffic critical gap and indicated that MLE technique can be regarded as the most accurate for estimating critical gap.

In this study, the MLE method [9] was used to model the spot-speed of vehicles. From a statistical aspect, as an example, there is a given data of spot speed of n vehicles which are observed at fields. Each vehicle i has a speed of X_i . Assuming $x_1, x_2 \dots x_n$ are observed from n independent and identically distributed random variables, where $f(x|\theta)$ is a probability density function (PDF) and θ is a representative parameter. The likelihood of θ is shown in Eq. (1).

$$L(\theta) = f(x_1, \dots, x_n | \theta) \tag{1}$$

Maximizing $L(\theta)$ is equivalent to maximizing $\log L(\theta)$ and $\log L(\theta)$ is defined as log likelihood function, and it is denoted as $l(\theta)$ shown in Eq. (2).

$$l(\theta) = \log L(\theta) = \sum_{i=1}^n \log(f(x_i | \theta)) \tag{2}$$

Maximizing $l(\theta)$ with respect to θ can be considered as MLE estimation.

2.2 Data Collection

The paper focuses on the analysis of traffic flow in Ha Noi that is a representative of mixed traffic in Vietnam. However, traffic in Ha Noi is generally very complicated and chaotic, especially at intersections with mixed traffic flows. Thus, the research scope of this paper focuses initially on modeling traffic flow on straight sections (continuous flow). Traffic flow at straight segments is important for traffic simulation of a road network, because traffic flow is usually generated at such straight segments before going to signalized intersections.

Therefore, the street segments selected for analysis are located on long straight streets and not near the intersections, then there will be no changing directions to other streets. The selected street segments have different widths. There is no raised median separator between the two directions. In this study, there are three road segments selected as shown Table 1. All segments locate in an urban area in Cau Giay District, Hanoi, Viet Nam. On each street segment, one straight section chosen for the analysis is about 50 m length. During the duration for data collection, there is no parked vehicle on the segment that affects behavior of running vehicles. Survey duration was conducted on each segment from 1 to 2 days, in good weather conditions and no rain. At each segment, an hour data during off-peak period from 9AM to 10AM was extracted for analysis.

Table 1 Parameters of the streets to be surveyed

No.	Name of the street	Width of the street surface (m)	No. of lane	Vehicles/Analysis direction/hour*	Direction for analysis
1	LS2	8.2	2	350	From Nguyen Chanh to Ringroad 3
2	Nguyen Quoc Tri (NTC)	10.8	2	614	From Trung Hoa to Cau Giay
3	Nguyen Chanh (NC)	15	4	2682	From Trung Hoa to Cau Giay

*Traffic volume was counted for a single direction which was chosen for analysis

The data collected here includes following parameters: (1) The geometry of the streets; (2) traffic volume and vehicle types; and (3) Speed of the vehicle.

To obtain traffic data, an image processing technology was used for analysis [10]. Whereby cameras were placed on high-rise buildings for recording video images of vehicles passing through a cross section of the street segment. The videos then were inputted into the traffic analysis tool [10] and through which traffic data was collected. At each street segment, a cross-section was chosen to determine the passing speed of vehicles. The speed data taken includes the free flow speeds, classified by vehicle types. Randomly, free-flow vehicles that include motorcycle and car were chosen for analysis.

3 Results and Discussion

Traffic volume is shown in the Table 1. The vehicle composition at these street segments includes mainly motorcycles and passenger cars, accounting for nearly 100%. In which, motorbikes account for 67–75%, while passenger cars are 23–31%. Buses and trucks account for a very small proportion, about 1–2%. Trucks and buses are mainly concentrated on Nguyen Chanh street while on the other two routes are negligible. So in this study, passenger cars, bus, trucks are considered as cars for analysis in general.

Figure 1 and Table 2 show statistic information of speed of vehicles when passing cross-section at LS2, Nguyen Quoc Tri and Nguyen Chanh street segment. The result shows that vehicles have a greater speed when the street segment width is wider. Moreover, speed of cars is smaller than those of motorbikes. This is quite reasonable because drivers will have more space to run freely, if the streets are wider. Moreover, in mixed traffic condition in urban streets in Viet Nam similar as in the observed sites, cars are usually slower than motorcycles because with the same width of street, they have less free space and flexibility for movement as comparing to motorcycles.

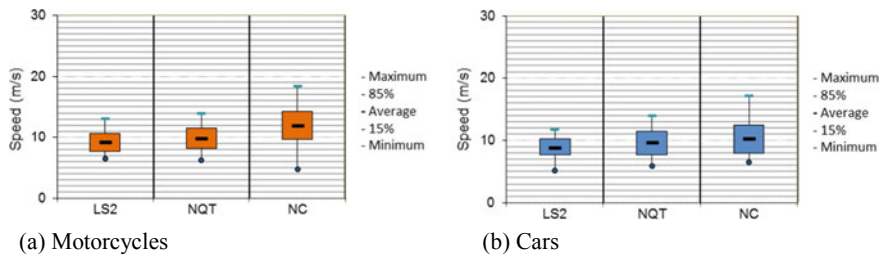


Fig. 1 Box analysis of free flows speed of vehicles

Table 2 Statistic values of free flow speed of vehicles

Statistic parameters	Unit	Motorcycles			Cars		
		LS2	NQT	NC	LS2	NQT	NC
Maximum	m/s	13.04	13.98	18.37	11.73	13.95	17.09
15%	m/s	7.73	8.19	9.69	7.62	7.67	7.95
85%	m/s	10.66	11.58	14.29	10.20	11.49	12.45
Average	m/s	9.23	9.79	11.92	8.86	9.72	10.34
Minimum	m/s	6.51	6.24	4.76	5.21	5.85	6.45
Standard deviation		1.36	1.56	2.31	1.43	1.77	2.15
Number of sample		57	108	180	31	55	90
Goodness of fit test for normal distribution (P-value)		0.391	0.450	0.357	0.969	0.450	0.070

3.1 Modeling Speed Behavior Using MLE Method

By using Individual Distribution Identification test, it is found that all of the distributions of observed data as shown in Table 2 follow a Normal distribution. Equation (3) shows a PDF function of a normal distribution for presenting speed.

$$f(x) = \frac{1}{\sigma\sqrt{2\pi}} * e^{-\frac{1}{2}*\left(\frac{x-\mu}{\sigma}\right)^2} \tag{3}$$

where: $f(x)$ is PDF; μ is average value and σ is standard deviation.

Through the results as shown in Table 3, it shows that the rule of free flow speed of vehicles depends on vehicle types and the width of the street segments. Thus assuming the parameters of μ , σ can be expressed as follows function:

$$f(X_1.X_2) = c_1X_1 + c_2X_2 + c_3 \tag{4}$$

where:

X_1 is the width of the street surface (m) and

X_2 is the dummy variable to represent vehicle type, $X_2 = 0$ for motorcycles and $X_2 = 1$ for cars

c_1 , c_2 and c_3 are the constant values determined by the MLE method.

Using Stata statistical software [11] and Stata programming language to build a normal distribution model with vehicle speed time data on LS2, Nguyen Quoc Tri, Nguyen Chanh street from which the model parameters were built (refer to Table 3). The variables have p values <0.05 , representing that the independent variables correlate well with the dependent variable and it is statistically significant.

Table 3 Summarizing statistical parameters of the model

Parameter	Constant value	Std. Err.	z	P > z
μ				
X1	0.696377	0.058232	11.96	0.000
X2	-0.73138	0.17169	-4.26	0.000
_cons	6.361763	0.347566	18.3	0.000
σ				
X1	0.266699	0.040831	6.53	0.000
_cons	0.271092	0.239868	1.13	0.258

Table 4 Statistic comparison between observed and simulated speed data

Statistic parameters	Unit	Motorcycles		Cars	
		Observed data	Simulated data	Observed data	Simulated data
Maximum	m/s	13.98	15.35	13.95	13.72
15%	m/s	8.20	8.17	7.67	7.67
85%	m/s	11.58	11.60	11.49	10.93
Average	m/s	9.81	9.89	9.72	9.28
Minimum	m/s	6.24	4.40	5.85	4.19
Standard deviation		1.56	1.69	1.77	1.60
Number of sample		108	770	55	250
T-value		-0.55		1.74	

3.2 Model Verification

By using Monte Carlo method [12], data was generated from the model that shows in Table 4 and comparing with observed value. As show in Table 4 generally, the simulated data fits well the observed data. By using the T-test, there is no statistically different between simulated data and the observed data.

4 Conclusions

The paper developed a stochastic model for representing speed of vehicles in mixed traffic condition for use in development of traffic simulation models. The MLE technique has been argued to be a powerful technique for presenting stochastic characteristic of behavior of road users. The result shows that the free flow speed of vehicles at a cross-section of urban streets in Ha Noi, Viet Nam follows a normal distribution. The result also shows that motorcycles generally have higher speed as

comparing with cars in such urban streets, and wider street contributes to higher speed of vehicles. Moreover, the developed model realistically represents the randomness characteristic of speed of vehicles and the impacts of vehicle type and width of street on vehicle speed. The developed model can be used as an integrated model in a traffic simulation model or in various applications of traffic operation and safety assessment in urban areas in Viet Nam with mixed traffic flows. For the future works, it is necessary to obtain more data in various geometric and traffic conditions to improve the applicability of developed model and necessary to intergrade the developed model into a simulation model.

References

1. Ashish D, Satish C (2013) Speed prediction models for urban arterials under mixed traffic conditions. *J Procedia Soc Behav Sci* 104:342–351
2. Dey PP, Chandra S, Gangopadhaya S (2006) Speed distribution curves under mixed traffic condition. *J Transp Eng ASCE* 132(6):475–491
3. Kay F, Paul JC, Mark DW, Marcus AB (1999) Report 1769-3, design factors that affect driver speed on suburban streets. Texas Department of Transportation, US
4. Do DD, Hisashi K (2013) Profile-speed data-based models to estimate operating speeds for urban residential streets with a 30 km/h speed limit, *IATSS Res* 36(2):115–122 (2013)
5. António L, Marco A, Carlos R, António C (2018) Modelling the operating speed in segments of two-lane highways from probe vehicle data: a stochastic frontier approach. *J Adv Transp* 2018
6. Tan DM, Alhajyaseen WK, Asano M, Nakamura H (2012) Development of microscopic traffic simulation model for safety assessment at signalized intersections, transportation research record. *J Transp Res Board* 2316
7. Taylor MAP (1981) Maximum likelihood estimation for a road traffic network model. *Appl Math Model* 5(1):34–38
8. Bunker JM (2012) Novel methods and the maximum likelihood estimation technique for estimating traffic critical gap. *J Adv Transp*
9. Myung IJ (2003) Tutorial on maximum likelihood estimation. *J Math Psychol* 47(1):90–100. [https://doi.org/10.1016/s0022-2496\(02\)00028-7](https://doi.org/10.1016/s0022-2496(02)00028-7)
10. Dang MT (2018) A smoothing method to reduce data noise: a functional analysis of speed profile of road users. In: Conference proceedings, ICSCE 2018 international conference
11. StataCorp (2015) Stata 14, 4905 Lakeway Drive, USA
12. Gamerman D (1997) Markov Chain monte carlo: stochastic simulation for bayesian inference. CRC Press, Boca Raton, FL

Transportation Development Strategy in Coordinating with Urban Dynamics: Case Study in Hanoi



Le Thu Huyen

Abstract The future cities will not be the same like today - cities will and have to change. For the urban development it requires on the one hand to consider and identify needs of the future and on the other hand to exploit upcoming opportunities. New social challenges owing to climate change, urbanization, globalization but also cultural and technical developments impose great challenges for city planners. Technical developments and new innovative systems enable new directions and changes of conventional considerations. These ongoing developments will also substantially increase the demands of future solutions in the urban transport, mobility and logistics environment. Therefore, new, innovative and future-oriented concepts are essential for sustainable, environmentally friendly and efficient transport, mobility and logistics. They will and have to become much more an integrated, networked and shaping component of modern urban development. The paper covers key issues, aiming at introducing the strategy for Hanoi sustainable development as the orientation for integrating urban dynamics and transportation development.

Keywords Sustainable transport · Urban dynamics · Integrated masterplan

1 Introduction

Urbanization has been one of the dominant contemporary processes globally. In this trend, urban dynamics issues are of the foremost importance to support mobility in agglomerations. Urban transport is highly complicated because of the modes involved, origin/destination multitude, also traffic quantity and variety. Traditionally, the passenger transportation has an essential role as cities were locations of utmost human interactions with intricate traffic patterns related to commuting, commercial transactions and leisure/cultural activities. Moreover, cities

L. T. Huyen (✉)

University of Transport and Communications, Hanoi, Vietnam

e-mail: lethuhuyen@utc.edu.vn

also involve activities of production, consumption and distribution, linking with cargo movement. Urban transit is an important dimension of mobility, notably in crowded areas.

Conceptually, the transport system is linked with urban form and spatial structure. Such elements, namely transportation modes, infrastructures and users, have a spatial imprint, which shapes the urban form. Considering that cities have different socio-economic and geographical characteristics, spatial transportation imprints may vary accordingly. The urban transport system is also represented by its spatial interactions with its own circulation pattern of passengers and freight. Urban transportation aims at fulfilling transport demands generated by activities' diversity. A key for understanding urban entities thus lies in analyzing the transport/land use system, which is complicated with interactions.

Transportation and land use are parts of a retroactive feedback system. Changes in transportation technology, investment and service characteristics can alter overall accessibility levels as well as the relative accessibility of different locations. Land use changes also affect activity patterns, leading to changes in trip generation, both for passenger and freight. Trip patterns may change in different ways, such as the number and timing of trips, their origin/destination, modes, and trip chaining. These changes in travel demand exert considerable influence on the development of transportation infrastructure/services. As such, interactions between transportation and land use are often referred as a "chicken-and-egg" conundrum: "You can start with land use, or start with transportation; in either case, the basic feedback lead inevitably to a hierarchy of central places and transportation links connecting them" [1].

Economics and social activities depend on the capacity of the urban transportation system. The transport system does not only allow mobility of passengers and freight, but also influences on urban development attributes and social and economics activities through different urban zones' accessibility. Meyer et al. [2] confirmed that urban activities and transport system own the interaction relationship, bounding and decide each other in the process of establishing, developing and implementing (Fig. 1).

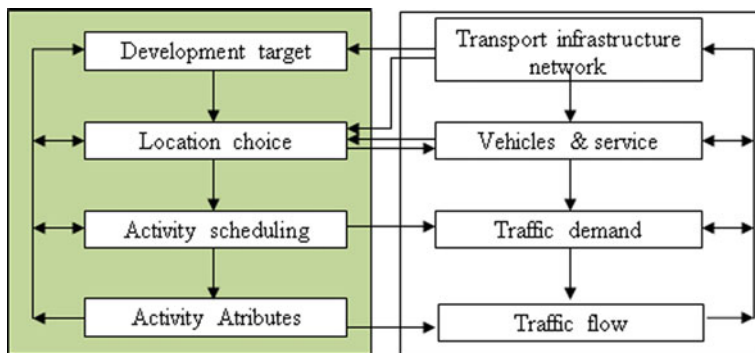


Fig. 1 Interaction relationship of urban activities and urban transport system. Source Mayer et al. [2]

Interacting relationship between urban and transportation system is the scientific and practical basis always requiring to ensure synchronous integration among urban development (economics, society, spatial) and transportation. They are required in all phases, from process of policy making, planning, conducting the financial plans, implementing the master plan and controlling impacts of development projects.

2 Current Issues and Solutions for Hanoi

In almost every urban area in Vietnam, there are still a lot of problems and issues in the system of urban transportation and urban management. Among which, the biggest issues are such problems of capacity of planning authority at city level; ability to cooperate and coordinate among bodies; ability of cooperate between authority at the city and district/commune levels when establishing and implementing projects of planning, of transportation and infrastructure development.

Currently, it can be seen that Hanoi assignment of urban planning meet many limitations. The capacity of authorized bodies is not appropriate with the requirements of social-economics development. The implementation process is rather slow, especially in the area of districts/communes. The common issue is unclosed coordination and cooperation between investment owners and consultant. The quality of master planning is not high, due to the lack of sufficient survey data, inconsistent reports, etc. Too ambitious goals and objectives without feasibility in finance and technology also lead to the failure (Fig. 2).

The limitation of Hanoi master plans can be seen in the current situation. In Hanoi and surrounding, people are affected by heavy emissions and smog incidents and threatened by increasing heavy rainfall events, sea level rise and flooding of the Red River. Furthermore, rapid and uncontrolled urbanization and growth of traffic,

Major Transport Development Criteria	Planned Performance (2020)	Actual Performance (2020)
Urban land for transport	15% total urban land	7% total urban land
Urban transport system characteristics	Intermodal, Integrated and Modernized	Motorcycle Dependent
Public transport ridership	45% vehicle travel demand	12% vehicle travel demand
Motorcycle ridership	30% vehicle travel demand	80% vehicle travel demand
Number of urban rail lines	5 lines	2 lines in construction
Parking area	796 ha	35 ha

Fig. 2 Difference between planning target and performance (updated from [3])

emissions and waste in the megacity are current challenges that need to be faced. The aforementioned master plan recognizes the need to reduce emissions and produce a better air quality. Macroscale solutions suggested are steering the cities development into an outer collar zone and into several satellite cities, in order to relax the stressful situation (traffic, pollution, SMOG) in the center. Furthermore, urban green spaces are planned to be conserved, established, and extended to improve environmental quality, including air quality and water retention. The Hanoi master plan, thus, develops a macroscopic perspective onto the cities' development.

In general, capacity of urban transport planning and other sectoral planning cannot meet the requirements of social economics development. TDSI [4] has released statistics data of the current situation, which shows that projects of transport system development are missing or slow in implementing. Railway system has the backward technology, with the small share in transport demand. Inland waterway covers the lower share than its potential as depending only on nature. Urban transport is seriously overloaded, with the low public transportation rate of 15% (40–60% as standard). There is lack of modern and advanced logistics infrastructure, as well as lack of intermodal transportation system in the city. 10–60% of urban roads including national, provincial and city roads are in poor surface conditions. The urbanization rate has a significant impact in terms of population growth, pressure on housing and land-use, demand on infrastructure capacity and service provision. Traffic congestions (with 60% travel time is delay within the urban area) are rather serious with the unbalance of supply and demand side. Flooding/drainage, traffic safety and parking are main problems. The traffic accidents, which occur mainly on the urban arterials and sub-urban highways, cover the high rate of fatalities with frequently occurring during night-time and off-peak period. The noise is the most serious environmental problem of motorcycle traffic flow. Two-stroke engine motorcycles cause terrible problems in air pollution (vehicle emission).

It can be determined the causes in the transport field and from external fields, such as urban and transport plans. They have failed by ambitious goals and objectives; foreigner dependent planning; lack of resources (technical, financial, human) and complicated structure and low competency institutions. Such problems (and others) raised the needs for integrating technical infrastructure planning, sectoral planning (as well as transport system planning) in a process of general master plan for an urban area's development toward a sustainable and efficient target.

The concept of urban and landscape planning integrates principle spatial strategies of climate mitigation and adaptation as nature development, urban restructuring and energy transformation by connecting divers' solutions of the transdisciplinary research and participative planning process on every spatial level: region–city–district–quarter–house.

Foci of resilient, sustainable urban and landscape planning are (i) structural transformative interventions within the existing building stock, enhancing green, energy, water and mobility management and resource saving, climate-neutral,

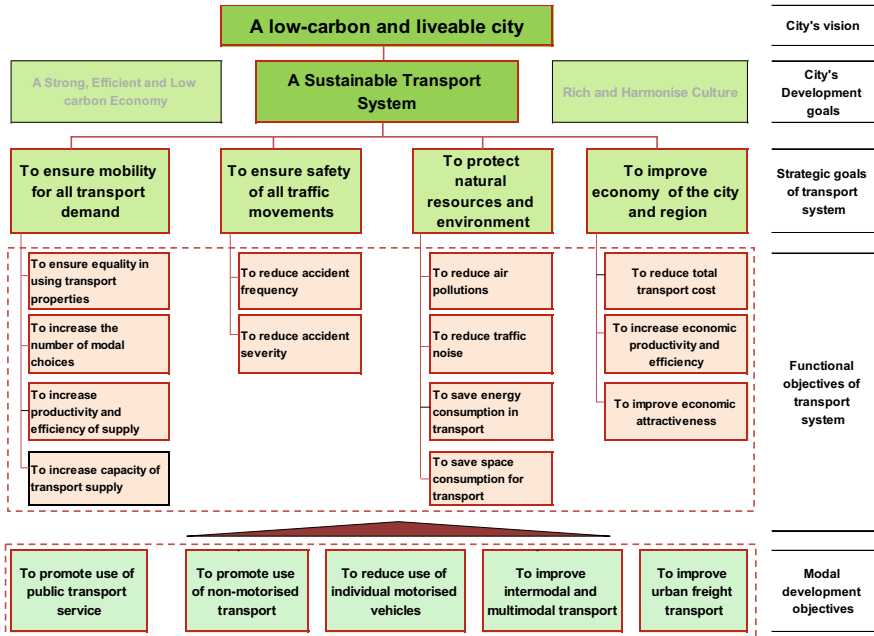


Fig. 3 The development scheme for major cities

(ii) implementation of renewable energy systems (urban and regional context), (iii) cultivation of organic farming land-use in the regional context. With the aim to balance urban and landscape development and the city-river-relation, the mentioned solutions will be conceived exemplarily in concrete urban quarters: implementable in the local context as well as connectable and transferrable through the integrative spatial concept for Hanoi megacity, which actually does not exist.

The urban development process includes a series of complicated issues with interacting relationships, which requires a comprehensive and synchronous set of solutions. Transportation development has great influences on land-use model and vice versa. The models of land-use and water are such elements determining living quality. Therefore, major strategies need to be established aiming at sustainable targets. Meanwhile, it can help establishing action plans of involved disciplines.

From the vision of orienting towards a low-carbon and livable city, the development frame for Hanoi (as well as other major cities in Vietnam) can be shown in the following Fig. 3.

Major strategies for Hanoi are described as follows:

Strategy 1: Establishing the spatial axes including “water”, “green trees” and “cultures” in order to ensure environmental stability and improve Hanoi’s image.

For remaining Hanoi unique history, the urban master plans should cover:

- The Red River and areas of Co Loa—Thang Long shall be protected to form the central axe of “water surface—green trees—culture”.
- The axe of “water surface—green trees—culture” then shall be extended to cover the whole city by combining all available resources, such as lakes, rivers, green streets, other open spaces, cultural and heritage places, ...

Strategy 2: *Developing the urban area in the public transport orientation in order to ensure people’s mobility capacity and encourage to equally develop the society in the balance with environment protection.*

It is essential for the city to provide a high qualified public transport system synchronously developed with the urban development process. The UMRT, metro and BRT form the backbone network of the system. Such transit modes shall efficiently connect and serve different urban areas, aiming at adjusting and modifying people’s travelling habit. The following issues shall be taken into consideration:

- Developing the satellite towns as well as CBDs along the transit corridors, so that the social and economics activities are connected at a high performance.
- Distributing reasonable shares with the private transport when living standards is increasing with the variety of demands. Private can play the role of feeders for public transport system.
- Committing in a long term period with the consistent policy, as well as public awareness and contribution.

Strategy 3: *Improving and recovering constructed areas both in city center and outer area in an appropriate manner with different areas.*

Hanoi is in need of mechanism to recover urban areas. Those are restructuring land use, renovating the urban area, building the suitable legislation and encouraging public contribution into the urban planning and implementation process.

Strategy 4: *Developing modern urban centers with a high competition in order to attract various investments at high quality, as well as encouraging job opportunity.*

This strategy may require mixed land-use, along with the clear functions and attributes of different urban centers. At the same time, it is required to organize the efficient transportation corridors to serve such new centers.

Strategy 5: *Developing the efficient infrastructure and service in order to ensure the convenient social economics activities with the high competitiveness as well as services at the reasonable prices.*

Infrastructure development must be planned and implemented in the comprehensive manner requiring good operation and management with the participation of private sector. This may push the efficiency and encourage the qualified service.

3 Conclusions

It can be summarized that in the coming time, Hanoi is still depending on motorcycle in term of accessibility and mobility. There is a serious unbalance between the demand and supply in transport infrastructure. Accelerating urbanization requires sustainable and balanced urban/regional development. The city's big challenge is transport planning and management capacity with such issues as:

- Car use is growing and evidently causing both congestion and accidents.
- Almost no chance to have balance car dependent situation, but cleaner and safer motorcycle with bus transport improvement should be emphasized.
- Transit Oriented Development is a solution, but may not be the optimal solution.
- Traffic Management must be key strategy in the urban transport development.

From the perspective of conducting master plans of development, there are several problems and conflicts during the process of establishing different projects of master plans. Therefore, it raises the need for developing and following the integrating process of planning to obtain the comprehensive and efficient results. Urban planning shall focus on the highly increasing population with the immigration rate. The urban areas at different levels require different planning criteria. The integrating process of urban planning raises the requirements for interaction and close cooperation among different industries and authorities. It is required not only to improve and extend the urban infrastructure system, but also to optimize the operation.

References

1. Moore T, Thorsnes P (2007) The transportation/land use connection. American Planning Association, ISBN-13: 978-1932364422
2. Meyer et al (2001) Urban Transportation planning: a decision-oriented approach. McGraw-Hill
3. Le TH, Tu NT (2020) Chapter 173 vehicle usage/ownership control for a sustainable transport system in the motorcycle dependent cities. Springer Science and Business Media LLC
4. TDSI (Transport development and strategy institute) (2020) Transport and logistics statistical yearbook